Radiation damage studies of silicon detectors and searching for an intermediate mass Higgs boson at ATLAS

Robert Stuart Harper
University of Sheffield

CERN-THESIS-2001-083
01/10/2001

A thesis submitted for the degree of
Doctor of Philosophy in the subject of Physics,
October 2001.

Parallel lines, move so fast,
towards the same point,
infinity is as near as it is far.

Parallel Lines, Kings of Convenience

Abstract

Parameterisations of bulk radiation damage in silicon are used to develop a model for the evolution of leakage currents in silicon microstrip detectors held under bias during irradiation. Leakage current measurements taken during proton irradiation of detectors at low temperatures are used to calculate the radiation damage parameters α, the current-related damage constant, and β, the rate of acceptor creation. It is found that $\alpha(20°\mathrm{C}) = (4.84 \pm 0.13) \times 10^{-17}$ A cm^{-1} and $\beta = 0.0630 \pm 0.0018$ cm^{-1} (for temperatures of -8 to $-10°$C), both in agreement with previous results. These parameters are subsequently used to model bulk characteristics of silicon detectors during operation at the ATLAS experiment. Although a significant increase in full depletion voltage is predicted during operational periods, due to a large contribution from unstable acceptor creation, the final results are in general agreement with previous experimental studies.

The weak boson fusion production process gives a distinctive signature for a Standard Model Higgs boson due to forward tagging jets in the final state. The decay $H \rightarrow WW^{(*)} \rightarrow l^+l^- p_T^{miss}$ is studied as a discovery channel for an intermediate mass Higgs boson, and acceptance cuts are developed to isolate the signal from the main Standard Model backgrounds. A signal can be observed above the 5σ level for $m_H = 160 - 180$ GeV with an integrated luminosity of 5 fb^{-1} and for $m_H = 150 - 200$ GeV with 10 fb^{-1}. Increasing the luminosity to 30 fb^{-1} gives a discovery range of $m_H = 140 - 200$ GeV and makes this channel robust against systematic uncertainties on signal and background rates. The discovery range could not, however, be extended to the light Higgs boson region with $m_H \approx 115$ GeV due to the small branching ratio for $H \rightarrow WW^{(*)}$ in this region.

Acknowledgements

First and foremost I would like to thank my supervisor Craig Buttar for all his help and patience over the last three years. Without his guidance and good humour I would never have got here. I would also like to thank everyone else in the Sheffield HEP group for making my time here so enjoyable, particularly Mark Lehto and Paul Hodgson for their help with PAW and other computer stuff, Dan Tovey for trying to teach me statistics, Ian Dawson my radiation guru and Chris Grigson for all his help with hardware matters.

For the detector irradiation work I would like to thank Craig, Ian and Chris again, plus Richard Nicholson for being great people to work with, and also Laci Andricek, Gianluigi Casse, Janet Carter, Lars Ecklund, Richard Fortin, Andreas Fürtjes, Maurice Glaser, Alick MacPherson, and Dave Robinson. Within the ATLAS Higgs working group I must thank Elzbieta Richter-Was, Karl Jakobs, Markus Klute, Rachid Mazini and Richard Steward for all of their help. For funding me through the last three years, including many trips to CERN, I am extremely grateful to my research council, PPARC.

Of course it's not been all work, so I'd firstly like to thank all of my housemates over the last few years; Russ, Paul, Rachel, Stuart, Ben and Gaz for putting up with my bad habits and occasional bad moods, and for generally being great. I'd also like to thank Glenn, Dave, Amanda, Ben, Jaz, Paul, Andy J, Andy H and all of the Hornets for beers, curries, parties and the like. And to anybody I still owe a pint to, I haven't forgotten, I'm just biding my time before repaying the favour, honest!

Of course, I couldn't have done any of this without the support of my family, so I'd like to save my biggest thanks for my parents, David and Linda, and my brother John for all that they've done for me over the years.

Contents

List of Figures

List of Tables

Chapter 1

Introduction

Since the discovery of the electron by Thompson in 1897 our knowledge of the fundamentals of physics have improved immeasurably. From the discovery of the neutron by Chadwick in 1932, through Pauli's postulation of the existence of the neutrino and it's discovery in 1956, to Gell-Mann and Zweig's quark model of hadrons in 1964 and the detection of the top quark at the Tevatron in 1995 great steps have been made towards a complete understanding of the microscopic world around us. The sum of all present theoretical understanding of the elementary particles and their interactions is known as the Standard Model of particle physics, and includes all particles so far observed experimentally and all forces between them except gravity. There are, however, still some gaps in our knowledge, and it is hoped that many of these will be addressed by experiments performed at the Large Hadron Collider at CERN.

In this chapter a brief summary of the Standard Model, the Large Hadron Collider and the ATLAS experiment will be presented, followed by an outline of the topics covered in this thesis.

1.1 The Standard Model of particle physics

The Standard Model of particle physics is a theoretical description of all the fundamental particles and the interactions between them. Only a brief summary will be given here, since it is covered in detail in many textbooks, for instance [1–3].

All matter is comprised of particles with spin 1/2, which are known as fermions. The fermions are divided into two groups, quarks and leptons, and into three generations (see Fig. 1.1). Each generation consists of two quarks and two leptons, and their anti-particles. The first generation, consisting of up and down quarks, electron and electron-neutrino, makes up all stable matter in the universe. However two other generations also exist, containing more massive counterparts to the particles of the first generation. The second generation contains the strange and charm quarks, the muon and its neutrino, whilst the third generation contains the bottom and top quarks, tau lepton and its neutrino.

The matter particles experience four different fundamental forces; electromagnetic (EM), weak, strong and gravity. Of these all but gravity are included in the Standard Model. The fundamental forces are described in the Standard Model by the exchange of spin-1 bosons, shown in Fig. 1.2. The EM force is described by the theory of Quantum Electrodynamics (QED) where charged particles interact through the exchange of the massless photon. The weak force is experienced by all fermions and is transmitted by the massive $W^{\pm}$ and Z^0 bosons. The fact that the $W^{\pm}$ and Z^0 are

Generation	1	2	3
q=−1/3 **Quarks** q=+2/3	d 3–9 MeV	s 75–170 MeV	b 4.0–4.4 GeV
	u 1–5 MeV	c 1.15 –1.35 GeV	t 174.3± 5.1 GeV
q=−1 **Leptons** q=0	e 0.511 MeV	μ 0.106 GeV	τ 1.78 GeV
	ν_e	ν_μ	ν_τ

Figure 1.1: Fermions in the Standard Model. Particle masses taken from Ref. [4]

Spin = 1			Spin = 0
Electromagnetic	**Weak**	**Strong**	**Higgs**
Photon, γ q = 0 m = 0	W , Z m_W= 80.41 GeV m_Z = 91.19 GeV q_W=±1 q_Z = 0	Gluon, g q = 0 m = 0	H q = 0 m > 114 GeV

Figure 1.2: Gauge and Higgs bosons in the Standard Model.

massive is responsible for the short range or "weakness" of this force compared to the electromagnetic force. Weak interactions conserve lepton flavour, so that W or Z bosons can only couple to leptons in the same generation. When interacting with quarks the weak interaction couples to linear combinations of the d, s, and b quarks thus allowing quark flavour changing processes. The coupling between the different quark generations is described by the Cabibbo-Kobayashi-Maskawa (CKM) mixing matrix. Weak interactions, though, violate charge and parity conservation; only left-handed neutrinos and right-handed anti-neutrinos are observed. In has also been found that weak interactions violate combined charge and parity transformations, CP-violation, first observed in the neutral kaon system in 1964 by Christenson, Cronin, Fitch and Turlay.

The EM and weak forces have been unified into a single electroweak theory. To explain the difference in mass between the (massless) photon and the (massive) $W^{\pm}$ and Z^0 bosons the Higgs mechanism is introduced. This allows the $W^{\pm}$ and Z^0 to gain their masses whilst retaining the consistency of the theory, a process known as electroweak symmetry breaking. It also results in the introduction of a massive spin-0 particle, the Higgs boson (also shown in Fig. 1.2). The mass of the Higgs boson is not predicted by the theory, but experimental searches at the Large Electron Positron collider have placed a lower limit of 114 GeV on it [5]. The Higgs mechanism and Higgs boson are explained in greater detail in Chapter 5.

The strong force is responsible for binding quarks into hadrons such as the proton

and neutron. It is transmitted by eight massless gluons, and couples to colour which is carried by both quarks and gluons; gluons can therefore couple to themselves. The strong interaction increases in strength as the quarks move further apart, which causes them to be "confined" into colour-neutral particles.

Whilst the Standard Model has to date been able to explain all experimental findings there are still problems and inconsistencies with it that suggest that ultimately a more fundamental theory may be constructed. For example, the Standard Model contains 19 free parameters whose values must be found experimentally, and it is expected that a complete theory would itself make predictions of these. Also, the successful combination of the electromagnetic and weak forces suggest that a complete theory would also unify the strong force too. Such "Grand Unified Theories" do exist but introduce additional problems; for instance a finite lifetime for the proton is predicted, which has never been observed experimentally. There is also the so-called "hierarchy problem"; the lack of new physics between the scales of electroweak symmetry breaking ($\approx 10^2$ GeV) and grand unification ($\approx 10^{15}$ GeV) requires a great deal of fine-tuning of the theory. Another popular area of theoretical research is that of supersymmetry, where all bosons have a fermionic superpartner and each fermion a bosonic superpartner. Supersymmetric theories solve many of the problems associated with other Grand Unified Theories, and also allow the inclusion of gravity. Of course, it should not be forgotten that one particle predicted by the Standard Model remains undiscovered, the Higgs boson. It is therefore of utmost importance to gather experimental evidence either for or against the Higgs boson.

1.2 The Large Hadron Collider

In order to investigate new physics it is necessary to produce interactions at higher energies. Whilst the Large Electron Positron (LEP) experiment has reached centre-of-mass energies of up to 210 GeV, its ultimate energy is limited by energy losses

due to the emission of synchrotron radiation. This affects light particles, such as electrons, much more than heavy particles; for a given particle energy and radius of curvature the rate of energy loss is proportional to $1/m^4$ where m is the particle mass. By using protons as the colliding particles the energy lost to synchrotron radiation is greatly reduced and higher centre-of-mass energies can be achieved. New physics beyond the Standard Model is expected to be found at energies below 1 TeV. However, with protons as the colliding particles the centre-of-mass energy needed is greater than this, since the proton is a composite body of quarks and gluons. In a hard proton-proton interaction only one quark or gluon from either proton will actually be involved, each of which will carry a fraction of the total energy of the proton. In addition to having a collider with a large centre-of-mass energy it is also important for it to have a high luminosity, so that the number of events containing interesting physics is maximised.

The Large Hadron Collider (LHC) [6] is currently under construction and when completed will be the world's most powerful particle accelerator. Situated in the same 27 km circumference tunnel as was used by LEP, the LHC will accelerate two beams of protons travelling in opposite directions and then collide them together at centre-of-mass energies of up to 14 TeV. The accelerator chain of Linac, Booster, PS and SPS will be used to inject protons into the LHC at energies of approximately 450 GeV. These are then accelerated using super-conducting cavities cooled to liquid helium temperature to energies of up to 7 TeV. Both beams are situated in the same physical structure and share the same yoke and cryostat; super-conducting dipole magnets are used to provide the magnetic fields of 8.36 Tesla needed to bend the particles around the LHC rings. The design luminosity of the LHC is 10^{34} cm^{-2} s^{-1}, and the protons will be in bunches of up to 10^{11} particles with a bunch spacing of 25 ns. The two beams can be collided at four insertion points, at each of which is situated a different experiment. At two diametrically opposite high luminosity insertion points are the general purpose experiments ATLAS [7] and CMS [8]. At two low luminosity insertion points are the LHCb experiment [9], designed specifically for studies of the physics associated with the bottom-quark, and

the ALICE experiment [10], designed for the study of heavy ions with the LHC used in its other mode of colliding two beams of Lead ions with centre-of-mass energy 1150 TeV and luminosity up to $10^{27}\,\mathrm{cm}^{-2}\,\mathrm{s}^{-1}$.

1.3 The ATLAS experiment

The ATLAS (A Toroidal Lhc ApparatuS) experiment is one of two general purpose detectors planned to operate at the LHC. As such, ATLAS has been designed with the intention of covering as many different physics signatures as possible. Foremost in this is the search for the origin of electroweak symmetry breaking, with coverage provided for the full range of allowed masses for a Standard Model Higgs boson, or the group of Higgs particles predicted by the Minimal Supersymmetric Standard Model (MSSM). Additional physics that can be searched for include evidence for supersymmetric particles, heavy gauge bosons W' and Z' and quark compositeness. The LHC will also be a b-factory, with vast production of b-quarks, allowing the study of CP-violation in the B_d^0 system.

The basic design priorities for ATLAS can be summarised by [7]

- Efficient electromagnetic calorimetry for the identification and measurement of electrons and photons, plus hadronic calorimetry for measurements of jets and missing transverse energy.
- Efficient tracking at high luminosity for the measurement of charged lepton momenta, electron and photon identification, b-tagging, tau and heavy-flavour identification, and vertex reconstruction at low luminosity.
- Precision measurements of muon momenta at high luminosity with muon system only, plus triggering ability on low p_T muons at low luminosity.
- A large acceptance in pseudorapidity η.
- Triggering and measurement of low p_T particles.

The ATLAS detector is constructed from several different sub-detectors, the layout of which is shown in Fig. 1.3. Closest to the interaction point is situated the Inner Detector, which is contained inside a solenoidal magnet providing a central field of 2 Tesla in the beam direction. Outside of this are located first the electromagnetic (EM) and then the hadronic calorimeters. Finally, there is the muon spectrometer and air-core muon toroid magnet system. The muon spectrometer defines the overall size of the ATLAS detector, which is 42 m in length and 11 m in radius, with a total weight of approximately 7000 tons.

1.3.1 The Inner Detector

The main aims of the ATLAS Inner Detector [11, 12] are to reconstruct particle tracks and vertices with high efficiency, and to provide information for electron, photon and muon identification over an acceptance of $|\eta| \leq 2.5$. This is achieved through a combination of both discrete and continuous measurements. Discrete measurements are performed by several layers of silicon pixel and microstrip devices. These provide very accurate spatial measurements but also introduce a large amount of material into the detector so their use must be limited. A large number of individual measurements for each track is retained by also using a straw tube tracker to provide continuous measurements.

A diagram of the Inner Detector layout is shown in Fig. 1.4. The innermost subsystem of the Inner Detector is the Pixel detector, designed to provide high-precision, high-granularity measurements as close to the interaction point as possible. It consists of three barrel layers at radii of 4 cm, 10 cm and 13 cm and four end-cap disks each side at distances from the interaction point of $|z| = 49 - 104$ cm. In total the pixel detector has 140 million individual detector elements and provides three precision measurements per track over the full acceptance. The innermost pixel layer, or B-layer, is important for providing secondary vertex measurements but will also suffer from a great deal of radiation damage by virtue of being so close to the beam-pipe; this element is therefore designed to be replaceable. The resolution of

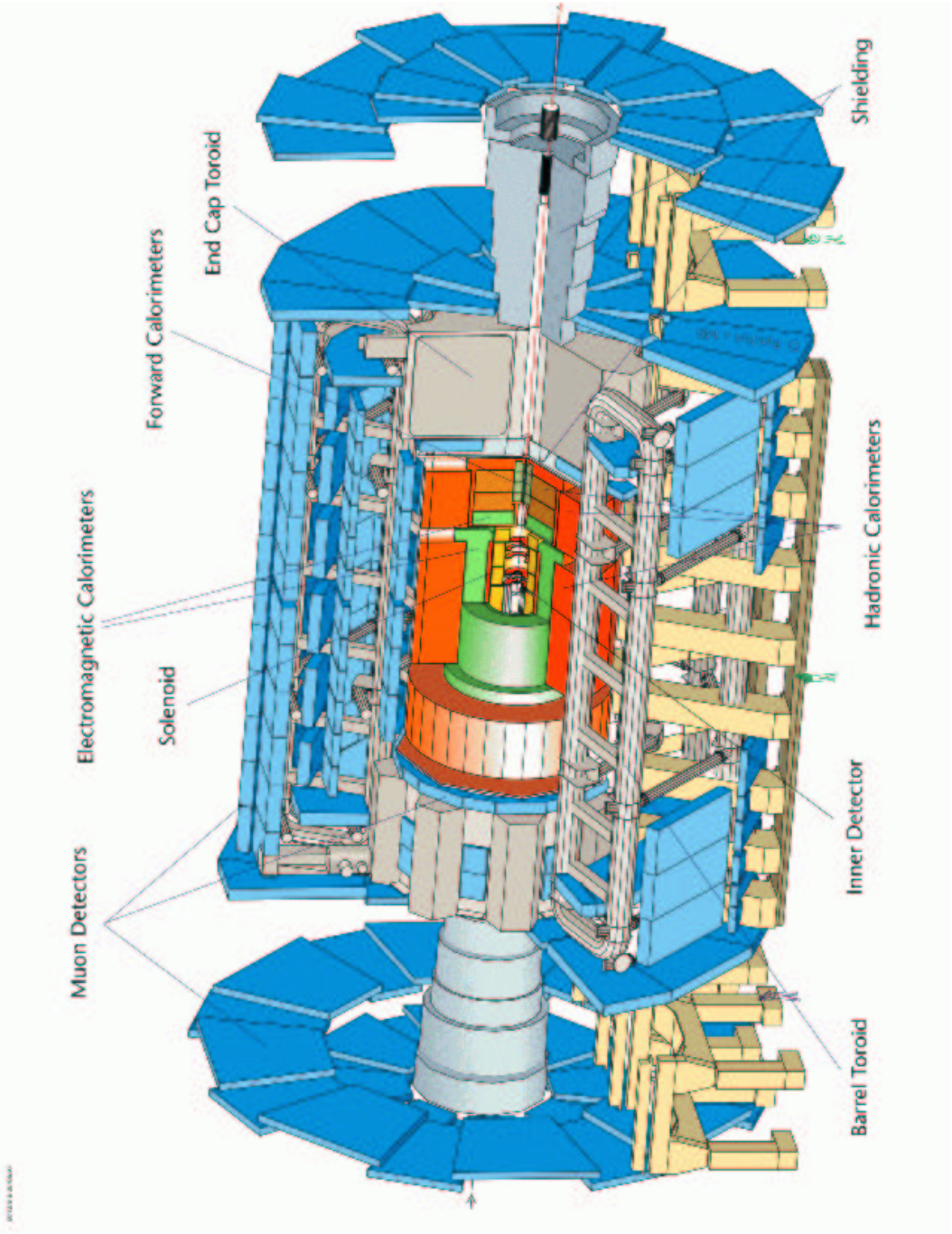

Figure 1.3: The ATLAS detector.

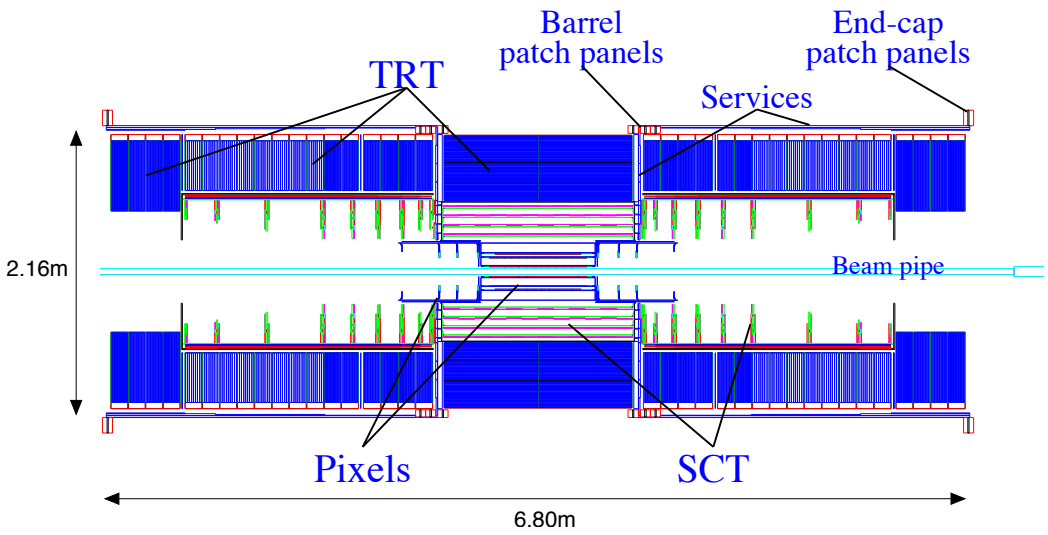

Figure 1.4: The ATLAS Inner Detector.

the pixel detector is (taking the barrel layers as an example) 12 μm in $r\phi$ and 66 μm in z.

Outside of the Pixel detector is the Semiconductor Tracker (SCT). This comprises over 16000 individual silicon microstrip detectors arranged into four barrel layers (at radii of 30.0, 37.3, 44.7 and 52.0 cm) and nine end-cap disks each side at distances from the interaction point of $|z| = 83.5 - 278.8$ cm. The individual detectors in the barrel are rectangular in shape having dimensions of 64 mm by 63.6 mm with 768 readout strips of pitch 80 μm. The detectors are arranged into modules, consisting of two layers of two detectors each, the detectors in each layer having their strips daisy-chained together. The two layers are then glued back-to-back with a stereo angle of 40 mrad between the strips in each layer. The barrel modules are positioned in the SCT so that the strips are parallel to the beam direction, and the resolution per module is 16 μm in $r\phi$ and 580 μm in z. The modules for the end-cap disks are constructed in a similar way, but using wedge shaped detectors with tapering strips, positioned so that the strips are radial. On average the SCT will provide four precision measurements for each track.

The outermost component of the Inner Detector is the Transition Radiation Tracker (TRT), which uses 4 mm diameter straw detectors. The TRT is divided into a barrel

region, containing $\approx$ 50000 straws of length 144 cm and covering a radial range of 56 - 107 cm, and two end-caps, consisting of 18 wheels containing $\approx$ 320000 straws and covering a radial range of 48 to 103 cm. The TRT will provide approximately 36 measurements per track with a resolution per straw of 170 μm. The use of Xenon in the straws also facilitates electron identification by detecting transition radiation photons created in a radiator between the straws.

1.3.2 Calorimetry

The ATLAS calorimeter system [13–15] is shown in Fig. 1.5. Four different subsystems are present; the electromagnetic (EM) calorimeter, with coverage of $|\eta| < 3.2$, the hadronic barrel and hadronic end-cap calorimeters, with coverage $|\eta| < 1.7$ and $1.5 < |\eta| < 3.2$ respectively, and the forward calorimeter (FCAL), with coverage $3.1 < |\eta| < 4.9$.

The EM calorimeter is designed to reconstruct electrons and photons with excellent energy and spatial resolution. It is a lead/liquid Argon detector with accordion geometry, and is divided into a barrel section covering $|\eta| < 1.475$ and two end-caps covering $1.375 < |\eta| < 3.2$. The total thickness is greater than 24 radiation lengths over the whole region. The EM calorimeter is divided into cells that are projective towards the interaction point over the entire pseudorapidity range. For pseudorapidities $|\eta| < 1.8$ the material seen by a particle before it reaches the EM calorimeter is more than 2 radiation lengths. A presampler is used in this region to correct for the energy lost by photons and electrons to the material already traversed. This consists of an active liquid Argon layer of thickness 1.1 cm in the barrel region and 0.5 cm in the end-cap region. The expected energy resolution of the EM Calorimeter is

$$\frac{\sigma(E)}{E} = \frac{10\%}{\sqrt{E}} \oplus 1\%$$

The hadronic calorimetry is designed for the reconstruction and measurement of jets, and also the measurement of missing transverse energy. The hadronic barrel

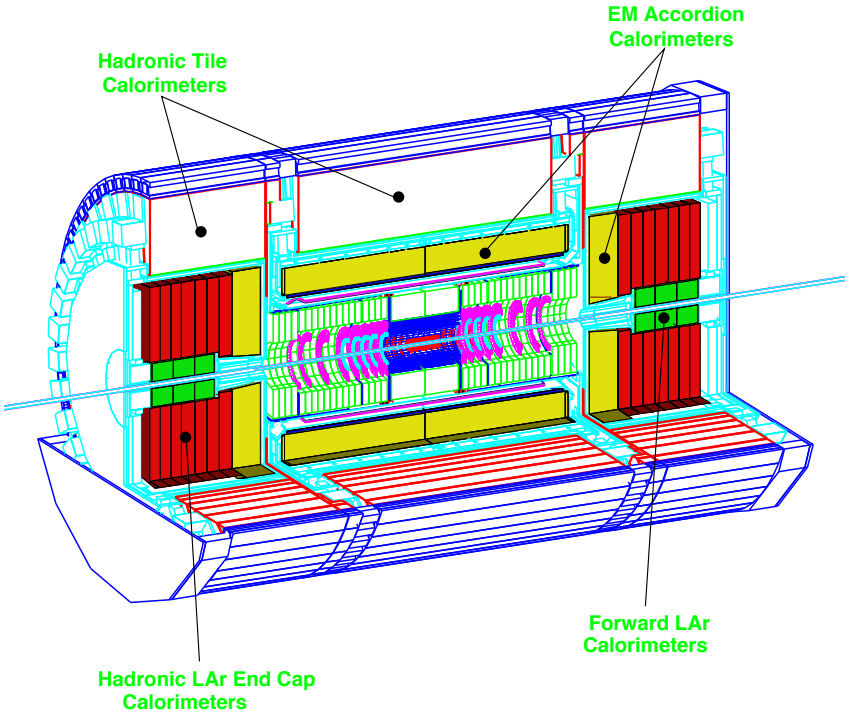

Figure 1.5: The ATLAS calorimeter system.

calorimeter is a sampling calorimeter using an iron absorber and scintillating tiles as the active medium. It covers a radial region of 2.28 to 4.25 m, equivalent to 7.2 interaction lengths, and the granularity is $\Delta\eta \times \Delta\phi = 0.1 \times 0.1$. The hadronic end-cap calorimeters utilise a liquid Argon active medium, with a copper absorber. The granularity is $\Delta\eta \times \Delta\phi = 0.1 \times 0.1$ for $1.5 < |\eta| < 2.5$ and 0.2×0.2 for $2.5 < |\eta| < 3.2$. The FCAL is perhaps the most challenging of the calorimeters from a design point-of-view, as it will be positioned in a high-radiation environment. Additionally, to limit the amount of neutrons it emits into the Inner Detector it is recessed from the front face of the EM calorimeter end-caps by 1.2m. Thus a high density design is required to provide sufficient interaction lengths. A metal matrix is used, copper in the first section and tungsten in the other two, with rod electrodes in regularly spaced tubes. Again, liquid Argon is used as the active medium, since it is inherently radiation hard. The expected jet energy resolution of the hadronic calorimetry for

the region $|\eta| \leq 3$ is

$$\frac{\sigma(E)}{E} = \frac{50\%}{\sqrt{E}} \oplus 3\%$$

1.3.3 The Muon Spectrometer

The muon spectrometer [16] is designed to provide high precision muon measurements, with a stand-alone triggering system so that it can be used independently of the inner detector and calorimetry. Deflection of the muon tracks is provided by superconducting air-core toroid magnets, which produce a field generally orthogonal to the direction of the muons. Magnetic bending is provided by the barrel toroid for pseudorapidities of $|\eta| < 1$, by the two smaller end-cap toroids for pseudorapidities $1.4 < |\eta| < 2.7$, and a combination of the two for the "transition region" of $1 < |\eta| < 1.4$. Separate systems are used for high-precision measurements and triggering. Precision measurements over most of the pseudorapidity range are provided by Monitored Drift Tubes, with Cathode Strip Chambers at large pseudorapidities and close to the interaction point. The triggering system covers $|\eta| < 2.4$, and utilises Resistive Plate Chambers in the barrel and Thin Gap Chambers in the end-cap regions. The momentum resolution of the muon spectrometer varies as a function of η and ϕ, but is better than 5% over more than three quarters of its area [17].

1.3.4 Triggering and DAQ

Due to the high luminosity of the LHC a sophisticated triggering system is required to reduce the event rate by only selecting events which appear to be of interest. The ATLAS trigger is in three levels, LVL1, LVL2, and EF (event filter), each level reducing the event rate before final event storage.

The LHC will have bunch crossings every 25 ns, a rate of 40 MHz, and this full rate is accepted by the LVL1 trigger. High transverse momentum muons are identified by the muon spectrometer, and high transverse momentum electrons and photons, jets

and large missing transverse energies are searched for using all of the calorimetry with reduced granularity. Information from the inner detector is not used. The maximum output rate for the LVL1 trigger is 75 kHz, and the latency (time taken to make the LVL1 trigger decision) is 2 μs, during which time all of the event information is stored in "pipeline" memory. Events selected by the LVL1 trigger have the data from the detectors transferred into readout drivers then readout buffers, and the event is passed to the LVL2 trigger. This makes use of "region of interest" (RoI) information provided by the LVL1 trigger, such as the position of candidate objects, to reduce the amount of detector data that must be analysed. Extra rejection power is provided by utilising the information from the inner detector and using the calorimetry with full granularity. The LVL2 trigger is expected to reduce the rate to approximately 1 kHz, with a latency of between 1 and 10 ms. Events passing the LVL2 trigger have the event data transferred to storage for the EF. The EF will use refined and more complex algorithms to make the final selection of physics events which will be stored for offline analysis. The event rate for final storage is expected to be approximately 100 Hz, equivalent to a data storage rate of approximately 100 $\mathrm{MB\,s^{-1}}$.

1.4 Topics covered in this thesis

Two major topics will be covered in this thesis. Firstly, the effect of radiation damage on silicon microstrip detectors will be investigated. It is essential for the ATLAS SCT that the detectors remain fully operational for the whole lifetime of the experiment, even though they will be subject to a harsh radiation environment. To this end silicon microstrip detectors have been irradiated to the predicted 10 year radiation dose, and measurements taken during irradiation can be used to study the radiation damage effects. In Chapter 2 a summary of the theory behind the operation of silicon microstrip detectors and the effects of radiation damage on them is presented. This is followed in Chapter 3 by a description of the ATLAS silicon microstrip

detectors, the radiation environment at ATLAS and the irradiation facility used for performing detector irradiations. In Chapter 4 a model is developed to explain the leakage current behaviour of detectors irradiated whilst held under bias. The observed leakage currents are investigated against the predictions of this model and the parameters that govern the radiation damage are calculated. These are then used to model detector behaviour during irradiation and also for the operational scenario of the ATLAS experiment.

The second major topic to be covered is the evaluation of a discovery channel for an intermediate mass Standard Model Higgs boson at ATLAS. In Chapter 5 a summary of the origin of the Higgs boson, the results of experimental searches for the Higgs to date and the prospects for its discovery in the future will be given. The channel investigated in this thesis will be introduced, its characteristic features and potential backgrounds to the signal identified and the simulation tools that are used outlined. In Chapter 6 the results of the analysis will be presented, including optimisation of the methods used, investigation of how systematic uncertainties may affect the potential for a discovery, determination of the Higgs boson mass and extension of the methods used for a light Higgs boson.

Finally, in Chapter 7 the main findings of this thesis will be summarised and areas for future work presented.

The following paragraph describes the relation between my own original work in this thesis and the work of others. Chapters 1 and 2 contain only introductory material and are essentially summaries of many references. Chapter 3 describes the irradiation facility at the CERN PS, the majority of the infrastructure of which was in place before I started, although I was involved in the subsequent maintenance and running of the facility, and was present at all irradiation periods for which data was taken that is analysed here. In Chapter 4 a model is developed from existing parameterisations of radiation damage in silicon, but the model itself is unique and has not to my knowledge been used before. All subsequent data analysis is original work. Chapter 5 contains mainly introductory material and is again a

summary of several references. Finally, in Chapter 6 the analysis techniques make use of those proposed by David Rainwater and Dieter Zeppenfeld in several papers. The study of the WBF $H \to WW^{(*)} \to e^{\pm}\mu^{\mp}p_T^{miss}$ channel starts with an analysis analogous to that used in Ref. [18], but the optimization of the acceptance cuts is original work, as is the study of the WBF $H \to WW^{(*)} \to (e^+e^-/\mu^+\mu^-)p_T^{miss}$ channel and the discussion of the combined results of both channels. The study of $H \to WW^{(*)} \to l^+l^-p_T^{miss}$ for a light Higgs boson was previously performed in Ref. [19], but the analysis used here does not draw on this work but instead follows from the studies already performed here for an intermediate mass Higgs.

Chapter 2

Semiconductor particle detectors

Semiconductor particle detectors, primarily based on silicon technology, are an integral part of almost all modern collider experiments due to their excellent spatial resolution which makes them ideal for tracking and vertexing applications. The ATLAS experiment is no exception, with approximately 16000 individual silicon microstrip detectors planned for the Semiconductor Tracker. Silicon detectors are essentially solid-state ionisation chambers; a charged particle traversing the detector creates electron-hole pairs which are then drifted in an electric field to give a signal. The one major drawback of silicon detectors is that they suffer from radiation damage. This is particularly so at the LHC, where a higher radiation level is expected than previously seen in any other experiment.

In this chapter the basic properties of semiconductors and the p-n junctions on which semiconductor particle detectors are based will be outlined. This will be followed by a description of some features specific to silicon particle detectors, including the energy loss through ionisation of incident particles and detector design issues. Finally the radiation damage processes of silicon detectors will be discussed. Further details on semiconductor physics and p-n junctions can be found in Ref. [20,21], and topics specific to silicon particle detectors in Ref. [22].

2.1 Semiconductor physics

In solid state physics materials can be divided into three different types; metals, insulators and semiconductors. The differences between them can be explained simply through the band theory of materials, and is shown diagrammatically in Fig. 2.1. In any material there are energies that atomic electrons are allowed to take, and other energy values that are forbidden. The allowed energies tend to be grouped together, forming energy bands. The forbidden values between energy bands are called band gaps. The allowed energy states are filled with electrons starting from the lowest values, and the last filled band is called the valence band. The band above this is called the conduction band. In a metal the valence and conduction bands overlap, with no forbidden region or band gap between them, and electrons can move freely from the valence band to the conduction band. In an insulator the valence and conduction bands are separated by a large band gap E_g, which is too large for the thermal excitation of electrons to the conduction band. In a semiconductor the band gap between valence and conduction bands is small enough that electrons can be thermally excited to the conduction band. The state from which the electron was excited is now empty, has net positive charge, and is referred to as a hole.

A semiconductor with no added impurities is termed "intrinsic". The thermal excitation of electrons into the conduction band leaves an equal number of holes in the

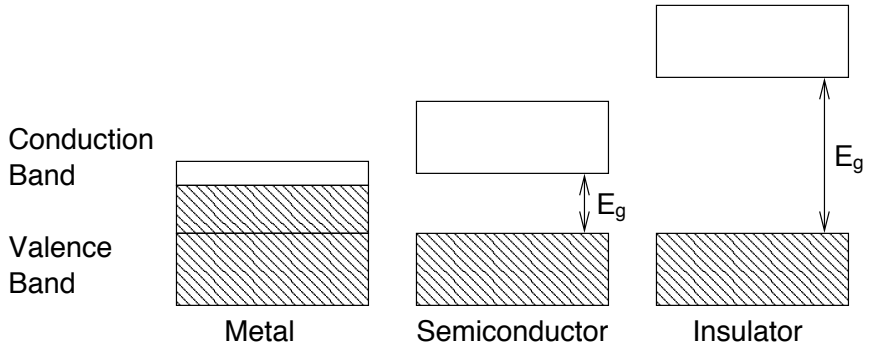

Figure 2.1: Band structure of metals, insulators and semiconductors.

valence band and

$$n_i = p_i \tag{2.1}$$

where n_i is the electron density in the conduction band and p_i is the hole density in the valence band. As has already been noted the electrons are thermally excited to the conduction band, therefore it is clear that the electron and hole densities are temperature dependent:

$$n_i = p_i \propto T^{3/2} exp(-E_g/2kT) \tag{2.2}$$

where T is the temperature and k is Boltzmann's constant. It should also be noted that the band gap is itself temperature dependent; for silicon at absolute zero $E_g = 1.17$ eV whereas at room temperature $E_g = 1.12$ eV.

The conductivity ρ of a semiconductor depends upon both the electrons and holes, since both are charge carriers:

$$\rho = e(\mu_n n + \mu_p p) \tag{2.3}$$

where e is the electron charge and $\mu_{n(p)}$ is the mobility of electrons (holes). The mobility is dependent on both the material and the type of charge carrier; in silicon the mobility is 1350 $cm^2\,V^{-1}\,s^{-1}$ for electrons and 480 $cm^2\,V^{-1}\,s^{-1}$ for holes [22].

All charge carriers in an intrinsic semiconductor are thermally generated. To increase the number of charge carriers the semiconductor can be doped. Considering silicon as the semiconductor, each silicon atom has four valence electrons that form covalent bonds with neighbouring atoms. To dope the silicon an impurity atom with a different number of valence electrons is added into the silicon lattice. Adding an atom with five valence electrons into a lattice site surrounded by silicon atoms, four of the valence electrons form bonds leaving the fifth electron only lightly bound to the atom. This is then easily thermally excited to the conduction band; these impurity atoms are known as "donors". Donor atoms introduce donor levels at the top of the band gap; only a small amount of thermal energy is required to ionise the donor levels. A typical donor atom with five valence electrons is Phosphorus.

When the donor concentration N_D is large compared to the intrinsic carrier density the doped silicon is referred to as n-type. Electrons are the majority carriers and holes the minority carriers, and the electrons density n is approximately equal to the donor concentration:

$$n \approx N_D \,. \tag{2.4}$$

Alternatively if an impurity atom with only three valence electrons is introduced into the silicon lattice the missing electron in the bond structure is effectively a hole, and the impurity atoms are known as "acceptors". Acceptor atoms introduce acceptor levels at the bottom of the band-gap, which can be filled by thermally excited electrons from the valence band, leaving free holes in the valence band. A typical acceptor atom with three valence electrons is Boron. When the acceptor concentration N_A is large then the doped silicon is referred to as p-type, holes are the majority carriers and the hole density p is approximately equal to the acceptor concentration:

$$p \approx N_A \,. \tag{2.5}$$

In reality no intrinsic semiconductor is entirely pure as various impurities are always present. The energy levels of these tend to be in the middle of the band gap and they are referred to as deep impurities; donor and acceptor impurities create energy levels at the edges of the band gap so are referred to as shallow impurities.

2.2 The p-n junction

The p-n junction is the basis of semiconductor particle detectors. It is formed simply by a transition between a p-type semiconductor and an n-type semiconductor. If the transition between n-type and p-type silicon is immediate then the junction is said to be "abrupt". In the n-type side of the junction there is a large electron density, compared to the p-type side where the electron density is small. This results in a diffusion of electrons from the n-type side to the p-type side, where recombination with holes (the majority carrier in the p-type material) occurs. Likewise there is

also a diffusion of holes from the p-type side to the n-type side. The diffusion of electrons from the n-type side leaves behind ionised donor atoms which build up a positive space-charge region on the n-type side of the junction. Similarly, ionised acceptor atoms build up a negative space charge on the p-type side. This creates an electric field across the junction which acts against the diffusion of carriers across the junction. The junction is said to be in equilibrium when the diffusion of carriers has produced an electric field across the junction that is sufficient to prevent further diffusion. The region around the junction where there is positive space charge (n-type side) or negative space charge (p-type side) is largely devoid of charged carriers, and is referred to as the depletion region. The depletion region is the key for semiconductor particle detectors. In non-depleted material any charge created by an ionising particle is lost through recombination with free carriers. In the depletion region there are no free carriers to permit recombination, and an electric field across the junction will cause the drift of the created charge carriers to give a signal.

2.2.1 Depletion region

The width of the depletion region can be calculated by solving Poisson's equation

$$\frac{d^2V}{dx^2} = -\frac{dE}{dx} = -\frac{\rho}{\epsilon_r \epsilon_0} \tag{2.6}$$

where V is the potential a distance x from the junction, E is the electric field, ρ is the charge density, ϵ_r is the relative permittivity of silicon and ϵ_0 is the permittivity of free space. Assuming that the junction is abrupt and that all donors and acceptors in the depletion region are ionised then the charge density on the p-type side is $-eN_A$ and on the n-type side is eN_D. Therefore on the p-type side Eqn. (2.6) becomes

$$\frac{dE}{dx} = -\frac{eN_A}{\epsilon_r \epsilon_0}\,. \tag{2.7}$$

This can be integrated to find E by applying the boundary condition that $E = 0$ at the edge of the depletion region on the p-type side of the junction, $x = -x_p$ (defining

$x = 0$ at the junction and from the junction towards the n-type side as positive in x), giving

$$E = -\frac{eN_A}{\epsilon_r \epsilon_0}(x + x_p) \,. \tag{2.8}$$

The electric field reaches a maximum at the junction, when $x = 0$, so

$$E_{max} = -\frac{eN_A x_p}{\epsilon_r \epsilon_0} \,. \tag{2.9}$$

Similarly on the n-type side of the junction,

$$\frac{dE}{dx} = \frac{eN_D}{\epsilon_r \epsilon_0} \tag{2.10}$$

which when integrated with the boundary condition that $E = 0$ at the edge of the depletion region on the n-type side of the junction, $x = x_n$, gives

$$E = \frac{eN_D}{\epsilon_r \epsilon_0}(x - x_n) \tag{2.11}$$

and

$$E_{max} = -\frac{eN_D x_n}{\epsilon_r \epsilon_0} \,. \tag{2.12}$$

The two expressions for the maximum electric field at the junction, Eqns. (2.9) and (2.12) must clearly give the same value; equating these gives

$$N_A x_p = N_D x_n \,. \tag{2.13}$$

This is an important relationship, since it shows that if one side of the junction is lightly doped, has a small impurity concentration, whereas the other side of the junction is heavily doped then the depletion region will extend further into the lightly doped side than the heavily doped side.

To find the potential on either side of the junction Eqns. (2.8) and (2.11) must be integrated once more with respect to x. The potential on the n-type side V_n and the p-type side V_p must be equal at the junction ($x = 0$), and the potential here is defined as zero. Therefore on the p-type side of the junction

$$V_p(x) = \frac{eN_A}{\epsilon_r \epsilon_0}\left(\frac{x^2}{2} + x_p x\right) \tag{2.14}$$

and on the n-type side of the junction

$$V_n(x) = \frac{eN_D}{\epsilon_r \epsilon_0}\left(x_n x - \frac{x^2}{2}\right) . \tag{2.15}$$

By setting $x = -x_p$ on the p-type side and $x = x_n$ on the n-type side then the potentials at the extremities of the junction can be found:

$$V_p(-x_p) = -\frac{eN_A}{\epsilon_r \epsilon_0}\frac{x_p^2}{2} \tag{2.16}$$

and

$$V_n(x_n) = \frac{eN_D}{\epsilon_r \epsilon_0}\frac{x_n^2}{2} . \tag{2.17}$$

The potential difference across the junction is then simply the difference between Eqns. (2.16) and (2.17),

$$V = \frac{e}{2\epsilon_r \epsilon_0}\left(N_D x_n^2 + N_A x_p^2\right) . \tag{2.18}$$

This is referred to as the built-in voltage V_{bi}. The total width of the depletion region W is equal to the sum of the depleted widths on either side, $W = x_n + x_p$, and using Eqns. (2.13) and (2.18)

$$W = \sqrt{V\frac{2\epsilon_r \epsilon_0}{e}\left(\frac{1}{N_A} + \frac{1}{N_D}\right)} . \tag{2.19}$$

If a positive voltage V_A is applied to the p-side of the junction it is said to be forward biased. The external potential difference is in the opposite direction to that of the built-in potential, and so the overall potential difference across the junction is now $V = V_{bi} - V_A$. From Eqn. (2.19) it can be seen that the width of the depletion region will decrease for a junction under forward-bias. On the other hand, applying a positive voltage to the n-side of the junction, reverse biasing it, the total potential across the junction is now $V = V_{bi} + V_A$ and the width of the depletion region will increase. For a particle detector a large depletion region is desired to maximise the amount of collectable charge produced by the passage of an ionising particle, therefore detectors are operated under reverse bias. The reverse bias also provides an electric field across the detector that ensures the electrons and holes are separated before they can annihilate, and then drifts the charge carriers to produce a signal.

As mentioned previously if one side of the junction is heavily doped whereas the other side is only lightly doped then the depletion region extends furthest into the lightly doped side of the junction. Particle detectors are typically p^+-n junctions, where the p-type side is very heavily doped and the n-type side is only lightly doped. Then the depletion region falls almost entirely in the n-type side of the junction and the extent of the depletion region into the heavily doped p-type side is negligible. The p^+ material can be extremely thin, since it is only required to deplete the junction, and the bulk of the material is n-type silicon.

For a p^+-n junction Eqn. (2.19) becomes

$$W \approx \sqrt{V \frac{2\epsilon_r \epsilon_0}{eN_D}}\,. \tag{2.20}$$

In practise it is almost impossible to produce p- or n-type silicon doped only with acceptor or donor atoms respectively. Instead, doped silicon usually contains both donor and acceptor impurities, and is said to be compensated. The effective doping concentration N_{eff} is defined as

$$N_{eff} = N_D - N_A\,. \tag{2.21}$$

For n-type material $N_D \gg N_A$, so $N_{eff} \approx N_D$. Similarly for p-type material $N_{eff} \approx N_A$. Substituting N_{eff} for N_D in Eqn. (2.20),

$$W = \sqrt{V \frac{2\epsilon_r \epsilon_0}{e|N_{eff}|}}\,. \tag{2.22}$$

The reverse bias voltage required to create a depletion region that extends throughout the whole of the material is called the full depletion voltage V_{dep} and from Eqn. (2.22) is given by

$$V_{dep} = \frac{ed^2|N_{eff}|}{2\epsilon_r \epsilon_0} \tag{2.23}$$

where d is the thickness of the junction. It should also be noted that the effective doping concentration depends upon the resistivity of the silicon:

$$\rho = \frac{1}{e\mu|N_{eff}|} \tag{2.24}$$

where μ is the mobility of the majority carriers, holes for p-type silicon and electrons for n-type silicon. To minimise the full depletion voltage it is necessary to minimise N_{eff}, therefore high-resistivity material is used for semiconductor particle detectors. Additionally, compared to the full depletion voltage the built-in voltage is generally negligible for these devices.

2.2.2 Capacitance of depletion region

The depletion region of a p-n junction is insulating, therefore the junction can be considered to be equivalent to a parallel plate capacitor. The capacitance of the junction C_j is given by

$$C_j = \frac{A\epsilon_r\epsilon_0}{W} \tag{2.25}$$

where A is the area of the junction and W is the width of the depletion region. The junction capacitance is inversely proportional to the width of the depletion region therefore the minimum capacitance will be found when the junction is fully depleted. This is a commonly used technique for finding the full depletion voltage of a detector; capacitance measurements are taken with increasing reverse bias voltages, and the voltage at which the capacitance reaches a minimum is defined as the full depletion voltage. This also allows the calculation of the effective doping concentration, provided the thickness of the device is known.

2.2.3 Leakage current

In an ideal p-n junction under no external bias the diffusion of majority carriers and drift of minority carriers across the junction cancel, and no current across the junction is observed. However when the junction is reverse biased a current is observed, called the leakage current. This is caused by three different effects; minority carrier current, surface current and generation current.

In a reverse biased p-n junction the electric field prevents the diffusion of majority

carriers across it. Minority carriers, though, will be drifted in the electric field and produce a current. In silicon, however, the minority carrier current is small and does not contribute greatly to the overall leakage current.

Surface currents can occur due to high electric fields at the edge of the junction or contamination of the surface. Surface currents are not easily quantifiable since they are dependent on a number of factors such as humidity, the fabrication process and irregularities and damage of the surface. However, surface currents normally only contribute a small amount to the total leakage current.

The majority of the leakage current therefore arises from the generation current. This is caused by the thermal generation of electron-hole pairs in the depletion region, which are then drifted in the electric field to produce a current. It is enhanced by the presence of deep impurity levels in the centre of the band-gap that increase the probability of the thermal excitation of an electron from the valence band to the conduction band. These are known as generation centres. The generation current I_g is given by

$$I_g = \frac{en_iAW}{2\tau} \tag{2.26}$$

where τ is the effective charge carrier lifetime. The effective charge carrier lifetime is inversely proportional to the density of generation centres, therefore the generation current is proportional to the density of generation centres. The generation current is temperature dependent since it is proportional to the intrinsic carrier density n_i (see Eqn. (2.2)), and so can be minimised by cooling the devices. At constant temperature the generation current is proportional to the depleted width of the junction, and so from Eqn. (2.22) $I_g \propto \sqrt{V}$. Therefore when observing leakage current with increasing reverse bias an increase in leakage current proportional to $\sqrt{V}$ should be seen, until $V = V_{dep}$ where, since the detector is fully depleted and the depletion width cannot increase any more, the leakage current reaches a plateau and remains constant with increasing reverse bias voltage. Any deviation from this behaviour is a possible indication of the leakage current not being dominated by the generation current.

If too great a reverse bias is applied to a p-n junction then a rapid increase in current can occur, termed as junction breakdown. There are two principle mechanisms behind breakdown, Zener breakdown and avalanche breakdown. Zener breakdown occurs by valence electrons tunnelling through the band-gap into the conduction band. Zener breakdown can only occur in high electric fields, and therefore high doping concentrations. The doping concentrations in material for particle detectors are normally too small for Zener breakdown to occur. Avalanche breakdown occurs when an electron in the depletion region is accelerated by the electric field and gains sufficient energy to create electron-hole pairs through ionisation, which are then accelerated themselves, more pairs are produced, until a cascade or avalanche is present in the detector. The avalanche breakdown voltage is found to be greater for material with lower doping, and is also found to increase with increasing temperature. Another effect that should be mentioned is that of thermal runaway. This occurs when there is sufficient leakage current in a device to cause self-heating, which in turn causes an increase in the (temperature dependent) leakage current, increasing the temperature further. Detectors should always be operated at bias voltages low enough so that none of these effects can occur.

2.3 Detector operation

Now that the basic properties of semiconductors and p-n junctions have been outlined some features of particular interest to semiconductor particle detectors will be described. As has been previously mentioned the most common type of junction used for particle detectors is the silicon p^+-n one sided junction. The highly doped p^+ silicon is present solely to deplete the junction and so only a thin layer is required. The bulk of the detector comprises the lightly doped n-type silicon and contains the depletion region. The junction is operated in reverse bias so that it is fully depleted, and a traversing particle causes ionisation in the depleted region creating electron-hole pairs which are drifted in the electric field and collected to

give a signal.

2.3.1 Energy loss of particles in silicon

A heavy charged particle traversing a silicon detector loses energy in two ways; elastic scattering from nuclei, which can be responsible for radiation damage of the detector and will be discussed later, and inelastic interactions with atomic electrons, which cause ionisation. Inelastic interactions account for the majority of the energy loss, and are described by the Bethe-Bloch equation (see for example [23]). This gives the differential energy loss dE/dx for a particle traversing a material as a function of the particle's charge and momentum. For particle energies of $0.1 - 1.0$GeV the differential energy loss reaches a broad minimum before undergoing a slow relativistic rise, and particles in this region are referred to as minimum ionising particles or mips. It should be noted that for electrons additional radiative methods of energy loss have to be considered, such as Bremsstrahlung, but the energy loss through inelastic interactions is the same as that of mips to a good approximation.

The most probable energy loss for a mip traversing a 300 μm thick silicon detector at normal incidence is 78 keV [22] and the energy required to create an electron-hole pair is 3.6 eV [4], therefore approximately 22000 pairs will be produced. In a reverse-biased detector electrons and holes are separated by the electric field, the holes being drifted towards the junction and the electrons being drifted towards the rear of the n-type silicon. The collection time for the created charge decreases with increasing full depletion voltage, and can be decreased further by over-biasing the detector, applying a reverse bias voltage greater than that required for full depletion. In a typical 300 μm thick silicon detector electrons are collected in 10 ns and holes in 25 ns, the longer collection time for holes being due to their smaller mobility.

2.3.2 Detector design

The most common use for silicon detectors is tracking, which requires accurate spatial measurements. This is achieved by dividing the p^+ layer into strips. A typical design for a silicon strip detector is shown in Fig. 2.2. The bulk of the detector is made from n-type silicon, with a back-plane of n^+ silicon to prevent the depletion region from reaching the edge of the detector, and to provide an ohmic contact. The p^+ side is divided into strips, each of which is covered with a metal such as aluminium to provide a contact to the readout electronics. In between the p^+ strips the n silicon bulk is covered in a layer of passivation, an insulator such as SiO_2. The arrangement of the p^+ side effectively divides the detector into a number of sub-detectors, each with its own independent readout. The electrons and holes created by an ionising particle drift in the electric field and the position where it traversed can be calculated from the strips on which the charge is collected.

There are several other important design features of a typical silicon microstrip detector. Firstly there is the manner in which the p^+ strips are coupled to the aluminium readout strips. If the aluminium is laid directly on top of the p^+ silicon they are "dc-coupled"; the drawback of this is that leakage current from the detector can flow directly into the readout electronics. If the aluminium and p^+ silicon are

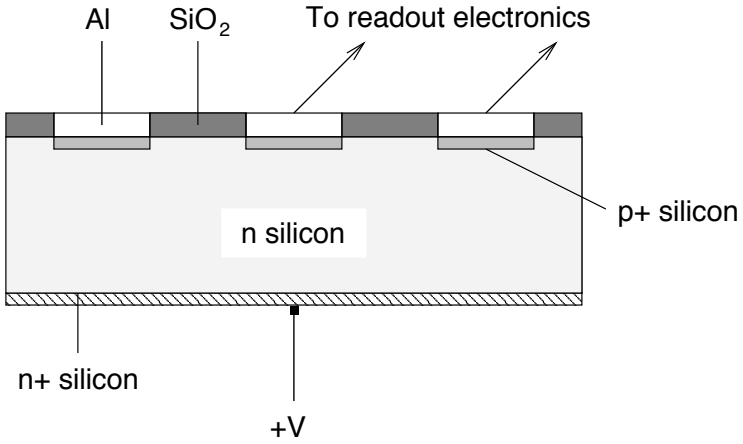

Figure 2.2: Cross-section through a typical silicon microstrip detector.

separated by a thin dielectric layer the strips are said to be "ac-coupled". The dielectric layer effectively introduces a capacitor into the circuit, preventing the flow of leakage current to the electronics. Another important feature is the biasing of the detector. A bias voltage has to be applied to every strip in the detector, which is done by connecting them all to a common line by bias resistors. The bias resistors ensure that the strips are insulated from each other and are typically made from polysilicon, which can provide resistances of up to 50 MΩ. Finally there is the question of electrically defining the edges of the detector. The electric field across the depleted junction reaching the physical edge of the device can cause dangerously high currents, due to generation from the damaged silicon lattice where the material has been cut. This can be prevented through the use of guard rings. These are successive rings of p^+ material surrounding the strips that are designed to reduce the electric field to zero before it reaches the edge of the detector. The design of the guard rings defines the active area of the detector, that which is depleted and used for particle detection.

2.4 Radiation damage effects

Radiation damage of silicon detectors is an increasingly important topic due to the need for high-rate experiments which consequently have higher radiation fields associated with them. Radiation damage can be divided into two types; bulk damage and surface damage. The first of these is generally the most important for the operation of silicon detectors.

2.4.1 Bulk damage

Bulk damage in silicon is caused by the disruption of the lattice structure due to the transfer of energy from incident particles to the silicon nuclei, termed the Non-Ionising Energy Loss (NIEL). Whilst heavy charged particles can lose energy

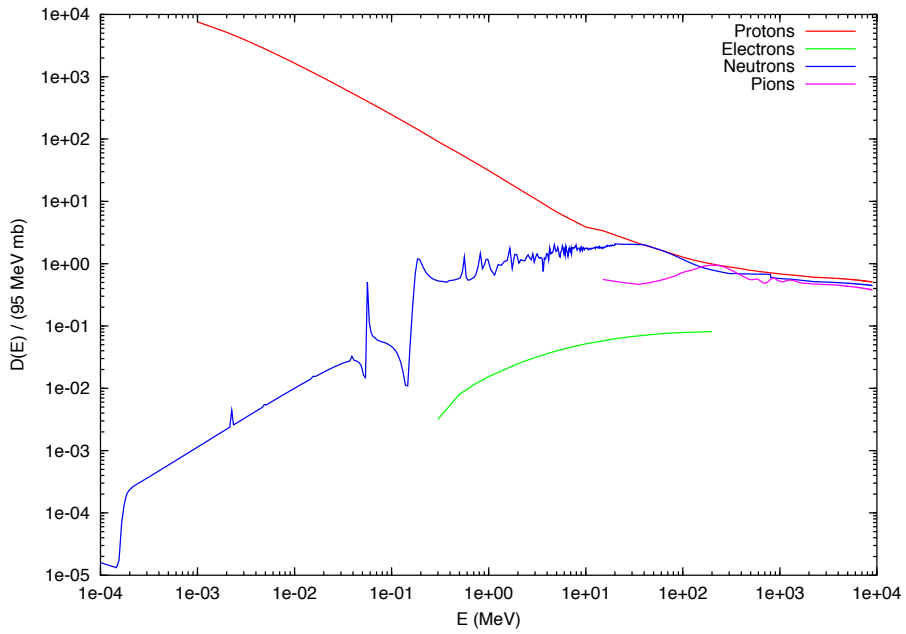

Figure 2.3: Non-Ionising Energy Loss in silicon. Data taken from Ref. [24].

through both inelastic interactions with atomic electrons (see Section 2.3.1) and NIEL, neutrons only exhibit the latter, whilst light particles such as electrons, muons and photons do not generally have sufficient energy to cause disruption of the lattice. Therefore the amount of damage to the lattice depends upon both the type of particle and its energy. The NIEL in silicon as a function of particle type and energy is shown in Fig. 2.3 normalised to the displacement damage cross-section for 1 MeV neutrons. For particle energies above $\approx$ 100 MeV the NIEL for protons, pions and neutrons is approximately equal, with that for electrons being more than an order of magnitude lower.

The result of NIEL from an incident particle to a silicon atom is to dislodge it from its site in the lattice; the dislodged atom is referred to as the Primary Knock-on Atom (PKA). This creates an empty lattice site - a vacancy - and an atom not in a lattice site - an interstitial. The vacancy and interstitial are point defects, and together are termed a Frenkel pair. Both vacancies and interstitials are mobile in the lattice at room temperature, and it is possible for the annihilation of a vacancy and an interstitial, with no remaining damage. Alternatively point defects may migrate

through the lattice and form stable defects. If the PKA has sufficient energy then it can itself dislodge other atoms, and this can lead to a cascade of displacements in a localised area - this is known as a cluster.

There are two main macroscopic changes of detector properties caused by bulk radiation damage, a change in the effective doping concentration N_{eff} and a change in the leakage current.

Changes in effective doping concentration

At room temperature, point defects created by radiation damage can migrate through the lattice and form stable defect complexes with either impurity atoms or other point defects. For example the vacancy-phosphorus (V-P) complex, which is stable at room temperature, effectively removes the phosphorus donor level from the band gap and reduces the number of donors. The rate of removal of donors is proportional to the donor concentration, and so an exponential reduction is expected. A similar process is responsible for the removal of acceptors. In addition, a negatively charged di-vacancy complex has been identified which acts like an acceptor defect. This leads to an increase in the number of acceptors, which has been found to be linear with fluence. Therefore the change of effective doping concentration with fluence $N_{eff}(\phi)$ can be described by

$$N_{eff}(\phi) = N_{D,0}\exp(-c_D\phi) - N_{A,0}\exp(-c_A\phi) - \beta\phi \tag{2.27}$$

where $N_{D,0}$ is the original donor concentration, c_D is the rate of donor removal, $N_{A,0}$ is the original acceptor concentration, c_A is the rate of acceptor removal and β is the rate of acceptor creation. In the case of an n-type bulk where $N_{D,0} \gg N_{A,0}$ then $N_{D,0} \equiv N_{eff,0}$, the original effective doping concentration, and $N_{A,0} \approx 0$. Eqn. (2.27) then reduces to

$$N_{eff}(\phi) = N_{eff,0}\exp(-c_D\phi) - \beta\phi\,. \tag{2.28}$$

With increasing fluence the effective doping concentration will initially decrease due to the removal of donors, until a point where the number of donors is equal to the

number of acceptors created by the radiation damage, and the detector is intrinsic. This is referred to as the inversion point. As the acceptor concentration continues to increase the bulk of the silicon becomes p-type, since the number of acceptors is greater than the number of donors; the silicon bulk has undergone type-inversion. As irradiation continues to higher fluences the number of donors decreases to zero and the effective doping concentration is dominated by the radiation created acceptor concentration.

After irradiation the effective doping concentration is not stable but changes with time, a process known as annealing. Two effects have been found; firstly a short term beneficial annealing process, causing the effective doping concentration to decrease (in a device irradiated past the inversion point), and secondly a long-term reverse-annealing process, causing N_{eff} to increase again. Therefore the effective doping concentration as a function of annealing time t after being exposed to a fluence ϕ can be described by

$$N_{eff}(\phi, t) = G_c(\phi) + G_a(\phi, t) + G_y(\phi, t) \tag{2.29}$$

where $G_c(\phi)$ describes the stable component of the effective doping concentration, $G_a(\phi, t)$ describes the short-term annealing of the unstable acceptor concentration and $G_y(\phi, t)$ describes long-term annealing. The stable component has been parameterised as a linear function [25, 26]

$$G_c(\phi) = g_c\phi \tag{2.30}$$

where g_c is the introduction rate for stable acceptors.

The short-term annealing of unstable acceptors has been parameterised by an exponential function [25, 26]

$$G_a(\phi, t) = g_a\phi \exp(-t/\tau_a) \tag{2.31}$$

where g_a is the introduction rate for unstable acceptors and τ_a is the time constant of short-term annealing. τ_a is temperature dependent; at room temperature values of $\tau_a = 1.8$ days [25] and $\tau_a = 55$ hours [26] have been found. Reducing the temperature

slows down the rate of annealing, and at $T = -10°\text{C}$ values of $\tau_a = 439.9$ days [25] and $\tau_a = 306$ days [26] have been found.

The reverse annealing process has been parameterised by [25]

$$G_y(\phi, t) = g_y \phi \left[1 - \exp(-t/\tau_y)\right] \tag{2.32}$$

where g_y is the introduction rate for reverse annealing and τ_y is the time constant of reverse annealing. Values for τ_y of 186 days at room temperature and 8650 days at 0°C being found. An alternative parameterisation was presented in Ref. [26]:

$$G_y(\phi, t) = g_y \phi \left(1 - \frac{1}{1 + t/\tau_Y}\right) . \tag{2.33}$$

Time constants for this reverse-annealing parameterisation of 475 days at room temperature and 516 years at $-10°\text{C}$ were found.

A sample annealing curve for a silicon detectors irradiated to a fluence of 1.0×10^{14} 1 MeV neutrons cm^{-2} then held at a temperature of 60°C is shown in Fig. 2.4. The annealing is modelled using Eqns. 2.30, 2.31 and 2.33, with constants taken from Ref. [26]. Initially the effective doping concentration decreases due to the short-term,

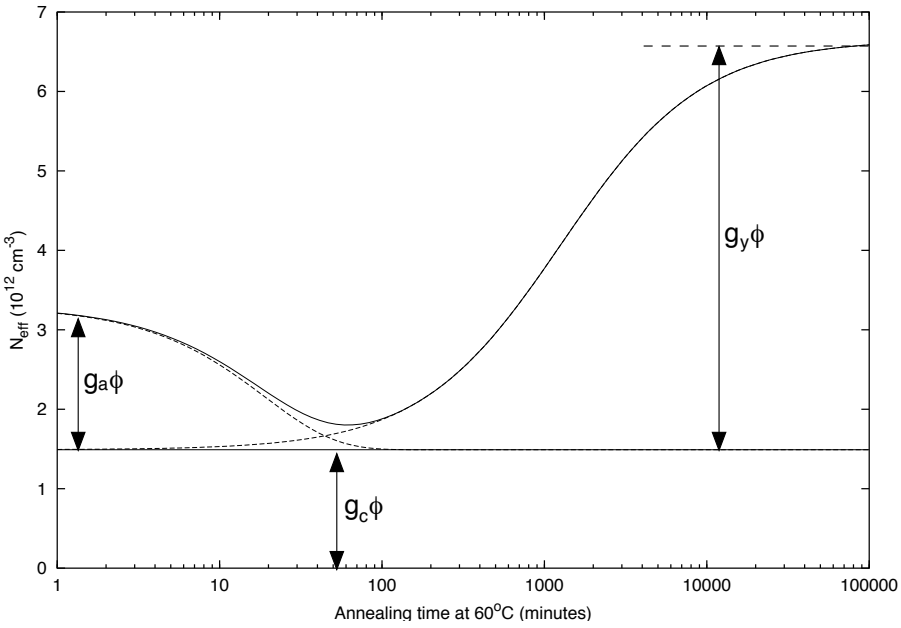

Figure 2.4: Annealing curve of a silicon detector held at 60°C.

"beneficial", annealing, until a minimum is reached, slightly higher than the stable component $g_c\phi$. At longer timescales the effective doping concentration increases again due to reverse annealing, which eventually saturates at the value $g_y\phi$.

Changes in leakage current

The creation of defects that introduce energy levels into the middle of the band gap enhances the leakage current due to the increased probability of the thermal excitation of valence electrons to the conduction band. The macroscopic effect on the leakage current has been widely shown to be a linear increase in the volume leakage current with increasing fluence [26, 27]

$$\frac{\Delta I}{Vol} = \alpha\phi \tag{2.34}$$

where ΔI is the increase in leakage current due to radiation damage, Vol is the depleted volume of the detector, ϕ is the radiation fluence and α is the current-related damage constant.

Thermal motion of these defects cause the radiation induced change in leakage current to decrease with time after irradiation has finished, known as leakage current annealing. This is temperature dependent, with more rapid annealing observed for higher temperatures. Leakage current annealing after irradiation has been parameterised by the sum of several exponentials [28, 29];

$$g(t) = \sum_{i=1}^{n} A_i \exp\left(-\frac{t}{\tau_i}\right) \tag{2.35}$$

so that the observed leakage current at a time t after the end of a short term irradiation is given by

$$I(\phi, t) = g(t)\alpha\phi.Vol \tag{2.36}$$

where α is the current-related damage constant found immediately after irradiation. The set of parameters shown in Table 2.1 for leakage current annealing at 20°C has been taken as representative of those found by several different experiments [28].

i	τ_i (min)	A_i
1	$(1.78 \pm 0.17) \times 10^1$	0.156 ± 0.038
2	$(1.19 \pm 0.03) \times 10^2$	0.116 ± 0.003
3	$(1.09 \pm 0.01) \times 10^3$	0.131 ± 0.002
4	$(1.48 \pm 0.01) \times 10^4$	0.201 ± 0.002
5	$(8.92 \pm 0.01) \times 10^4$	0.093 ± 0.007
6	∞	0.303 ± 0.006

Table 2.1: Time constants and amplitudes for leakage current annealing after irradiation for a temperature of 20°C, taken from Ref. [29].

Temperature dependence of the leakage current annealing is introduced by scaling the time axis with an Arrhenius relationship [28]

$$\Theta(T_A) = \exp\left(\frac{E_I}{k}\left[\frac{1}{T_R} - \frac{1}{T_A}\right]\right) \tag{2.37}$$

where T_A is the annealing temperature, E_I is the activation energy and T_R is the reference temperature, 20°C. Therefore Eqn. (2.36) becomes

$$I(\phi, t, T_A) = g(\Theta(T_A)t)\alpha\phi Vol\,. \tag{2.38}$$

The leakage current annealing parameterisation given in Eqn. (2.35), though, assumes that no annealing occurs during the irradiation period itself but only after the end of irradiation. In practice this is not the case, especially for irradiations of an extended duration as leakage current annealing is a continual process. Leakage current annealing both during and after irradiation has been parameterised by [30, 31]

$$g(t_{ir}, t') = \sum_{i=1}^{n} A_i \frac{\tau_i}{t_{ir}}\left[1 - \exp\left(-\frac{t_{ir}}{\tau_i}\right)\right]\exp\left(-\frac{t'}{\tau_i}\right) \tag{2.39}$$

where t_{ir} is the irradiation time and t' is the annealing time (time after irradiation). As $t_{ir} \to 0$ and annealing during irradiation becomes negligible then Eqn. (2.39) reduces back to Eqn. (2.35). The set of parameters in Table 2.2 was found for the irradiation of silicon diodes with 21 MeV protons [30] at room temperature, and has also been shown to represent irradiations with 24 GeV protons [31].

i	τ_i (min)	A_i
1	$(1.2 \pm 0.2) \times 10^6$	0.42 ± 0.11
2	$(4.1 \pm 0.6) \times 10^4$	0.10 ± 0.01
3	$(3.7 \pm 0.3) \times 10^3$	0.23 ± 0.02
4	124 ± 25	0.21 ± 0.02
5	8 ± 5	0.04 ± 0.03

Table 2.2: Time constants and amplitudes for leakage during and after irradiation for a temperature of 20°C, taken from Ref [31].

2.4.2 Surface damage

As opposed to radiation damage effects in the bulk of the silicon, caused by disruption of the silicon lattice, surface damage is concerned with radiation effects in the surface passivation layers, typically silicon dioxide SiO_2, and the boundaries between the silicon and the passivation. Surface damage effects are the result of the formation of electron-hole pairs in the oxide by ionising radiation. With no electric field across the oxide electron-hole pairs have a very high probability of recombination. However in the presence of an electric field the electron and hole can be separated, increasing the number of free carriers in the oxide. Electrons have a higher mobility than holes, and so are swept out of the oxide by the electric field, leaving the holes behind. The holes are slowly drifted to the edges of the oxide where they become trapped. This leads to two macroscopic surface damage effects. Firstly an increase in the flat-band voltage, caused by an increase in the oxide charge; this effectively raises the bias-voltage required for full-depletion [32]. Secondly there is a surface current due to the introduction of surface generation centres.

Surface effects are extremely dependent on the exact design and manufacturing process of the detector, and the quantitative effects on detector parameters are not as well understood as those resulting from bulk damage effects. However, surface damage effects have generally been found to be less important than bulk damage effects for macroscopic changes of detector properties.

Chapter 3

Irradiation of ATLAS silicon detectors

One of the major challenges facing the ATLAS Semiconductor Tracker is the intense radiation environment within which it will have to operate. Exposure to radiation damages silicon detectors causing their operational parameters to change. No plan is foreseen to replace the detectors within the SCT, so it is essential that they are able to operate effectively for the entire 10 year lifetime of the ATLAS experiment. A great deal of effort by the ATLAS SCT community has gone into providing a detector design that will withstand the predicted radiation levels, and then testing the designs through detector irradiation. To facilitate the irradiation of a large number of prototype silicon detectors a dedicated irradiation facility has been established in the East Hall of the CERN Proton Synchrotron complex.

In this chapter the design of the silicon microstrip detectors for the ATLAS SCT, the predicted radiation levels within the SCT and the layout and apparatus of the irradiation facility will be described.

3.1 ATLAS silicon microstrip detectors

The main influence on the design of the ATLAS silicon microstrip detectors has been the radiation environment within which they will have to operate. Radiation damage causes both the full depletion voltage and the bulk leakage current to increase. During operation the detectors must be fully depleted to obtain 100% charge collection efficiency (CCE). Therefore the full depletion voltage towards the end of the lifetime of the experiment must remain low enough that the detectors may be operated fully depleted without the fear of breakdown. Additionally, the power output of the detector is governed by both the bias voltage and the leakage current; this must be removed from the detectors by the cooling system to prevent thermal runaway.

The first major design choice for the detectors was between highly doped n-type strips on a lightly doped n-type bulk (n^+-n, or n-in-n) and the more common highly doped p-type strips on an n-type bulk (p^+-n, or p-in-n). The original specification [11] was for n-in-n devices, which were chosen because after type inversion the junction remains at the strip side of the detector and thus 100% CCE can be obtained with the detector operated under-depleted. This was thought necessary due to the expected full depletion voltage being greater than 300 V for a 300 μm thick detector after the predicted SCT radiation dose [33]. However, the fabrication of n-in-n devices is more complicated than the more standard p-in-n devices commonly used in HEP experiments, so the final design choice was for p-in-n detectors which were shown to be operational with full depletion even after receiving the expected fluence.

To populate both the barrel and forward regions of the SCT six different geometrical designs of detector are required. The detectors in the barrel are rectangular in shape whereas the forward regions consist of five different wedge shaped designs, each with a similar area to the barrel detectors. The dimensions for all different detector designs are shown in Table 3.1. All detectors are 285 ± 15 μm thick with

Detector	B	W12	W21	W22	W31	W32
Length (mm)	64.000	61.060	65.085	54.435	65.540	57.515
Inner Width (mm)	63.360	45.735	55.734	66.152	56.475	64.653
Outer Width (mm)	63.360	55.488	66.130	74.847	64.636	71.810
Active Area (cm^2)	38.13	31.59	40.45	38.15	39.75	38.74

Table 3.1: Dimensions of the SCT silicon microstrip detectors.

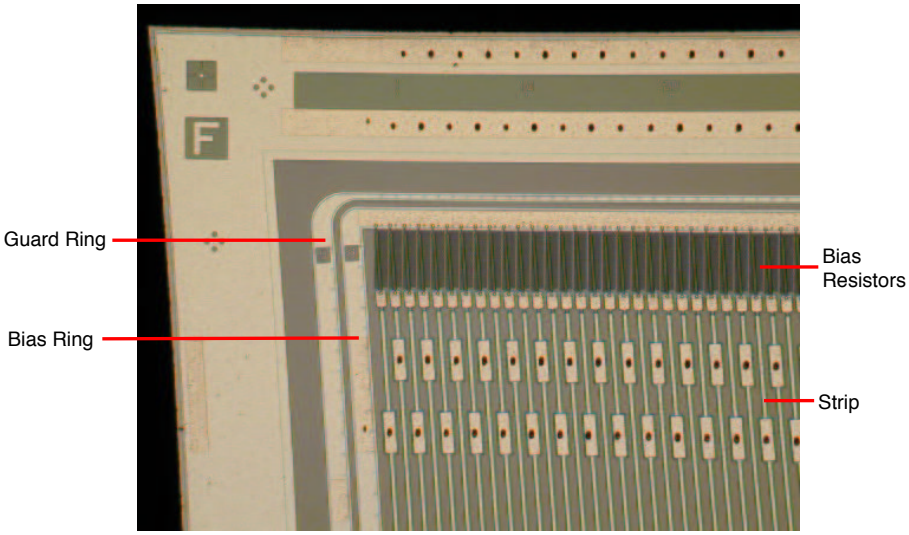

Figure 3.1: Corner detail of a wedge-shaped ATLAS silicon microstrip detector.

768 ac-coupled readout strips. For the barrel detectors the strips are parallel with 80 μm pitch, and for the wedge designs the strips are radial with pitch $70 - 90$ μm. The strips are connected to the bias ring by bias resistors, and outside of the bias ring is the guard ring, the exact design of which is manufacturer dependent. A photo of the corner detail of a wedge-shaped detector is shown in Fig. 3.1.

Whilst the above specifications represent the final design of the SCT detectors, it should be noted that not all of the detectors considered in this thesis match these exactly. This is because many of the devices irradiated were prototypes manufactured before the final design specifications had been decided. All are, however, p-in-n devices between 250 μm and 300 μm thick and of similar dimensions to those shown in Table 3.1.

3.2 Radiation levels in the SCT

To be able to test whether the silicon microstrip detectors for the SCT will still operate towards the end of the expected 10 year lifetime of the ATLAS experiment it is important to know the radiation dose that they will receive as accurately as possible. To this end several studies of the radiation environment within ATLAS have been performed. The most recent study of the ATLAS radiation environment [34] used DTUJET [35, 36] to generate minimum bias events, and the particles produced by this were transported and showered using FLUKA [37]. 900 individual regions were used to define the geometry of the ATLAS detector. The results of this study are shown in Table 3.2 [38]. Whilst a significant amount of the fluence for the innermost barrel layer comes from protons and pions (which originate from the primary interaction), the fluence for the far forward disk is dominated by neutrons. This is due to back-splashing from the calorimeters, and causes the fluence for this region to be greater than that for positions closer to the interaction point. The total fluence for 10 years of ATLAS running is calculated assuming three years of low-luminosity running ($L = 10^{33}$ cm^{-2} s^{-1}) and seven years of high-luminosity running ($L = 10^{34}$ cm^{-2} s^{-1}). Taking the predicted dose for the far forward disk from Table 3.2 then the maximum expected fluence received by a silicon detector in the SCT during 10 years of operation is 1.3×10^{14} 1 MeV equivalent neutrons cm^{-2}.

SCT Region	Neutrons	Pions	Protons	Total
Innermost Barrel Layer	0.95	0.66	0.12	1.73
Outermost Barrel Layer	0.68	0.26	0.06	1.00
Far Forward Disk	1.42	0.32	0.09	1.83

Table 3.2: Predicted radiation dose for 1 year of high luminosity running for several regions of the ATLAS SCT. Fluences quoted in 10^{13} 1 MeV equivalent neutrons cm^{-2}.

3.3 The irradiation facility

To enable a large number of full-sized ATLAS silicon microstrip detectors to be irradiated efficiently a dedicated facility has been established in the East Hall of the CERN Proton Synchrotron. A proton beam is used to irradiate the detectors, which are cooled to the ATLAS SCT design operating temperature and held under bias during irradiation. An x-y stage is used to scan the detectors through the proton beam to ensure that they receive a uniform fluence. The apparatus inside the irradiation area is shown in Fig. 3.2. The temperature of the detectors and their leakage currents are monitored throughout irradiation, the measurement apparatus being situated in a barrack located approximately 15 m from the beam-line.

In the following sections the various components of the irradiation facility will be described in more detail.

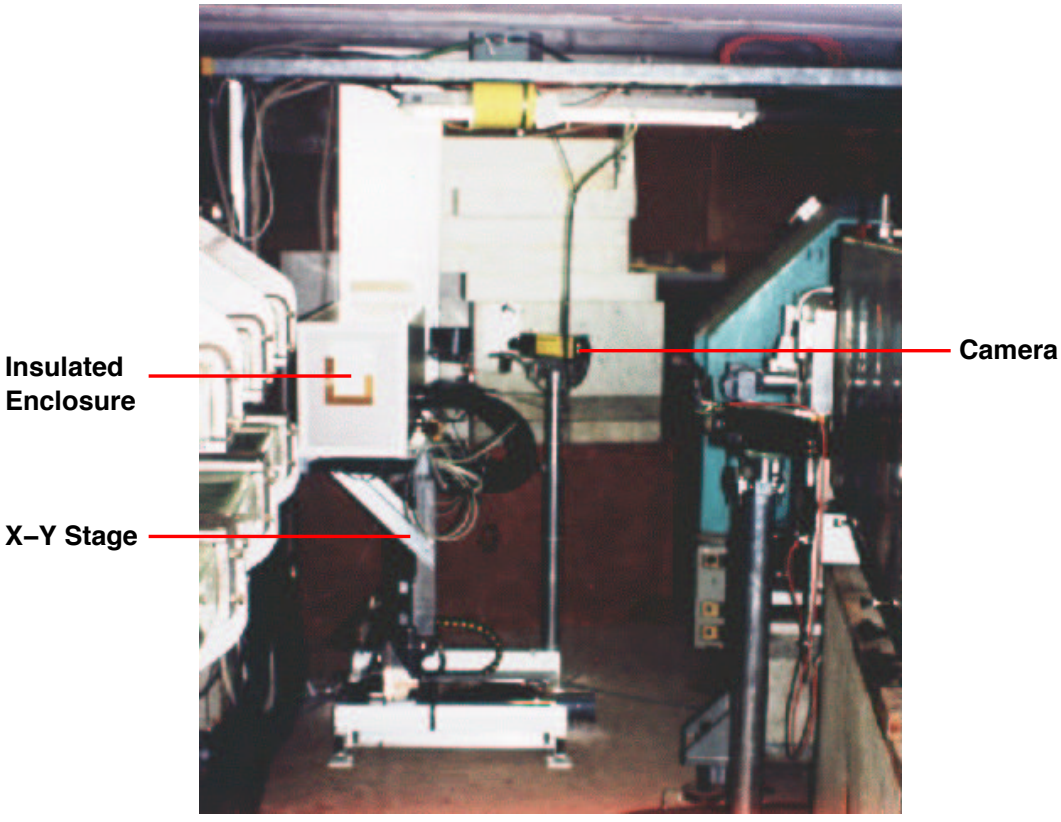

Figure 3.2: Insulated enclosure and x-y stage inside the irradiation area.

3.3.1 The proton beam

The proton beam used for the detector irradiations is the primary T7 beam [39] which is extracted directly from the CERN PS. It provides 24 GeV/c protons with a momentum resolution of approximately 1%. The PS operates on a "super-cycle" of duration 14.4 s during which beam is extracted for various areas. Between one and three spills of $300 - 400$ ms duration and each containing $20 - 40 \times 10^{10}$ protons are received in the irradiation facility during each super-cycle. The beam is focused by quadrupole magnets and the beam spot size is approximately 2 cm by 2 cm. The target fluence for proton irradiation is 3.0×10^{14} p cm^{-2}, which is derived from the estimated 1 MeV equivalent neutron fluence of 1.3×10^{14} cm^{-2} using a proton hardness factor of 0.69 and a 50% overestimation [11]. Recent results suggest that the proton hardness factor for the 24 GeV CERN PS may in fact be 0.61 [40], implying a target fluence for proton irradiation of 3.4×10^{14} p cm^{-2}. However for consistency across the series of irradiations the target fluence of 3.0×10^{14} p cm^{-2} has been retained.

The received proton fluence is measured by calibrating a Secondary Emission Monitor (SEM) located in the beam upstream of the irradiation area through the activation of aluminium foils. The SEM operates by the collection of electrons liberated from the surface of a metal plate by the passage of charged particles [41]. The collected charge is proportional to the intensity of the beam, and is converted to a number of counts which is therefore proportional to the number of particles in the beam. Aluminium foils placed in the beam are activated via the reaction ^{27}Na(p, 3pn)^{24}Na; after irradiation the ^{24}Na decays to ^{24}Mg by β and γ emission with a half-life of 15 hours. The activity in the foil is found by measuring the intensity of the 1368 keV peak from γ emission with a NaI spectrometer. The number of counts in the peak N_c measured during time t_c in a foil irradiated for time t_i, a time t_e since the end of irradiation is given by [41]

$$N_c = \epsilon A_{sat} \tau (1 - e^{-t_i/\tau})(1 - e^{-t_c/\tau}) e^{-t_e/\tau} \tag{3.1}$$

where τ is the lifetime of ^{24}Na, ϵ is the counting efficiency of the spectrometer,

$A_{sat} = \phi\sigma\rho_{Al}\delta N_{AV}/A_{Al}$ is the saturation activity, corresponding to the activity measured in a foil a time $t_e = 0$ since the end of an irradiation for which $t_i \to \infty$, ϕ is the number of incident protons per second, σ is the cross-section of ^{27}Na(p, 3pn)^{24}Na for high-energy protons, ρ_{Al} is the density of Aluminium, N_{AV} is Avagadro's number, A_{Al} is the atomic weight of Aluminium and δ is the thickness of the Aluminium foil. The fluence calculated from the foils is then equivalent to the number of SEM counts recorded during their irradiation.

3.3.2 Detector mounting

In order to be irradiated the detectors need to be held securely in position but with minimum contact to the detector itself. This has been achieved by using thin ceramic plates with hollow centres, to which the detectors are glued by their corners with epoxy resin (see Fig. 3.3). Each strip metal on the detector is wire bonded to a pitch adaptor used to connect the detector to readout electronics for post-irradiation

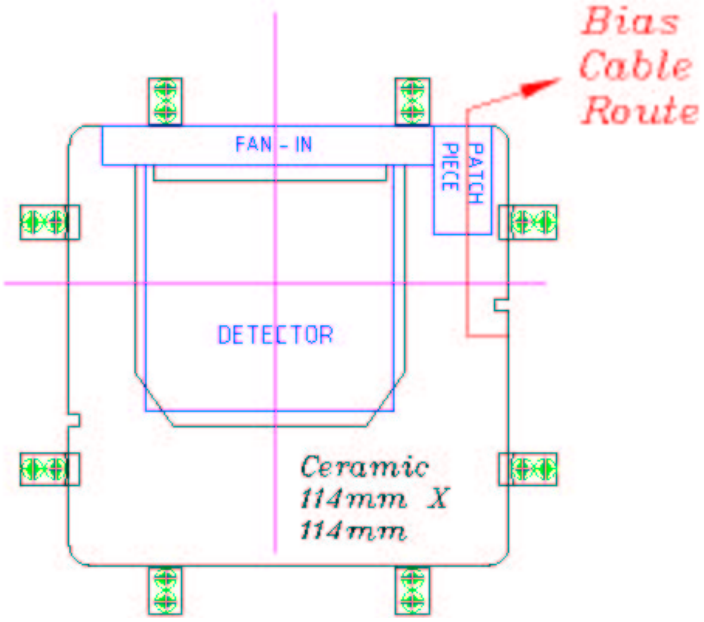

Figure 3.3: Detector mounted on a ceramic plate.

studies. For the irradiation each strip on the pitch adaptor is bonded to a common rail. A patch piece is fixed to the ceramic as an intermediate connection between the detector and wires to connect to the detector basket. The bias rail and the common rail on the pitch adaptor are wire-bonded to one connection on the patch piece, and the back plane of the detector to the other connection. A wire is soldered onto each connection on the patch piece, and then both wires soldered onto either pin of a two-way header. During irradiation the strip metals and bias rail are grounded and the back plane biased at 100 V (unless stated otherwise).

The detector baskets are constructed from Formica-backed Styrofoam and Plexiglas and use a comb structure to hold the ceramics by their edges. The header pins from the patch piece plug into sockets in a loom attached to the detector basket. This is connected to two 50-way sockets and a 40-way socket on top of the detector basket for the bias cables and temperature monitoring cables respectively.

3.3.3 Cooling and temperature monitoring

The detectors are kept at low temperature by containing the detector baskets inside an insulated enclosure cooled by the circulation of coolant fluid through heat exchangers (see Fig. 3.4). The insulated enclosure is constructed from Formica backed Styrofoam which has excellent structural and insulating properties. The insulated enclosure is divided into two completely independent halves, each capable of containing a 48-detector basket and each cooled by its own circuit. At the base of each half of the enclosure is a fan tray containing two flat pack blower fans, of entirely plastic construction apart from the motors. Directly above these is situated the heat exchanger which is a lightweight wire finned aluminium unit. When the detector basket is placed in the enclosure the detectors are positioned directly above the heat exchanger and surrounded by a chimney to promote air-flow through them. A liquid coolant mixture of 70:30 water to ethylene glycol is continually circulated through the heat exchangers by two Haake [42] chiller units, one for each cooling circuit. The chillers are situated outside of the irradiation area and are connected to the

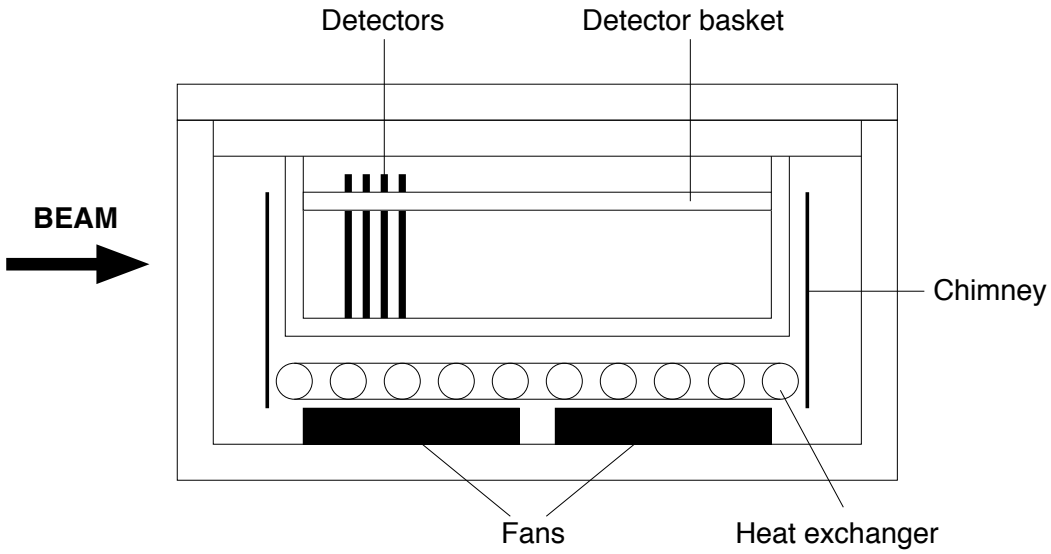

Figure 3.4: Cross section through one half of the insulated enclosure, showing position of fans, heat exchanger and detectors.

heat exchangers by 15 m runs of 10 mm diameter foam lagged nylon tubing, split a metre from the insulated enclosure by quick release self-sealing fittings to enable the replacement of the entire insulated enclosure in the event of equipment failure. Each half of the insulated enclosure is also equipped with a dry nitrogen pipe to maintain a constant dry atmosphere during irradiation.

The temperature inside the enclosure is monitored at several positions by pt100 thermistors. One pt100 is permanently attached to the heat exchanger and a further seven can be attached to each detector basket in various positions, so that the ambient temperature within the insulated enclosure can be measured as accurately as possible. The pt100's are connected through a Pickering [43] switching matrix to a Keithley [44] 2001 multimeter via a 4-point connection. This enables temperature measurements of all pt100's to be taken by cycling through each one in turn.

3.3.4 Bias supply and current monitoring

Throughout irradiation each detector is held under bias. The bias voltages are supplied by two CAEN [45] HV units, one for each detector basket, and each providing

48 independent channels. The CAEN units are controlled by a dumb terminal which enables the bias voltage for each detector to be set, monitored and altered easily. Detector currents are measured using a Keithley 487 picoammeter. A switching matrix is used to insert the picoammeter into the bias supply circuit of each detector in turn, using a make-before-break method so that the bias supply to the detector is not interrupted. A beam-veto signal is received from the PS control room which is synchronised to the receipt of beam in the area. This allows the measurement cycle to be paused for a short time so that the detector currents can stabilise after the large deposition of charge caused by the beam passing through the detectors.

3.3.5 The motion system

Due to the beam spot size being considerably smaller than the area of the detectors it is necessary to scan the detectors through the beam to obtain a uniform irradiation. The insulated enclosure is placed on an x-y stage (where z is the beam direction) with each axis controlled by a stepper motor providing 400 mm of travel. A motion program is operated that is designed to ensure that the whole area of the detector

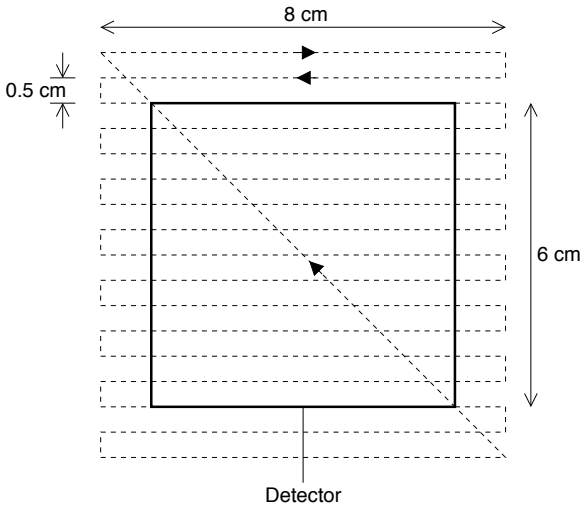

Figure 3.5: Diagram of motion program used by x-y stage, showing motion of the centre of the beam spot relative to the detector.

receives a uniform fluence, a diagram of which is shown in Fig. 3.5. It should be noted that a scanning area of 8 cm by 8 cm must be used for a uniform irradiation of the detectors.

The position of the stage is monitored in two ways. A potentiometer on each axis provides a measurement of the position of the stage relative to a fixed datum; this is monitored by computer. Additionally two radiation hard video cameras are situated inside the irradiation area. The first is placed below and to the front of the irradiation apparatus and is focused on the front of the enclosure; the second is behind and to the side of the apparatus and is focused on the front of the Irrad 1 shuttle. The rear of the enclosure is observed using a mirror on a motor controlled arm that can be swung into a position where the image of the enclosure is reflected into the rear camera. On both ends of the enclosure is a diagram showing the position of the detectors inside and this is covered by a sheet of transparent scintillating material which emits light when the beam passes through it. This enables the position of the beam relative to the detectors inside the enclosure to be observed on television screens in the control barrack. Having the insulated enclosure on a movable platform also allows irradiation of the detectors to be halted without actually stopping the beam by moving it into a park position below and to the side of the beam-line. This makes it possible to end the irradiation without disrupting other users of the beam.

3.3.6 Computer monitoring and alarm system

The temperature monitoring, current monitoring, position monitoring and SEM count are all interfaced to a PC running LabVIEW [46] software. This provides a graphical display of the most recent current measurement for each detector and the temperature measurements for each pt100 thermistor as a function of time. The position information obtained from the axis potentiometers of the x-y stage is displayed on an x-y graph and updated in real time, and the SEM count is displayed numerically and updated after each current measurement cycle. The time, SEM

count, thermistor temperatures and detector currents are also recorded in data-files to allow post irradiation study.

An alarm system is operated whereby an SMS text message is sent to a mobile phone if predefined limits for certain parameters are exceeded. This can include detector currents or thermistor temperatures rising above a defined maximum, or motion of the stage being halted for longer than a time specified. The control PC is connected to an Uninterruptable Power Supply, and the alarm system is also triggered in the event of a power failure.

3.3.7 Irradiation procedure

Detectors to be irradiated are brought to CERN several days before the start of the irradiation period, already mounted on ceramics and wired as outlined in section 3.3.2. Aluminium foils are prepared for the SEM calibration; several small pieces of aluminium are mounted onto card or perspex sheets in positions equivalent to each corner, each side and the centre of a detector inside the thermal enclosure.

Several hours before installation into the irradiation area the detectors are mounted in the detector baskets and transported to the irradiation control barrack. Dummy cables are used to connect the detector baskets to the bias supply/current measurement and temperature measurement circuits, and checks are made to ensure that all detectors draw the expected current when under bias and that all of the temperature sensors are operating. In the event of any detectors appearing to be unconnected then they can be re-wired or their position in the detector basket changed.

When all of the systems are operating properly the detectors can be installed into the irradiation area. This can only be done at pre-arranged times as all beam into the irradiation area has to be shut off for several hours prior to an access to allow the radiation level to drop. The PS control room is then contacted so that all beam into the East Area is stopped. The detector baskets are taken into the irradiation area, placed into the insulated enclosure and the bias and temperature measuring cables

connected. A visual inspection is made for leaks from the radiators, any misplaced apparatus that may jam the motion system and any cables that may snag. The aluminium foil arrangements are installed into holders on the front and back of the insulated enclosure for the SEM calibration. The irradiation area is then cleared; the whole installation process should take no longer than five minutes. The bias supply, current monitoring and temperature monitoring systems are immediately powered up to check that they are still operating correctly. The chillers are set to bring the temperature in the insulated enclosure down to that desired for the irradiation and the dry nitrogen flow into the insulated enclosure is started. The beam is turned on, with the enclosure in the park position, and the rear camera is used to check the profile and position of the beam by viewing it on the front of the Irrad 1 shuttle. When the beam profile is satisfactory and the temperature inside the insulated enclosure is as desired then the x-y stage is moved into the position expected to place the beam directly through the centre of the detectors. The cameras focused on the front and rear of the insulated enclosure are used to check the alignment of the beam. If the beam is out of position then adjustments can be made by either altering the scanning program used by the x-y stage, moving the position of the beam or in extreme cases moving the stage manually.

The irradiation can now begin; the x-y stage scanning program is started, the SEM counter is set to zero and the alarm systems are switched on. After eight to twelve hours of irradiation the x-y stage is sent to the park position and the beam to the area is halted. This allows the radiation level inside the area to fall so that a short access can be made to remove the aluminium foils. The beam and stage scanning are then restarted and the foils taken for analysis, after which the SEM count needed to reach the target fluence can be calculated. The foil calibration also provides a second check on the alignment of the beam from the fluence calculated for individual foils that were mounted at different positions. Irradiation now continues 24 hours a day (except for beam stops due to machine development, problems with the PS or accesses by other groups) until the target fluence is reached. During this time the alarm systems are always enabled and the equipment is checked manually

at least three times a day. Once the target fluence is reached the stage is parked and the beam halted to prepare for extraction of the detectors. In the event of other users still using the beam-line or a high radiation level in the irradiation area then the detectors may be left in the insulated enclosure parked out of the beam-line for up to a week, during which time cooling and monitoring continues. When ready for extraction the chillers are set to raise the temperature inside the insulated enclosure to the ambient temperature of the irradiation area. The detectors can then be removed from the irradiation area and their radiation level checked by TIS Radiation Protection. Finally, the detectors are removed from the detector baskets and placed in freezers to await post-irradiation testing.

Chapter 4

Study of current evolution in irradiated detectors

During detector irradiations at the CERN PS leakage currents are monitored and can be used to investigate radiation damage effects specifically for ATLAS silicon microstrip detectors at temperatures similar to those envisaged for operation at ATLAS. In this section a model of how the leakage currents of detectors held under bias during irradiation should change due to bulk radiation damage effects is developed. The predictions of this are then tested against leakage currents observed during irradiation, and used to calculate the radiation damage parameters α, the current-related damage constant, and β, the rate of acceptor creation specifically for ATLAS microstrip detectors at low temperature. Finally, detector characteristics both during irradiation and for the ATLAS operational scenario are modelled using the calculated damage parameters.

4.1 Leakage current evolution from bulk effects

Whilst the radiation damage of silicon has been studied extensively by many groups, the majority of work has involved the irradiation of simple silicon pad diodes at room temperatures with measurements performed after irradiation. Very little study has been performed with measurements taken during irradiation, or with devices cooled to minimise annealing. The detector irradiations performed at the CERN PS with the detectors held in a cold environment during irradiation allow a study of bulk radiation damage effects to be undertaken specifically for ATLAS silicon microstrip detectors with annealing effects minimised. Multiple measurements are taken during irradiation, allowing the progression of radiation damage as the fluence increases to be investigated.

The only measurements taken during irradiation are of detector leakage currents. Capacitance measurements, commonly used to determine the full depletion voltage and hence effective doping concentration, are not practical due to the operating conditions of the irradiation facility. However, information can be obtained on the changes to both the leakage current and the effective doping concentration due to radiation damage from the characteristics of the leakage current of a device held under constant bias throughout irradiation. This is done by considering two separate regions, one at low fluence and the other at high fluence.

Considering the low-fluence region first, before irradiation the full depletion voltage for a typical 300 μm thick detector is approximately $60 - 80$ V. Therefore when held under bias at 100 V the detector will be fully depleted. As irradiation commences the donor removal term in Eqn. (2.28) causes the effective doping concentration, and hence also the full depletion voltage, to decrease as the detector moves towards the inversion point. As the acceptor creation term starts to dominate, the effective carrier density then increases again as the inversion point is left. Providing that the detector is held under bias throughout this region it will remain fully depleted and the active volume is constant, equal to the bulk volume of the detector Ad where

A is the detector area and d is the detector thickness. Therefore using Eqn. (2.34) which parameterises the effect of radiation damage on the volume leakage current then the leakage current I in this low fluence region should be described by

$$I = \alpha A d \phi \tag{4.1}$$

where α is the current-related damage constant and ϕ is the fluence. The initial (unirradiated) leakage current I_0 is assumed to be negligible compared with the radiation induced change in leakage current; pre-irradiation leakage currents of $I_0 \approx 0.1\ \mu$A are observed for detectors inside the irradiation area and cooled to $-10°$C.

As irradiation progresses to higher fluences the donor removal term in Eqn. (2.28) becomes negligible compared with the acceptor creation term, as all of the initial concentration of donors is removed. The expression for the effective doping concentration Eqn. (2.28) then reduces to

$$N_{eff}(\phi) = -\beta\phi \tag{4.2}$$

and the effective doping concentration increases linearly with fluence. This causes an increase in the full depletion voltage, which consequently becomes greater than the applied bias voltage. The detector is therefore no longer fully depleted, and the active volume is no longer equal to the entire volume of the detector. Making the assumption that an under-depleted detector of depleted width W is equivalent to a fully depleted detector of thickness W then from Eqn. (2.22) the depleted width is

$$W = \sqrt{\frac{2\epsilon_0\epsilon_r}{e}\frac{V_{bias}}{|N_{eff}|}}\,. \tag{4.3}$$

By substituting for the effective doping concentration with Eqn. (4.2) the depleted width can be given as a function of fluence,

$$W = \sqrt{\frac{2\epsilon_0\epsilon_r}{e}\frac{V_{bias}}{\beta\phi}}\,. \tag{4.4}$$

The active volume for the detector is $Vol = AW$, and so from Eqn. (2.34) the leakage current of a detector during irradiation at high-fluence should be given by

$$I = \alpha A \sqrt{\frac{2\epsilon}{e}\frac{V_{bias}}{\beta}}\ \phi^{0.5}\,. \tag{4.5}$$

Therefore when considering the evolution of detector leakage currents through an entire irradiation, two distinct regions should be observed. Initially the leakage current should increase linearly with fluence, whilst the detector is fully depleted and its active volume is constant. Then at higher fluences where the effective doping concentration is dominated by acceptor creation and the full depletion voltage is greater than the applied bias voltage the leakage current increases at a slower rate, proportional to the square root of the fluence. At the point where the detector leaves the low-fluence region and is no longer fully depleted a kink should be observed on a current-fluence plot as the rate of increase of leakage current with fluence changes.

4.2 Preparation of data

To investigate the predictions for leakage current behaviour during irradiation given in Section 4.1 analysis is performed on leakage current data from detectors irradiated at the CERN PS whilst held under bias. As mentioned in Section 3.3.6 the following data are recorded during irradiation; time of measurement, temperature of thermistors inside the insulated enclosure, SEM count and detector leakage currents. A number of steps must be taken before these data are in a format suitable for analysis and it should be noted that there are slight differences in this process between irradiations carried out during 1999 and irradiations carried out in 2000 due to a software upgrade.

First the temperature and current data must be combined, since they have different measurement cycles and are stored in separate data-files. The two data-files are synchronised by comparing the time of measurement for each set of readings and matching temperature readings to the equivalent leakage current readings. This procedure was rendered obsolete for irradiations taking place after January 2000 as a software upgrade combined the temperature and leakage current readings into a single measurement cycle and data-file.

Next, the time of measurement for each set of current readings is converted into

the time since the start of irradiation and the SEM count is converted into a fluence measurement using the calibration factor obtained from the foil calibration. A representative detector temperature for each set of leakage current measurements is calculated by taking the mean of the temperature readings from all thermistors located in the detector basket. To eliminate detector current fluctuations due to temperature changes during irradiation each leakage current measurement is normalised to a reference temperature using [27]

$$\frac{I(T_1)}{I(T_2)} = \left(\frac{T_1}{T_2}\right)^2 exp\left[\frac{E_g}{2k_B}\left(\frac{1}{T_2} - \frac{1}{T_1}\right)\right] \tag{4.6}$$

where T_1 and T_2 are the measurement and reference temperatures respectively, E_g is the effective energy gap (a value of 1.12 eV has been used [20]) and k_B is Boltzmann's constant.

The data are now in a format ready for analysis. A naming convention is used for all detectors, taking into account the irradiation period, the detector group and the individual detector. The irradiation period is defined by a three letter and 2 number code for the month and year, for instance "apr99" for the April 1999 irradiation. Within each irradiation period the detectors are divided into groups with similar properties, depending upon the manufacturer of the detector, detector thickness and detector design. For example all 300 μm thick barrel detectors from manufacturer x could be labelled as group "a", which when combined with the irradiation period becomes group "apr99-a". Finally, individual detectors within groups are identified by a number; the first detector in group "apr99-a" is denoted as detector "apr99-a-1". Additionally, in the following detector descriptions "B" indicates barrel detectors and "W" wedge-shaped detectors for the forward regions.

4.3 Irradiation conditions

Detectors were irradiated in four separate irradiation periods. Each of these contained different detectors and was subject to slightly different conditions regarding the duration of the irradiation, beam flux and temperature of the detectors during irradiation. The specific conditions and detectors irradiated are described for each irradiation period in the following sections.

4.3.1 April 1999 irradiation

The April 1999 irradiation took place between 26th April and 4th May 1999. Beam conditions were favourable, with 2 spills per super-cycle each containing $30-40\times10^{10}$ protons being received between 0800 and 1800 hrs and 3 spills per super-cycle of a similar intensity received between 1800 and 0800 hrs. This allowed the target fluence to be reached within 7 days and the fluence profile is shown in Fig. 4.1. Apart from a beam stop of approximately 10 hours duration, 9 hours into the irradiation, the proton flux was fairly constant at $\approx 6 \times 10^8$ cm^{-2}s^{-1}. Unfortunately automatic recording of the SEM count from which the fluence is calculated was not active for the first 9 hours of irradiation due to technical problems. Instead the fluence is calculated for this period by extrapolating between SEM count readings recorded manually after approximately 30 minutes, 1 hour, 1 hour 10 minutes and 9 hours of irradiation assuming a constant flux between these points. Therefore the fluence profile for this initial period may be subject to some uncertainty in the event of a variable flux between the known points. The temperature profile for the irradiation is also shown in Figure 4.1; the temperature was held between -10.1°C and -10.0°C for the duration of the irradiation, apart from the initial hour when the temperature of the chillers was raised by one degree. Before analysis all leakage current measurements were normalised using this temperature profile to a reference temperature of -10.0°C.

In total 17 detectors were irradiated in April 1999 and a summary of these is shown

in Table 4.1. All of the detectors were manufactured on ⟨111⟩ orientation substrates with resistivity $2-5\,\mathrm{k}\Omega\,\mathrm{cm}$. All detectors were biased at 100V for the duration of the irradiation.

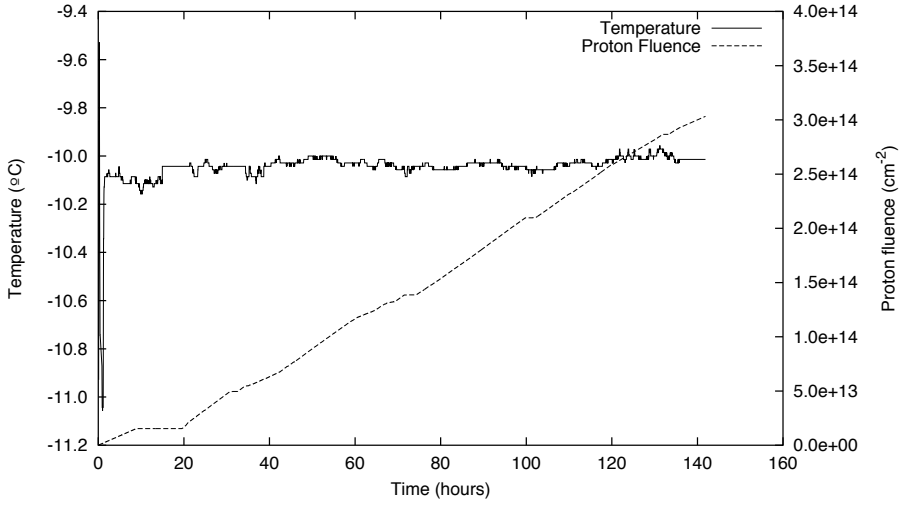

Figure 4.1: Temperature inside the insulated enclosure and fluence profile for the April 1999 irradiation.

Group	Quantity	Thickness (μm)	Design
apr99-a	2	300 ± 15	W
apr99-b	5	300 ± 15	B
apr99-c	4	250 ± 15	W
apr99-d	6	300 ± 15	1×B, 5×W

Table 4.1: Summary of detectors in the April 1999 irradiation.

4.3.2 June 1999 irradiation

The June 1999 irradiation took place between 22nd June and 4th July 1999. Two beam spills per super-cycle were received for the duration of the irradiation, each containing $30-40\times10^{10}$ protons. The target fluence was reached after approximately 250 hours and the fluence profile is shown in Figure 4.2. The flux was reasonably constant for the first 100 hours of irradiation, at $\approx 3.5\times10^{8}\,\mathrm{cm}^{-2}\mathrm{s}^{-1}$,

after which the irradiation was interrupted by several short beam stops of $5-10$ hours duration (required to perform measurements on a module being irradiated at the same time). The temperature profile of the irradiation is also shown in Figure 4.2. Due to technical problems temperature measurements inside the insulated enclosure were not recorded automatically. Instead, the temperature profile is taken from thermistor measurements recorded manually, typically three to four readings per day. The temperature inside the insulated enclosure increased steadily throughout the irradiation which necessitated lowering the temperature of the chillers by 1°C after 90 hours of irradiation. Before analysis all leakage current measurements were normalised using the temperature data to a reference temperature of -9.0°C.

In total 25 detectors were irradiated and a summary of their characteristics is shown in Table 4.2. All of the detectors were manufactured on $\langle 111 \rangle$ orientation substrates with resistivity $2-5$ kΩ cm. All detectors were biased at 100V for the duration of the irradiation.

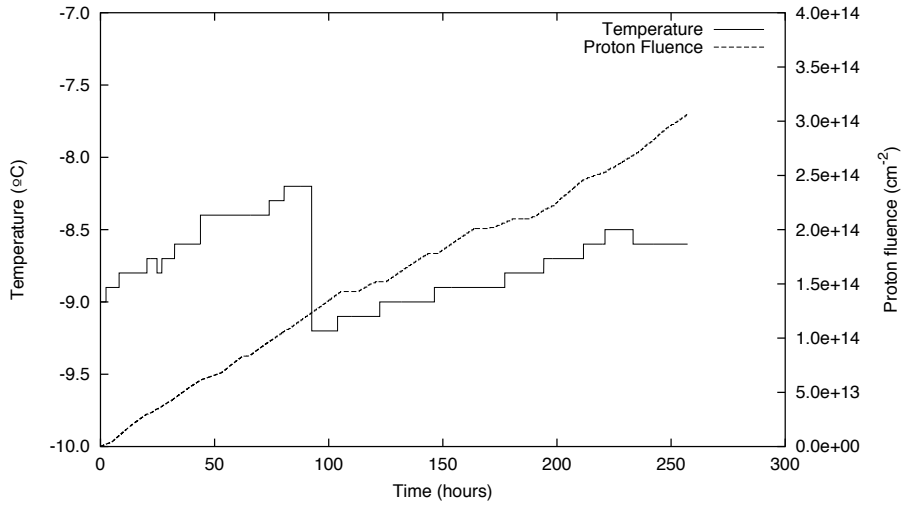

Figure 4.2: Temperature inside the insulated enclosure and fluence profile for the June 1999 irradiation.

Group	Quantity	Thickness (μm)	Design
jun99-a	9	300 ± 15	B
jun99-b	2	300 ± 15	W
jun99-c	5	285 ± 15	B
jun99-d	6	305 ± 15	B
jun99-e	3	300 ± 15	B

Table 4.2: Summary of detectors in the June 1999 irradiation.

4.3.3 October 1999 irradiation

The October 1999 irradiation took place between 27th October and 8th November 1999. One beam spill per super-cycle containing $30 - 40 \times 10^{10}$ protons was received between 0800 and 1800 hrs and two spills per super-cycle of a similar intensity were received between 1800 and 0800 hrs. The target fluence was reached after approximately 260 hours of irradiation and the fluence profile is shown in Figure 4.3. A computer crash after approximately 240 hours of irradiation prevented data being taken after this point. Apart from three short beam-stops in the first 75 hours of irradiation and one longer beam-stop of approximately 20 hours duration after 85 hours of irradiation, the proton flux was reasonably constant at $\approx 3.4 \times 10^8$ cm^{-2} s^{-1}. The temperature profile of the irradiation is also shown in Figure 4.3. Again problems with the automatic temperature recording meant that temperature measurements recorded manually had to be used for the temperature profile. The temperature inside the thermal enclosure was quite stable, with an increase of only 0.4°C for the entire irradiation period. Before analysis all leakage current measurements were normalised using the temperature data to a reference temperature of −9.5°C.

In total 19 detectors were irradiated and a summary of these is shown in Table 4.3. All of the detectors were manufactured on $\langle 111 \rangle$ orientation substrates with resistivity $2 - 5\,\mathrm{k}\Omega\,\mathrm{cm}$. Both oxygenated and standard (unoxygenated) detectors were irradiated, groups oct99-a, oct99-c and oct99-e being oxygenated, and groups oct99-b, oct99-d and oct99-f respectively acting as control samples of standard sili-

con to these. The oxygenation process used the high-temperature diffusion method, where silicon wafers have a layer of silicon oxide grown on each surface and are then baked for several hours at temperatures of $\approx 1150°C$. This produces an oxygen concentration in the silicon bulk of $\approx 10^{17}$ atoms cm^{-3} [47]. All detectors were biased at 100V for the duration of the irradiation.

Oxygenation has recently been shown to change the post-irradiation characteristics of silicon detectors [40]. This is apparent in the behaviour of the effective doping concentration after irradiation with protons (no difference between oxygenated and standard silicon is seen after irradiation with neutrons). For oxygenated silicon the rate of stable acceptor introduction g_c is found to be significantly lower than for standard silicon. Additionally the long term reverse annealing is found to be suppressed for oxygenated silicon relative to standard silicon. The net result is for a lower full depletion voltage after proton irradiation and subsequent annealing for oxygenated silicon devices compared with those manufactured on standard silicon.

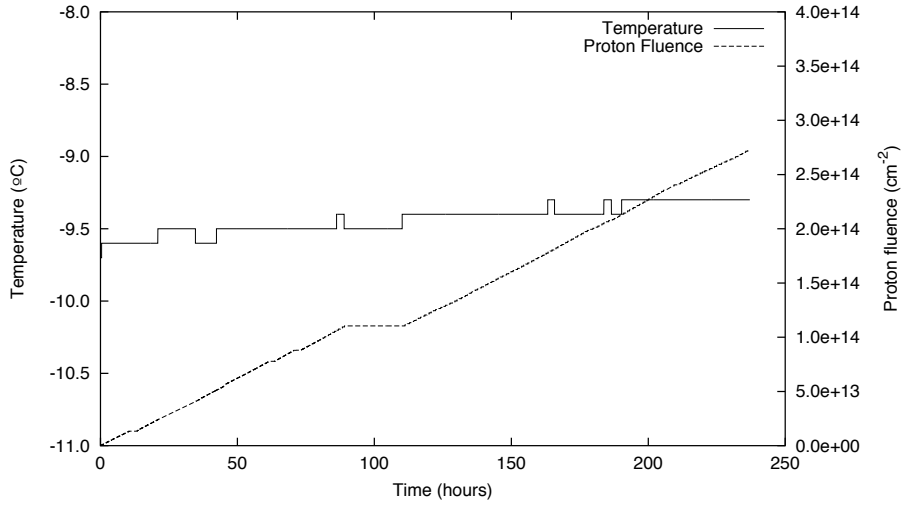

Figure 4.3: Temperature inside the insulated enclosure and fluence profile for the October 1999 irradiation.

Group	Quantity	Thickness (μm)	Design	Comments
oct99-a	3	280 ± 15	W	Oxygenated
oct99-b	3	280 ± 15	W	Standard
oct99-c	4	300 ± 15	B	Oxygenated
oct99-d	1	300 ± 15	B	Standard
oct99-e	5	300 ± 15	W	Oxygenated
oct99-f	3	300 ± 15	W	Standard

Table 4.3: Summary of detectors in the October 1999 irradiation.

4.3.4 May 2000 irradiation

The May 2000 irradiation took place between 21st May and 31st May 2000. Two beam spills per super-cycle were received for the majority of the irradiation, each containing $30 - 40 \times 10^{10}$ protons. The target fluence was reached after approximately 200 hours of irradiation and the fluence profile is shown in Figure 4.4. For the first 35 hours of irradiation the proton flux was relatively high, $\approx 6.5 \times 10^8$ cm^{-2} s^{-1}, until a beam stop of 15 hours duration. After this a reduced proton flux was received, $\approx 4.0 \times 10^8$ cm^{-2} s^{-1}. The temperature profile of the irradiation is also shown in Figure 4.4. Several temperature fluctuations are evident, with the temperature varying between -9.7 and -8.3°C during the irradiation. Before analysis, all detector currents were normalised using the temperature data to a reference temperature of -9.0°C.

In total 36 detectors were irradiated and a summary of these is shown in Table 4.4. All detectors were manufactured on material with resistivity $2 - 5$ kΩ cm, and are a mixture of $\langle 111 \rangle$ and $\langle 100 \rangle$ orientation substrates. Groups may00-b, may00-d and may00-f were manufactured on $\langle 100 \rangle$ substrates, with groups may00-a, may00-c and may00-e respectively acting as control samples manufactured on $\langle 111 \rangle$ substrates. Groups may00-g and may00-h were standard devices manufactured on $\langle 111 \rangle$ substrates. All detectors were biased at 100V for the duration of the irradiation.

The motivation for studying the different substrate orientations is that their silicon-

oxide interfaces have different characteristics [48–50]. ⟨111⟩ orientation substrates have a larger density of dangling bonds than ⟨100⟩ orientation substrates by approximately a factor of 10, and the density of trapped charge at the interface, responsible for surface damage effects, is proportional to the density of dangling bonds. Therefore whilst the bulk properties of the two substrate orientations will be similar, surface damage should affect them differently.

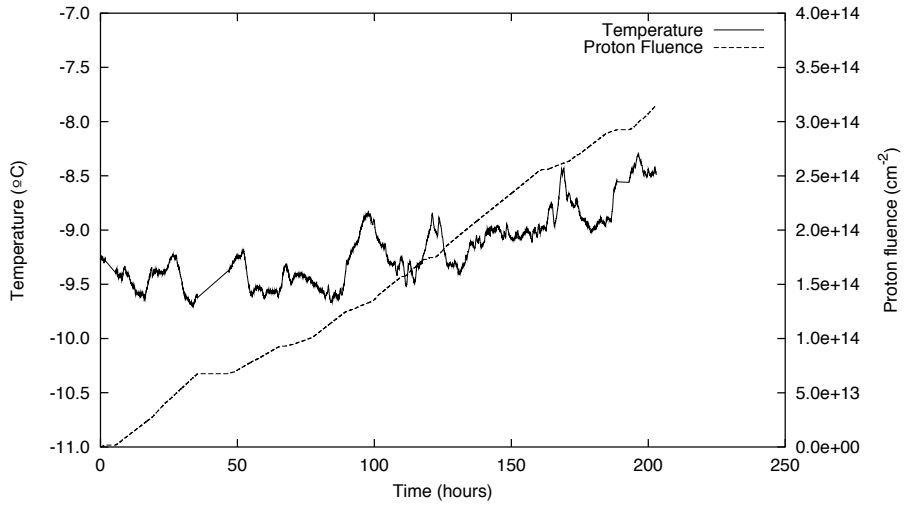

Figure 4.4: Temperature inside the insulated enclosure and fluence profile for the May 2000 irradiation.

Group	Quantity	Thickness (μm)	Design	Substrate
may00-a	7	285 ± 15	W	⟨111⟩
may00-b	3	285 ± 15	W	⟨100⟩
may00-c	2	260 ± 15	W	⟨111⟩
may00-d	2	260 ± 15	W	⟨100⟩
may00-e	3	285 ± 15	B	⟨111⟩
may00-f	5	285 ± 15	B	⟨100⟩
may00-g	5	285 ± 15	B	⟨111⟩
may00-h	9	285 ± 15	B	⟨111⟩

Table 4.4: Summary of detectors in the May 2000 irradiation.

4.4 Leakage currents during irradiation

From the model presented in Section 4.1 bulk radiation damage effects are expected to be manifested by a linear increase in leakage current with fluence at low fluences and an increase proportional to the square root of the fluence at high fluences. Before the model can be used to calculate the radiation damage parameters the characteristics of the leakage current data in these regions must be investigated for any significant deviations from this behaviour, which could indicate the presence of additional effects. This is performed separately for the low and high fluence regions.

4.4.1 Low fluence behaviour

In the low fluence region a relationship between current and fluence of the form $I \propto \phi^{a_{low}}$ with $a_{low} = 1.00$ is expected from bulk damage effects. This is investigated by performing a least-squares fit on a function

$$\log I = a_{low} \log \phi + b \tag{4.7}$$

which is equivalent to

$$I = 10^b \phi^{a_{low}} . \tag{4.8}$$

The value of a_{low} given by the fit will indicate whether the bulk damage model is sufficient to explain leakage current behaviour during irradiation, or if other effects appear to be present. For this to be valid it is important that the data range for the fit is chosen correctly so that only leakage current measurements taken when the detector is fully depleted are used. The point where the detector leaves the low-fluence region can be identified by a distinct change in gradient of the current-fluence plot, and typically occurs at fluences of $2.0 - 3.0 \times 10^{13}\,\mathrm{p\,cm^{-2}}$. The low-fluence region is therefore defined on a detector to detector basis so that the maximum amount of data can be analysed without straying from the low-fluence region. Uncertainties on the given values of a_{low} are estimated from the spread of data-points, and it should be noted that for clarity only a small subset of the data used to calculate

a_{low} is shown in the following graphs. Typically $400-500$ individual leakage current measurements are taken for each detector in the low-fluence region.

April 1999 Data

A low-fluence data range of $\phi = 0.5 - 2.0 \times 10^{13}\,\mathrm{p\,cm^{-2}}$ is used for all detectors in the April 1999 irradiation; the lower limit was imposed due to erratic current readings in the early stages of the irradiation. In addition, detector apr99-d-3 is observed to have a large spike in leakage current at a fluence of $1.0 \times 10^{13}\,\mathrm{p\,cm^{-2}}$; this detector is therefore excluded from further analysis. Eqn. (4.7) is fitted to the leakage current data in the defined low-fluence region for all other detectors. Data and the results of the fits are shown for detectors apr99-a-1 and apr99-b-1 in Fig. 4.5; the vertical lines on these graphs indicate the region used to perform the fits. It is clear that the fits are not a very good representation of the data. The most obvious cause of this is a decrease in current by approximately $5-10\,\mu$A after a fluence of $1.55 \times 10^{13}\,\mathrm{p\,cm^{-2}}$. This occurred during a period without beam of duration 10 hours. Additionally the rate of increase of leakage current with fluence appears to increase after $\phi = 0.6 \times 10^{13}\,\mathrm{p\,cm^{-2}}$. It should be remembered that until a fluence of $1.55 \times 10^{13}\,\mathrm{p\,cm^{-2}}$ the automatic recording of fluence was not operational, and the fluence values had to be extrapolated from a small number of manual readings

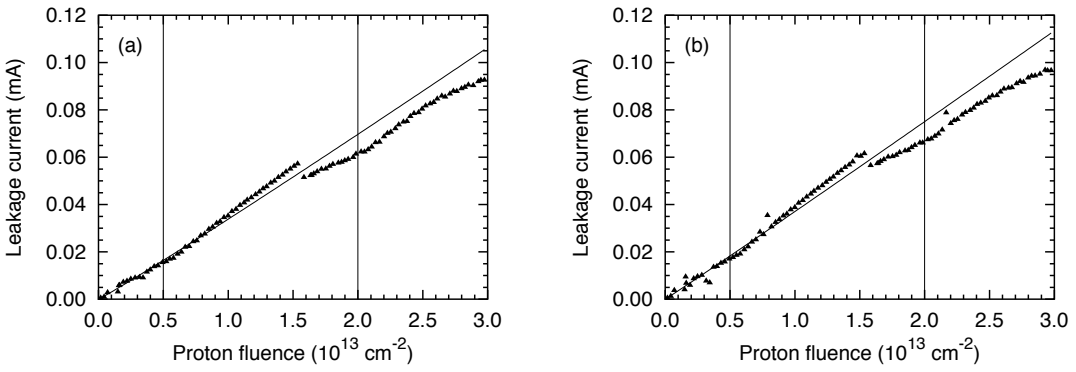

Figure 4.5: Low fluence leakage current data and fits for detectors (a) apr99-a-1 and (b) apr99-b-1.

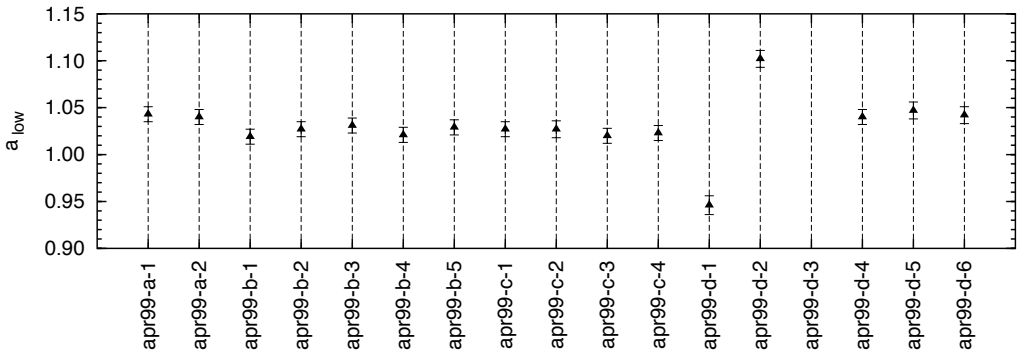

Figure 4.6: Values of a_{low} for all detectors in the April 1999 irradiation.

assuming a constant flux between these points. Variations in proton flux between the known fluence points could mean that the fluence values for leakage current measurements in this region are not correct.

The values of a_{low} found for all of the detectors in the April 1999 irradiation are shown in Fig. 4.6. For almost all detectors values of $a_{low} = 1.02 - 1.04$ are found, with only detectors apr99-d-1 (with $a_{low} = 0.95$) and apr99-d-2 ($a_{low} = 1.10$) differing significantly from this. However, these results should be treated with care due to the aforementioned decrease in current during a beam-stop and potential problems with the fluence measurements.

June 1999 Data

A low-fluence data range of $\phi = 0.1 - 2.0 \times 10^{13}\,\mathrm{p\,cm^{-2}}$ is used for all detectors in the June 1999 irradiation, except for detectors from the group jun99-e which appear to leave the low fluence region at a fluence of approximately $1.7 \times 10^{13}\,\mathrm{p\,cm^{-2}}$; a low-fluence data range of $\phi = 0.1 - 1.5 \times 10^{13}\,\mathrm{p\,cm^{-2}}$ is used for these detectors. Several detectors exhibit leakage current irregularities at low fluences; this is seen for detectors jun99-a-3, jun99-a-5, jun99-a-7 and jun99-b-1 (see Fig. 4.7), and these four detectors are consequently excluded from further analysis.

For the remaining detectors Eqn. (4.7) is fitted to the data in the defined low-

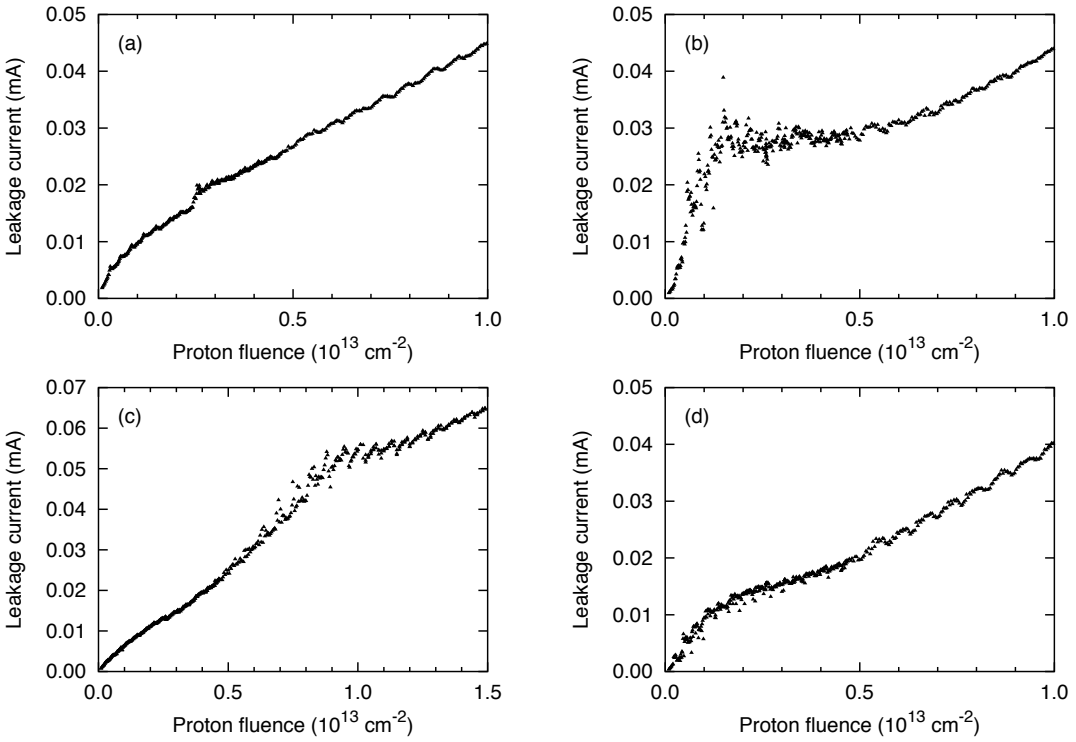

Figure 4.7: Low-fluence leakage current data for detectors (a) jun99-a-3, (b) jun99-a-5, (c) jun99-a-7, and (d) jun99-b-1.

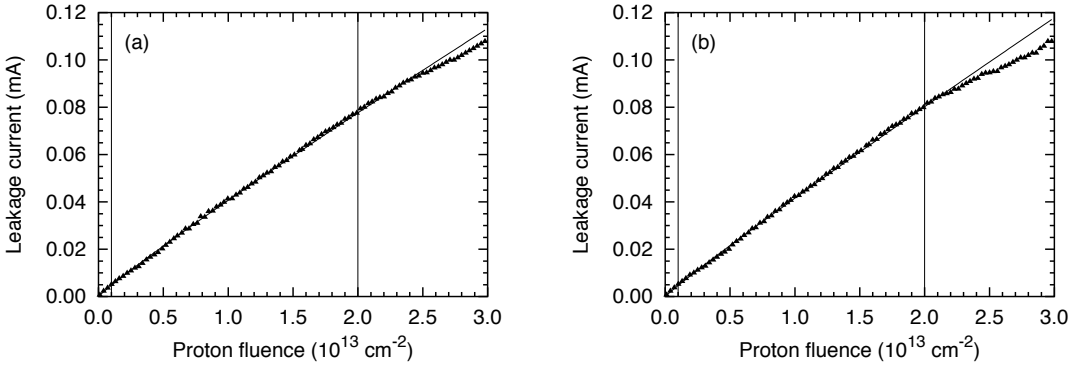

Figure 4.8: Low-fluence leakage current data and fits for detectors (a) jun99-a-1 and (b) jun99-c-1.

fluence region. Data and the results of the fits are shown for detectors jun99-a-1 and jun99-c-1 in Fig. 4.8 and for detectors jun99-e-1 and jun99-e-3 in Fig. 4.9. The vertical lines on these graphs represent the data range used to perform the fits. Considering detectors jun99-a-1 and jun99-c-1 first, the observed leakage currents exhibit a smooth increase with fluence and are well represented by the fits. The deviation of the data from the fit at a fluence of $2.2 - 2.4 \times 10^{13}\,\mathrm{p\,cm^{-2}}$ indicates where the low-fluence region is left. For detectors jun99-e-1 and jun99-e-3 the observed leakage currents take slightly higher values than predicted by the fit for fluences $\gtrsim 1.0 \times 10^{13}\,\mathrm{p\,cm^{-2}}$. The low-fluence region is left for these two detectors after a fluence of approximately $1.7 \times 10^{13}\,\mathrm{p\,cm^{-2}}$.

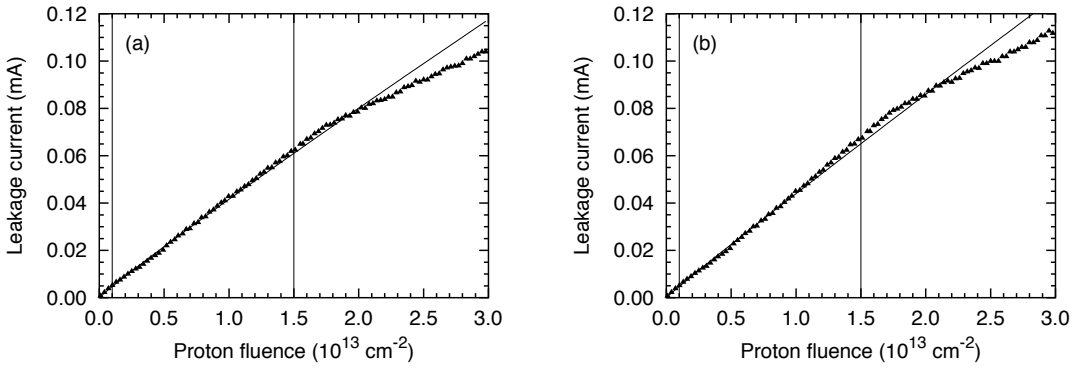

Figure 4.9: Low fluence leakage current data and fits for detectors (a) jun99-e-1 and (b) jun99-e-3.

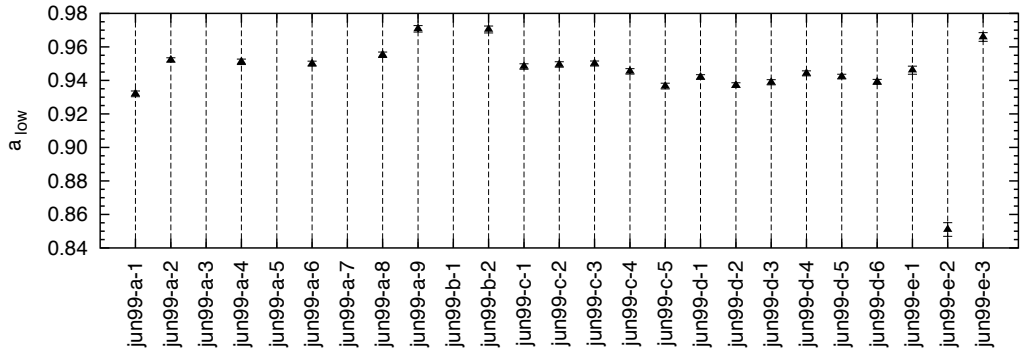

Figure 4.10: Values of a_{low} for all detectors in June 1999 irradiation.

The values of a_{low} found from the fits for all of the detectors are shown in Fig. 4.10. All detectors are found to have $a_{low} = 0.93 - 0.97$ apart from detector jun99-e-2 which has a significantly lower value, $a_{low} = 0.85$.

October 1999 data

A low-fluence data range of $\phi = 0.1 - 1.3 \times 10^{13}\,\mathrm{p\,cm^{-2}}$ is used for all detectors in the October 1999 irradiation. This relatively low upper limit is applied to avoid a small decrease in leakage current seen after a fluence of $1.33 \times 10^{13}\,\mathrm{p\,cm^{-2}}$, during a beam-stop of duration 2.8 hours. Detector oct99-a-2 is observed to have an abnormally large current until a fluence of $1.0 \times 10^{13}\,\mathrm{p\,cm^{-2}}$ and is consequently excluded from further analysis.

For all other detectors Eqn. (4.7) is fitted to the leakage current data in the defined low-fluence region. Data and the results of the fits are shown in Fig. 4.11 for detectors oct99-a-1 and oct99-b-1. For detector oct99-a-1 there is a regular increase in leakage current with fluence and the data are well represented by the fit. At a fluence of $1.33 \times 10^{13}\,\mathrm{p\,cm^{-2}}$ the leakage current falls by approximately $4\,\mu$A, during the period without beam. Immediately irradiation is restarted the leakage current appears to increase at a faster rate than observed before the beam-stop, until a fluence of $1.5 \times 10^{13}\,\mathrm{p\,cm^{-2}}$ where the data are again well represented by the fit. After a fluence of $2.2 \times 10^{13}\,\mathrm{p\,cm^{-2}}$ the data deviate from the fit, indicating where the low-fluence region is left. Almost identical behaviour is shown by detector oct99-b-1.

The values of a_{low} found for all detectors are shown in Fig. 4.12. Whilst there is a considerable spread in values, covering a range of $a_{low} = 0.82 - 0.93$, the majority of detectors have $a_{low} = 0.87 - 0.91$. Comparing the oxygenated detectors (oct99-a, oct99-c and oct99-e) with the control detectors (oct99-b, oct99-d and oct99-f respectively), whilst the detectors in the oxygenated groups oct99-c and oct99-e all take slightly lower values of a_{low} than their control detectors in groups oct99-d and oct99-f, this is not seen between detectors in groups oct99-a and oct99-b. For

detectors in these groups similar values of a_{low} are found. Therefore no systematic difference in values of a_{low} is observed between standard and oxygenated detectors.

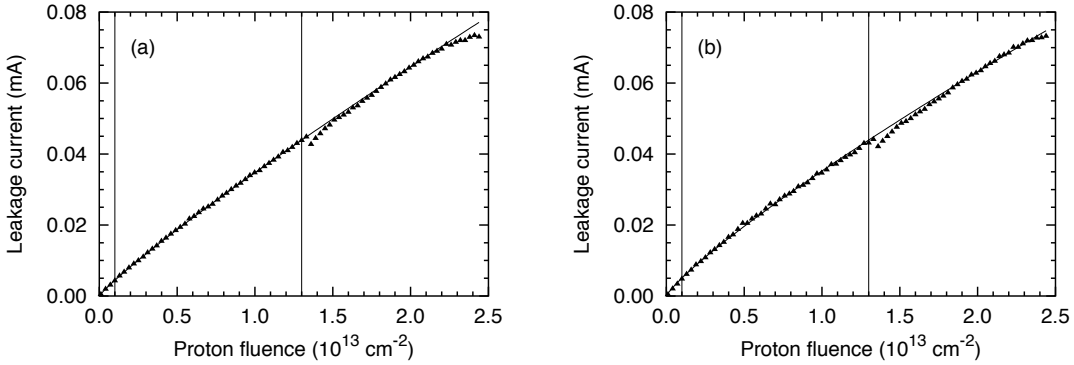

Figure 4.11: Low-fluence leakage current data and fits for detectors (a) oct99-a-1 and (b) oct99-b-1.

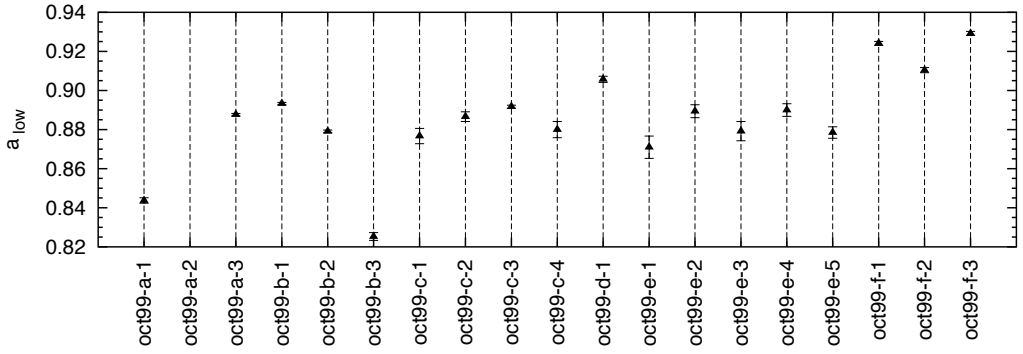

Figure 4.12: Values of a_{low} for all detectors in the October 1999 irradiation.

May 2000 data

A low-fluence data range of $\phi = 0.1 - 1.5 \times 10^{13}\,\mathrm{p\,cm^{-2}}$ is used for all detectors in the May 2000 irradiation since several of the detectors appear to leave the low-fluence region at a fluence of approximately $1.8 - 1.9 \times 10^{13}\,\mathrm{p\,cm^{-2}}$. Detector may00-h-3 is excluded from further analysis due to the presence of a large spike in current at a fluence of $1.0 \times 10^{13}\,\mathrm{p\,cm^{-2}}$.

For all other detectors Eqn. (4.7) is fitted to the leakage current data in the defined low-fluence region. Leakage current data and fits are shown for detectors may00-b-1 and may00-c-1 in Fig. 4.13. Both of these detectors display a regular increase in leakage current with fluence and are well represented by the fits both during and after the defined low-fluence region. The data deviate from the fit at a fluence of $\approx 2.4 \times 10^{13}\,\mathrm{p\,cm^{-2}}$, indicating the low-fluence region being left. For detector may00-a-5 (see Fig. 4.14a) the low-fluence region is left at a lower fluence, $\approx 1.8 \times 10^{13}\,\mathrm{p\,cm^{-2}}$. Additionally, several detectors are observed to have a slight ripple in leakage current, shown for detector apr99-a-1 in Fig. 4.14b. The origin of this is unclear, but it is not a large effect.

The values of a_{low} found for all detectors are shown in Fig. 4.15. The majority of detectors are found to have $a_{low} = 0.88 - 0.94$, although four detectors are seen to have significantly lower values; detectors may00-c-2, may00-e-3, may00-f-4 and may00-g-5 have $a_{low} = 0.80 - 0.86$. Comparing detectors manufactured on $\langle 100 \rangle$ orientation substrates (groups may00-b, may00-d and may00-f) with their control samples manufactured on $\langle 111 \rangle$ substrates (groups may00-a, may00-c and may00-e respectively) no systematic difference in values of a_{low} is evident.

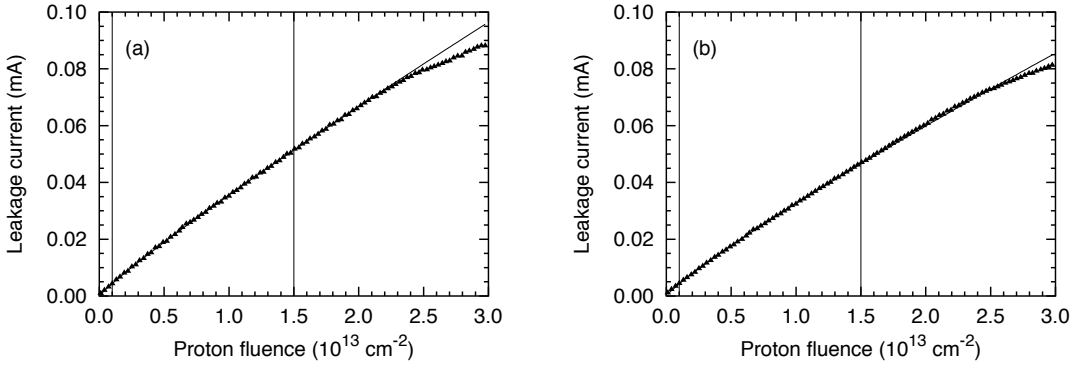

Figure 4.13: Low-fluence leakage current data and fits for detectors (a) may00-b-1 and (b) may00-c-1.

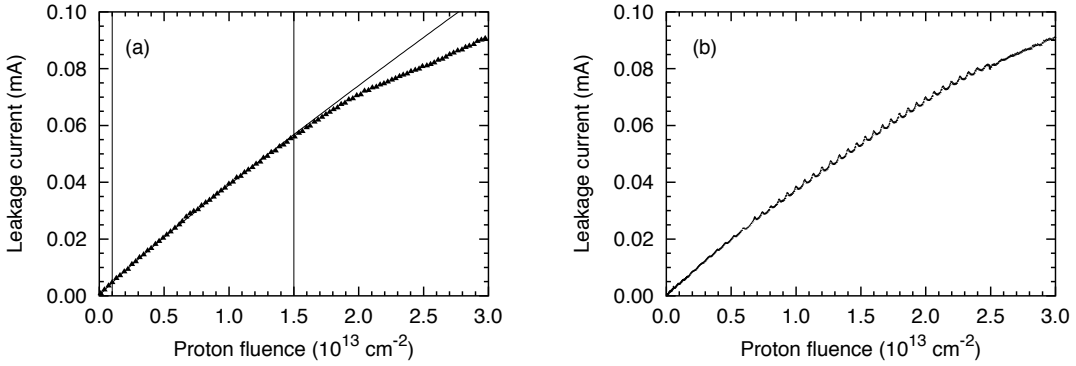

Figure 4.14: Low-fluence leakage current data for detectors (a) may00-a-5, and (b) may00-a-1.

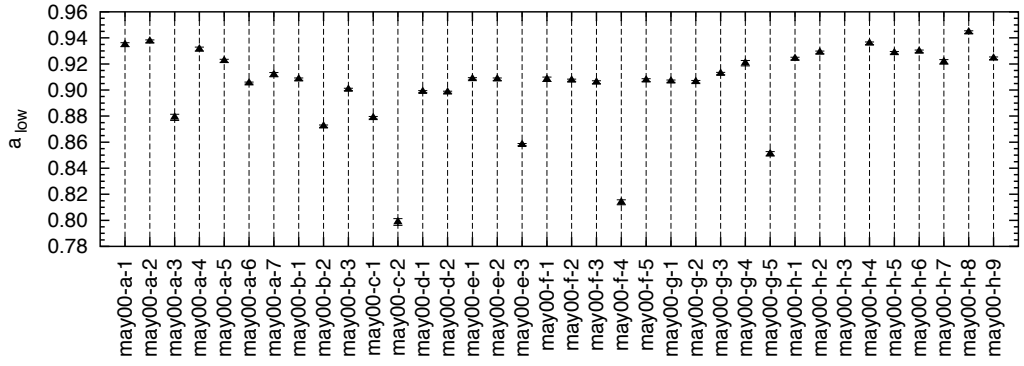

Figure 4.15: Values of a_{low} for all detectors in the May 2000 irradiation.

Discussion

Considering the results found from all four irradiations together, there is a clear tendency for detectors to take values of a_{low} lower than the expected $a_{low} = 1.00$. This is the case for detectors in all irradiations apart from April 1999 where, as explained earlier, the results must be treated with care due to problems in the low fluence region. For the other irradiations the values found for a_{low} are; June 1999 $a_{low} = 0.93 - 0.97$, October 1999 $a_{low} = 0.87 - 0.91$ and May 2000 $a_{low} = 0.88 - 0.94$. The distribution of a_{low} values from these three irradiations is shown in Fig. 4.16; the peak of the distribution is for $a_{low} \approx 0.93$. The fact that a_{low} does consistently differ from the expected $a_{low} = 1.00$ hints at the possible presence of other effects in addition to the linear increase in leakage current expected from bulk damage. The current decreases seen during periods without beam also imply a more complex situation than the simple model proposed in Section 4.1. Several possibilities

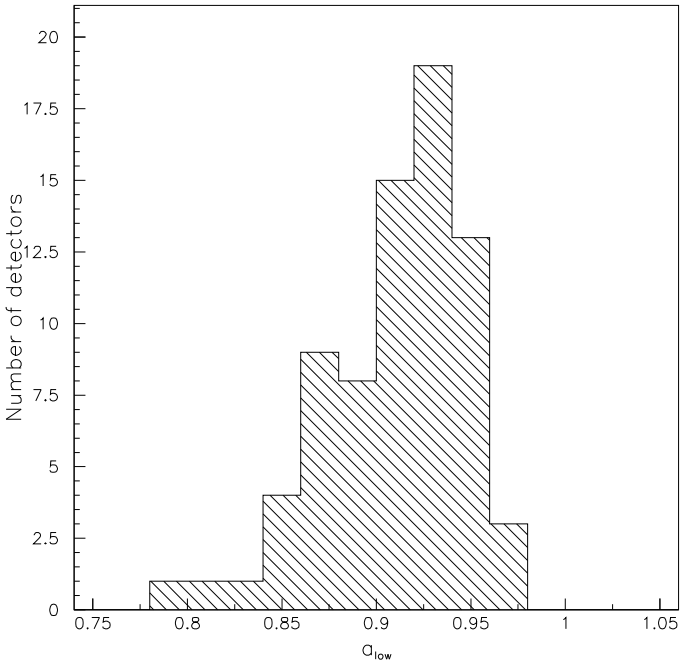

Figure 4.16: Distribution of a_{low} values for detectors in June 1999, October 1999 and May 2000 irradiations.

for explaining the observed behaviour of leakage currents during irradiation in the low-fluence region will now be considered.

The first possibility is leakage current annealing. As explained in Section 2.4.1 in addition to a linear increase in leakage current with fluence during irradiation it has been found that after irradiation annealing of defects causes a time dependent decrease in the leakage current. This could clearly explain the decrease in current seen during beam-stops. Leakage current annealing occurring during irradiation, which would be manifested by a time dependent decrease in the current-related damage constant and hence a decreasing gradient of a current-fluence plot, could also explain the observed non-linearity of the leakage current with fluence. Leakage current annealing is temperature dependent, with a slower decrease in leakage current seen at lower temperatures. Therefore at the irradiation temperatures considered here, -8 to $-10°$C, leakage current annealing effects are expected to be small. However, since little study has previously been carried out on low temperature annealing it is important to investigate whether this could be responsible for the observed low-fluence leakage current behaviour.

The most common way of parameterising leakage current annealing is with the sum of several exponentials. For example the parameterisation given in Eqns. (2.35) to (2.38) was used to perform a simulation of the evolution of ATLAS silicon detectors over the lifetime of the experiment in Ref. [28]. This parameterisation allows temperature dependence of the annealing process to be included through a scaling of the time axis with Eqn. (2.37). For an annealing temperature of $T_A = -10°$C, the temperature during the April 1999 irradiation, the scaling factor for the time axis relative to a temperature of 20°C is

$$\Theta(-10°\text{C}) = 0.00732\,. \tag{4.9}$$

This indicates that the equivalent of one days annealing at 20°C is 137 days at $-10°$C, implying that leakage current annealing should indeed be only a small effect at the low temperatures considered here. This parameterisation can also be used to calculate $g(t)$, the ratio of leakage current a time t after the end of irradiation

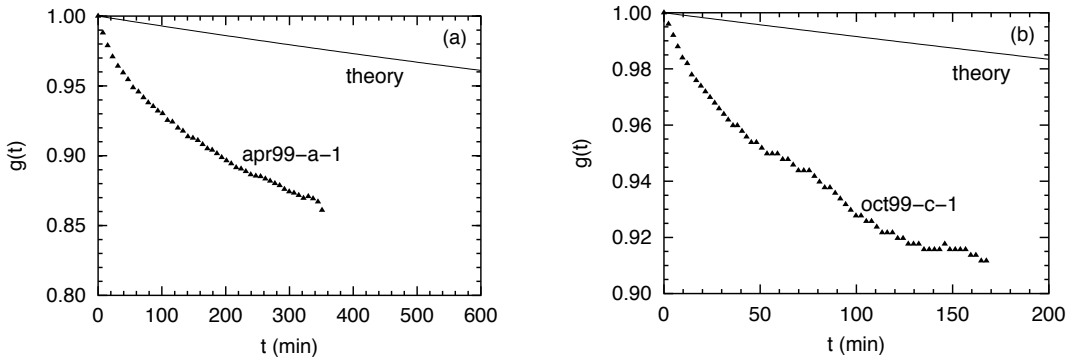

Figure 4.17: Ratio of leakage current a time t after the end of irradiation to leakage current at $t = 0$ for prediction of Eqn. (2.35) and data for low-fluence beam-stops during (a) April 1999 and (b) October 1999 irradiation.

to the leakage current at time $t = 0$. Eqn. (2.35) is used (with the parameters given in Table 2.1) to calculate $g(t)$ for time periods and temperatures equivalent to the beam-stops of the April 1999 ($-10°$C) and October 1999 ($-9°$C) irradiations, shown along with data in Figs. 4.17a and 4.17b respectively. For both irradiation periods the predicted values of $g(t)$ show a much smaller decrease than is observed from the data. For example, in the April 1999 irradiation a time $t = 350$ minutes after the end of irradiation Eqn. (2.35) predicts $g(t) \approx 0.98$, whereas the data for detector apr99-a-1 give $g(t) \approx 0.87$. Similarly, in the October 1999 irradiation a time $t = 170$ minutes after the end of irradiation the data give $g(t) \approx 0.91$, whereas the prediction is for $g(t) \approx 0.99$. Therefore it would appear that the leakage current behaviour observed during beam-stops is not consistent with the leakage current annealing parameterisation of Eqn. (2.35).

The above does not, however, reflect annealing that occurs during irradiation, assuming instead that annealing only occurs during periods without beam. Whilst this may be sufficient for annealing periods that are much longer than the irradiation period, in both the April 1999 and October 1999 irradiations the irradiation time is of a duration similar to or longer than the beam-stop. Therefore annealing during irradiation must be considered as well. This is included in the parameterisation presented in Eqn. (2.39), which was found in Ref. [31] to be a good representation

of the annealing behaviour of diodes irradiated in the PS with 24 GeV protons, and was used to correct leakage current measurements for annealing that occurred during irradiations performed at room temperature. Eqn. (2.39) can be used (with the parameters given in Table 2.2) to calculate $g(t_{ir}, t')$, the ratio of observed leakage current after time t_{ir} of irradiation and time t' of annealing to the leakage current had no annealing occurred either during or after irradiation. This is shown in Fig. 4.18a for a scenario equivalent to the April 1999 irradiation, where a 9.1 hour irradiation period is followed by a 10 hour period without beam, for temperatures of both 20°C and −10°C. The temperature dependence is again introduced by scaling the time axis with Eqn. (2.37). After 9.1 hours of irradiation $g(t_{ir}, t') \approx 0.78$ at 20°C, but at −10°C the annealing effect is much smaller with $g(t_{ir}, t') \approx 0.98$. After 9.1 hours of irradiation and 10 hours without beam $g(t_{ir}, t') \approx 0.70$ at 20°C and $g(t_{ir}, t') \approx 0.96$ at −10°C. This again supports the assumption that leakage current annealing is only a small effect at low temperature.

To compare this parameterisation of leakage current annealing during and after irradiation with data taken during the beam-stop of the April 1999 irradiation the ratio of leakage current a time t' after the end of irradiation to leakage current at $t' = 0$, $I(t')/I(t' = 0)$, can be examined. This is shown in Fig. 4.18b for leakage current

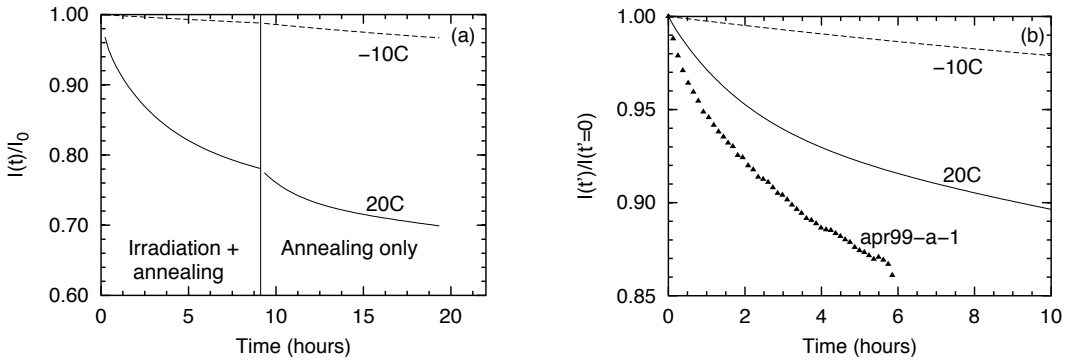

Figure 4.18: (a) Ratio of observed leakage current to leakage current with no annealing during and after irradiation for scenario of April 1999 irradiation, calculated using Eqn. (2.39). (b) Ratio of leakage current a time t' after the end of irradiation to leakage current at $t' = 0$ for data and parameterisation of Eqn (2.39).

data from detector apr99-a-1 and the prediction of Eqn. (2.39) for temperatures of 20°C and −10°C. The data display a much greater decrease of $I(t')/I(t'=0)$ over a 6 hour period than is predicted for irradiation and annealing at −10°C, and a considerably greater decrease even than predicted for a temperature of 20°C. Therefore, again, it appears that the observed leakage current behaviour is not consistent with the parameterisation for leakage current annealing given in Eqn. (2.39).

Whilst neither of the annealing parameterisations considered above appear to describe the observed leakage current behaviour it should be remembered that the temperature dependence was introduced by a scaling of the time axis, not with an independent parameter set calculated from the observed annealing behaviour of devices maintained at low temperatures. Although most of the literature concentrates on long-term annealing at room temperature or higher, in Ref. [51] the leakage current annealing behaviour of silicon diodes at temperatures of +20°C to −20°C after irradiation with 24 GeV protons to fluences of up to 1.1×10^{14} p cm^{-2} was studied. Leakage currents were monitored over periods of several months after the end of irradiation. The decrease in the damage constant α, and hence the leakage current from Eqn. (2.34), as a function of time after irradiation t was found to be described by

$$\alpha(t) = A_1 \exp(-t/\theta_1) + A_2 \exp(-t/\theta_2) + A_3 \,. \tag{4.10}$$

The parameters found in Ref. [51] for this function for a range of temperatures are shown in Table 4.5. As the temperature decreases the length of the time constants increase, implying a slowing down of the rate of annealing. Eqn. (4.10) is found to be a good representation of the leakage current data taken during the April 1999 beam-stop for all detectors, and the parameters found from fitting Eqn. (4.10) to the data are shown in Table 4.6. Comparing the parameters found here with those from Ref. [51], what is noticeable is that the time constants θ_1 and θ_2 found here are much smaller, being of order hours rather than days, and also the relative contribution of the stable component A_3 is much greater.

T (°C)	θ_1 (days)	θ_2 (days)	A_1 10^{-17} A cm^{-1}	A_2 10^{-17} A cm^{-1}	A_3 10^{-17} A cm^{-1}
20	-	5.3 ± 1.1	0.0	1.9 ± 0.2	2.63 ± 0.05
0	0.70 ± 0.14	48 ± 11	0.53 ± 0.06	0.21 ± 0.02	0.44 ± 0.01
-20	3.6 ± 0.5	43 ± 9	0.17 ± 0.01	0.06 ± 0.05	0.070 ± 0.002

Table 4.5: Parameters of leakage current annealing function Eqn. (4.10) for a range of temperatures, taken from Ref. [51].

	θ_1 (hours)	θ_2 (hours)	A_1 (μA)	A_2 (μA)	A_3 (μA)
apr99-a-1	0.35 ± 0.02	4.70 ± 0.12	1.46 ± 0.04	8.78 ± 0.07	47.5 ± 0.1
apr99 av.	0.33 ± 0.01	4.54 ± 0.04	1.16 ± 0.02	8.72 ± 0.03	46.530 ± 0.004

Table 4.6: Parameters of leakage current annealing function Eqn. (4.10) found from fits to the observed leakage currents during the beam-stop of the April 1999 irradiation.

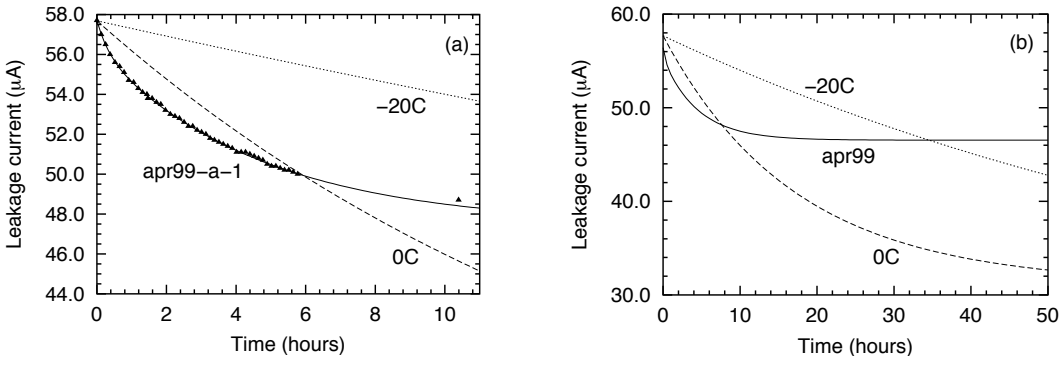

Figure 4.19: (a) Fit of Eqn. (4.10) to leakage current data for detector apr99-a-1 (solid line) and parameterisations from Ref. [51] for $T = 0$°C (dashed line) and $T = -20$°C (dotted line). (b) As the previous plot but for a longer time-scale.

Fig. 4.19a shows leakage current data for detector apr99-a-1 accompanied by the fit to the data of Eqn. (4.10). Also shown are the parameterisations found in Ref. [51] for temperatures of 0°C and −20°C, with the values of the amplitudes A_1, A_2 and A_3 scaled to the observed leakage current for detector apr99-a-1 at $t = 0$. Whilst the shape of the data for detector apr99-a-1 is very different to that of the two parameterisations from Ref. [51], having a much more pronounced decay curve, the leakage currents predicted after 10 hours of annealing by the fit to the data and the two other parameterisations are consistent. The fit to the data (with temperature $T = -10$°C) predicts a higher leakage current (less annealing) than the parameterisation for $T = 0$°C and a lower leakage current (more annealing) than the parameterisation for $T = -20$°C, consistent with the expectation for more annealing at higher temperatures. However, if the parameterisations are extrapolated to longer time-scales, shown in Fig. 4.19b, this consistency is lost as the decrease in leakage current given by the parameterisation from Ref. [51] for annealing at −20°C overtakes that found here for −10°C after ≈ 35 hours. The parameterisation found by fitting to the April 1999 data actually becomes constant ≈ 25 hours after the end of irradiation, whereas the two parameterisations from Ref. [51] still give a decreasing current even after 50 hours. These differences could be due to the different measurement time-scales. For the data collected in April 1999 measurements were taken every few minutes for a duration of 6 hours (monitoring was stopped for the last 4 hours of the beam-stop). However for the results presented in Ref. [51] the measurement period was several months, and only two measurements were taken during the first day. Therefore whilst the April 1999 data are sensitive only to short time constants of order hours, the data from Ref. [51] are sensitive to longer time constants. It is in any case difficult to conclude whether the leakage current behaviour seen in the April 1999 beam-stop is consistent with the results of Ref. [51].

Another possibility that can be considered to explain the observed leakage current behaviour is a radiation induced photocurrent in the detectors. The creation of electron-hole pairs in the depleted bulk of the detector by the passage of charged particles from the ambient radioactivity in the irradiation area could cause an additional

current in the detector. A radiation induced photocurrent should be proportional to the dose rate inside the irradiation area, which will increase when irradiation starts then decrease when the beam is halted. Adding an additional current with this behaviour to a bulk leakage current that is linear with fluence may explain the observed detector currents during irradiation.

The radioactivity induced by high-energy particle radiation as a function of irradiation time T and decay time t can be expressed by [4, 52]

$$D = D_0 \phi \log\left(\frac{T+t}{t}\right) \tag{4.11}$$

where D is the dose rate, D_0 is a constant and ϕ is the flux of irradiating hadrons. The constant D_0 was found in Ref. [52] for a position 1m away from a thick target, such as a beam dump, which is almost exactly the situation of the detectors in the irradiation area:

$$D_0 = 3.6 \times 10^{-13}\ (\mathrm{rad\,hr^{-1}})/(\mathrm{particle\,cm^{-2}s^{-1}})\,.$$

The dose rate in the irradiation area can now be calculated as a function of irradiation time. Assuming a typical beam scenario of two spills per 14 second super-cycle each containing 40×10^{10} protons, and a beam spot size of 2×2 cm^2 then the beam flux is

$$\phi = 7.14 \times 10^9\ \mathrm{protons\,cm^{-2}\,s^{-1}}\,.$$

Note that this beam flux is not the same as the irradiating flux received by the detectors themselves, due to their being scanned through the beam-line. The dose rate as a function of irradiation time T is modelled by Eqn. (4.11) using a constant decay time of $t = 1$ hour, and is shown in Fig. 4.20a. A sharp increase in dose rate is predicted at the start of irradiation, with the rate of increase falling with irradiation time, so that a plateau will eventually be reached. The dose rate can also be modelled as a function of decay time t, shown in Fig. 4.20a for a scenario similar to that of the April 1999 irradiation; 9.1 hours of irradiation followed by 10 hours of decay. As soon as the beam is halted (indicated by the solid vertical line on the graph) there is a sharp decrease in the dose rate, with the rate of decrease

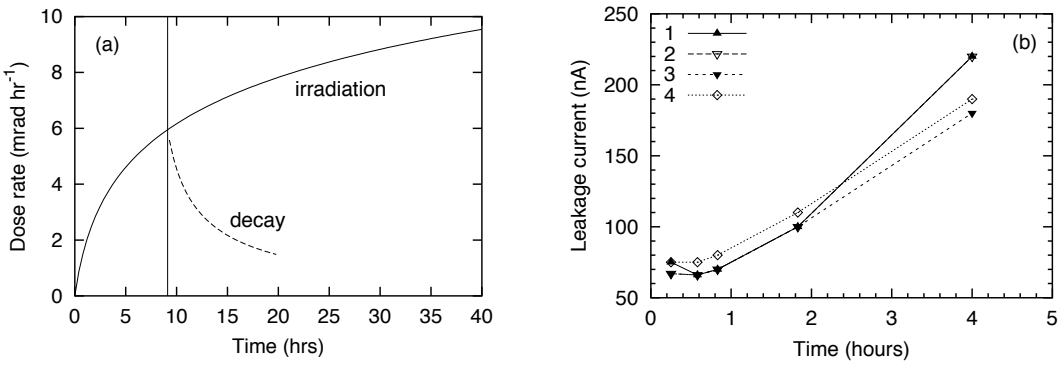

Figure 4.20: (a) Predicted dose rate inside irradiation area as a function of irradiation time. Also shown is dose rate as a function of decay time after 9.1 hours of irradiation time (dashed line). (b) Measured leakage currents before irradiation; beam on but detectors parked out of beam.

falling with time. After 10 hours of decay time the dose rate is approximately a third of the level it was immediately the beam was halted.

Therefore a radiation induced photocurrent proportional to the dose rate would appear to exhibit characteristics consistent with the observed leakage current both before and after irradiation. A non-linear increase in photocurrent with fluence added to a linear bulk leakage current could explain the observed non-linearity of current with fluence, and a decrease in photocurrent could explain the observed decrease in current when the beam is halted. However the expected magnitude of such an effect still needs to be determined. During a detector irradiation in July 2001 detectors were installed into the irradiation area, cooled and the beam started (2 spills each containing 40×10^{10} protons being received every 14 seconds). Instead of irradiation of the detectors commencing immediately they were left parked out of the beam for four hours prior to the start of the irradiation. Detector currents were measured during this period, when no increase in leakage current due to bulk radiation damage should be observed; any increase in current can be attributed to a radiation induced photocurrent. The variation of detector currents with time is shown in Fig. 4.20b [53]. The increase in current with time appears to be described better by a linear function, rather than the logarithmic function of Eqn. (4.11)

that governs the increase in dose rate. In addition the magnitude of the increase in current is small; the measured current after four hours is $\approx$ 200 nA. Taking Fig. 4.20a as representative of the dose rate in the irradiation area, and assuming a radiation induced photocurrent proportional to this, then the photocurrent after four hours of beam should be approximately 2/3 of the photocurrent after 9.1 hours of beam, the point in the April 1999 irradiation when the beam was halted. Scaling the observed current seen in July 2001 after 4 hours of beam time to 9.1 hours of irradiation a photocurrent of $\approx$ 300 nA would be expected. Then, during a 10 hour period without beam the dose rate in Fig. 4.20a falls to one third of the dose rate immediately after the beam is halted; the July 2001 data would imply a fall in photocurrent of $\approx$ 200 nA during this time. However, in the April 1999 irradiation a decrease in current of $\approx$ 9 μA is observed, a far greater effect. This indicates that the magnitude of the observed decrease in leakage current is much too large to be consistent with a decrease in radiation induced photocurrent after the beam is halted. Additionally, given the reasonably linear nature of the observed increase in current shown in Fig. 4.20b it is possible that this increase is not due to a photocurrent, but is in fact caused by bulk radiation damage from, for instance, a background of neutrons emitted from the beam-dump.

The final possibility considered to explain the observed leakage current behaviour in the low-fluence region is that of surface damage. Additional current can be produced by generation centres at the silicon-oxide interface. Surface generation only occurs where there is a silicon-oxide interface, not where there is a junction between different types of silicon. For simple diodes, where almost the entire surface area consists of a p-n junction, surface effects are not important compared to bulk effects. However for the highly segmented silicon microstrip detectors considered here where a considerable proportion of the detector surface takes the form of a silicon-oxide interface surface effects may be significant. Compared with the study of bulk damage much less information is available on surface damage effects. However, experiments have been performed by irradiating silicon devices with 20 keV electrons [32, 54]; these do not have enough energy to cause bulk damage, so only surface damage can

occur. In Ref. [32] a surface generation current of $1.5 - 2.0\ \mu\mathrm{A\,cm^{-2}}$ was observed in biased silicon diodes at room temperature after a dose of 5 kGray, equivalent to a proton irradiation fluence of $\approx 1.5 \times 10^{13}\ \mathrm{cm^{-2}}$. The surface generation current is dependent on the intrinsic carrier density [54] and therefore should be reduced at low temperatures; a smaller surface generation current should be present during the irradiations considered here. However, it could still be of sufficient magnitude as to be significant compared to the bulk leakage current. Assuming a surface generation current that increases non-linearly with fluence, then this added to a bulk leakage current linear with fluence could explain the non-linearity of the observed leakage current during irradiation. A decrease in surface generation current when irradiation ends due to an annealing process of the surface damage could also explain the observed decrease in leakage current during beam stops. However since surface damage is highly dependent on the exact design and manufacturing process of the detector it is impossible to quantitatively predict the surface generation current without a systematic study, unfortunately beyond the scope of this thesis.

Having investigated the three most probable causes of the observed leakage current behaviour during low-fluence irradiation it appears that the only one that can definitely be ruled out is a radiation-induced photocurrent, as the magnitude of this was found to be far too small to explain the observed decrease in leakage current during beam stops. Investigation of leakage current annealing proved inconclusive. Neither of the parameterisations that rely upon scaling of the time axis to introduce temperature dependence were found to be representative of the data, both predicting much smaller decreases in current than observed. Previous data taken for low temperature annealing appeared to give consistent results with those found here over short time-scales, but when extrapolated to cover larger times the agreement was lost. Further investigation of leakage current annealing for short time-scales at low temperature is therefore required in order to decide whether this effect is responsible for the observed leakage current behaviour. Finally, surface damage effects were considered. Whilst previous studies have found a surface generation current of a non-negligible magnitude compared to bulk damage effects surface damage is entirely material and

manufacturing process dependent and so is impossible to quantify for the detectors irradiated here without additional systematic study. However, even though a firm conclusion about the origin of the observed leakage current behaviour cannot be made, it should be remembered that only a small deviation from the prediction of the bulk damage model is seen, and to a good approximation the increase in leakage current with fluence is described by a linear function.

4.4.2 High fluence behaviour

In the high fluence region a relationship between current and fluence of the form $I \propto \phi^{a_{high}}$ with $a_{high} = 0.50$ is expected, since in this region both leakage current and effective carrier density damage effects must be considered (see Section 4.1). Analogous to the investigation of low-fluence leakage current behaviour in the previous section the observed leakage current behaviour at high-fluences is studied by performing a least squares fit on a function

$$\log I = a_{high} \log \phi + b \tag{4.12}$$

which is equivalent to

$$I = 10^b \phi^{a_{high}} . \tag{4.13}$$

The values of a_{high} found will indicate whether the bulk damage model is sufficient to explain high-fluence leakage current behaviour during irradiation, or if other effects appear to be present.

A fluence range of $\phi = 1.0 - 2.5 \times 10^{14}$ p cm^{-2} is used to perform high-fluence analysis for all detectors, so as to ensure that analysis is performed only in the region where the donor removal term of Eqn. (2.28) is negligible and the effective doping concentration is dominated by acceptor creation. Uncertainties on the values of a_{high} are estimated from the spread of the data points. It should be noted that for clarity only a small subset of the data used to calculate a_{high} is shown in the following graphs; typically $2000 - 3000$ individual leakage current measurements are taken for each detector during the high-fluence region.

April 1999 Data

High fluence analysis is carried out on all detectors in the April 1999 irradiation, except for detector apr99-d-3 which was excluded during the low-fluence analysis. Data and the results of the fits are shown for detectors apr99-a-1 and apr99-b-1 in Fig. 4.21. For detector apr99-a-1 a considerable spread of the data-points is observed, and whilst the fit is a reasonable approximation of the data there is a scatter of points to $\approx 5\mu$A either side of it. This is not the case for detector apr99-c-1, where the fit is a much better representation of the data. It is also worth noting that whilst there were several beam-stops in the high-fluence region there is no evidence of any net decreases of leakage current from the current-fluence plot.

The values of a_{high} found for all detectors analysed are shown in Fig. 4.22. There is a considerable variation in values, with $a_{high} = 0.38-0.58$. What is also noticeable is a consistency for detectors within individual groups, but differences between detectors in different groups. The detectors in groups apr99-a and apr99-d are all found to have values of a_{high} in the range $a_{high} = 0.38-0.43$, whereas all detectors in group apr99-b have $a_{high} = 0.49 - 0.50$ and detectors in group apr99-c all have $a_{high} = 0.53 - 0.58$.

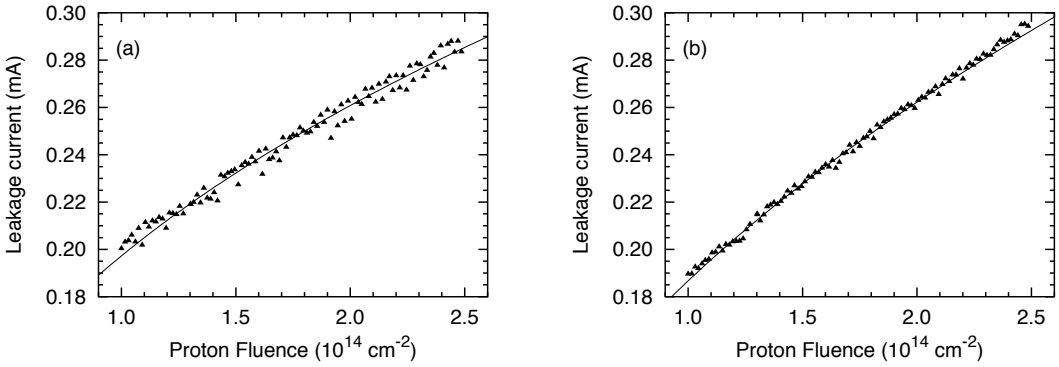

Figure 4.21: High fluence leakage current data and fits for detectors (a) apr99-a-1 and (b) apr99-b-1.

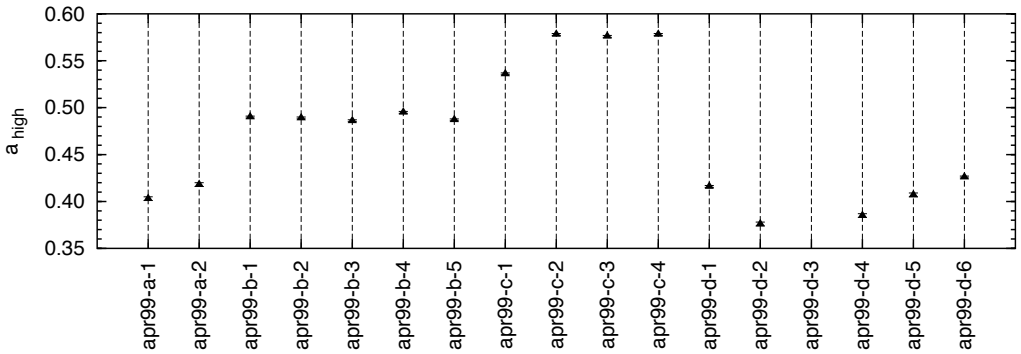

Figure 4.22: Values of a_{high} for all detectors in the April 1999 irradiation.

June 1999 Data

High fluence analysis is performed on all detectors in the June 1999 irradiation apart from the four excluded during the low-fluence analysis, detectors jun99-a-3, jun99-a-5, jun99-a-7 and jun99-b-1. Data and the results of the fits are shown for detectors jun99-a-1 and jun99-c-1 in Fig. 4.23. For both of these detectors the fits are a good representation of the data, although the spread of the data appears to increase as higher fluences are reached. Again there is no indication of net decreases in leakage current during beam-stops from the current-fluence plots.

The values of a_{high} found for all detectors analysed are shown in Fig. 4.24. Again, a considerable variation in values is seen with $a_{high} = 0.43 - 0.52$, although more than half of the detectors have $a_{high} = 0.50 - 0.52$. The consistency within detector groups is again evident; all detectors in groups jun99-c and jun99-d have $a_{high} = 0.50 - 0.52$, whereas all detectors in groups jun99-a and jun99-e take lower values, $a_{high} = 0.43 - 0.45$.

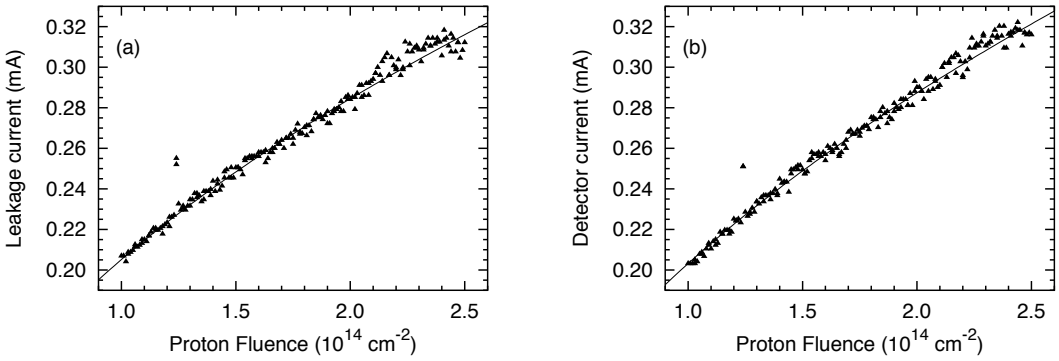

Figure 4.23: High fluence leakage current data and fits for detectors (a) jun99-a-1 and (b) jun99-c-1.

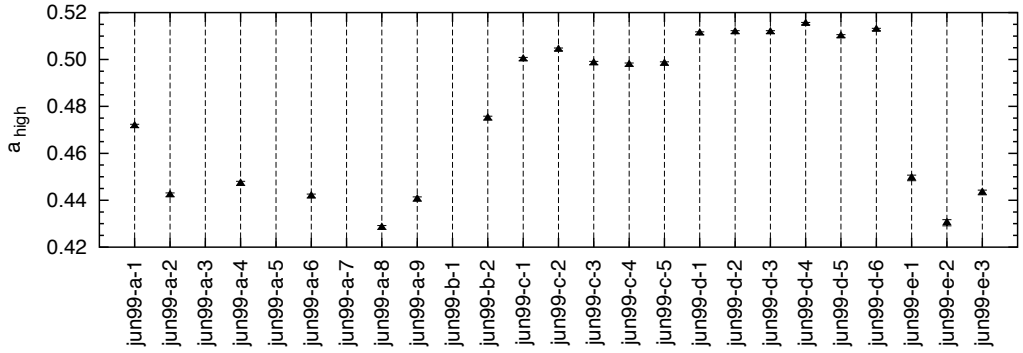

Figure 4.24: Values of a_{high} for all detectors in the June 1999 irradiation.

October 1999 Data

High fluence analysis is performed on all detectors in the October 1999 irradiation except for detector oct99-a-2 which was excluded during the low-fluence analysis. Data and the results of the fits are shown in Fig. 4.25 for detectors oct99-a-1 and oct99-b-1. Considering detector oct99-a-1 first, there is a significant deviation of the data from the fit until a fluence of approximately 1.5×10^{14} p cm^{-2}, after which the fit is a good representation of the data. This is also seen for detector oct99-b-1. Once more there is no indication of net decreases in leakage current during beam-stops from the current-fluence plots.

The values of a_{high} found for all detectors analysed are shown in Fig. 4.26. A considerable variation is found, with $a_{high} = 0.42-0.58$ across all detectors, although again more than half of the detectors analysed have $a_{high} = 0.48 - 0.51$. Within each detector group the values of a_{high} found for individual detectors are fairly consistent; detectors in groups oct99-a and oct99-e all have $a_{high} = 0.56 - 0.59$, whereas all detectors in groups oct99-b, oct99-c (apart from detector oct99-c-3), oct99-d and oct99, have $a_{high} = 0.48 - 0.51$. Comparing the oxygenated detectors (groups oct99-a, oct99-c and oct99-e) with the control detectors (groups oct99-b, oct99-d and oct99-f respectively) the detectors in oxygenated groups oct99-a and oct99-e all have considerably higher values of a_{high} than the detectors in their respective control groups. However this is not observed for detectors in oxygenated group oct99-c which take similar values of a_{high} to their control detectors in group oct99-d, and indeed those of detectors in the other control groups.

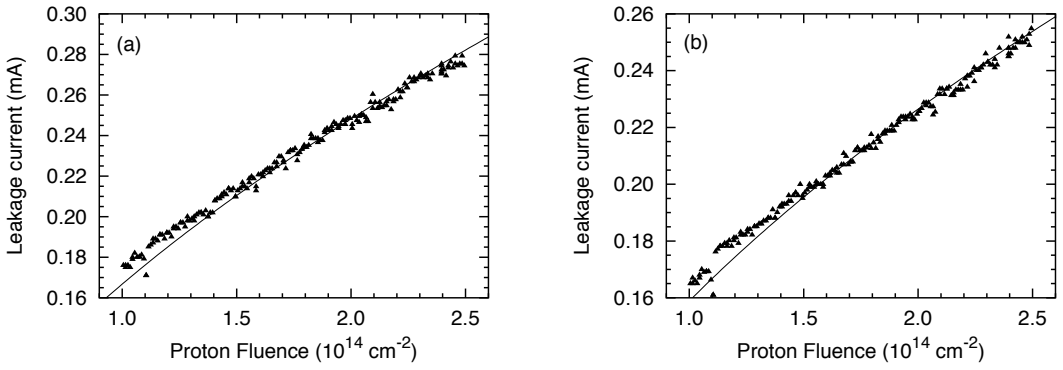

Figure 4.25: High fluence leakage current data and fits for detectors (a) oct99-a-1 and (b) oct-99-b-1.

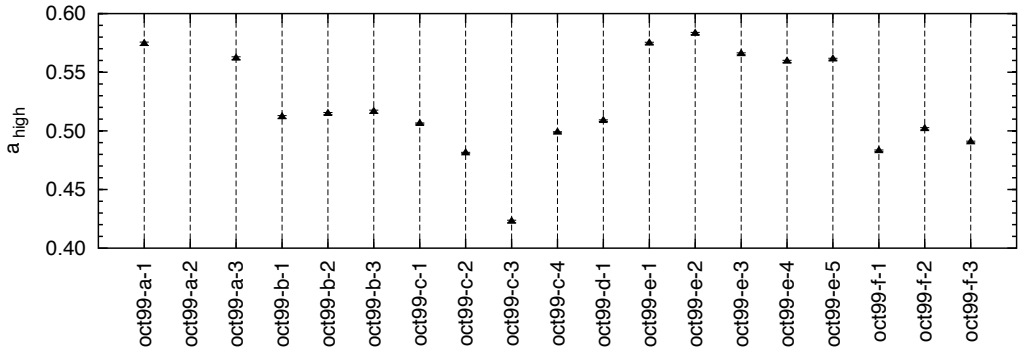

Figure 4.26: Values of a_{high} for all detectors in the October 1999 irradiation.

May 2000 Data

High fluence analysis is performed on all detectors in the May 2000 irradiation apart from detector may00-h-3 which was excluded during the low-fluence analysis. Data and the results of the fits are shown in Fig. 4.27 for detectors may00-a-1 and may00-b-1. For both detectors the fit is a good representation of the data. Again there is no indication of net decreases in leakage current during beam-stops from the current-fluence plots.

The values of a_{high} found for all detector analysed are shown in Fig. 4.28. The majority of detectors have $a_{high} = 0.47 - 0.54$, apart from a cluster of detectors from groups may00-a, may00-b, may00-c and may00-d with $a_{high} = 0.56 - 0.59$. Looking at the different detector groups, whilst the individual detectors in groups may00-c, may00-d, may00-e and may00-f all display consistent values of a_{high}, this is not true for groups may00-a, may00-b, may00-g and may00-h whose individual detectors take a range of values. Comparing detectors manufactured on $\langle 100 \rangle$ orientation substrates (groups may00-b, may00-d and may00-f) with their control groups manufactured on $\langle 111 \rangle$ orientation substrates (groups may00-a, may00-c and may00-e respectively), the $\langle 100 \rangle$ detectors from groups may00-d and may00-f all take slightly higher values of a_{high} than their control detectors. However, this is not the case for $\langle 100 \rangle$ detectors from group may00-b compared with $\langle 111 \rangle$ detectors in group may00-

a, where considerable variation in a_{high} values is seen between individual detectors in both groups.

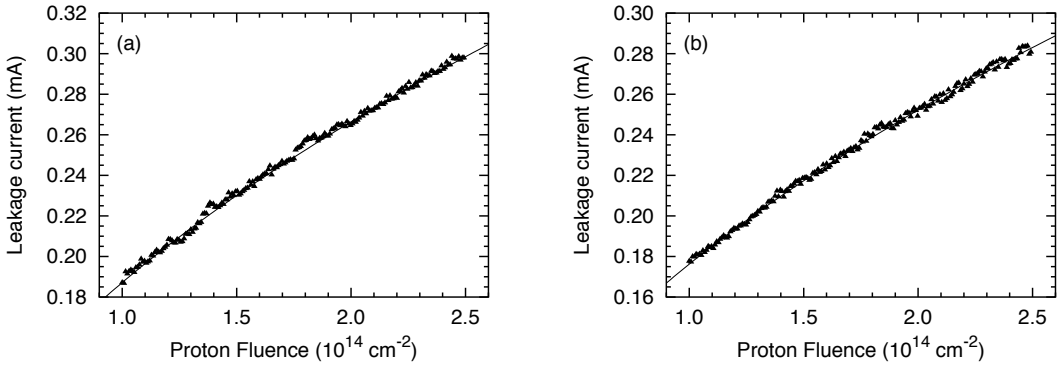

Figure 4.27: High fluence leakage current data and fits for detectors (a) may00-a-1 and (b) may00-b-1.

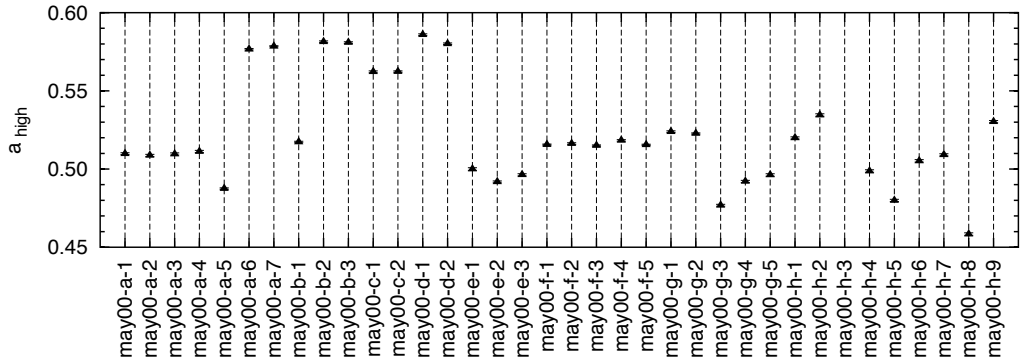

Figure 4.28: Values of a_{high} for all detectors in the May 2000 irradiation.

Discussion

The distribution of a_{high} values found for detectors in all irradiations is shown in Fig. 4.29. Whilst there are a number of detectors that take values of a_{high} both higher and lower than the expected $a_{high} = 0.50$ from bulk radiation damage the majority do agree favourably with this, with the peak of the distribution falling at around $a_{high} = 0.51$. There is also, though, a smaller subsidiary peak at $a_{high} \approx 0.57$, the origin of which is not understood; either a statistical fluctuation or a systematic effect

of the different detector groups could be responsible. Even taking this into account there does not appear to be any overall systematic deviation from the expected behaviour, with the numbers of detectors with lower and higher values of a_{high} being approximately equal. Data for detectors in the April 1999, June 1999 and May 2000 irradiations were well represented by the high-fluence fits, but for the October 1999 irradiation some deviation of the fits from the data was seen at the low fluence end of the fit region.

The lack of a systematic deviation from the expected leakage current behaviour indicates that the bulk damage model developed in Section 4.1 is a good representation of detector leakage currents at high-fluences. There is no evidence for any visible annealing effect during irradiation, of either the leakage current or the effective doping concentration. It also implies that the assumptions made when developing the bulk damage model in Section 4.1, particularly the equivalence of an under-depleted detector with depleted width W to a fully depleted detector of thickness W, are

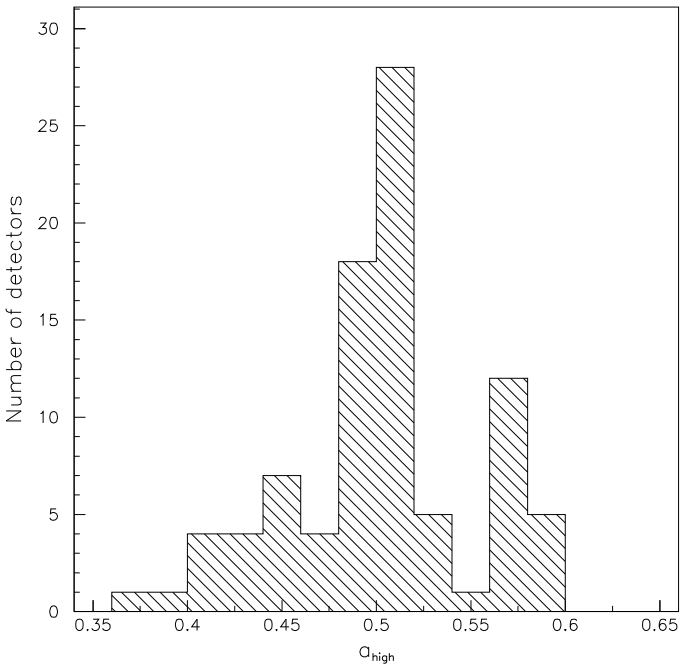

Figure 4.29: Distribution of a_{high} values for detectors in all irradiations.

justified. Recently it has been found that when irradiated past the inversion point silicon detectors exhibit a double-junction effect [55–58]. In a p^+-n junction with a backplane of n^+ material the junction is initially (pre-irradiation) between the p^+ and n silicon, and the depletion region grows from the p^+ side towards the backplane as the reverse bias voltage is increased. After type-inversion the junction switches to the n^+-p transition at the backplane (the bulk now having inverted to p-type silicon) and the depletion region grows from the backplane. However, measurements have found an additional depleted region at the p^+ side of the detector, so the simple model of the detector after type-inversion being described by a n^+-p structure is not sufficient. It is expected, though, that the leakage current from this additional depleted region will not be significant compared with that from the main depleted region [59], and the fact that no systematic deviation from the expected leakage current behaviour is observed would appear to support this.

One noticeable feature of the calculated values of α_{high} is the tendency for consistency between values found for detectors within the same group, but differences between detectors in different groups. This behaviour is shown particularly clearly for the detectors in the April 1999 irradiation (see Fig. 4.22), and would imply the presence of a group specific effect. Detector groups generally contain detectors produced by the same manufacturer; different detector groups may therefore be from different manufacturers. Each manufacturer has its own processing techniques and sources of materials; this could be responsible for the observed differences between different detector groups. It is, unfortunately, not possible to investigate this further.

A final feature worth pointing out is the behaviour of detector leakage currents during beam stops in the high-fluence region. When the beam is halted the leakage current decreases, rapidly at first with the rate of decrease slowing with time, similar to that seen in beam-stops in the low-fluence region. However, immediately irradiation restarts a rapid increase in leakage current is observed, taking it back to the value seen before the beam-stop. Thereafter, the leakage current increases in a similar manner to before the beam-stop. This is shown in Fig. 4.30 for detectors in

both the April 1999 and October 1999 irradiations, and explains why no net decrease in leakage current is observed on a current-fluence graph in the high-fluence region. This behaviour is not consistent with an annealing effect, and a radiation induced photocurrent has already been shown to be of far too small a magnitude to describe current decreases during beam stops. The origin of this behaviour is therefore not clear.

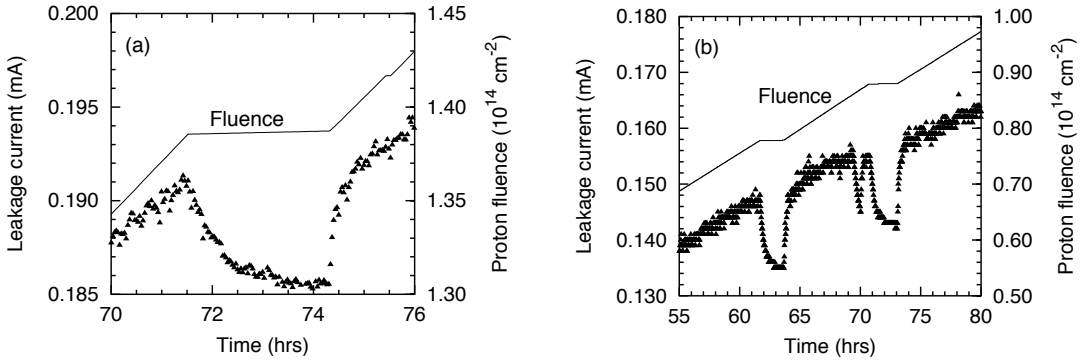

Figure 4.30: Leakage currents during beam stops in the high-fluence region for detectors (a) apr99-c-3 and (b) oct99-a-1.

4.5 Calculating the radiation damage parameters

Now that the bulk radiation damage model of detectors held under bias during irradiation has been shown to adequately describe observed leakage currents during irradiation it can be used to calculate the parameters governing the radiation damage, namely the current-related damage constant α and the rate of acceptor creation β.

To calculate the current-related damage constant α the low-fluence region is used. Here, from Eqn. (4.1), a linear relationship between current and fluence is expected. Fitting a function $I = m_\alpha \phi$ to the low fluence current data then α is given by

$$\alpha = \frac{m_\alpha}{Ad} \tag{4.14}$$

where A is the active area of the detector and d is the detector thickness.

The uncertainty on the value of α is calculated by combining individual uncertainties on the values of A, d and m_α. The uncertainty on the active area of the detector A has been included to take into account small variations in detector dimensions and also the possibility of the active area of the detector not being precisely defined by the guard rings. A value of $\Delta A = \pm 1$ cm^2 is used for all detectors. In some cases wedge detectors have been irradiated where the exact species of wedge is unknown. For these a generic wedge has been defined, with an active area equal to the mean of all five wedge designs (see Table 3.1); the uncertainty on this area is taken as $\Delta A = \pm 1.5$ cm^2. Detector thicknesses are dependent upon the manufacturing process, and are generally quoted by the manufacturers with an uncertainty of $\Delta d = \pm 15 \mu$m. The uncertainty on the gradient m_α is calculated from the spread of the data points.

Additionally, a systematic uncertainty on the value of α is considered due to the possibility of the fluence value for each current measurement being incorrect. The fluence for each leakage current measurement is calculated from the fluence calibration of the SEM with aluminium foils (see Section 3.3.1), and the fluence given for the aluminium foils comes with a quoted uncertainty. The fluence calibration being incorrect would have the effect that the actual fluence ϕ^{real} for each leakage current

measurement in an irradiation is shifted by a factor f relative to the calculated fluence ϕ^{meas},

$$\phi^{real} = f\phi^{meas}$$

thus altering the gradient m_α of the current-fluence plot. The actual gradient m_α^{real} would then be

$$m_\alpha^{real} = \frac{\Delta I}{f\Delta\phi} = \frac{m_\alpha^{meas}}{f} \tag{4.15}$$

and the actual current-related damage constant α^{real}

$$\alpha^{real} = \frac{\alpha^{meas}}{f}\,. \tag{4.16}$$

The uncertainty on the current-related damage constant due to this is calculated by assuming that the fluence calibration is correct, $f = 1$, and assigning it an uncertainty equal to that found from the analysis of the aluminium foils. The fluence values for individual foils are typically quoted with an uncertainty of 8 - 10%, but for each irradiation several foils are analysed and the fluence taken as the mean of these; the uncertainty on the foil calibration is taken as 5%. Therefore the fluence calibration factor is taken as $f = 1.00 \pm 0.05$ for all irradiations, and is used to calculate the systematic uncertainty on α. When comparing values of α for detectors in the same irradiation this systematic uncertainty need not be considered since it will affect all detectors equally. For comparisons between detectors in different irradiations, though, it must be taken into account.

To calculate the rate of acceptor creation β the high-fluence region is used, where the observed leakage current is dependent on both the change in leakage current and the change in effective doping concentration. From Eqn. (4.5) a relationship between current and fluence of $I \propto \sqrt{\phi}$ is expected. Fitting a function $I = m_\beta\sqrt{\phi}$ to the high-fluence data then β is given by

$$\beta = \left(\frac{\alpha A}{m_\beta}\right)^2 \frac{2\epsilon_0\epsilon_r}{e} V_{bias} = \left(\frac{m_\alpha}{m_\beta d}\right)^2 \frac{2\epsilon_0\epsilon_r}{e} V_{bias} \tag{4.17}$$

where $\epsilon_0\epsilon_r$ is the dielectric constant of silicon, e is the electron charge and V_{bias} is the bias voltage applied to the detector.

The uncertainty on β is calculated by combining individual uncertainties on the gradients m_α and m_β (both calculated from the spread of data-points), detector thickness d and bias voltage V_{bias}. The uncertainty on the bias voltage is included to take into account calibration errors on individual channels of the HV supplies, and a value of $\Delta V_{bias} = \pm 1$V is used. Again, a systematic error due to the possibility of the fluence calibration being incorrect is also considered. It is applied in a similar way to that described above for the current-related damage constant, and

$$\beta^{real} = \left(\frac{(m_\alpha / f)}{(m_\beta / \sqrt{f}) d} \right)^2 \frac{2\epsilon_0 \epsilon_r}{e} V_{bias} = \frac{\beta^{meas}}{f} . \tag{4.18}$$

The values for α and β and associated errors are calculated as explained above for all detectors apart from those that were excluded in Section 4.4.1 due to leakage current irregularities in the low-fluence region. The results are shown in Figs. 4.31, 4.32, 4.33 and 4.34 for detectors in the April 1999, June 1999, October 1999 and May 2000 irradiations respectively. The error bars in these plots reflect only the random errors; the systematic uncertainty due to the fluence calibration is not shown.

Considering the detectors in the April 1999 irradiation first the mean of all detectors for the current-related damage constant is $\overline{\alpha} = (3.06 \pm 0.07) \times 10^{-18}$ A cm^{-1}. All detectors from groups apr99-a, apr99-b and apr99-d (apart from detector apr99-d-1) are consistent with the mean within the given uncertainties. What is also noticeable is the tendency for detectors in the same group to have similar values of α, whereas there appear to be systematic differences between the different detector groups. The mean value for the rate of acceptor creation is $\overline{\beta} = (0.0572 \pm 0.0015)$ cm^{-1}. All detectors apart from apr99-a-1, apr99-a-2 and apr99-d-1 are consistent with the mean within the given uncertainties. The tendency for detectors in the same group to take similar values of β is again evident, although not so pronounced as for the values of α.

Looking at detectors in the June 1999 irradiation next, the mean of all detectors for the current-related damage constant is $\overline{\alpha} = (3.61 \pm 0.02) \times 10^{-18}$ A cm^{-1}. All detectors are consistent with this mean within the given uncertainties apart from jun99-b-2, jun99-e-2 and jun99-e-3. The mean value for the rate of acceptor creation

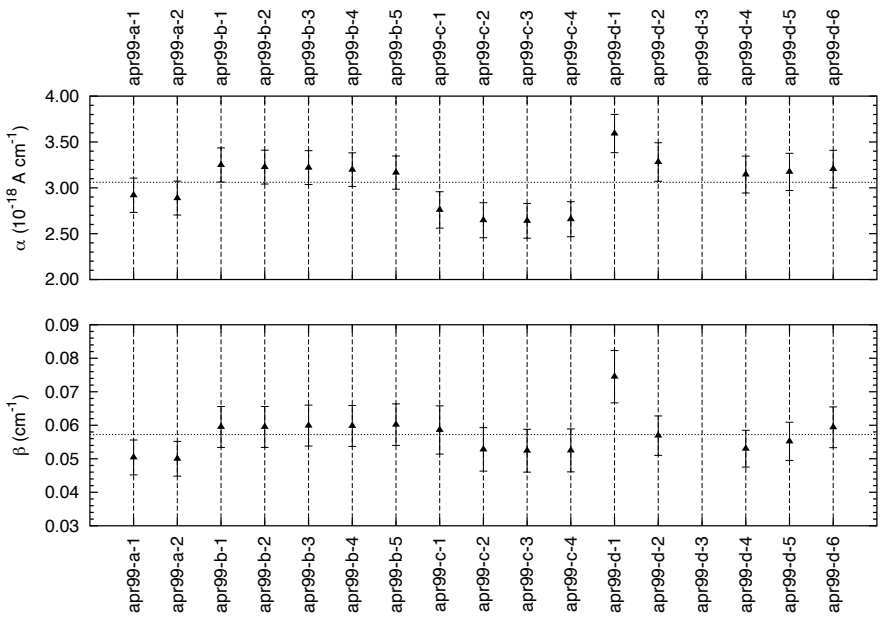

Figure 4.31: Calculated α and β values for detectors in April 1999 irradiation. The mean α and β are also shown (dotted line).

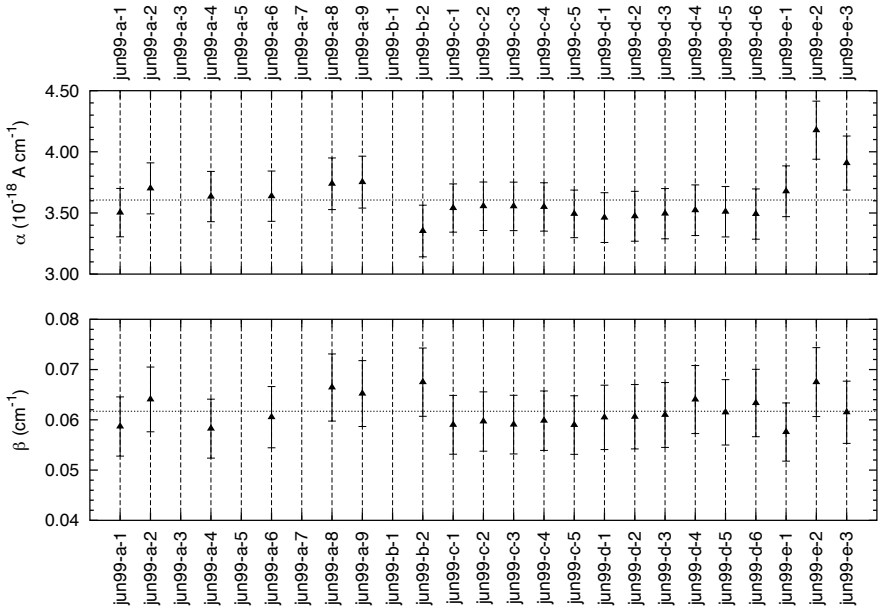

Figure 4.32: Calculated α and β values for detectors in June 1999 irradiation. The mean α and β are also shown (dotted line).

is $\overline{\beta} = 0.0617 \pm 0.0006$ cm^{-1}. All detectors are consistent with this within errors. No systematic deviations between detectors in different groups for either α or β are apparent.

The mean current-related damage constant for all detectors in the October 1999 irradiation is $\overline{\alpha} = (3.43 \pm 0.05) \times 10^{-18}$ A cm^{-1}. The majority of the detectors are consistent with the mean within uncertainties. Both oxygenated (groups oct99-a, oct99-c and oct99-e) and unoxygenated control (groups oct99-b, oct99-d, oct99-f respectively) detectors are present in this irradiation. No systematic difference between the oxygenated detectors of groups oct99-a and oct99-c is seen when compared with their control detectors in groups oct99-b and oct99-d. The mean value for the rate of acceptor creation is $\overline{\beta} = 0.0786 \pm 0.0016$ cm^{-1}. Again, the majority of detectors have values of β consistent with the mean, and no systematic difference between oxygenated and control detectors is evident.

Finally, in the May 2000 irradiation the mean value for the current-related damage constant is $\overline{\alpha} = (3.33 \pm 0.03) \times 10^{-18}$ A cm^{-1}, and the majority of the detectors are consistent with this within the given uncertainties. Comparing detector within their groups, whilst the detectors in groups may00-c, may00-d, may00-e, may00-f and may00-g generally have consistent values of α, this is not true for groups may00-a, may00-b and may00-g where a range of α values are observed. In this irradiation similar detectors manufactured on both $\langle 100 \rangle$ (groups may00-b, may00-d and may00-f) and $\langle 111 \rangle$ (may00-a, may00-c and may00-e respectively) orientation substrates were present. No systematic difference in values of the current-related damage constant between detectors manufactured on $\langle 100 \rangle$ and $\langle 111 \rangle$ orientation substrates is apparent. The mean value for the rate of acceptor creation is $\overline{\beta} = 0.0655 \pm 0.0006$ cm^{-1}, and again the majority of detectors are consistent with this. Within detector groups the values for β are generally similar, apart from group may00-h where a large range of values is observed. No systematic difference in values of β between $\langle 100 \rangle$ and $\langle 111 \rangle$ orientation substrates is seen.

Overall the values found for the current-related damage constant α and the rate of

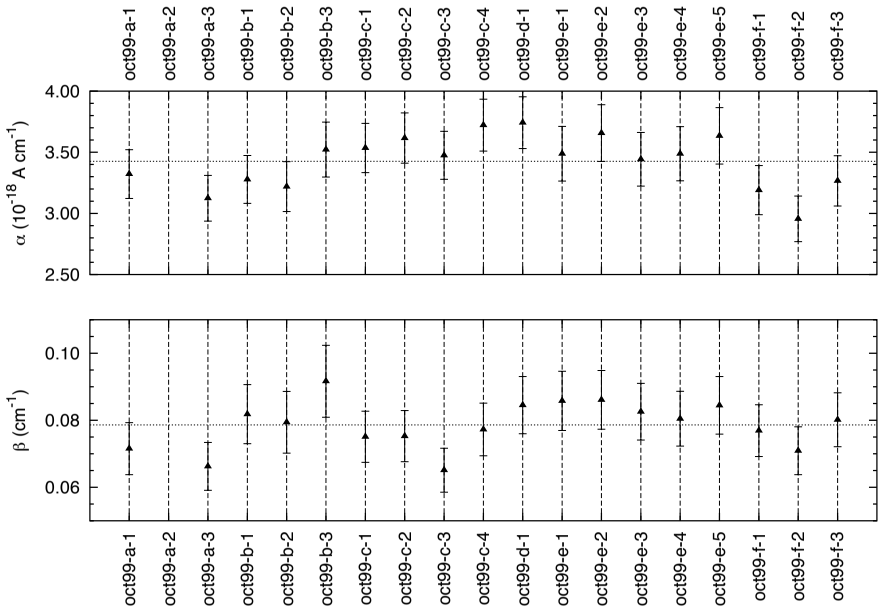

Figure 4.33: Calculated α and β values for detectors in October 1999 irradiation. The mean α and β are also shown (dotted line).

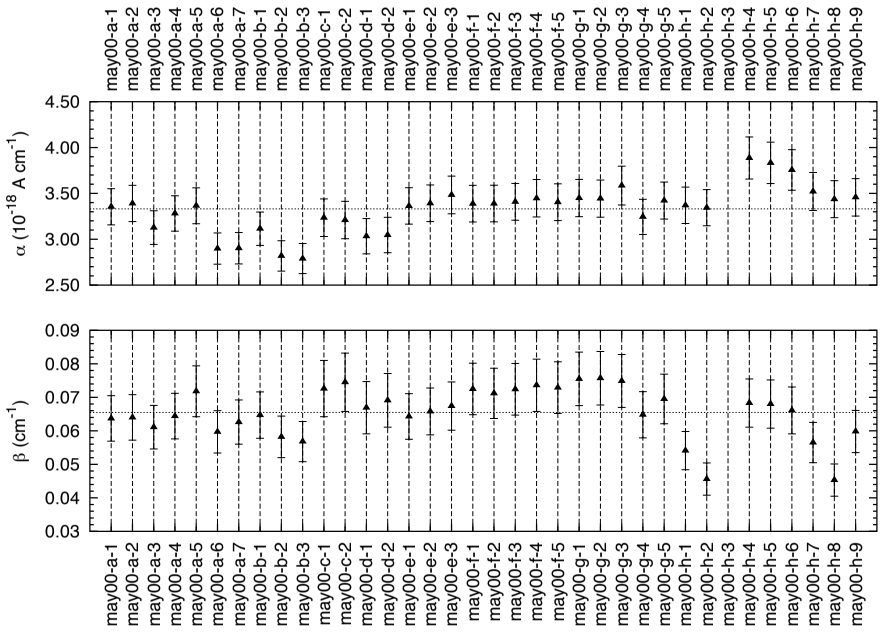

Figure 4.34: Calculated α and β values for detectors in May 2000 irradiation. The mean α and β are also shown (dotted line).

acceptor creation β for detectors in the same irradiation show good agreement with each other and only a small number of detectors have a significant deviation from the mean. For values of α no systematic difference between standard, oxygenated and $\langle 100 \rangle$ detectors is observed. This is in agreement with previous studies, which have found the current-related damage constant to be independent of the detector material [26, 60]. Also, no systematic difference in values of β is seen for the different detector materials. This is certainly as expected when comparing between standard $\langle 111 \rangle$ detectors and $\langle 100 \rangle$ detectors, since only the surface properties of the silicon-oxide interface should show differences; the bulk radiation damage of these two types of detector should be similar. As was mentioned in Section 4.3.3 oxygenated detectors have previously been found to have lower values for the rate of stable acceptor concentration g_c and the amount of reverse annealing. Reverse annealing can be ignored for the temperatures and time-scales during the irradiations performed here, but a difference in the rate of creation of stable acceptors between oxygenated and standard silicon might have been expected to give different values of β. However, it should be remembered that the rate of acceptor creation β as calculated here contains both stable and unstable acceptor creation since little annealing of the unstable fraction is expected during irradiation, and

$$\beta = g_a + g_c \tag{4.19}$$

where g_a is the rate of unstable acceptor creation. The rate of stable acceptor creation for proton irradiation of standard (unoxygenated) detectors has been found as $g_c = 0.0115 \pm 0.0009$ cm^{-1} [28]. This value of g_c is much smaller than the values of β found here, implying that the rate of acceptor creation is dominated by the unstable component. Any change in the rate of stable acceptor creation for oxygenated material is likely to be masked in the calculated value of β by the much larger unstable acceptor creation, which has not as yet been found to be dependent on oxygenation.

To compare results between different irradiation periods the irradiation temperatures must be taken into account. The current-related damage constant exhibits

temperature dependence through its direct relationship with the leakage current. For the purposes of comparison it is standard practise to normalise values of α to a reference temperature of 20°C using an analogous method to Eqn. (4.6),

$$\frac{\alpha(T_1)}{\alpha(T_2)} = \left(\frac{T_1}{T_2}\right)^2 exp\left[\frac{E_g}{2k_B}\left(\frac{1}{T_2} - \frac{1}{T_1}\right)\right] . \tag{4.20}$$

The rate of acceptor creation also exhibits temperature dependence, but only indirectly through the amount of annealing that occurs during irradiation. At higher temperatures a larger amount of the unstable acceptor creation will anneal out during irradiation, leading to a smaller value of β. All detectors considered here were irradiated at temperatures between -10°C and -8°C; it is expected that at these temperatures and over the irradiation time-scales considered here annealing will only be a small effect, and the difference in annealing between the different irradiation temperatures will be negligible. No temperature normalisation of β values is applied.

The weighted averages of α and β are calculated for detectors in each irradiation period, and the systematic and random uncertainties combined in quadrature to give an overall uncertainty for each point. The average values of α are then normalised to a reference temperature of 20°C using Eqn. (4.20). The weighted averages of $\alpha(20°C)$ and β for detectors in each irradiation period are shown in Figs. 4.35a and 4.35b respectively. The mean values of $\alpha(20°C)$ and β for all four irradiation periods are also shown in these graphs, being $\overline{\alpha}(20°C) = 4.87 \times 10^{-17}$ A cm^{-1} and $\overline{\beta} = 0.0645$ cm^{-1}.

Considering the values for the current-related damage constant first, the $\alpha(20°C)$ values for all four irradiation periods are consistent with the mean within the quoted uncertainties, and all values fall within the range $\alpha(20°C) = 4.6 - 5.1 \times 10^{-17}$ A cm^{-1}. Previous studies have found values of $\alpha(20°C)$ for irradiation of silicon diodes at the CERN PS of

$$\alpha(20°C) = (5.0 \pm 0.4) \times 10^{-17} \text{ A cm}^{-1} \quad [31]$$
$$\alpha(20°C) = (5.4 \pm 0.5) \times 10^{-17} \text{ A cm}^{-1} \quad [61].$$

These values were both calculated from diodes irradiated at room temperature and

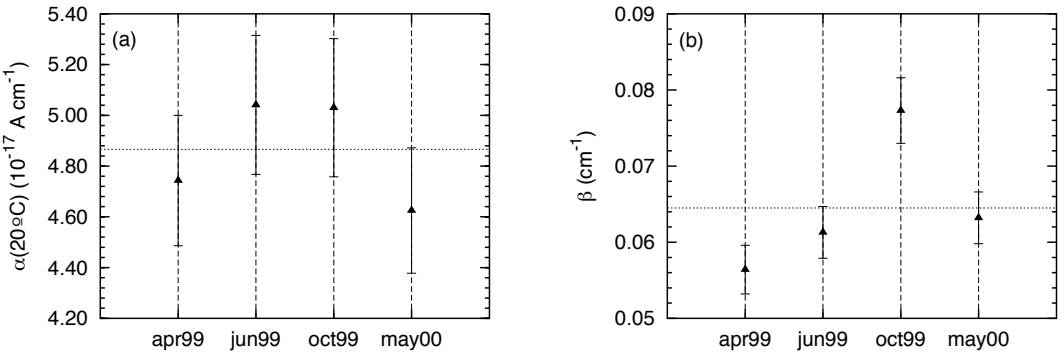

Figure 4.35: Weighted averages of (a) $\alpha(20°\mathrm{C})$ and (b) β values for detectors in each irradiation period. The mean values of $\alpha(20°\mathrm{C})$ and β are also shown.

corrected for annealing that occurred during irradiation. The values of α found here for irradiation at low temperatures compare favourably with these. This is further evidence for the assumption that at the irradiation temperatures used here the amount of leakage current annealing is small.

The weighted average of the current-related damage constant for detectors in all four irradiation periods is

$$\overline{\alpha}(20°\mathrm{C}) = (4.84 \pm 0.13) \times 10^{-17}\ \mathrm{A\,cm^{-1}}\,. \tag{4.21}$$

The average values for each irradiation of the rate of acceptor concentration β show considerably more variation than those for the current-related damage constant. Only the values from the June 1999 and May 2000 irradiations are consistent with the mean within the given uncertainties and whilst the value for the April 1999 irradiation is only slightly lower than these, and agrees within uncertainties, that for the October 1999 irradiation is significantly higher. The reason for this is unclear. The discrepancy being due to a problem with the fluence calibration is unlikely since this should also show in the value of $\alpha(20°\mathrm{C})$ found for the October 1999 irradiation, which is in agreement with the other irradiations. It does not appear to be due to a temperature dependence of the rate of acceptor creation either. If the irradiation temperature did cause a systematic difference in values of β between the different irradiation periods due to annealing then it would be expected that

β for the April 1999 irradiation would be the largest, since this had the lowest temperature and shortest duration, hence the least amount of annealing. The June 1999 irradiation should have the smallest value of β since it was carried out at the highest temperature and over the longest time-scale, so a greater amount of the unstable acceptor concentration would be expected to anneal away. This ordering of β values between different irradiations is not observed. It should be remembered, though, that the data for detectors in the October 1999 irradiation appeared to be less well represented by the high-fluence fits performed in Section 4.4.2 than detectors in the other three irradiations.

Few comparisons of the β values can be made with those from previous experiments, since the vast majority feature irradiations performed at room temperatures where annealing of the unstable component of acceptor creation cannot be ignored. The standard way to compare results between these experiments is to anneal the devices for 4 minutes at 80°C, thus taking them to the bottom of the annealing curve where only the stable acceptor creation is seen. As mentioned earlier the values found here will include both stable and unstable acceptor creation. Values of β for silicon diodes irradiated with 24 GeV protons at the CERN PS at low temperatures were, however, reported in Ref. [51], where it was found that

$$\begin{aligned} \beta(0°\mathrm{C}) &= 0.0470 \pm 0.0002 \text{ cm}^{-1} \\ \beta(-20°\mathrm{C}) &= 0.109 \pm 0.001 \text{ cm}^{-1}. \end{aligned}$$

The values found here of $\beta = 0.056 - 0.078$ cm^{-1} for detectors irradiated at -9 to -10°C are consistent with these, lying as they do between the values found for irradiation at 0°C and -20°C.

The weighted average of the rate of acceptor creation for detectors in all four irradiations periods is

$$\overline{\beta} = 0.0630 \pm 0.0018 \text{ cm}^{-1}. \tag{4.22}$$

4.6 Bulk characteristics of detectors during irradiation

The values of the current-related damage constant and the rate of acceptor creation calculated in the previous section can now be used to model the evolution of the bulk characteristics of detectors during irradiation. The effective doping concentration is given as a function of fluence by Eqn. (2.28) as

$$N_{eff}(\phi) = N_{eff,0}\exp(-c_D\phi) - \beta\phi$$

where the first term represents the removal of donors and the second term represents the creation of acceptors. No calculation of the rate of removal of donors c_D is available from the leakage current data taken during irradiation, therefore the value of c_D for proton irradiation given in Ref. [28] as representative of several experiments is used,

$$c_D = (0.96 \pm 0.19) \times 10^{-13}\ \mathrm{cm}^2\,.$$

The initial effective doping concentration $N_{eff,0}$ can be calculated using Eqn. (2.24). Taking the electron mobility as $\mu_e = 1350\ \mathrm{cm}^2\,\mathrm{V}^{-1}\,\mathrm{s}^{-1}$ [22] then for a resistivity of 2(5) kΩ cm the effective doping concentration is $2.3(0.93)\times10^{12}\ \mathrm{cm}^{-3}$. An intermediate value of

$$N_{eff,0} = 1.5 \times 10^{12}\ \mathrm{cm}^{-3}$$

for the initial effective doping concentration is used. The rate of acceptor creation is taken as the weighted average of the detectors in all irradiations given in Eqn. 4.22.

The evolution of the effective doping concentration with fluence is shown in Fig. 4.36. The inversion point is reached after a proton fluence of $\approx 0.9 \times 10^{13}\ \mathrm{cm}^{-2}$. After a fluence of $\approx 5.0 \times 10^{13}\ \mathrm{cm}^{-2}$ the donor removal term has become negligible and the effective doping concentration is entirely dominated by acceptor creation, and thus increases linearly with fluence. The full depletion voltage is related to the effective doping concentration via Eqn. (2.23), and is shown in Fig. 4.36 for a

detector of thickness 300 μm. The full depletion voltage is greater than 100 V after a proton fluence of $\approx 2.5 \times 10^{13}$ cm^{-2}, and at fluences greater than this a detector biased at 100 V will be under-depleted. After a proton fluence of 3.0×10^{14} cm^{-2}, equivalent to the end of irradiation, the full depletion voltage is ≈ 1300 V.

For a detector irradiated when held at a fixed bias voltage of 100 V the change in effective doping concentration, and hence full depletion voltage, causes the depleted width to be a function of fluence, given by Eqn. (4.3). The evolution of depleted width for a 300 μm thick detector reverse biased at 100 V is shown in Fig. 4.37a. As shown in Fig. 4.36 the full depletion voltage initially decreases and remains lower than the applied bias voltage of 100 V. In this region the detector is fully depleted and the depleted width is constant at the physical thickness of the detector. The full depletion voltage rises above 100 V after a proton fluence of $\approx 2.5 \times 10^{13}$ cm^{-2} and at this point in Fig. 4.37a the depleted width leaves the constant region and decreases sharply. As the fluence increases the rate of decrease of the depleted width slows. After a proton fluence of 3.0×10^{14} cm^{-2} only ≈ 80 μm of the bulk is depleted.

Finally the evolution of leakage current with fluence can be modelled using the depleted width profile shown in Fig. 4.37a to calculate the active volume of the detector. The leakage current is calculated using the expression for the radiation induced increase in leakage current given in Eqn. (2.34). For the current-related damage constant α the weighted average of $\alpha(20°\text{C})$ for detectors in all irradiation periods given in Eqn. 4.21 is used normalised to a temperature of $-10°$C with Eqn. (4.20):

$$\overline{\alpha}(-10°\text{C}) = (3.11 \pm 0.09) \times 10^{-18}\ \text{A cm}^{-1}\,. \tag{4.23}$$

The predicted leakage current as a function of fluence is shown in Fig. 4.37b for a 300 μm thick barrel detector biased at 100 V. As expected the leakage current initially increases linearly with fluence whilst the detector is fully depleted. At the fluence where the depleted width is no longer constant the linear region is left and the leakage current increases at a slower rate with fluence. The current predicted after a proton fluence of 3.0×10^{14} cm^{-2} is ≈ 300 μA. This same model of leakage current is

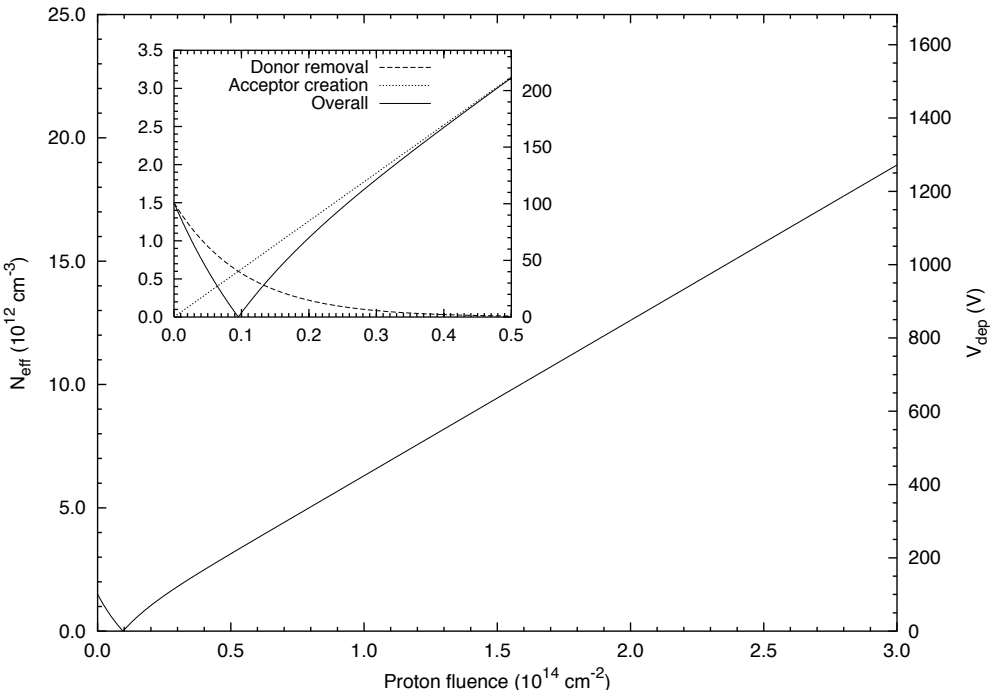

Figure 4.36: Change in effective doping concentration and full depletion voltage with fluence. Inset shows detail for low fluence, including separate donor removal and acceptor creation terms.

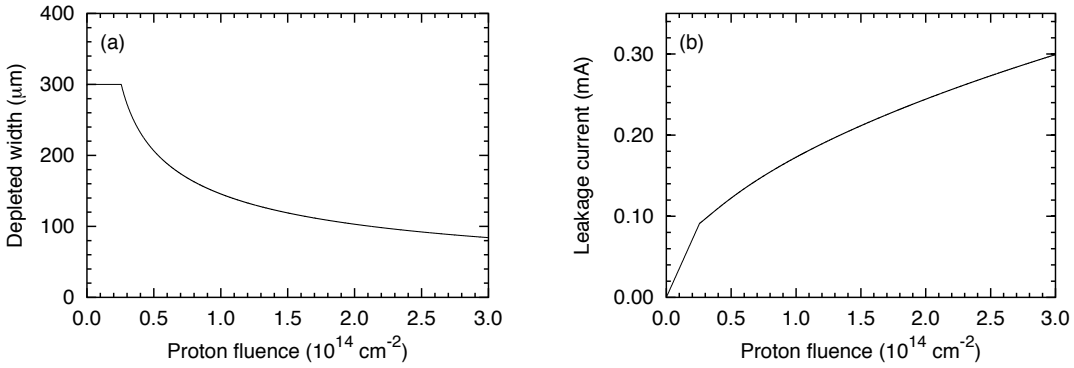

Figure 4.37: Variation of (a) depleted width of detector and (b) leakage current of detector with fluence.

compared with leakage current data for detectors from all irradiations (with currents normalized to a temperature of $-10°C$) in Fig. 4.38. All detectors shown are barrel designs of 300 μm thickness, apart from detector may00-f-1 which is 285 μm thick. Initially, in the linear region, the predicted leakage current is a good representation of all four detectors shown. As higher fluences are reached the different detectors do show some variation in leakage currents, but the value predicted by the model lies between the observed currents for the different detectors. At the end of irradiation the observed leakage currents for all detectors shown are within ± 20 μA of that predicted, less than 10% of the actual leakage current. Therefore the observed detector leakage currents during irradiation can be concluded to be in reasonable agreement with the predictions of the bulk radiation damage model.

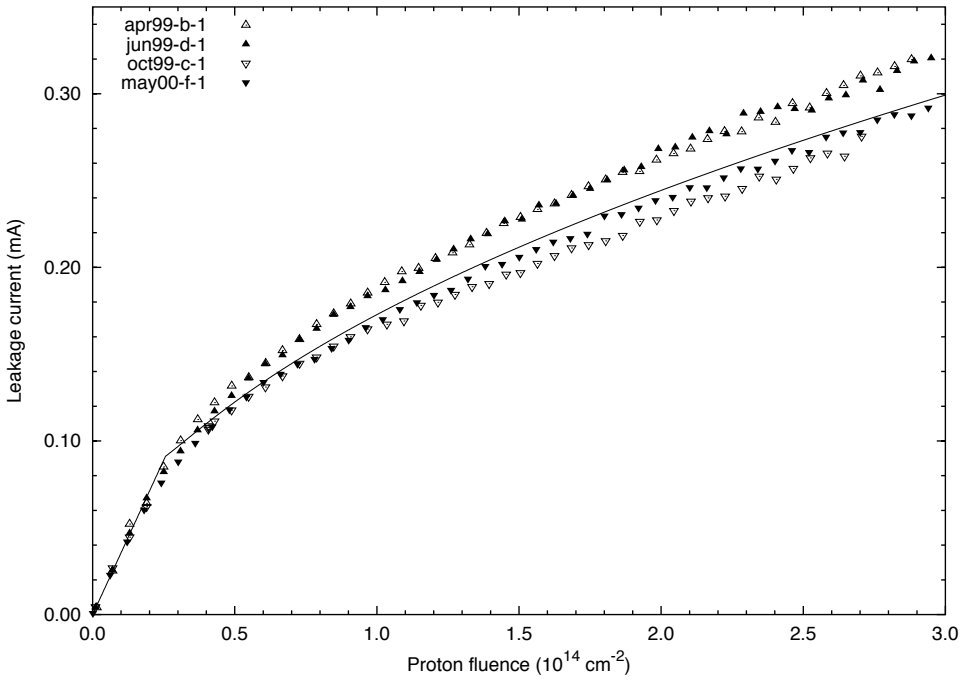

Figure 4.38: Predicted leakage current at $-10°C$ from bulk radiation damage model and measured leakage currents from all irradiations (normalized to $-10°C$).

4.7 Implications for detectors at ATLAS

During operation of silicon detectors at the ATLAS experiment the two most important detector parameters affected by radiation damage are the full depletion voltage and the leakage current. In order to achieve 100% charge collection efficiency the detector must be fully depleted, so the full depletion voltage must remain at a safe operational level low enough to avoid breakdown for the whole 10 year lifetime of the experiment. The power output of the detector is governed by both the leakage current and the full depletion voltage. A high leakage current may lead to a power output greater than can be removed by the cooling system, which could result in thermal runaway. It is therefore important to model the leakage current and full depletion voltages that will be expected for detectors through the whole 10 year lifetime of the ATLAS experiment.

4.7.1 ATLAS operational scenario

Whilst the silicon detectors in ATLAS will be cooled for the majority of the time in order to reduce leakage current and slow down annealing it is envisaged that the detectors will have to be warmed up for a short period each year for maintenance purposes. Therefore a standard access procedure (SAP) for the SCT has been defined [12,62] detailing the time spent at different temperatures. This is shown in Table 4.7. The operational scenario for the LHC is expected to be three years of low luminosity running ($L = 10^{33}\,\mathrm{cm}^{-2}\,\mathrm{s}^{-1}$) followed by seven years of high luminosity running ($L = 10^{34}\,\mathrm{cm}^{-2}\,\mathrm{s}^{-1}$)' The predicted radiation doses for silicon detectors in the SCT have already been shown in Table 3.2; to introduce a margin of error in the following calculations the radiation dose for silicon detectors in the SCT is taken as 2×10^{12} 1 MeV equivalent neutrons per cm^2 for one year of low luminosity running and 2×10^{13} 1 MeV equivalent neutrons per cm^2 for one year of high luminosity running. The integrated dose as a function of time is shown in Fig. 4.39; the overall dose after 10 years is $\approx 1.45 \times 10^{14}$ 1 MeV equivalent neutrons per cm^2.

Days	Temperature	Status
100	−7°C	operation
100	−7°C	off
2	+20°C	access
14	+17°C	maintenance
149	−7°C	off

Table 4.7: Standard Access Procedure for the ATLAS SCT.

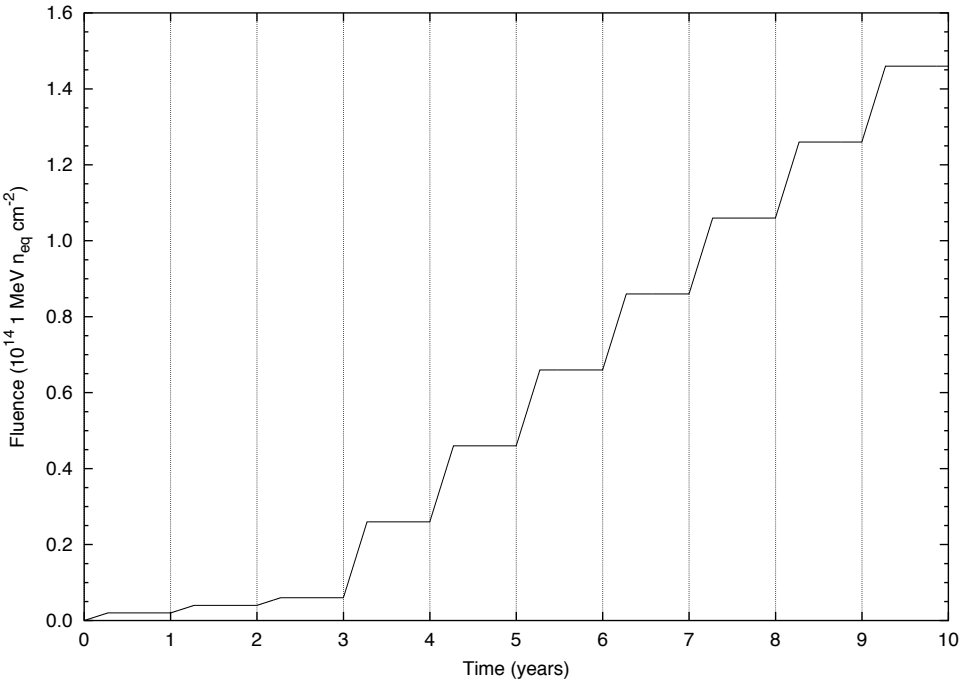

Figure 4.39: Integrated 1 MeV equivalent neutron fluence received by ATLAS silicon detectors over the lifetime of the experiment.

4.7.2 Leakage current

To model the change in leakage current over the lifetime of the ATLAS experiment both the increase in leakage current due to radiation damage during operational periods and the decrease in leakage current due to annealing must be taken into account. The familiar linear relationship between the volume leakage current and fluence of Eqn. (2.34) is used for the increase in leakage current with irradiation, adjusted for annealing as a function of beam-time t_{ir} and annealing (beam-off) time t' with Eqn. (2.39). Temperature dependence of the annealing is introduced by scaling the time axis with an Arrhenius relationship taking into account the annealing temperature T_A relative to a reference temperature T_R. Therefore the change in leakage current as a function of fluence ϕ, beam-time t_{ir}, annealing time t' and temperature T_A is given by

$$I(\phi, t_{ir}, t', T_A) = g(\Theta(T_A)t_{ir}, \Theta(T_A)t')\alpha\phi Vol\,, \tag{4.24}$$

$$\begin{aligned} g(\Theta(T_A)t_{ir}, \Theta(T_A)t') \;=\; & \sum_{i=1}^{n} \left\{ A_i \frac{\tau_i}{\Theta(T_A)t_{ir}} \left[1 - \exp\left(-\frac{\Theta(T_A)t_{ir}}{\tau_i} \right) \right] \right. \\ & \left. \exp\left(-\frac{\Theta(T_A)t'}{\tau_i} \right) \right\}\,, \end{aligned} \tag{4.25}$$

$$\Theta(T_A) = \exp\left(\frac{E_I}{k_B} \left[\frac{1}{T_R} - \frac{1}{T_A} \right] \right)\,. \tag{4.26}$$

The value for the current-related damage constant α is taken as the weighted average value of $\alpha(20°\mathrm{C})$ for all detector irradiations, given in Eqn. (4.21), normalised to the ATLAS operational temperature of $-7°\mathrm{C}$ with Eqn. (4.20) and scaled for radiation damage by 1 MeV equivalent neutrons using a proton hardness factor of 0.61 [63]. The resulting current-related damage constant for 1 MeV neutrons at $-7°\mathrm{C}$ is

$$\alpha_{eq}(-7°\mathrm{C}) = (6.90 \pm 0.20) \times 10^{-18}\ \mathrm{A\,cm^{-1}}$$

and it should be noted that the quoted uncertainty does not include any contribution from an uncertainty on the proton hardness factor. The values given in Table 2.2 are used for the parameters A_i and τ_i of the annealing function. The activation

energy of the temperature scaling function Eqn. (4.26) E_I is taken as 1.09 eV [28] and the reference temperature $T_R = 20°\text{C}$.

The predicted evolution of leakage current with time for a fully depleted barrel detector of thickness 285 μm over the lifetime of the ATLAS experiment is shown in Fig. 4.40. During the 100 day periods when the experiment is in operation the leakage current increases sharply, and during the periods when the experiment is off but the temperature still maintained at $-7°\text{C}$ the leakage current only decreases very slowly as leakage current annealing is almost frozen out at this temperature. During the maintenance periods at elevated temperatures significant decreases in leakage current due to annealing are observed, and in each ATLAS operational year the decrease in current is larger than in the preceding year.

After 10 years of operation the predicted leakage current is ≈ 380 μA. This can be compared with experimental results where detectors have been irradiated with 24 GeV protons at the CERN PS to a proton fluence of 3.0×10^{14} p cm^{-2} and

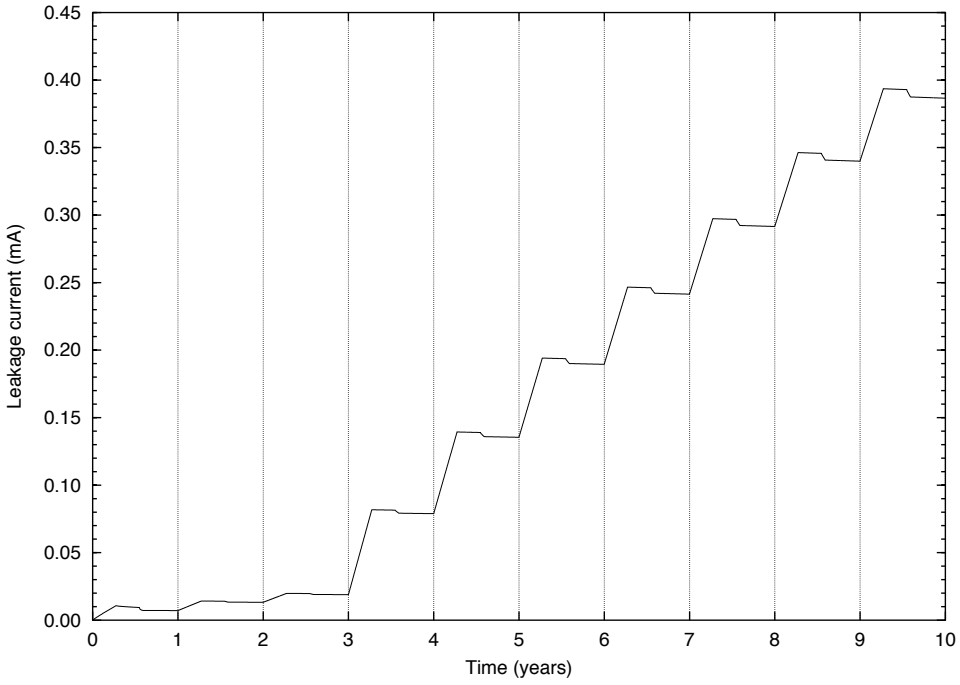

Figure 4.40: Predicted leakage current for a fully depleted 285 μm thick barrel detector over the lifetime of the ATLAS experiment.

subsequently annealed for 21 days at a temperature of 25°C, equivalent to the 10 year ATLAS access scenario [64]. Leakage currents for fully depleted 280 μm thick detectors of $I \approx 600$ μA and $I \approx 400$ μA were found for measurement temperatures of -5.9°C and -8.1°C respectively [65]. The value of ≈ 380 μA at a temperature of -7.0°C predicted by the model is in reasonable agreement with these results, which would be expected to give slightly higher leakage currents since a proton fluence of 3.0×10^{14} p cm^{-2} is equivalent to a 1 MeV equivalent neutron fluence of 1.8×10^{14} cm^{-2}, 20% larger than the 10 year integrated fluence used here.

4.7.3 Effective doping concentration

To model the evolution of the effective doping concentration during the lifetime of the ATLAS experiment several different components must be considered; the removal of donors, the stable creation of acceptors, the unstable creation of acceptors and reverse annealing. For the removal of donors the exponential function given in Eqn. (2.28) is used, the stable and unstable creation of acceptors are taken as Eqns. (2.30) and (2.31) respectively, and the reverse annealing is taken as Eqn. (2.33). Temperature dependence for both the unstable acceptor concentration and the reverse annealing are included by scaling the time axis with Arrhenius relationships [26]. Overall the effective doping concentration as a function of fluence ϕ, temperature T_A and annealing time t is given by

$$\begin{aligned} N_{eff}(\phi, t, T_A) &= N_{eff,0}\exp(-c_D\phi) - g_c\phi - g_a\phi\exp(-\Theta(T_A)_a\, t/\tau_a) \\ &\quad -g_y\phi\left(1 - \frac{1}{1+\Theta(T_A)_y t/\tau_y}\right), \end{aligned} \tag{4.27}$$

$$\Theta(T_A)_a = \exp\left(\frac{E_a}{k_B}\left[\frac{1}{T_R} - \frac{1}{T_A}\right]\right), \tag{4.28}$$

$$\Theta(T_A)_y = \exp\left(\frac{E_y}{k_B}\left[\frac{1}{T_R} - \frac{1}{T_A}\right]\right). \tag{4.29}$$

The parameters used in these functions are shown in Table 4.8. The rate of unstable acceptor creation is calculated using the value for the rate of acceptor creation β

Parameter	Value	Source
$N_{eff,0}$	$(1.5 \pm 0.5) \times 10^{12}$ cm^{-3}	Sec. 4.6
c_D	$(2.29 \pm 0.63) \times 10^{-13}$ cm^2	Ref. [28]
g_c	0.0149 ± 0.0004 cm^{-1}	Ref. [26]
g_a	0.0884 ± 0.0078 cm^{-1}	–
τ_s	2.3 days	Ref. [26]
E_a	1.09 ± 0.03 eV	Ref. [26]
g_y	0.0516 ± 0.0009 cm^{-1}	Ref. [26]
τ_y	475 days	Ref. [26]
E_y	1.33 ± 0.03 eV	Ref. [26]

Table 4.8: Parameters used to model the change in effective doping concentration over the lifetime of the ATLAS experiment.

found in Section 4.5. β includes both the stable and unstable contributions to acceptor creation, since at the low irradiation temperatures for which it was found little annealing of the unstable acceptor is expected. Assuming only a small difference in values of β between the irradiations performed here at temperatures of -8 to -10°C and operation at ATLAS at a temperature of -7°C then the rate of unstable acceptor creation is given by

$$g_a = \beta - g_c \,. \tag{4.30}$$

The rate of stable acceptor creation g_c was found in Ref. [26] for irradiation of standard silicon with 1 MeV equivalent neutrons as

$$g_c = 0.0149 \pm 0.0004 \text{ cm}^{-1} \,.$$

Scaling the mean value of β from all detector irradiations given in Eqn. (4.22) for irradiation with 1 MeV equivalent neutrons using a proton hardness factor of 0.61 gives

$$\beta_{eq} = 0.1033 \pm 0.0030 \text{ cm}^{-1}$$

and it should be noted that the uncertainty on this value does not include any contribution from an uncertainty on the proton hardness factor. The rate of unstable acceptor creation for 1 MeV equivalent neutrons is therefore

$$g_a = 0.0884 \pm 0.0034 \text{ cm}^{-1} \,.$$

Eqns. (4.27) to (4.29) are used to model the effective doping concentration over 10 years of ATLAS operation. The individual components of the effective doping concentration are shown as a function of ATLAS operational time in Fig. 4.41. The stable removal of donors (see Fig. 4.41a) is completed during the fourth year of operation, and thereafter this term is zero. The stable acceptor creation (see Fig. 4.41b) increases linearly with fluence during the operational periods, and reaches $\approx 2.2 \times 10^{12}$ cm^{-3} by the end of the 10 years of operation. The unstable acceptor creation (see Fig. 4.41c) increases at a faster rate with fluence during operational periods than the stable creation of acceptors (since $g_a \approx 6g_c$), so that $N \approx 1.8 \times 10^{12}$ cm^{-3} after each year of high luminosity operation. However, annealing causes this to decrease after the operational period, with a rapid decrease to zero during the maintenance periods at elevated temperature. Therefore this term is only of consequence during operation and does not cause a long-term in-

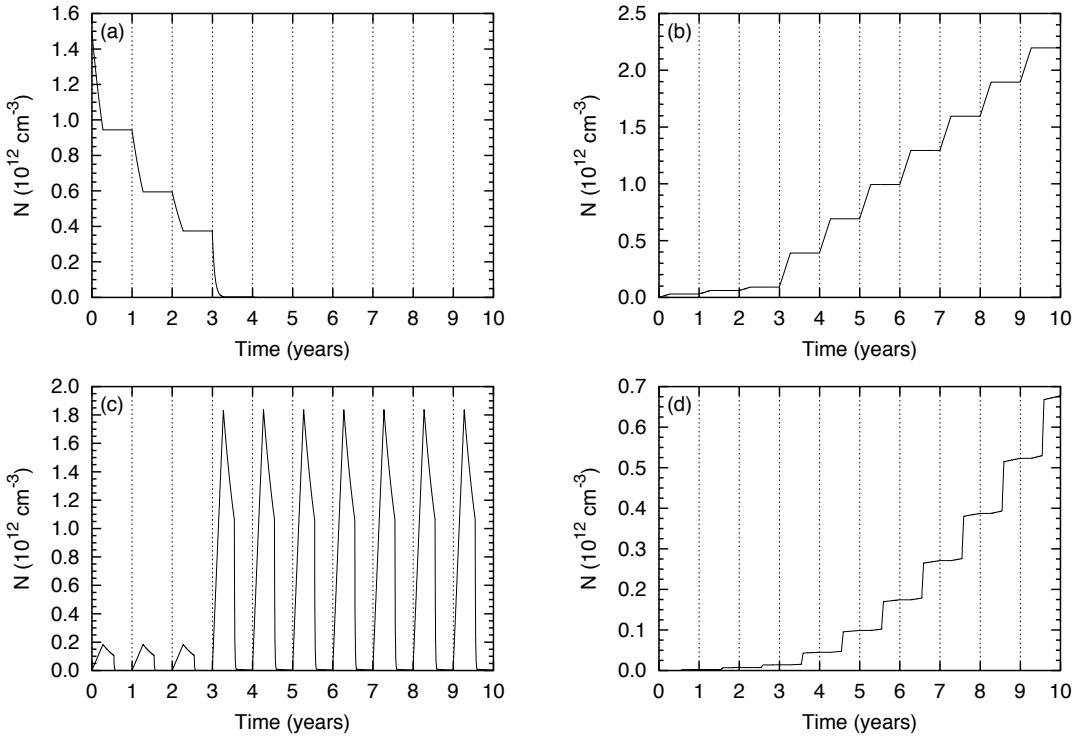

Figure 4.41: Variation of (a) stable donor removal, (b) stable acceptor creation, (c) unstable acceptor creation, and (d) reverse annealing of effective doping concentration during lifetime of ATLAS experiment.

crease in the effective doping concentration. It should be noted that annealing of the unstable acceptor creation is only applied during periods when the experiment is not operational, with no annealing included during the 100 day operational periods. Finally, the reverse annealing term (see Fig. 4.41d) builds up steadily over the 10 year operational period, and reaches a value of $N \approx 0.7 \times 10^{12}$ cm^{-3}, less than a third of the contribution from stable acceptor creation. Overall, the stable acceptor creation is dominant in the long term, but unstable acceptor creation is dominant during operational periods.

The overall evolution of the effective doping concentration is shown in Fig. 4.42. The unstable creation of acceptors causes large increases in N_{eff} during operational periods, taking N_{eff} well above the long-term increase from, predominantly, the stable creation of acceptors and, to a lesser extent, reverse annealing. During periods when the experiment is not running the annealing of the unstable acceptor creation causes a sharp decrease in N_{eff}. Also shown in Fig. 4.42 is the full depletion

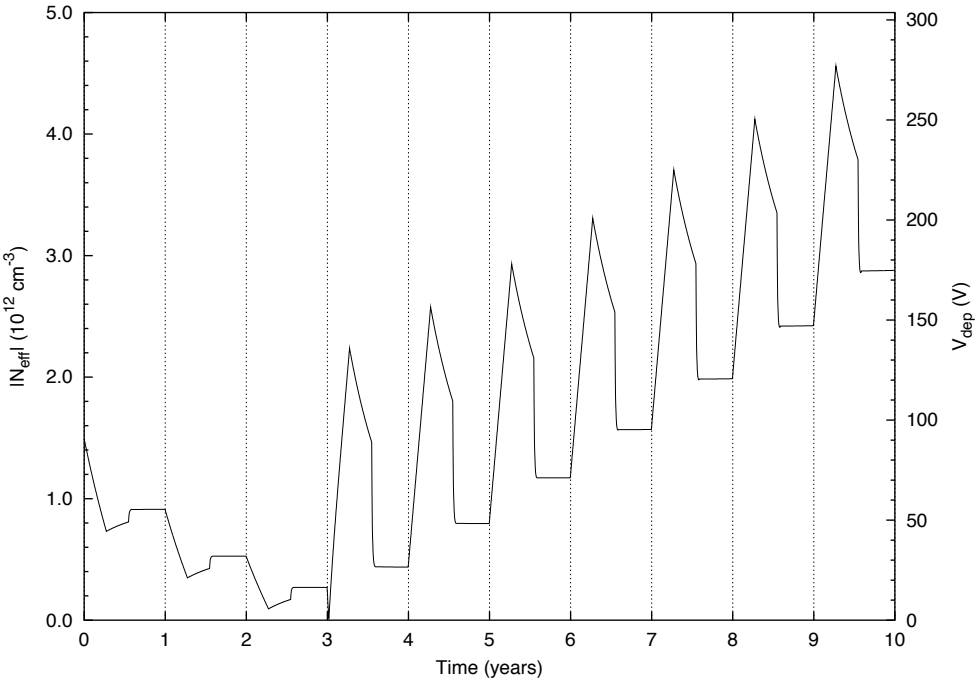

Figure 4.42: Effective doping concentration and full depletion voltage for a 285 μm thick detector over the lifetime of the ATLAS experiment.

voltage for a 285 μm thick detector. An increase in V_{dep} of over 100 V is seen during operational periods, mainly due to unstable acceptor creation, taking it to a maximum of $\approx$ 280 V in the final year, within the detector specifications for a maximum operating voltage of 350 V. The long-term full depletion voltage over the 10 years after all annealing has been completed is significantly lower, $\approx$ 175 V.

The model of effective doping concentration shown in Fig. 4.42 can be compared with a similar study in Ref. [12] for which the unstable acceptor creation term was not included. Whilst the final full depletion voltage found here is smaller, $\approx$ 175 V compared with $\approx$ 220 V from Ref. [12], the maximum predicted full depletion voltage is significantly greater, $\approx$ 280 V compared with, again, $\approx$ 220 V from Ref. [12]. This discrepancy can be attributed to the unstable acceptor creation which has been found here to give a large contribution during operational periods. Other studies have included the unstable acceptor creation term; for instance the full depletion voltage for a 300 μm thick detector after 10 years of operation was found to be $\approx$ 240 V [62], also the maximum full depletion voltage, with no large increases in V_{dep} observed during operational periods. This is because a significantly lower value for the rate of unstable acceptor creation was used, $g_a = 0.0193$ cm^{-1}. Other values for g_a found experimentally are also significantly lower than used here, for instance $g_a = 0.0181$ cm^{-1} [26]. These values were, however, found from devices irradiated at room temperatures, therefore a large proportion of the unstable acceptor concentration will have annealed out during irradiation, and will therefore not be reflected in the calculated value of g_a. The value of g_a used here is, though, probably an over-estimate when applied to operation at the ATLAS experiment. Whilst it was calculated from irradiations performed at similar temperatures to that envisaged for operation at ATLAS the time-scale of irradiation was extremely short, with over 10 years of ATLAS operational fluence received in $7 - 14$ days. In the actual experiment a larger proportion of the unstable acceptor concentration would be expected to anneal out during operational periods, since a lower flux will be received over a longer time. This will lead to a lower rate of unstable acceptor creation and hence a smaller increase in the full depletion voltage during operational periods than is

shown in Fig. 4.42.

The predicted final value for the full depletion voltage can also be compared with experimental results of detectors irradiated then annealed to the equivalent of the 10 year ATLAS operational scenario. For instance, a standard 280 μm thick detector irradiated to a proton fluence of 3×10^{14} cm^{-2} and then annealed for 21 days at 25°C was found to have a full depletion voltage of $\approx$ 190 V [66], in reasonable agreement with the $\approx$ 175 V shown in Fig. 4.42.

Finally, now that both the expected leakage current and full depletion voltage for silicon detectors after 10 years of ATLAS operation are known the power output can be calculated. Taking the maximum leakage current as 400 μA and the maximum full depletion voltage as 300 V (to allow for a small amount of over-bias) then the power output for one detector is 0.12 W. This is well below what has been budgeted for in the cooling system, which is 240 μW mm^{-2} of detector area [67], equivalent to 0.98 W for a barrel detector. The results of the models of leakage current and effective doping concentration presented here therefore do not have any adverse implications for the cooling system.

4.8 Summary

A model to explain the evolution of silicon microstrip detector leakage currents for detectors held under bias during proton irradiation at low temperature through bulk radiation damage effects has been developed. Two distinct regions are predicted, one for low fluences and the other for high fluences. At low fluence the leakage current is expected to increase linearly with fluence. Investigation of observed leakage currents during irradiation at low-fluence revealed a small systematic deviation from this. Several different mechanisms were investigated to explain the observed behaviour; leakage current annealing, radiation induced photocurrent and surface damage. Whilst it was found that radiation induced photocurrent could be ruled out the evidence both for and against leakage current annealing was inconclusive,

and a full study of surface damage was not possible. At high fluences the leakage current is expected to be described by a function $I \propto \sqrt{\phi}$. Investigation of observed leakage currents at high-fluence did not reveal any systematic deviation from this behaviour.

The leakage current data taken during irradiation are used to calculate the radiation damage parameters α, the current-related damage constant, and β, the rate of acceptor creation, for irradiation with 24 GeV protons. A value for α normalised to a temperature of 20°C of

$$\alpha(20°\mathrm{C}) = (4.84 \pm 0.13) \times 10^{-17}\ \mathrm{A\,cm^{-1}}$$

is found, comparable with those of previous experiments. A value of β for irradiation at temperatures of -8 to -10°C of

$$\beta = 0.0630 \pm 0.0018\ \mathrm{cm^{-1}}$$

is found, in general agreement with previous values of β found for proton irradiation at low temperature.

The calculated values of α and β are used to model the evolution of the bulk characteristics of a detector biased during irradiation. The predicted leakage current is in agreement with observed leakage currents for detectors in all irradiations studied. The evolution of leakage current and full depletion voltage for detectors during the 10 year lifetime of the ATLAS experiment is also modelled. The leakage current after 10 years for a fully depleted 285 μm thick barrel detector is predicted to be $\approx$ 380 μA, comparable with experimental results from detectors irradiated to the expected SCT fluence and then annealed to the equivalent of the ATLAS access scenario. The full depletion voltage of a 285 μm thick detector after the full 10 year scenario is $V_{dep} \approx 175$ V, again comparable with experimental results. However, the maximum full depletion voltage is found to be $V_{dep} \approx 280$ V. This is due to a large contribution from unstable acceptor creation which causes an increase in the effective doping concentration during each operational period, but anneals away completely during the maintenance periods at elevated temperatures. The rate of

unstable acceptor creation is calculated from the value found for β, the overall rate of acceptor creation, from proton irradiation at low temperature and is considerably larger than previously published values. These have predominantly been calculated from detectors irradiated at room temperature where a large proportion of the unstable acceptor concentration anneals out during irradiation and is consequently not seen. However, the value for the rate of unstable acceptor creation used here is expected to be an overestimation for operation at ATLAS since more annealing of the unstable acceptor component should occur due to the much longer time-scale during which fluence is received compared with high flux detector irradiation. The predicted maximum values of the leakage current and full depletion voltage give a power output per detector well below that budgeted for the cooling system.

Chapter 5

Higgs boson physics

The search for the Higgs boson is possibly the premier task for the ATLAS experiment at the LHC, as a discovery will confirm the approach to electroweak symmetry breaking formulated in the Standard Model. In this chapter the origin of the Higgs boson and theoretical constraints on its mass will be described. A summary of experimental searches performed at LEP and the Tevatron will be presented, along with the prospects for the discovery of the Higgs at both the Tevatron Run 2 and ATLAS. Next, the weak boson fusion production mechanism will be discussed, and in particular the $H \rightarrow WW^{(*)} \rightarrow l^+l^-p_T^{miss}$ decay channel, in the context of finding a light or intermediate mass Higgs boson at ATLAS. The particular features of this channel will be described, as will the major physics backgrounds. Finally, the simulation tools used for the subsequent analysis are introduced and the events generated for signal and background processes detailed.

5.1 The Higgs boson

Only a brief description of the theory behind the origin of the Higgs boson will be given here as this topic is covered in many textbooks, for instance [2].

In the Standard Model interactions between particles are closely connected with gauge symmetries. Taking Quantum Electrodynamics as an example, in order for the Lagrangian to be invariant under the $U(1)$ group of local phase transformations an additional gauge field must be introduced. The quantum of this field is a massless gauge boson, the photon. The emergence of the photon in the theory is a direct result of requiring local gauge invariance.

Applying this to the weak interaction, the Lagrangian is required to be invariant under the $SU(2)^W$ group of local weak isospin rotations. This requires the addition of a charge triplet of gauge bosons. However, the finite range of the weak force requires that the gauge bosons be massive; introducing a mass term into the Lagrangian destroys the gauge invariance and makes the theory non-renormalisable.

A way around this problem is provided by Spontaneous Symmetry Breaking. A hypothetical complex scalar field is considered with a Lagrangian that has a non-zero vacuum expectation value; the lowest energy state is asymmetric. By requiring that the Lagrangian is invariant under a global gauge transformation and redefining the Lagrangian in terms of the lowest energy state the global gauge symmetry is spontaneously broken; the Lagrangian is no longer invariant under the original gauge transformation. Additionally the redefined fields give rise to two particles; a massive scalar particle and a massless scalar "Goldstone" boson. Therefore whilst mass has been introduced this is at the cost of another massless particle, and both particles are scalar whereas the W and Z bosons are spin-1. Instead, the Lagrangian is demanded to be invariant under a local gauge transformation; as mentioned above this requires the addition of a gauge particle. Now, when the Lagrangian is redefined in terms of the lowest energy state there remains one massive spin-0 particle, as before, but the massless spin-0 Goldstone boson is no longer present, having been "eaten" by the

gauge boson, which in doing so acquires a mass. This is the Higgs Mechanism, first proposed by Peter Higgs in 1964 [68, 69], and the massive scalar particle is known as a Higgs boson.

Such a process is applied during the formulation of the combined $SU(2)_L^W \times U(1)^W$ Glashow-Weinberg-Salam model of electroweak interactions [70, 71] in the Standard Model. A doublet of complex scalar Higgs fields is included in such a way that whilst the photon remains massless and the $U(1)$ gauge symmetry of QED is unbroken the $SU(2)_L^W$ symmetry is broken and the $W^{\pm}$ and Z bosons each acquire a mass through the absorption of a Goldstone boson. One massive neutral scalar Higgs boson is left, but its mass is not predicted. Interactions with the Higgs fields also generate quark and lepton masses; again the actual masses are not predicted and have to be entered by hand, but the coupling of the Higgs boson to fermions is proportional to the fermion mass.

Although the Higgs boson mass is not predicted by the Standard Model there are still some theoretical constraints on it. Firstly, there is the unitarity bound, which gives an upper limit of [72]

$$m_H \lesssim 1 \text{ TeV}$$

above which weak interactions exhibit features associated with strong interactions, and perturbation theory breaks down. Secondly, there are lower limits placed on the Higgs mass by requiring stability of the electroweak vacuum, and upper limits through the "triviality" condition, which demands the validity of the theory up to some energy scale Λ. By choosing Λ as the Planck mass, so that no new physics emerges below this, strong constraints are placed on the Higgs mass [73, 74]

$$130 \lesssim m_H \lesssim 190 \text{ GeV}$$

If instead Λ is set at a lower level, say 1 TeV, then the Higgs mass is less constrained,

$$50 \lesssim m_H \lesssim 800 \text{ GeV}$$

This would also imply that the Standard Model is an effective theory only, and at energies above this scale new physics beyond the Standard Model would be apparent.

Further constraints can be placed on the Higgs boson mass through precision fits to electroweak data. The Higgs boson is present in radiative corrections to electroweak processes and measurements of, for instance, the Z mass and width and the W mass allow limits to be placed on the Higgs mass, assuming the validity of the Standard Model. The most recent calculations from data taken at LEP and the Stanford Linear Collider (SLC) give [75]

$$m_H = 98^{+58}_{-38}\ \text{GeV}$$

with $m_H < 212$ GeV at 95% C.L. These results strongly suggest that the Higgs is relatively light, and is most likely to be found in the light and intermediate mass region of $100 - 200$ GeV.

5.2 Experimental searches for the Higgs boson

Since the discovery of the top quark at the Tevatron in 1995 the Higgs boson remains the only particle in the Standard Model yet to be observed. Searches for it have therefore been an important part of recent experiments. A brief summary of the results of direct searches for a Standard Model Higgs boson performed by the LEP experiments and at Tevatron Run 1, and the prospects for Tevatron Run 2 will now be presented.

5.2.1 Searches at LEP

After several years study of the Z boson, the LEP collider was upgraded to increase the centre of mass energy in order to search for new physics, including the Higgs boson. By the end of the year 2000, when the machine was decommissioned, between the four different LEP experiments 2465 pb^{-1} of data had been taken at centre of mass energies greater than 189 GeV, of which 542 pb^{-1} was taken at centre of mass energies greater than 206 GeV.

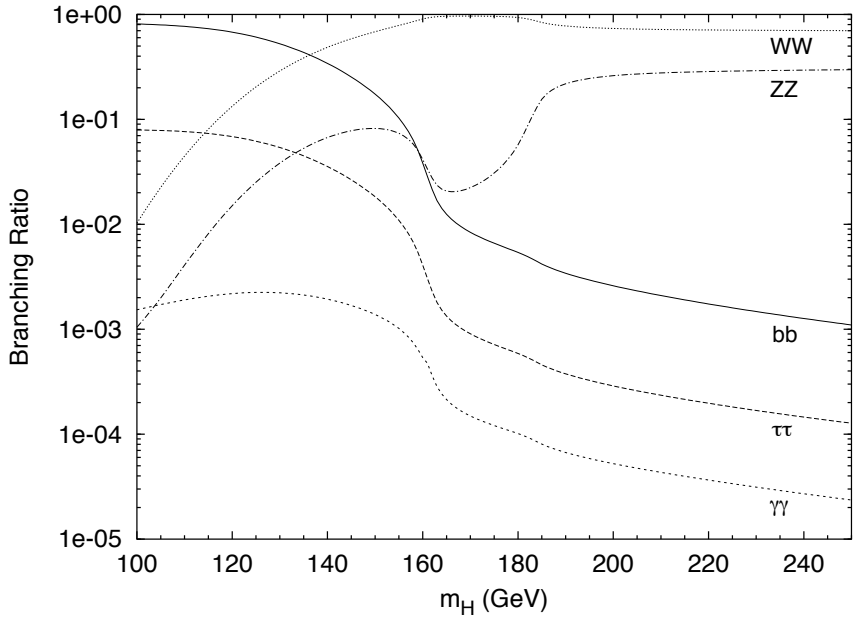

Figure 5.1: Branching ratios for main decay modes of the Standard Model Higgs boson, calculated with the HDECAY [76] package.

At LEP the main production mechanism for a Standard Model Higgs boson is through Higgsstrahlung, $e^+e^- \to HZ$, and the maximum Higgs boson mass that can be produced at a centre-of-mass energy of 206 GeV is ≈ 115 GeV. At this mass the dominant decay channel is $H \to b\bar{b}$, other decay modes such as $H \to WW^*$ and $H \to \tau^+\tau^-$ having branching ratios an order of magnitude lower (see Fig. 5.1). Therefore searches for the Higgs boson at LEP have concentrated on final states with a $b\bar{b}$ pair from the decay of the Higgs and either $q\bar{q}$, $\nu\nu$, l^+l^- (where $l = e$ or μ) or $\tau^+\tau^-$ from the decay of the Z boson.

Up until the year 2000, as the centre of mass energy of LEP collisions was increased, observations were consistent with the expected Standard Model background, and the lower bound on the Higgs mass was increased due to the null results of the experimental searches. However, in September 2000 as the centre of mass energy was increased to above 206 GeV the ALEPH experiment reported an excess of events above the expected SM background, consistent with a Higgs boson of mass

$\approx$ 115 GeV, predominantly in the four jet final state [77]. Although this was not supported by the other LEP experiments an extra month of LEP running was undertaken to attempt to clarify this situation, after which the L3 experiment also reported candidate Higgs events. After a review of all data the combined results of all four LEP experiments now impose a lower bound at 95% C.L. of [5]

$$m_H > 114.1 \text{ GeV}$$

An excess of events consistent with a Standard Model Higgs boson with mass 115.6 GeV was observed, with the probability for this to be due to a fluctuation in the Standard Model background of 3.4%, equivalent to 1.83 Gaussian standard deviations.

These results therefore leave the particle physics community in a state of uncertainty; although they appear to suggest a relatively light Higgs boson, the statistical significance is not sufficient to claim a discovery. Now that LEP has been closed down to make way for the construction of the LHC it is up to other experiments to either confirm or refute these findings.

5.2.2 Searches and prospects at the Tevatron

Approximately 90 pb^{-1} of data were collected in $p\bar{p}$ collisions at centre-of-mass energy $\sqrt{s} = 1.8$ TeV during Tevatron Run 1 by both the CDF and D0 experiments. SM Higgs searches were limited to masses below 140 GeV, where the $H \to b\bar{b}$ decay mode dominates. Although direct production through gluon fusion has the largest cross-section this was not considered due to the large di-jet background; instead, searches were performed for the associated production of the Higgs with a W or Z boson. The channels $WH \to l\nu b\bar{b}$ and $(W/Z)H \to q\bar{q}b\bar{b}$ [78], and $ZH \to \nu\bar{\nu}b\bar{b}$ and $ZH \to l^+l^-b\bar{b}$ [79] were considered; the overall distribution of events was consistent with the expected SM background.

Both the accelerators and the detectors at the Tevatron have recently undergone upgrades; the accelerator will deliver a higher luminosity at a centre-of-mass energy

of $\sqrt{s} = 2.0$ TeV and the detectors have gained new vertex detectors and improved triggering. The mass reach for a SM Higgs boson has been increased to 190 GeV and several search modes have been investigated [80] which can be split into two mass regions. Firstly, in the mass range $90 - 130$ GeV, where the decay $H \to b\bar{b}$ dominates, the same channels have been studied as were used for Run 1. Secondly, in the mass range $130 - 190$ GeV the decay $H \to WW^{(*)}$ dominates. The associated production of a Higgs boson with a W or Z boson leading to 2-lepton plus 2-jet or 3-lepton final states, and also direct production with decay to $l^+l^-\nu\overline{\nu}$ are considered. As there is no single "golden" channel it is necessary to combine the results of all of the SM Higgs search channels. Fig. 5.2 shows the integrated luminosity required by each experiment to exclude a SM Higgs at 95% C.L., or make a 3σ or 5σ observation. With the 2 fb^{-1} expected by 2003 for Run 2a it is only possible to improve slightly on the LEP results, with no discovery possible but exclusion at 95% C.L. up to $m_H \approx 115$ GeV. However, for the proposed Run 2b where it is planned to take 15 fb^{-1} of data by the year 2007 the situation is improved, with the possibility

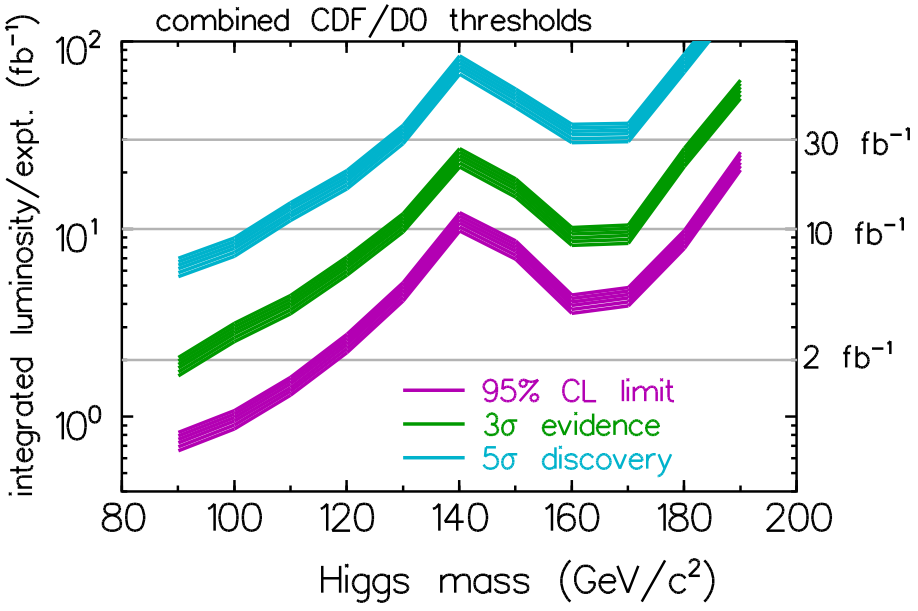

Figure 5.2: Integrated luminosity per experiment required to exclude a SM Higgs at 95% C.L., observe it at 3σ level or observe it at 5σ level at the Tevatron as a function of Higgs mass. Taken from Ref. [80].

of exclusion over the mass range $m_H = 100 - 180$ GeV, a 3σ observation for the majority of this mass range (apart from a region around $m_H \approx 140$ GeV) and a 5σ discovery for $m_H \lesssim 115$ GeV.

Therefore if the Higgs mass is ≈ 115 GeV as suggested by LEP then there is a possibility that it will be discovered at the Tevatron before the start of LHC running. If the Higgs mass is in fact greater than this then the Tevatron will not be able to make a 5σ discovery without additional data. In either case it seems likely that by the time the LHC experiments start taking data a clearer idea of the search region for a SM Higgs boson will be available.

5.3 Higgs searches at ATLAS

In the absence of a discovery at the Tevatron it will be left to the ATLAS and CMS experiments at the LHC to search for a SM Higgs boson. The whole of the theoretically allowed mass range can be covered, therefore if the SM Higgs does exist then it should be discovered.

The dominant production process for a SM Higgs boson at the LHC is that of gluon fusion, which has a production cross-section several times greater than the other production processes (see Fig. 5.3). The gluon fusion process proceeds almost exclusively through a top-quark loop due to the strong coupling of the Higgs to the heavy top-quark (see Fig. 5.4a). The next largest production cross-section is for weak boson fusion, where each of the incoming quarks radiates a W or Z boson, which then fuse into a Higgs boson (see Fig. 5.4b). Additional contributions come from the associated production of the Higgs with a W or Z boson (see Fig. 5.4c). Overall, the production cross-section for the SM Higgs boson is of order $10 - 30$ pb for the most likely Higgs mass range of $100 - 200$ GeV. Therefore even during the initial low luminosity period where a luminosity of 10^{33} cm^{-2}s^{-1} is expected approximately 10^5 Higgs events will be produced each year in this mass range. The challenge of finding a SM Higgs boson at the LHC is not a low event rate but of

isolating the signal from the very large QCD backgrounds.

Many possible search channels for a SM Higgs boson have been investigated within the context of the ATLAS experiment, covering the whole allowed mass range. A summary of these will now be presented, concentrating on the most promising channels for the favoured intermediate mass range. Further details can be found in Ref. [81, Ch. 19].

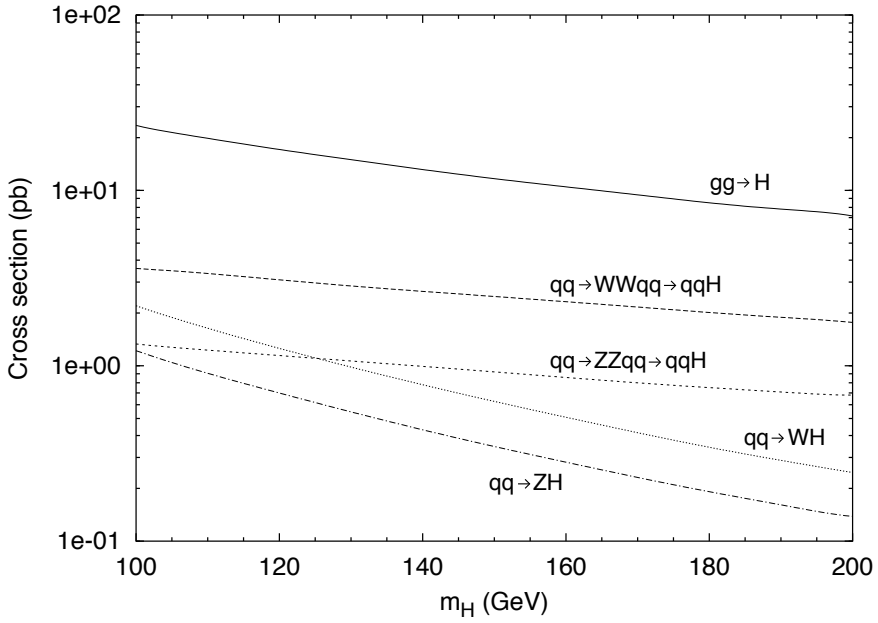

Figure 5.3: Production cross-sections for the Standard Model Higgs boson at the LHC, calculated with the PYTHIA Monte Carlo [82].

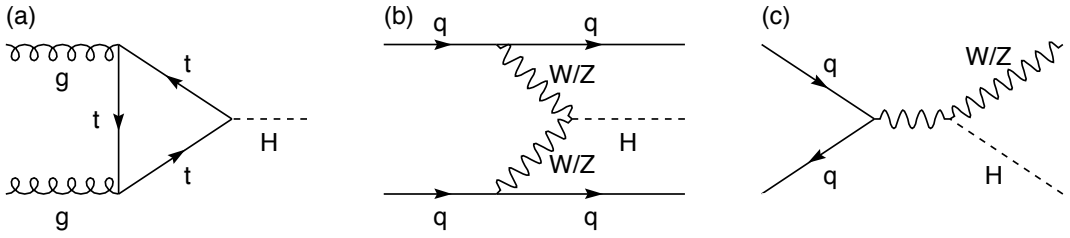

Figure 5.4: Feynman diagrams for the dominant Higgs production mechanisms at the LHC; (a) gluon fusion, (b) weak boson fusion and (c) associated production with a W or Z boson.

$H \to \gamma\gamma$

Although $H \to \gamma\gamma$ is a rare decay mode with only a small branching ratio (see Fig. 5.1) it has been considered for finding a relatively light Higgs boson, with mass $100 \leq m_H \leq 150$ GeV. Direct production through gluon fusion and associated production with a W or Z boson, a $t\bar{t}$ pair or QCD jets have all been studied, of which the direct production mode is the most promising; a 5σ signal can be observed in the mass range 105 to 145 GeV with an integrated luminosity of 100 fb^{-1}. A mass peak can be reconstructed, although excellent performance of the EM Calorimeter will be required. Whilst the discovery potential in the associated W or Z boson or $t\bar{t}$ pair modes is less than for direct production they can provide an independent confirmation of a discovery with a higher integrated luminosity.

$H \to b\bar{b}$

As can be seen from Fig. 5.1 the dominant decay channel for a Higgs boson of mass < 140 GeV is $H \to b\bar{b}$. The direct production mode cannot be used because of the huge QCD di-jet background. Therefore this decay channel is only considered in the context of associated production. Associated production with a W boson, giving a lepton and two b-quarks in the final state, has not been found to be very promising. Associated production with a $t\bar{t}$ pair gives a complex final state, with two b-quarks and two W bosons coming from the decay of the top-quarks, as well as the two b-quarks from the Higgs decay. One W is required to decay leptonically for triggering purposes, whereas the other is assumed to decay to jets. With the combination of 30 fb^{-1} of data taken during low luminosity operation and 70 fb^{-1} during high luminosity operation a 5σ signal can be obtained for the mass range 80 to 120 GeV.

$H \to ZZ^* \to 4l$

The $H \to ZZ^* \to 4l$ (with $l = e, \mu$) final state can give a clean signature for Higgs masses between 120 and 180 GeV. The branching ratio of $H \to ZZ^*$ is large and increases with m_H, except in the region $160 \leq m_H \leq 180$ GeV where this channel is suppressed. This is due to the opening up of the decay of the Higgs boson to two on mass shell W bosons for $m_H > 2m_W$, which dominates the total width of the Higgs until $m_H > 2m_Z$ where the decay to two on mass shell Z bosons becomes available. All three possible final states have been considered; 4 electron, 4 muons, 2 electrons and 2 muons. A mass peak can be reconstructed from the decay products, with the best resolution being for the 4 muon final state. With an integrated luminosity of 30 fb^{-1} a 5σ signal can be obtained for $130 \leq m_H \leq 180$ GeV with the combination of all three final states, apart from the region around $m_H = 170$ GeV. With 100 fb^{-1} the whole of the mass range is covered.

$H \to WW^{(*)} \to l\nu l\nu$

To cover the region $150 \leq m_H \leq 180$ GeV where the ZZ^* channel is suppressed the $H \to WW^{(*)} \to l\nu l\nu$ channel has been investigated [83]. The decay $H \to WW^{(*)}$ has a very large branching ratio, but unfortunately no mass peak can be reconstructed due to the neutrinos in the final state. Therefore an excess of events above the expected SM background must be observed for a discovery. It has been found that a 5σ signal can be observed for the Higgs mass range 150 to 190 GeV with an integrated luminosity of 30 fb^{-1} [83], even taking into account a 5% systematic uncertainty on the absolute knowledge of the background. Information on the Higgs mass can be found from the transverse mass, and it is hoped that a resolution of ≈ 5 GeV will be possible.

WH; $H \to WW^{(*)}$

The $H \to WW^{(*)}$ channel has also been investigated in the context of associated production of the Higgs boson with a W boson. Two different final states have been investigated; firstly a three lepton final state where all three W's decay via $W \to l\nu$, secondly a two-lepton two-jet final state where one W from the Higgs decay and the associated W decay through $W \to l\nu$ and the other W from the decay of the Higgs decays to a $q\overline{q}$ pair. This combination is chosen because it gives like-sign leptons in the final state which eliminates many backgrounds. It has been found that the three lepton final state can give a 5σ signal for $m_H = 160 - 170$ GeV, and the two-lepton two-jet final state for $m_H = 160 - 190$ GeV [84], with an integrated luminosity of 100 fb^{-1}. Again, no mass peak can be reconstructed so an excess of events above the expected SM background must be observed.

Overall sensitivity

The overall sensitivity of the ATLAS detector for the discovery of a light and intermediate mass Higgs boson is shown in Fig. 5.5 for integrated luminosities of both 30 fb^{-1} and 100 fb^{-1}. By combining all channels a 5σ signal can be obtained for the whole of this region, $80 \leq m_H \leq 190$ GeV, with an integrated luminosity of 30 fb^{-1}, equivalent to three years of low luminosity LHC running. All Higgs masses are covered by at least two different channels giving the possibility of independent checks of any discovery. With the increased integrated luminosity of 100 fb^{-1} a discovery can be confirmed and consolidated. For all values of m_H there is also a channel for which a mass peak can be reconstructed; $H \to \gamma\gamma$ for $m_H < 130$ GeV and $H \to ZZ^* \to 4l$ for $130 < m_H < 190$ GeV.

For a heavier Higgs boson the $H \to ZZ \to 4l$ decay provides a reliable channel for the mass range $200 \leq m_H \leq 600$ GeV, with a very low background. A 5σ signal can be observed after less than one year of low luminosity running. The $H \to ZZ \to ll\nu\nu$ can provide a 5σ signal for $400 \leq m_H \leq 900$ GeV with an integrated luminosity

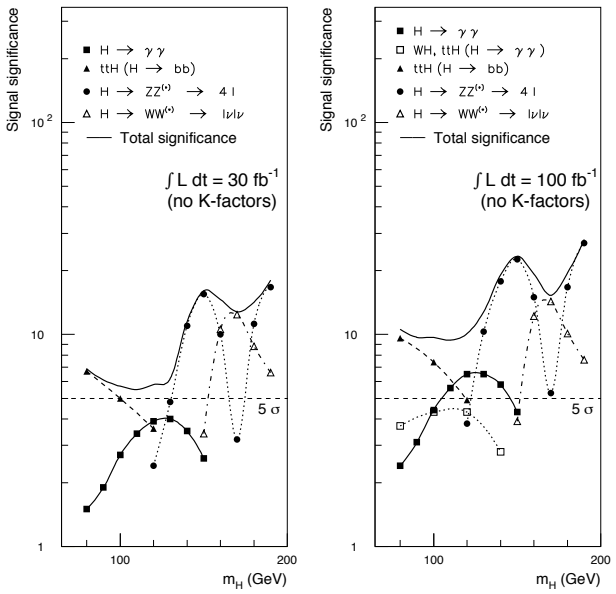

Figure 5.5: Sensitivity of the ATLAS experiment for the discovery of an intermediate mass SM Higgs boson for both 30 fb^{-1} and 100 fb^{-1}integrated luminosity. Taken from Ref. [81].

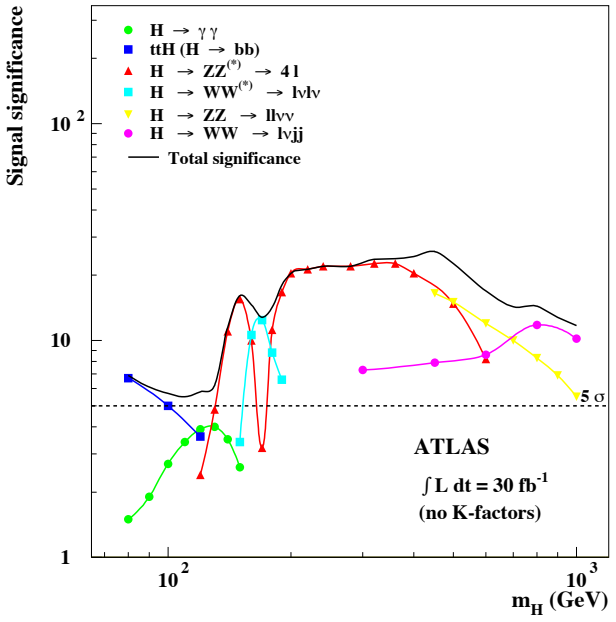

Figure 5.6: Sensitivity of the ATLAS experiment for the discovery of a SM Higgs boson over whole theoretically allowed mass range for 30 fb^{-1} integrated luminosity. Taken from Ref. [81].

of 100 fb^{-1}. Finally, the $H \rightarrow WW \rightarrow l\nu jj$ decay channel from a Higgs boson produced via weak boson fusion gives a 5σ signal for $300 \leq m_H \leq 1000$ GeV with an integrated luminosity of 30 fb^{-1}. The sensitivity of ATLAS for the discovery of a SM Higgs boson for the whole theoretically allowed mass range is shown in Fig. 5.6.

5.4 Higgs via weak boson fusion at ATLAS

The weak boson fusion (WBF) process has the second largest production cross-section for an intermediate mass Higgs boson at the LHC (see Fig. 5.3). In addition the initial state quarks are scattered by the emission of W or Z bosons and give rise to forward tagging jets in the detector, thus giving a distinctive characteristic to the signal. Previously SM Higgs production via WBF has been studied mainly for searches for a heavy Higgs boson with mass of order 1 TeV. The production cross section for WBF is $25-30\%$ of that for gluon fusion in this region.

More recently studies of the WBF production mechanism for an intermediate mass Higgs boson have been performed through parton level simulations. Several different decay channels have been investigated, including $H \rightarrow \tau^+\tau^-$ [85,86], $H \rightarrow \gamma\gamma$ [87] and $H \rightarrow WW^{(*)}$ [18,19]. The most promising of these was found to be the $WW^{(*)}$ channel, due to the large branching ratio of this decay in the intermediate mass region. Both of the W's were required to decay leptonically and a final state of $e^{\pm}\mu^{\mp}p_T^{miss}$ was selected. It was found that a 5σ signal could be isolated with a signal to background ratio greater than 1/1 for the mass range $m_H = 140-190$ GeV with an integrated luminosity of only 5 fb^{-1}, equivalent to six months low luminosity running at the LHC.

To confirm these findings it is important that this channel is revisited using a particle level simulation, where events are generated including hadronisation of partons into physical hadrons and a detector simulation, since parton level analyses often give optimistic results. In the following chapter the $H \rightarrow WW^{(*)} \rightarrow e^{\pm}\mu^{\mp}p_T^{miss}$ channel is

re-analysed using a particle level simulation. The $H \to WW^{(*)} \to (e^+e^-/\mu^+\mu^-)p_T^{miss}$ channel is also investigated, which was neglected in Ref. [18]. Finally these channels are considered in the context of the search for a light Higgs boson with mass as suggested by the results from the LEP experiments. First, though, the distinctive characteristics of the signal process shall be described, as will the physics backgrounds which must be considered.

5.4.1 The WBF $H \to WW^{(*)} \to l^+l^-p_T^{miss}$ signal

The signal process considered is a Standard Model Higgs boson produced via weak boson fusion, followed by the decay $H \to WW^{(*)} \to l^+l^-p_T^{miss}$. Therefore the basic final state consists of two jets from the scattered quarks, and two charged leptons and missing transverse momentum from the decay of the Higgs boson. Two different lepton combinations can be considered; firstly a final state with one electron and one muon, which has the advantage of not having to take into account lepton pair-production backgrounds, and secondly the two electron or two muon final state. The basic signal process has several distinctive features that enable it to be distinguished from the physics backgrounds.

The quarks in the final state of the signal process are an important characteristic that distinguishes it from production via gluon fusion. The incoming quarks have relatively high energies and are then scattered by the emission of W or Z bosons, which tend to take a small fraction of the quark energy. Their transverse momentum, though, is of order M_W. The final state quarks therefore have relatively large energy and modest transverse momentum, so the scattering angle with respect to the beam-line is small and the resulting jets will be found in the forward regions of the detector [88]. In contrast, the dominant QCD background processes tend to have centrally produced jets [89]. From similar arguments the QCD processes also tend to have smaller invariant masses of the tagging jets compared with EW processes such as the signal. Additionally, since in the signal process the two W or Z bosons have relatively small longitudinal momentum the Higgs boson is produced

centrally leading to central decay products between the two forward tagging jets.

The angular distribution of the charged leptons is also an important characteristic of the signal. The decay of the scalar Higgs boson into two W bosons results in the W's having anti-correlated spins due to conservation of angular momentum. In the rest frame of the Higgs boson the W's are produced almost at threshold for $m_H \lesssim 2m_W$ and the lepton and neutrino from each W decay are emitted back-to-back with equal energy. When the W^+ decays into an anti-lepton and a neutrino the (left-handed) neutrino is emitted in the opposite direction to the W^+ spin, the anti-lepton therefore being preferentially emitted in the same direction as the W^+ spin. Similarly the (right-handed) anti-neutrino from the decay of the W^- is emitted in the same direction as the W^- spin, the lepton being preferentially emitted in the opposite direction. Therefore since the W^+ and W^- have opposite spins the lepton and anti-lepton tend to be emitted in the same direction [90, 91], and this characteristic remains when boosted back to the lab frame. A substantial proportion of the background does not have the same anti-correlation of the W spins, therefore the angular distribution of the charged leptons will not show the same features as the signal. A further consequence of the anti-correlated spins is that the invariant masses of the charged lepton system and the neutrino system are approximately equal, and must both be less than half of the Higgs boson mass.

Finally, the signal process has a lack of additional radiation emitted into the central region of the detector. In the weak boson fusion process the interaction between the initial state quarks proceeds through the exchange of weak bosons, which do not carry colour. Any additional hadronic radiation from the signal process can only come from gluons radiated from the initial or final state quarks; it is therefore most likely to be found in the forward and backward regions of the detector. The dominant QCD backgrounds, on the other hand, proceed by the exchange of colour between the initial state partons and additional hadronic radiation is more likely to be emitted into the central region.

5.4.2 Physics Backgrounds

Given the signal process under investigation, any other process that can produce two charged leptons and two or more jets in the final state must be considered as a potential source of background events. Accurate determination of the background is particularly important for the $H \rightarrow W^+W^- \rightarrow l^+l^-p_T^{miss}$ channel, since due to the neutrinos in the final state no mass peak can be reconstructed and a discovery relies upon observing an excess of events above the expected SM background.

The processes that will be used to calculate the background are outlined below, divided into those necessary for both the $e\mu$ and $ee/\mu\mu$ channels and those that need only be taken into account for the $ee/\mu\mu$ channel. Potential sources of background that have not been considered are also mentioned.

Background for $e\mu$ and $ee/\mu\mu$ channels

The dominant background process is $t\bar{t} + jets$ which has a large cross-section at the LHC, of order 500 pb. The basic process is $t\bar{t}$ production, which is predominantly gluon-gluon initiated (see Fig. 5.7a). The branching ratio $B(t \rightarrow Wb)$ is almost 100%, and leptonic decays of the W bosons then provide a similar final state to the signal. The emission of extra jets from this basic process must also be considered.

Additional background comes from WW production in association with two or more jets. This can happen via both QCD processes, where colour is exchanged by the initial state partons (see Fig. 5.7b), and EW processes, where the initial state quarks are scattered by electroweak boson exchange (see Fig. 5.7c). Whilst the production cross-section for EW processes is considerably smaller than for QCD processes it should be remembered that the EW WW background includes graphs that are kinematically very similar to the signal, such as four point vertices (see Fig. 5.7d), and are thus hard to suppress with cuts.

Finally $\tau^+\tau^-$ production, from $Z/\gamma^* \rightarrow \tau\tau$, in association with two or more jets is

considered; leptonic decays of the taus to electrons or muons can be misidentified as leptonic W decays. Again, both QCD (see Fig. 5.7e) and EW (see Fig. 5.7f) processes are considered.

Background for $ee/\mu\mu$ channel only

Backgrounds that need only be considered for the $ee/\mu\mu$ channel are those where an e^+e^- or $\mu^+\mu^-$ pair is produced in association with two or more jets. The dominant process is $Z/\gamma^* \to e^+e^-/\mu^+\mu^-$ in association with two or more jets (see Fig. 5.7g), which has a large cross-section at the LHC. Additionally ZZ processes are considered, where one Z decays to an $e^+e^-/\mu^+\mu^-$ pair and the other hadronically to give jets, or where one Z again decays to an $e^+e^-/\mu^+\mu^-$ pair, and the other to neutrinos, with two jets coming from additional radiation. Finally, a similar process

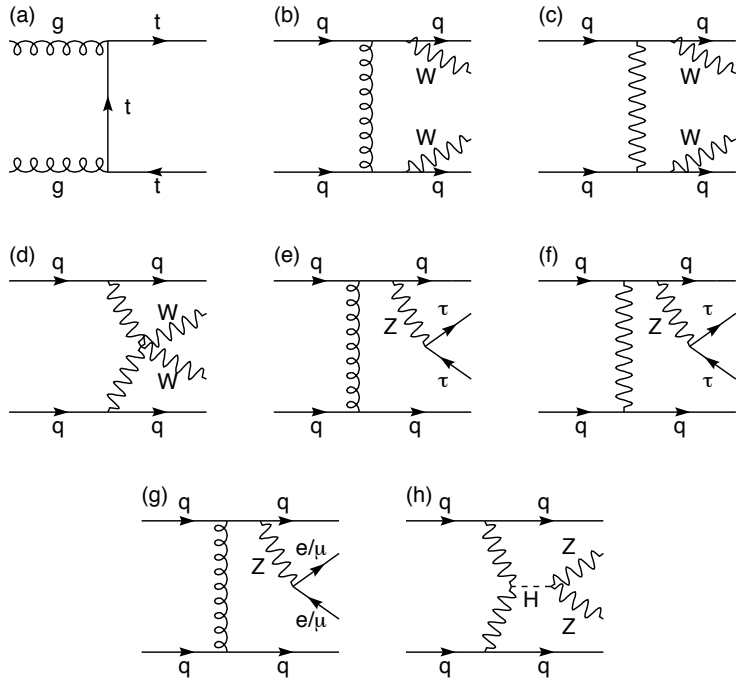

Figure 5.7: Feynman diagrams for background processes; (a) $t\bar{t}$ production, (b) QCD $WW + jets$ (c) EW $WW + jets$ (d) EW $WW + jets$; 4 point vertex (e) QCD $\tau\tau + jets$ (f) EW $\tau\tau + jets$ (g) $Z \to ee/\mu\mu$ (h) $H \to ZZ$.

to that above is included, but where the ZZ comes from the decay of a SM Higgs boson $H \to ZZ$ produced by either gg fusion or weak boson fusion (see Fig. 5.7h).

Potential sources of background not considered

There are other processes that may contribute to the overall background but which are not included in the analysis. Foremost, $b\bar{b}$ production has a huge cross-section at the LHC, or order 500 μb, and the generation of many hundreds of millions of events would be needed to investigate this background properly. Semi-leptonic decays of b-quarks tend to produce very soft leptons that are almost collinear with the final state quark. It is expected that since the leptons are required to be isolated and a minimum transverse momentum cut is applied $b\bar{b}$ processes will not provide a significant contribution to the total background. Furthermore, a statistical study of the $b\bar{b}$ background found it to have a cross-section of order 1 fb for two isolated, high-p_T leptons before other cuts [84]. This is much smaller than the signal cross-section.

Additionally, the decay of W bosons to electrons or muons via an intermediate tau has not been considered, for example $W^+ \to \tau^+\nu_\tau \to e^+\nu_e\overline{\nu}_\tau\nu_\tau$. This decay mode is suppressed compared to $W^+ \to e^+\nu_e$ by the additional branching ratio involved, and also the final state electron is considerably softer due to the additional neutrinos in the final state. Therefore by requiring leptons with reasonable transverse momentum the additional contribution from this should be small.

5.5 Simulation Tools

For the analysis presented in the following chapter simulation of both signal and background processes is performed using the parton shower based Monte Carlo event generators PYTHIA [82] and HERWIG [92, 93]. These differ from parton level simulations (previously used to study weak boson fusion processes) in that the

whole structure of the event is described, including the hadronisation of partons into physical particles which can then be passed through a detector model. In this way a better representation of the performance of the ATLAS detector can be obtained. The combination of event generation with a parton shower Monte Carlo followed by a fast detector simulation is henceforth referred to as "particle level simulation".

A brief summary of the main features of parton level simulations, parton shower Monte Carlo generators and the ATLFAST [94] fast detector model will now be presented.

5.5.1 Parton level simulations

Parton level (or matrix element) simulations are typically used for studying multi-parton final states. A process is calculated at a certain order, for example $t\bar{t} + 2$ additional jets, by generating a phase space point and summing over all possible Feynman graphs for the process. The final state partons are then assumed to lead to observable jets in the detector and acceptance cuts can be applied directly to the partons. The limitations of parton level simulation are that there is no hadronisation of the final state partons therefore it is not possible to use a detector simulation. There is also no treatment of additional physics in the event, for example the emission of soft radiation or the underlying event.

5.5.2 Parton shower Monte Carlo event generators

In a parton shower Monte Carlo event generation starts with the hardest interaction at leading order, typically a $2 \rightarrow 2$ process. This gives the basic structure of the event. Additional partons are then produced through the evolution of the initial and final state partons from the hard process via parton showers. For parton showers from the outgoing partons (final state radiation or FSR) the partons are evolved downwards from the scale of the hard process Q^2_{max} with the branching of partons via $1 \rightarrow 2$ splittings, such as $g \rightarrow q\overline{q}$ and $q \rightarrow qg$. The evolution is halted at a

lower scale Q_0. Parton showers from the incoming partons (initial state radiation or ISR) are treated in reverse, with the partons being evolved backwards from the hard process to the interacting parton in the proton.

After parton shower evolution is halted the partons are hadronised into physical hadrons. Different hadronisation models are used in PYTHIA and HERWIG. In PYTHIA a string fragmentation model is used. A quark and anti-quark are connected via a colour string and as they move further apart the energy stored in the string increases until it is energetically favourable to split the string by the creation of a $q\overline{q}$ pair. Further splits in the string are allowed until a cut-off where the $q\overline{q}$ pairs are converted into physical hadrons. Unstable particles are then allowed to decay. In HERWIG a cluster model is used. Outgoing gluons are converted into light $q\overline{q}$ pairs, and each quark is then linked to an anti-quark via a colour line to form colour singlet clusters. The clusters then decay into physical hadrons.

Parton shower Monte Carlos also take into account the partons in the proton that are not involved in the hard process. These are known as beam remnants; for instance if a u-quark from a proton is involved in an interaction with a parton from the other proton it would leave behind a ud di-quark, colour connected to the hard interaction. Again, different models are used in PYTHIA and HERWIG. In HERWIG the two beam remnants are cut off from the main interaction and undergo a soft collision. In PYTHIA, on the other hand, the beam remnants remain colour connected to the hard interaction and are involved in the hadronisation process.

5.5.3 The ATLFAST fast detector simulation

The addition of a detector model is essential to account for the efficiency and accuracy with which the ATLAS detector will be able to find various types of particles and reconstruct jets. Full simulation of the detector, where particles are individually transported through all of the various subsystems, are extremely time consuming and therefore impractical for performing rapid analyses of channels or generating

large numbers of events. Therefore a fast detector simulation is used, which parameterises detector effects to reproduce the expected performance. This involves the selection of isolated leptons and photons, the reconstruction and labelling of jets and the calculation of missing transverse momentum. The ATLFAST fast detector model used here will be briefly described below; further information can be found in Ref. [94].

The first stage of the ATLFAST model is to find calorimetric clusters. The transverse energies of all undecayed particles (except muons and neutrinos) are summed into calorimeter cells with granularity $\eta \times \phi$ of 0.1×0.1 for $|\eta| < 3$ and 0.2×0.2 for $3 < |\eta| < 5$. The effect of a solenoidal magnetic field of 2 Tesla is parameterised for charged particles with $p_T > 0.5$ GeV. Any calorimeter cell with $E_T > 1.5$ GeV is taken as a possible initiator, and all cells within a cone of radius $\Delta R = 0.4$ from the initiator are summed. This is then defined as a reconstructed cluster if the summed transverse energy is greater than 10 GeV. The coordinates of the cluster are determined from the weighted average of all calorimeter cells in the cluster.

Next, isolated photons, electrons and muons are identified. The event record is scanned for these particles, which then have their momenta smeared to account for expected detector performance. For electrons and photons with transverse momenta and pseudorapidity within the coverage of the detector ($|\eta| < 2.5$; $p_T > 10$ GeV for photons, $p_T > 20$ GeV for electrons) the associated calorimetric cluster is found, and subjected to isolation criteria in terms of minimum distance from other clusters and maximum energy deposition in a cone around the particle. For muons with $|\eta| < 2.5$ and $p_T > 6$ GeV similar isolation criteria are applied. No efficiencies for photon, electron or muon identification are applied by ATLFAST and therefore must be added by the user if needed.

For jet reconstruction all clusters not identified with isolated electrons or photons are smeared with a Gaussian energy resolution. The energies of non-isolated muons which fall inside these clusters are added to the smeared cluster energy, and if the resulting proto-jet has $E_T > 15$ GeV it is labelled as a reconstructed jet. Jet

reconstruction efficiencies are included in ATLFAST, and have been tested against full simulation for both low p_T jets, for a central jet veto, and forward jet tagging [17, Ch. 9]. Comparisons between full simulation and ATLFAST for a central jet veto were made for both a signal process of a weak boson fusion produced heavy Higgs boson, and a background process of $t\bar{t} + jets$. The probability of vetoing events by finding a jet in the central region was tested as a function of the p_T threshold for veto candidates. At low luminosity the veto probability for the heavy Higgs process was $\approx 5\%$ greater with ATLFAST than with full simulation, and for the $t\bar{t} + jets$ process the agreement between full simulation and ATLFAST was very good. Forward jet tagging was tested as a function of jet pseudorapidity for a weak boson fusion produced heavy Higgs boson. A good agreement between ATLFAST and full simulation was found for pseudorapidities up to $|\eta| = 4.0$. Beyond this transverse development of the shower leads to energy losses in the full simulation not fully accounted for by ATLFAST; the ATLFAST efficiency is $5 - 10\%$ higher than that from full simulation in this far-forward region.

Finally the missing transverse energy in the event is calculated. The transverse momenta of all identified isolated photons, electron, and muons, all reconstructed jets, all clusters not accepted as jets and all remaining non-isolated muons are summed, along with cells not included into clusters, which are first smeared with a Gaussian energy resolution. The missing transverse energy is then given by $E_T^{miss} = E_T^{obs}$, and the components of this by $p_x^{miss} = -p_x^{obs}$ and $p_y^{miss} = -p_y^{obs}$.

5.5.4 Event generation

Samples of events have been generated for the signal and background processes using both the PYTHIA and HERWIG event generators with ATLFAST to perform fast detector simulation. PYTHIA events are generated with version 6.136, and include the effects of ISR, FSR, hadronisation and multiple interactions. HERWIG event are generated with version 6.201, and include ISR, FSR and hadronisation. The CTEQ5L [95] set of proton structure functions are used for both PYTHIA and

HERWIG event generation.

All signal and QCD background processes were generated with the internal PYTHIA or HERWIG functions. Signal events are generated with a leading order hard process, $qq \to qqH$, and additional hadronic radiation is provided by parton showers. The decay of the Higgs boson is forced $H \to WW$, and the W bosons are forced to decay leptonically into electrons and muons. The $t\bar{t} + jets$ background is generated with a hard process of a $t\bar{t}$ final state, additional hadronic radiation being provided by parton showers. The decays $t \to Wb$ and $W \to e/\mu$ are forced. The QCD $WW + jets$ background is generated with a hard process of $q\bar{q} \to W^+W^-$. Jets in the final state are generated through parton showers. The QCD $\tau\tau + jets$ background is generated with a hard process of either $gq \to q(Z/\gamma^*)$ or $q\bar{q} \to g(Z/\gamma^*)$ with additional hadronic radiation provided by parton showers. The decays $Z\gamma^* \to \tau\tau$ and $\tau \to e/\mu$ are forced. The $Z/\gamma^* \to ee/\mu\mu$ background is generated with a similar hard process. The ZZ background has a hard process of $q\bar{q} \to ZZ$ with jets in the final state generated by parton showers. All decays of the Z bosons are allowed. Finally, the $H \to ZZ$ background is generated with Higgs produced by either $gg \to H$ or $qq \to qqH$, with the decay $H \to ZZ$ forced. All decays of the Z bosons are allowed.

As the EW backgrounds are not presently included in either PYTHIA or HERWIG these backgrounds are generated by an interface of matrix element generation code to PYTHIA [96]. The matrix element code generated $WWjj$ or $\tau\tau jj$ hard processes which were then transported to PYTHIA which performed ISR, FSR, hadronisation and multiple interactions. PYTHIA unweights the events generated by the matrix element code using a hit-or-miss method so that only hard processes with a high weight relative to the maximum weight for the process are chosen. This was the cause of some problems due to the weight distributions having long tails towards high weights, particularly for the $WWjj$ process, leading to impractically long event generation times. In order to speed up event generation the maximum weight used by PYTHIA for unweighting was set to a value below the actual maximum of the weight

distribution. Events with a weight greater than the maximum were treated as having a weight equal to the maximum, thereby still being selected by PYTHIA. The total cross-section for the process as calculated by PYTHIA does not include the tail of the distribution and is consequently lower than the actual cross-section. There are two ways that these events can then be used. First, all events with weight greater than the maximum used for unweighting can be assigned a weighting factor equal to the ratio of the event weight to the maximum. Then during analysis the contributions of these events are multiplied by the weighting factor, so that an event with a weighting factor of three is equivalent to three identical events of unit weighting factor. Events with weight less than the maximum are assigned a unit weighting factor. In this way the total cross-section provided by PYTHIA is corrected to the actual cross-section due to the extra contribution of events with weighting factors greater than one. However, problems are caused during analysis when events with large weighting factors occur in kinematic regions near to acceptance cut values. Small changes in the acceptance cuts can then lead to large changes in cross-section thus skewing the results. The second way of treating these events is to calculate the total cross-section of the process independently of PYTHIA, taking into account the whole weight distribution including the tail. This therefore gives the correct total cross-section. All PYTHIA events can then be treated equally with no need for event weighting during analysis. It is this latter approach that is used for all event generation of the EW background processes.

Summaries of all signal and background events generated are shown in Tables 5.1 and 5.2. For the background processes marked with * events were generated by Markus Klute on behalf of the ATLAS Higgs Working Group. All other events generated by the author.

m_H	PYTHIA		HERWIG	
(GeV)	N_{ev}	σ (fb)	N_{ev}	σ (fb)
110	10^5	7.1	-	-
115	10^5	13.0	-	-
120	10^5	21.5	10^5	95.5
130	10^5	46.0	-	-
140	10^6	75.9	10^5	69.5
150	10^5	104.1	-	-
160	10^6	133.3	10^5	119.7
170	10^5	134.3	-	-
180	10^5	121.1	10^5	109.1
190	10^5	21.5	-	-
200	10^6	84.7	10^5	76.9

Table 5.1: Summary of all signal events generated.

process	generator	p_T (GeV)	σ (pb)	N_{ev}	
$t\bar{t} + jets$	PYTHIA		24.44	10^7	
$t\bar{t} + jets$	HERWIG		17.91	2.10^6	
QCD $WW + jets$	PYTHIA		7.40	4.10^6	*
EW $WW + jets$	PYTHIA		0.078	5.10^5	*
QCD $\tau\tau + jets$	PYTHIA	$10 - 30$	171	4.10^6	*
QCD $\tau\tau + jets$	PYTHIA	> 30	44.8	4.10^6	*
EW $\tau\tau + jets$	PYTHIA		0.171	10^6	*
$Z/\gamma^* \to ee/\mu\mu$	PYTHIA	$10 - 30$	2763	12.10^6	
$Z/\gamma^* \to ee/\mu\mu$	PYTHIA	> 30	725	2.10^7	
ZZ	PYTHIA		37.8	10^6	
$H \to ZZ$	PYTHIA		$0.26 - 2.5$	10^5 each m_H	

Table 5.2: Summary of all background events generated. p_T is the cut on Z or γ^* transverse momentum applied during generation. Events marked * generated by Markus Klute on behalf of the ATLAS Higgs Working Group.

Chapter 6

Analysis of WBF Higgs boson discovery channel

In order to assess the discovery potential of the weak boson fusion $H \to WW^{(*)} \to l^+l^-p_T^{miss}$ channel for an intermediate mass Higgs boson particle level analysis of the signal and main physics backgrounds is now performed. First, the $H \to WW^{(*)} \to e^{\pm}\mu^{\mp}p_T^{miss}$ channel is investigated, starting from the analysis defined in Ref. [18] and then improving the effectiveness of the acceptance cuts with different jet-tagging algorithms and an optimisation of the cut values. Next, the $H \to WW^{(*)} \to (e^+e^-/\mu^+\mu^-)p_T^{miss}$ channel is studied, initially using the same analysis as for the $e\mu$ channel then developing extra acceptance cuts to reduce the additional background processes that must be considered. The combined discovery potential of the two channels is calculated, including the effect of systematic uncertainties on signal and background rates, comparison with other channels and determination of the Higgs boson mass. Finally, the $e\mu$ and $ee/\mu\mu$ channels are investigated in the context of a light Higgs boson with mass similar to that suggested by the LEP results.

6.1 The $H \to WW^{(*)} \to e^{\pm}\mu^{\mp}p_T^{miss}$ channel

The $H \to WW^{(*)} \to e^{\pm}\mu^{\mp}p_T^{miss}$ channel has the advantage of different flavour leptons in the final state, so that backgrounds from pair production processes such as $Z \to e^+e^-$ need not be considered. This channel was studied with a parton level analysis in Ref. [18] and was found to be a promising discovery channel for an intermediate mass Higgs boson with only low luminosity. Therefore the first stage is to repeat the analysis of Ref. [18] with events generated using the PYTHIA Monte Carlo and the ATLFAST fast detector simulation so that direct comparisons can be made between the results of particle level and parton level simulations. Optimisation of the acceptance cuts and jet tagging algorithm is then performed in order to maximise the discovery potential before the final results for this channel are presented.

6.1.1 Comparison with parton level study

In Ref. [18] the $H \to WW^{(*)} \to e^{\pm}\mu^{\mp}p_T^{miss}$ channel was studied via a parton level analysis. Cross-sections were calculated for fixed orders of α_s from the full tree level matrix elements. The signal process was generated at leading order, Hjj, and the EW and QCD $WWjj$ and $\tau\tau jj$ background processes were both generated at the two jet level. The $t\bar{t}+jets$ background was considered at $t\bar{t}$, $t\bar{t}j$ and $t\bar{t}jj$ levels. Final state partons were assumed to represent physical jets in the detector. A basic acceptance for the signal was applied, requiring the observation of one electron, one muon and two (or more) jets in the detector. Forward jet tagging criteria were then applied. For all but the $t\bar{t}+jets$ backgrounds the tagging jets were simply the only two jets in the final state. For the $t\bar{t}+jets$ backgrounds different tagging jet combinations were chosen to identify different regions of phase space. The $t\bar{t}$ process had the tagging jets taken as the two b-jets from the decay of the t-quarks, the $t\bar{t}j$ process had one of the b-jets and the other jet as the tags, and the $t\bar{t}jj$ process had the two other (non-b) jets as the tags. Next, a b-jet veto was applied to the

$t\bar{t}+jets$ backgrounds; the $t\bar{t}j$ and $t\bar{t}jj$ processes events were vetoed where a b-jet not used as a tag was found between the two tags. A set of cuts on the angular separation of the final state leptons was then applied to signal and background processes, followed by reconstruction of the $\tau\tau$ system to reduce the contribution from the $\tau\tau+jets$ backgrounds. A minijet veto for events to be rejected due to the presence of additional hadronic radiation in the central region was applied by multiplying the signal and background rates by a factor representing the probability of events to survive the veto. This factor is dependent on the process; a value of 0.89 was used for the signal, 0.75 for the EW backgrounds and 0.29 for the QCD and $t\bar{t}+jets$ background. Finally, an efficiency for reconstructing two forward tagging jets was applied (0.86 per tag). It was found that a 5σ signal could be observed for the Higgs boson mass range $m_H = 140-190$ GeV with an integrated luminosity of only 5 fb^{-1}.

For the particle level study performed here both signal and background events are generated with the PYTHIA Monte Carlo in conjunction with the ATLFAST fast detector simulation. The use of initial and final state radiation means that these events are generated with n jets in the final state, not to a fixed order like in the parton level approach. In order to make a comparison with the original parton level study an analysis is applied which is as similar to that used in Ref. [18] as is possible considering the differences in the two different simulation techniques.

The first stage in the analysis is to define a basic acceptance for the signal. The final state of the signal at leading order contains one electron and one muon from the decay of the W bosons, plus two forward tagging jets from the scattered quarks. These are required to be observed in the detector and trigger the experiment, therefore one electron, one muon and two or more jets (since additional jets may be present in the signal process due to additional hadronic radiation) must be found which satisfy

$$\begin{aligned} p_{T,j} &\geq 20.0 \text{ GeV} \quad ; \quad \eta_j \leq 5.0 \\ p_{T,l} &\geq 20.0 \text{ GeV} \quad ; \quad \eta_l \leq 2.5\,. \end{aligned} \tag{6.1}$$

Furthermore, the jets are required to be well separated in the lego plot, as are the

	signal	background					
		$t\bar{t}+jets$	$WW+jets$		$\tau\tau+jets$		Total
			EW	QCD	EW	QCD	
Basic Acceptance	18.7	3740	9.00	16.2	2.85	198	3970
+ Forward Tagging	9.09	113	4.51	1.18	0.71	9.29	129
+ Central Jet Veto	7.98	20.0	4.25	0.91	0.68	6.92	32.8
+ Lepton Angular	4.88	1.59	0.32	0.04	0.37	0.95	3.27
+ Real τ rejection	4.64	1.47	0.28	0.03	0.05	0.10	1.94
+ Lepton ID efficiency	3.76	1.19	0.23	0.03	0.04	0.08	1.57

Table 6.1: Signal (for $m_H = 160$ GeV) and background rates in fb for $e\mu$ channel with acceptance cuts outlined in Eqns. (6.1) to (6.6).

leptons from the jets. The jet-jet separation ΔR_{jj} and jet-lepton separation ΔR_{jl} requirements are (where $\Delta R_{12} = \sqrt{(\eta_1 - \eta_2)^2 + (\phi_1 - \phi_2)^2}$)

$$\Delta R_{jj} \geq 0.7\,;\ \Delta R_{lj} \geq 0.7\,. \tag{6.2}$$

Whilst these separation criteria are not strictly required for a particle level simulation, since lepton and jet separation criteria are included in the detector model, they are still applied for the purposes of comparison with the parton level results, where they are used in lieu of a detector model. Equations (6.1) and (6.2) are defined as the *Basic Acceptance cuts*, and the signal and background rates found after their application are shown in the first line of Table 6.1. The dominant background process by far is $t\bar{t}+jets$ production, which accounts for almost 95% of the total background. The signal rate is negligible compared with that of the background at this stage, the signal to background ratio for $m_H = 160$ GeV being $\approx 1/212$.

The next stage is to define the tagging jets. Here the particle level analysis must differ from the parton level analysis since in the final state more than two jets may be present in both signal and background processes due to additional hadronic radiation. An algorithm must therefore be defined to select the tagging jets. As a representative algorithm the tagging jets are chosen as the jet with highest p_T, which will almost always be from the hard scattering process, and the jet furthest from this

in pseudorapidity. It should be noted that whilst the selection of tagging jets does affect the application of the following acceptance cuts for the background processes the signal is largely independent of the tagging algorithm since in the majority of events only two jets are found in the final state. The effect of different tagging algorithms is investigated in Section 6.1.2. As explained in Section 5.4.1 the tagging jets for the signal are expected to be further forward than those from the dominant QCD background processes. Consequently the separation of the tagging jets in pseudorapidity $\Delta\eta_{tags}$ should be greater for the signal than the QCD backgrounds. This is shown in Fig. 6.1a; the signal shows a clear tendency for relatively widely separated tags compared to the background, which at this stage is dominated by the $t\bar{t}+jets$ process. A cut is therefore applied on the minimum separation of the tagging jets. Additionally, the tags are required to be in opposite pseudorapidity hemispheres, one backwards and one forwards, and the charged leptons are required to be found in the central region, between and well separated from the two tags in pseudorapidity. The *Forward Tagging cuts* are thus defined as

$$\Delta\eta_{tags} = |\eta_{tag1} - \eta_{tag2}| \geq 4.4\,,$$

$$\eta_{tag1}.\eta_{tag2} < 0.0\,,$$

$$\eta_{tag}^{min} + 0.7 \leq \eta_{e,\mu} \leq \eta_{tag}^{max} - 0.7\,. \tag{6.3}$$

The signal and backgrounds rates after application of the Forward Tagging cuts are shown in the second line of Table 6.1. Immediately apparent is the reduction of the QCD backgrounds; more than 90% of $t\bar{t}+jets$, QCD $WW+jets$ and QCD $\tau\tau+jets$ events are rejected by these cuts. However, the signal is only reduced by a factor of 2. The $t\bar{t}+jets$ process still dominates the background, and the signal to background ratio is $\approx 1/14$ for $m_H = 160$ GeV.

A central jet veto is applied to all remaining events; as explained in Section 5.4.1 more hadronic radiation is expected in the central region for the QCD backgrounds than for the signal. Here the particle level analysis must again differ from the parton level analysis, where at this stage only an explicit veto for $t\bar{t}+jets$ events where one

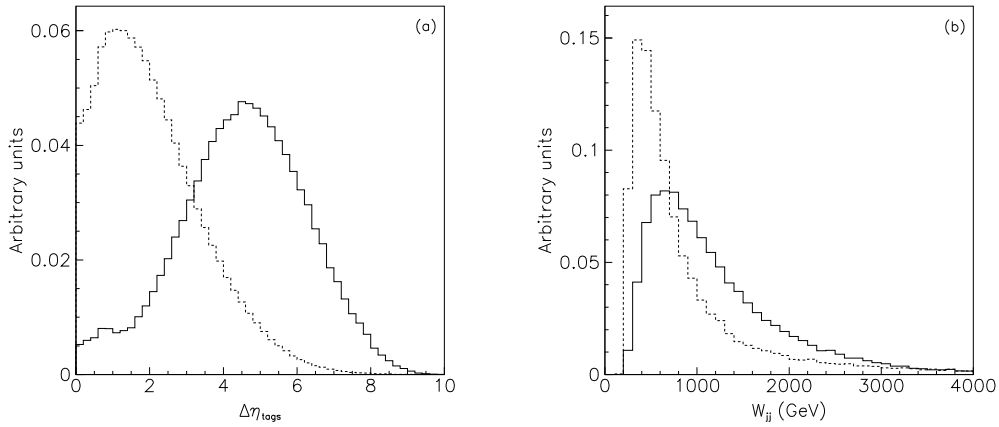

Figure 6.1: (a) Separation of tagging jets and (b) tagging jet invariant mass for signal ($m_H = 160$ GeV, solid line) and combined backgrounds (dashed line). Histograms normalised to 1.

or more of the b-jets from the decay of the top quarks were found between the two tagging jets was applied. A minijet veto on additional hadronic activity between the tagging jets was applied at a later stage in the analysis. In the particle level analysis these two vetos are combined into a single *Central Jet Veto*, where an event is rejected if one or more jets are found that satisfy the conditions

$$\eta_{tag}^{min} \geq \eta_j \geq \eta_{tag}^{max} \; ; \; p_{T,j} \geq 20 \text{ GeV} \, . \tag{6.4}$$

The signal and background rates after application of the Central Jet Veto are shown in the third line of Table 6.1. The rate from the $t\bar{t} + jets$ background has been reduced by more than 80%, and the QCD $WW + jets$ and QCD $\tau\tau + jets$ backgrounds have both been reduced by approximately 25%. In contrast the signal rate is reduced by little more than 10%. The $t\bar{t} + jets$ process no longer dominates the background with significant contributions coming from the EW $WW + jets$ and QCD $\tau\tau + jets$ processes.

The relatively wide separation of the tagging jets in the signal also leads to a large tagging jet invariant mass W_{jj} compared with the QCD backgrounds (see Fig. 6.1b). Therefore a cut on the minimum tagging jet invariant mass is applied. The dif-

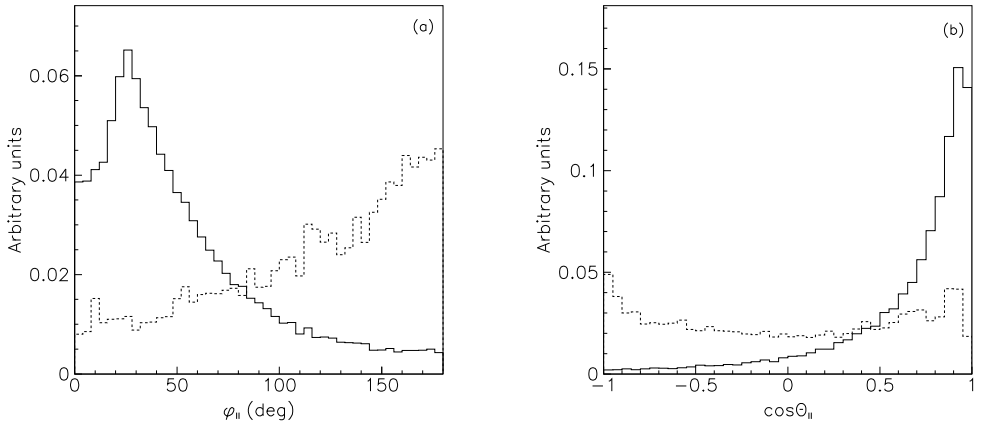

Figure 6.2: (a) Azimuthal opening angle of leptons and (b) cosine of polar opening angle between leptons for signal (with $m_H = 160$ GeV, solid line) and combined backgrounds (dashed line). Histograms normalised to 1.

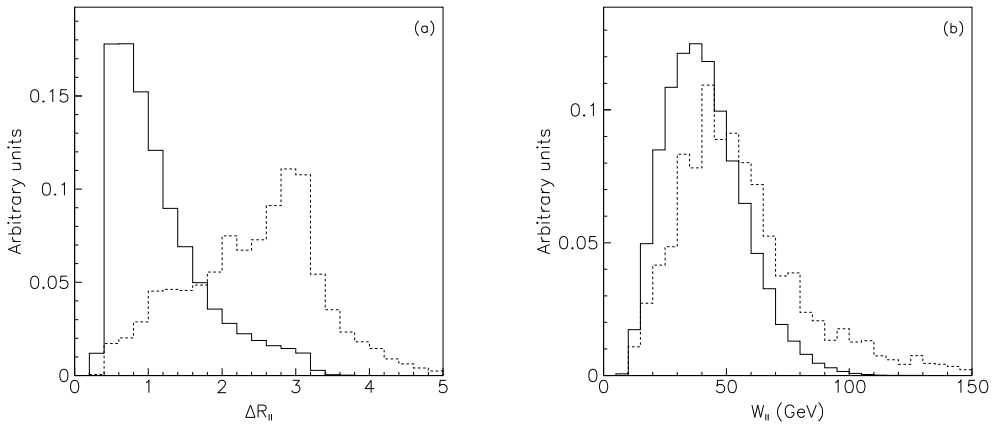

Figure 6.3: (a) Separation of leptons in the lego plot and (b) di-lepton invariant mass for signal (with $m_H = 160$ GeV, solid line) and combined backgrounds (dashed line). Histograms normalised to 1.

ferences between the angular distributions of the charged leptons for signal and background processes due to the anti-correlated W spins of the signal are exploited through a series of cuts on the separation of the charged leptons. Distributions of signal and background events for the azimuthal opening angle of the leptons ϕ_{ll}, the cosine of the polar opening angle $\cos\theta_{ll}$ and the separation of the leptons in the lego plot ΔR_{ll} are shown in Figs. 6.2a, 6.2b and 6.3a respectively. The tendency for leptons in background events to have a much wider separation than those in signal events is evident from all three of these plots. Cuts are also applied on the minimum invariant mass of the di-lepton system W_{ll} boson (see Fig. 6.3b) and the maximum p_T of the leptons. The *Lepton Angular cuts* are therefore defined as

$$\begin{aligned} W_{jj} \geq 650 \text{ GeV} \quad &; \quad \phi_{ll} \leq 105^\circ \\ \cos\theta_{ll} \geq 0.2 \quad &; \quad \Delta R_{ll} \leq 2.2 \\ W_{ll} \leq 110 \text{ GeV} \quad &; \quad p_{T,l} \leq 120 \text{ GeV}\,. \end{aligned} \tag{6.5}$$

The rates for signal and backgrounds after the application of the Lepton Angular cuts are shown in the fourth line of Table 6.1. These cuts have reduced the rates for all of the background processes by large amounts. Especially significant is the reduction of the contribution from the EW $WW + jets$ background process, which had not been greatly affected by any of the preceding cuts due to its kinematic similarity to the signal. Overall the background has been reduced to a rate lower than that of the signal, with the signal to background ratio now being $\approx 1.5/1$ for $m_H = 160$ GeV.

At this stage of the analysis a significant proportion of the total background comes from the two $\tau\tau + jets$ processes. A reconstruction of the $\tau\tau$ system from the observed decay products allows their contribution to be reduced [18, 85, 86, 97]. This cannot be done exactly, since several neutrinos are involved in the final state. However, assuming the collinear approximation, where all decay products inherit the same directional vector as that of the parent particle, the τ momenta can be reconstructed from the observed lepton momenta and the momentum vector of the missing transverse momentum. The energy of the charged lepton from each τ decay

is given by $E_{l_{1(2)}} = x(\tau_{1(2)})E_{\tau_{1(2)}}$ where $x(\tau_{1(2)})$ is the fraction of the energy of $\tau_{1(2)}$ taken by lepton $l_{1(2)}$. Equating the momentum vectors gives

$$\overrightarrow{p}^{miss} = \left(\frac{1}{x(\tau_1)} - 1\right)\overrightarrow{p}_{l_1} + \left(\frac{1}{x(\tau_2)} - 1\right)\overrightarrow{p}_{l_2}\,.$$

This can be solved for p_x^{miss} and p_y^{miss} to find $x(\tau_1)$ and $x(\tau_2)$ and hence reconstruct the momentum of each τ. Where the two charged leptons in the final state come from the decay of a real $\tau\tau$ system a physical solution should be obtained, with $0 < x(\tau_1), x(\tau_2) < 1$, shown in Fig. 6.4a. However for the signal (and the other background processes) this reconstruction is not valid and the tendency is instead for $x(\tau_1) < 0$ or $x(\tau_2) < 0$, shown in Fig. 6.4b. Therefore by vetoing events where both x_{τ_1} and x_{τ_2} are greater than zero a large proportion of the $\tau\tau$ backgrounds should be eliminated whilst leaving the signal relatively untouched. Additionally, once the τ momenta have been reconstructed the invariant mass of the $\tau\tau$ system $W_{\tau\tau}$ can be calculated. Real $\tau\tau$ pairs are produced predominantly via $Z \to \tau\tau$, therefore the invariant mass of the $\tau\tau$ system should fall around the Z mass; applying a cut rejecting events where $W_{\tau\tau}$ is near the Z mass will further reduce the $\tau\tau + jets$ backgrounds. The *Real τ rejection* is therefore defined as vetoing any event where

$$x_{\tau_1}, x_{\tau_2} \geq 0.0 \;\;;\;\; M_Z - 25 \geq W_{\tau\tau} \geq M_Z + 25 \text{ GeV}\,. \tag{6.6}$$

The rates for the signal and backgrounds after the application of the Real τ rejection are shown in the fifth line of Table 6.1. The EW and QCD $\tau\tau + jets$ background processes have both been reduced by a large amount, factors of 7 and 10 respectively, so that their contribution to the total background is now only $\approx 5\%$. In contrast the signal rate is only reduced by $\approx 5\%$. The signal to background ratio for $m_H = 160$ GeV is now $\approx 2.4/1$.

The final stage of the parton level analysis in Ref. [18] was the application of the minijet veto and the forward tagging efficiency. These are not applied for the particle level simulation since the minijet veto is included in the central jet veto and the tagging efficiency in the ATLFAST detector simulation.

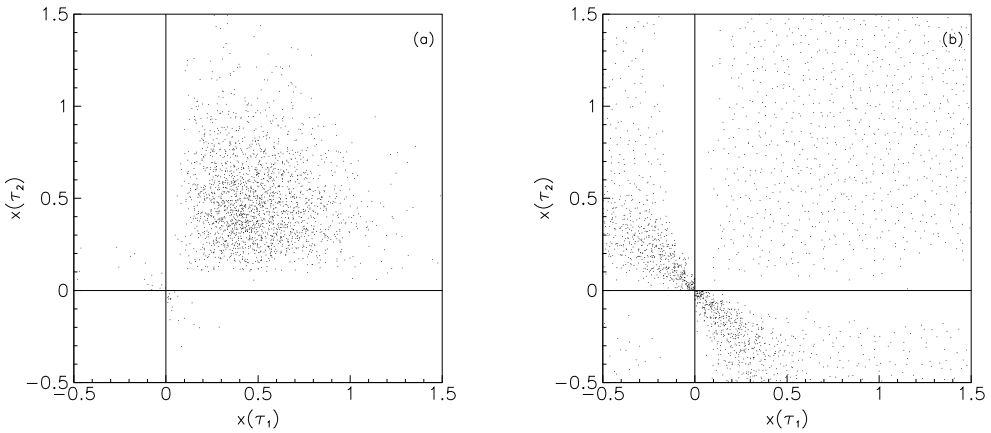

Figure 6.4: Fraction of tau 1 momentum taken by lepton 1 versus fraction of tau 2 momentum taken by lepton 2 for (a) $\tau\tau + jets$ background and (b) signal (with $m_H = 160$ GeV).

A position has now been reached where the two different analyses can be compared. Signal and background rates after the application of all acceptance cuts are shown in Table 6.2 for the particle level analysis performed here and the parton level analysis of Ref. [18, Table I]. It is clear that the particle level analysis presents a more pessimistic view, with a smaller signal rate and a larger background rate. This leads to a signal to background ratio of only $\approx 2.4/1$ for the particle level analysis, compared with $\approx 4.6/1$ for the parton level analysis. Whilst this is not entirely unexpected, since parton level analyses do tend to give optimistic results, it is still a large difference and requires further examination.

	signal	background					
		$t\bar{t} + jets$	$WW + jets$		$\tau\tau + jets$		Total
			EW	QCD	EW	QCD	
This analysis	4.64	1.47	0.28	0.03	0.05	0.10	1.94
Ref. [18, Table I]	7.5	1.09	0.25	0.11	0.05	0.13	1.63

Table 6.2: Comparison between particle level analysis and parton level analysis of Ref. [18, Table I] for signal (with $m_H = 160$ GeV) and backgrounds. Rates in fb.

Considering the background first, the dominant $t\bar{t} + jets$ process has a considerably larger rate from the particle level simulation and is responsible for the majority of the overall increase in background. There are several possible reasons for this. Firstly, the approach of the actual event generation between the two analyses is quite different. For the parton level simulation events were generated at fixed orders of $t\bar{t}$, $t\bar{t}j$ and $t\bar{t}jj$, whereas for the particle level simulation the event generation was started from the leading order $t\bar{t}$ process then relied upon parton showers to generate additional jets in the final state. Secondly, in the parton level simulation the final state partons from the hard process were assumed to result in physical jets in the detector, with only a nominal jet reconstruction efficiency applied. In the particle level simulation hadronisation and detector simulation is applied thus giving a more realistic model of jet finding. Finally, an important cut for the $t\bar{t} + jets$ background is the central jet veto. Here the parton and particle level simulations differ considerably. In the particle level analysis a combined central jet veto on any additional hadronic radiation in the central region was applied. For the parton level analysis this was split into a b-jet veto and a minijet veto that was applied only as a nominal survival probability factor. This difference could be expected to be responsible for some of the variation in rate between the two analyses.

Of the other backgrounds, the two EW processes have very similar rates between the two different analyses. This is to be expected since the hard processes in the particle level simulation are generated with the same code as was used for the parton level simulation. The QCD $\tau\tau + jets$ background is also comparable, but the QCD $WW + jets$ background rate for the particle level simulation is considerably lower than for the parton level simulation. The hard process for the PYTHIA generation of this process gives only WW in the final state, relying upon parton showers to produce the two or more jets needed for the event to pass the basic acceptance cuts. In this instance it is possible that the parton shower approach is not a good approximation for generating the two hard jets required.

The most important difference between the particle level and parton level analyses,

Cuts	Ref. [18, Table I]	PYTHIA
Basic Acceptance		31.06
+ Forward Tagging	17.1	15.91
+ Central Jet Veto	17.1	15.91
+ Lepton Angular	11.8	10.82
+ Real τ rejection	11.4	10.41

Table 6.3: Signal rates for parton level simulation of Ref. [18, Table I] and parton level simulation generated with PYTHIA for successive levels of cuts. Rates in fb.

however, is for the signal, with the particle level simulation giving a considerably smaller rate. There are two possibilities for the origin of this difference; either the physics of the hard process is different between the PYTHIA simulation used here and the parton level simulation of Ref. [18], or the additional physics and detector model provided by the particle level simulation is responsible. To find out which of these is the most probable cause of the discrepancy further simulation is carried out using PYTHIA to generate the hard process only. No initial or final state radiation is added and no hadronisation performed, with partons assumed to represent physical jets in the detector. In this way PYTHIA can be used to produce a parton level simulation analogous to that of Ref. [18]. Events generated in this way are subject to the acceptance cuts outlined in Eqns. (6.1) to (6.6) and the results shown compared to the parton level simulation of Ref. [18] in Table 6.3. The rates found with the PYTHIA parton level analysis are comparable with those from Ref. [18] to within 10% at all stages of the analysis. Therefore it may be concluded that the majority of the differences in signal rate are due to the additional physics and the detector simulation of the particle level analysis.

Comparing the results for the PYTHIA particle level (Table 6.1) and parton level (Table 6.3) analyses for the signal process the rate after application of the Real τ rejection is more than twice as large for the parton level analysis. The majority of this difference is already apparent at the Basic Acceptance level of cuts. Simply by requiring one electron, one muon and two or more jets to be found in the detector

the signal rate for the particle level analysis is $\approx 40\%$ lower than that for the parton level analysis. This is predominantly due to problems with jet-finding, caused by both the additional physics included in the particle level simulation and the effect of the detector simulation. For instance, jets may be lost from the final state of the particle level simulation due to development outside of the 0.4 radius cone used; the loss of transverse momentum from the jet due to particles not being contained within the cone can lead to it having transverse momentum below the threshold for being observed [17, 94]. Alternatively, branchings of the outgoing partons from the hard process during parton showering can alter the properties of the jets in the final state. Further reduction of the rate for the particle level analysis relative to the parton level analysis occurs during the central jet veto, where particle level events may be rejected due to the emission of additional hadronic radiation into the central region.

To conclude this section the analysis presented in Eqns. (6.1) to (6.6) is applied to signal events for Higgs boson masses in the range $m_H = 120 - 200$ GeV. As a final stage of the analysis signal and background rates are multiplied by a *Lepton ID efficiency* of 0.9 per lepton (0.81 for finding two leptons), shown in the final line of Table 6.1. The signal and background rates and signal to background ratio after the application of all acceptance cuts are shown in Table 6.4. A signal to background

m_H (GeV)	120	130	140	150	160	170	180	190	200
S (fb)	0.30	0.75	1.52	2.39	3.76	3.95	3.47	2.52	2.05
B (fb)	1.57	1.57	1.57	1.57	1.57	1.57	1.57	1.57	1.57
S/B	0.19	0.48	0.97	1.52	2.39	2.51	2.20	1.60	1.30

Table 6.4: Signal and background rates in fb and signal to background ratios for $e\mu$ channel with $m_H = 120 - 200$ GeV.

ratio greater than 1/1 is achieved for the Higgs boson mass range $m_H = 150 - 200$ GeV.

The signal significance for integrated luminosities of 5, 10 and 30 fb^{-1} is shown in Fig. 6.5. For integrated luminosities of 5 and 10 fb^{-1} the number of signal and background events is relatively small so the signal significance is calculated using Poisson statistics as the probability for the background to fluctuate up to the level of the signal, expressed in the equivalent number of Gaussian standard deviations. With 30 fb^{-1} of data the number of signal and background events is sufficient that the Gaussian approximation may be used, and the signal significance is calculated as $S/\sqrt{B}$. With an integrated luminosity of 5 fb^{-1} a 5σ discovery can be claimed for the Higgs boson mass range $m_H = 160 - 170$ GeV. With 10 fb^{-1} this is increased to $m_H = 150 - 190$ GeV, and ultimately with the 30 fb^{-1} of data afforded by 3 years of low luminosity running the discovery range is $m_H = 140 - 200$ GeV, with the majority of this well above the 5σ level. These significances do not include a systematic uncertainty on the background rate, which will be discussed later.

Therefore compared with the parton level study in Ref. [18] the discovery potential for an intermediate mass Higgs boson with an integrated luminosity of 5 fb^{-1} is considerably less, with a 5σ discovery only available for $m_H = 160 - 170$ GeV at this low luminosity. However, with 30 fb^{-1} of data almost all of the intermediate mass

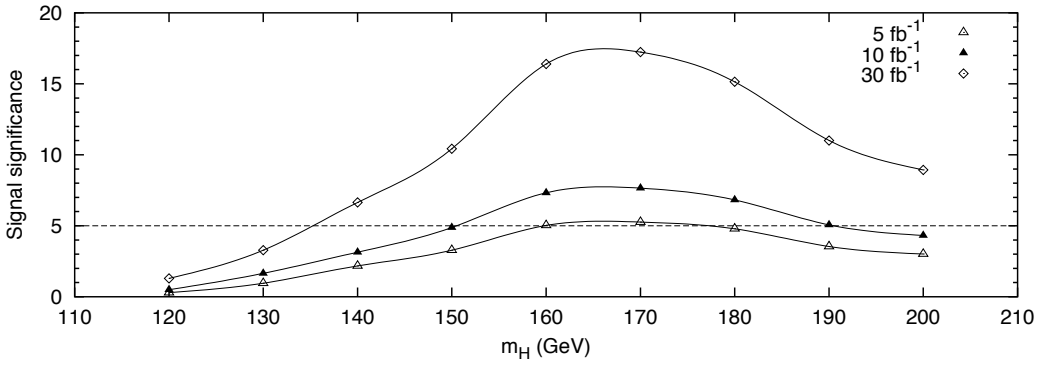

Figure 6.5: Signal significance as a function of Higgs mass for the $e\mu$ channel with 5, 10 and 30 fb^{-1} integrated luminosity.

region can be covered, with a discovery at the 5σ level available for $m_H = 140 - 200$ GeV.

6.1.2 Selection of tagging jets

Thus far the analysis has used tagging jets defined as the jet with the highest transverse momentum and the jet furthest away from the highest p_T jet in pseudorapidity (henceforth referred to as the $p_T - \eta$ tagging algorithm). The motivation for this combination is that the jet with highest p_T almost always comes from the hard scattering process, and the second tag is then chosen as the most separated jet so as to maximise the chance of events passing the Forward Tagging cuts. An obvious alternative to this tagging algorithm is to choose the two highest p_T jets as the tags (the $p_T - p_T$ tagging algorithm). At this point it is worth noting that for the signal process the choice of tagging jets is largely irrelevant; less than 20% of the signal events that pass the Basic Acceptance cuts have more than two jets. Therefore the best tagging jet algorithm may be freely chosen as that which reduces the background by the greatest amount.

A comparison of the $p_T - \eta$ and $p_T - p_T$ tagging algorithms is shown in Table 6.5; all other elements of the analysis are identical apart from the tagging algorithm used. For both the signal and background processes the rate after application of the

	signal		$t\bar{t} + jets$		EW $WW + jets$	
	$p_T - \eta$	$p_T - p_T$	$p_T - \eta$	$p_T - p_T$	$p_T - \eta$	$p_T - p_T$
Basic Acceptance	18.7	18.7	3740	3740	9.00	9.00
+ Forward Tagging	9.09	8.73	113	44.3	4.51	4.39
+ Central Jet Veto	7.98	8.13	20.0	19.4	4.25	4.29
+ Lepton Angular	4.88	4.98	1.59	1.59	0.32	0.32
+ Real τ rejection	4.63	4.74	1.47	1.46	0.28	0.28

Table 6.5: Comparison between signal (for $m_H = 160$ GeV) and $t\bar{t} + jets$ and EW $WW + jets$ background rates (in fb) for $p_T - p_T$ and $p_T - \eta$ tagging algorithms.

Forward Tagging cuts is lower for the $p_T - p_T$ analysis than for the $p_T - \eta$ analysis. This can be understood by considering a three jet event where the hardest jet is found in one pseudorapidity hemisphere and the two other jets are in the other hemisphere. With the $p_T - \eta$ tagging algorithm the hardest jet is chosen as the first tag, and then the furthest forward jet in the other hemisphere chosen as the second tag. The separation of the tagging jets is therefore maximised, and the distribution of $\Delta\eta_{tags}$ shifted to higher values relative to that for the $p_T - p_T$ tagging algorithm, where the hardest of the other two jets is chosen as the second tag, not necessarily the most separated from the first tag. This is illustrated in Fig. 6.6a which shows the $\Delta\eta_{tags}$ distribution for the $t\bar{t} + jets$ background with both tagging algorithms. The cut applied on minimum tagging jet separation will reject more events with the $p_T - p_T$ tagging algorithm than the $p_T - \eta$ tagging algorithm.

In contrast, the Central Jet Veto rejects a smaller amount of events when the $p_T - p_T$ tagging algorithm is used. This can again be explained in terms of the three jet event example used above. With the $p_T - \eta$ tagging algorithm the third jet will always be found between the tags and the event will be vetoed. This is not the case for the $p_T - p_T$ tagging algorithm where the third jet may just as well lie forward of the

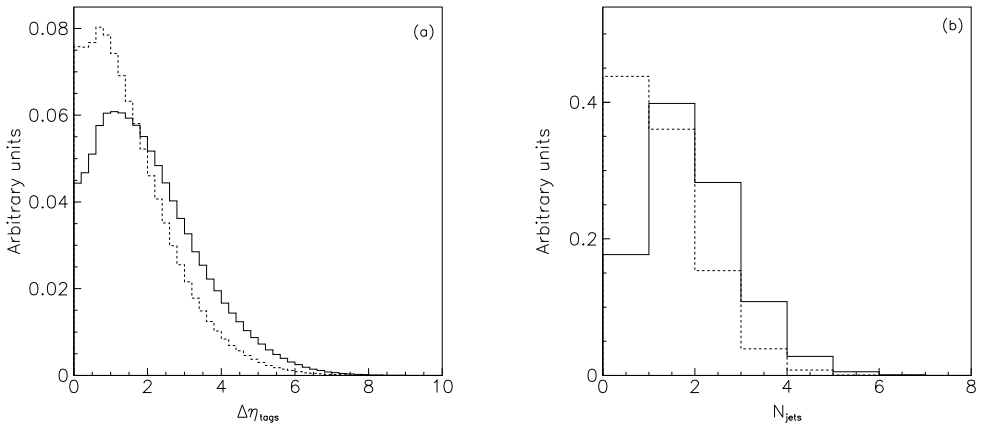

Figure 6.6: (a) Separation of tagging jets in pseudorapidity and (b) multiplicity of jets in the veto region for the $t\bar{t} + jets$ background with $p_T - \eta$ (solid) and $p_T - p_T$ (dashed) tagging algorithms. Histograms normalised to 1.

second tag, outside of the veto region. Fig. 6.6b shows the jet multiplicity inside the veto region for $t\bar{t} + jets$ events with both tagging algorithms; more jets are found in the veto region when the $p_T - \eta$ tagging algorithm is used.

Therefore when choosing the tagging algorithm on the basis of eliminating the most background there is a trade off between the effectiveness of the Forward Tagging cuts and the Central Jet Veto. After all cuts have been applied (the fourth line of Table 6.5) the $p_T - p_T$ tagging algorithm retains the most signal whilst rejecting the most background; it is therefore concluded that the $p_T - p_T$ tagging algorithm performs slightly better than the $p_T - \eta$ tagging algorithm, and will be used for the remainder of this study.

6.1.3 Optimisation of acceptance cuts

Although Fig. 6.5 shows that a favourable signal significance can be achieved for a range of Higgs boson mass with the acceptance cuts as stated in Eqns. (6.1) to (6.6) it is possible that this may be improved by performing a multi-variate optimisation of the cuts. The values of six different cuts are chosen as variables; the separation of tagging jets $\Delta\eta_{tags}$, invariant mass of tagging jets W_{jj}, the lepton angular separation cuts on ϕ_{ll}, $\cos\theta_{ll}$ and ΔR_{ll}, and the di-lepton invariant mass W_{ll}. This six-dimensional cut space is then scanned to find the optimum combination of values for the cuts, taken as being that which maximises the signal significance $S/\sqrt{B}$ for an integrated luminosity of 30 fb^{-1}. The optimisation is performed independently of the Higgs boson mass since some of the cuts are dependent on m_H, particularly the angular separation of the charged leptons. This is achieved by summing the results found for analyses of signal events with Higgs boson masses of 120, 140, 160, 180 and 200 GeV, with the initial cross-sections normalised to that of $m_H = 160$ GeV. For the background only the $t\bar{t} + jets$ and EW $WW + jets$ processes are used for performing the optimisation, since these account for the majority of the total

	signal	background					
		$t\bar{t}+jets$	$WW+jets$		$\tau\tau+jets$		Total
			EW	QCD	EW	QCD	
Basic Acceptance	18.7	3740	9.00	16.2	2.85	198	3970
+ Forward Tagging	10.8	83.3	4.64	1.49	0.97	12.6	103
+ Central Jet Veto	10.1	41.2	4.53	1.35	0.96	11.2	59.2
+ Lepton Angular	4.25	1.00	0.25	0.03	0.44	0.63	2.35
+ Real τ rejection	4.04	0.92	0.22	0.02	0.06	0.08	1.31
+ Lepton ID efficiency	3.27	0.75	0.18	0.02	0.05	0.06	1.06

Table 6.6: Signal (for $m_H = 160$ GeV) and background rates in fb for $e\mu$ channel with optimised cuts outlined in Eqn. (6.7) and $p_T - p_T$ tagging algorithm.

background. The optimum combination of acceptance cut values is found to be

$$\begin{aligned} \Delta\eta_{tags} \geq 3.6 \quad &; \quad W_{jj} \geq 800 \text{ GeV} \\ \phi_{ll} \leq 95^\circ \quad &; \quad \cos\theta_{ll} \geq 0.2 \\ \Delta R_{ll} \leq 1.8 \quad &; \quad W_{ll} \leq 90 \text{ GeV}\,. \end{aligned} \tag{6.7}$$

Compared with the original cuts shown in Eqns. (6.1) to (6.6) the optimised cuts rely less on the separation of the forward tagging jets, with this cut considerably loosened, but more on the angular separation of the charged leptons, with tighter cuts applied on ϕ_{ll} and ΔR_{ll}.

The results of applying the optimised acceptance cuts to signal and background events (with jet tagging performed with the $p_T - p_T$ algorithm) are shown in Table 6.6. Comparing with the original cuts shown in Table 6.1 the signal rate after the application of all cuts is slightly lower, by just over 10%. However, the total background is reduced by a greater amount, more than 30%, predominantly from a reduced rate for the $t\bar{t}+jets$ background. The signal to background ratio after all cuts for $m_H = 160$ GeV is now $\approx 3.1/1$, compared with $\approx 2.4/1$ with the original acceptance cuts.

6.1.4 Results for the $e\mu$ channel

Now that the acceptance cuts have been studied in some detail a final set of results for the $e\mu$ channel is calculated. The analysis presented in Eqns. (6.1) to (6.6) is applied with the optimised cuts shown in Eqn. 6.7 and the $p_T - p_T$ tagging algorithm to signal events for a range of Higgs boson masses and all background processes. The lepton ID efficiency of 0.9 per lepton is then applied to signal and background rates. The final signal and background rates and signal to background ratio are shown in Table 6.7 for $m_H = 120 - 200$ GeV. Compared with the cuts before optimisation (Table 6.4) the signal to background ratios are improved for all values of m_H; a signal to background ratio greater than 1/1 is found for the Higgs boson mass range $m_H = 140 - 200$ GeV.

m_H (GeV)	120	130	140	150	160	170	180	190	200
S (fb)	0.26	0.67	1.32	2.06	3.27	3.42	2.92	2.06	1.64
B (fb)	1.06	1.06	1.06	1.06	1.06	1.06	1.06	1.06	1.06
S/B	0.24	0.63	1.25	1.94	3.09	3.23	2.76	1.94	1.55

Table 6.7: Signal and background rates in fb and signal to background ratios after application of all cuts for $e\mu$ channel with optimised cuts.

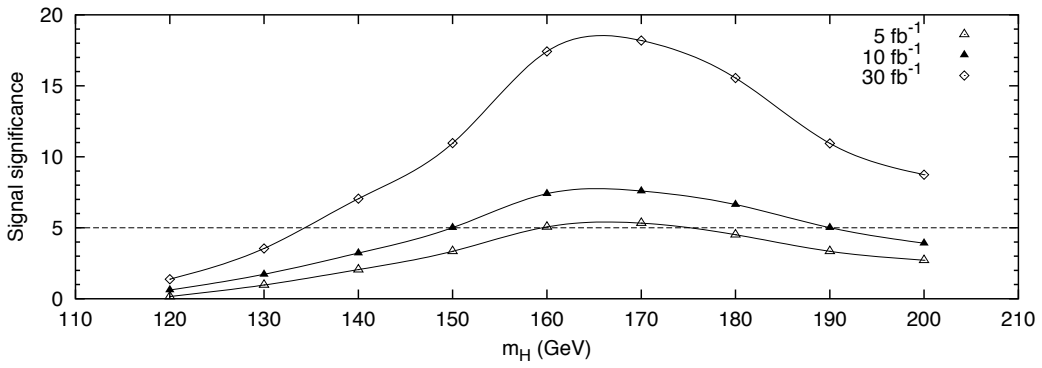

Figure 6.7: Signal significance as a function of Higgs mass for $e\mu$ channel with optimised cuts for integrated luminosities of 5, 10 and 30 fb^{-1}.

The signal significance is shown as a function of Higgs boson mass for integrated luminosities of 5, 10 and 30 fb^{-1} in Fig. 6.7. With 5 fb^{-1} a 5σ discovery can be claimed for $m_H = 160 - 170$ GeV, and the discovery range increases to $m_H = 150 - 190$ GeV for an integrated luminosity of 10 fb^{-1} and $m_H = 140 - 200$ GeV for 30 fb^{-1}. Comparing with the results obtained before optimisation, shown in Fig. 6.5, the discovery range has not been widened, but the signal significances are slightly increased.

6.2 The $H \to WW^{(*)} \to (e^+e^-/\mu^+\mu^-)p_T^{miss}$ channel

So far only the $e\mu$ final state has been considered. However, not taking into account ee and $\mu\mu$ final states immediately reduces the signal rate by a factor of two before any acceptance cuts have been applied. Although extra background processes must be taken into account when considering the $ee/\mu\mu$ channel for pair production processes such as $Z \to ee$, it may still be able to provide a useful contribution to the overall sensitivity for discovery of an intermediate mass Higgs boson.

6.2.1 Initial analysis

To start the investigation of the $ee/\mu\mu$ channel it is assumed that the basic signal and background characteristics will be the same as for the $e\mu$ channel. Therefore the analysis defined in Section 6.1.1 is used, with the $p_T - p_T$ tagging algorithm and optimised acceptance cuts shown in Eqn. (6.7), except for the Basic Acceptance where two electrons or two muons are required to be observed inside the detector, instead of one electron and one muon. In addition to the five background processes considered for the $e\mu$ channel (henceforth referred to as the $e\mu$ background) the processes $Z/\gamma^* \to ee/\mu\mu$, $ZZ \to ee/\mu\mu + X$ and $H \to ZZ \to ee/\mu\mu + X$ are also considered as sources of background. The rates for the signal and backgrounds after

Cuts	signal	$e\mu$ bg	Z/γ^*	ZZ	$H \to ZZ$	total bg
Basic Acceptance	21.0	4010	88900	562	11.0	92900
+ Forward Tagging	12.1	105	4570	14.8	1.82	4670
+ Central Jet Veto	11.3	59.6	3790	9.48	1.19	3850
+ Lepton Angular	4.88	2.45	42.8	0.00	0.14	45.4
+ Real τ rejection	4.67	1.36	21.1	0.00	0.09	22.5
+ $ee/\mu\mu$ cuts	4.24	1.24	0.76	0.00	0.05	2.06
+ lepton ID efficiency	3.43	1.01	0.62	0.00	0.04	1.67

Table 6.8: Signal and background rates for $ee/\mu\mu$ channel in fb after application of successive levels of cuts.

application of cuts up to and including Real τ rejection are shown in the first five lines of Table 6.8. Compared to the $e\mu$ channel the signal and $e\mu$ background rates are slightly higher, but it is the additional background that is most noticeable. Whilst the ZZ background is eliminated entirely by the lepton angular cuts, and $H \to ZZ$ only gives a small additional contribution, the Z/γ^* process now dominates the background. After Real τ rejection the rate for this process is approximately 15 times greater than that for the $e\mu$ background. Consequently the signal to background ratio is only $\approx 1/5$ (for $m_H = 160$ GeV), compared with $\approx 3.1/1$ for the $e\mu$ channel.

Therefore additional acceptance cuts need to be developed to reduce the rate of the Z/γ^* background if the $ee/\mu\mu$ channel is to give a significant contribution towards observing an intermediate mass Higgs boson.

6.2.2 Additional acceptance cuts for $ee/\mu\mu$ channel

There are several features of the Z/γ^* background that may allow it to be distinguished from the signal. Firstly, for $Z \to ee/\mu\mu$ events the di-lepton invariant mass W_{ll} should cluster around the Z mass, whereas for $\gamma^* \to ee/\mu\mu$ events the di-lepton invariant mass should be relatively small. The W_{ll} distributions for the signal and Z/γ^* background after the application of all acceptance cuts up to and including Real τ rejection are shown in Fig. 6.8a. Only a small peak at the Z mass from

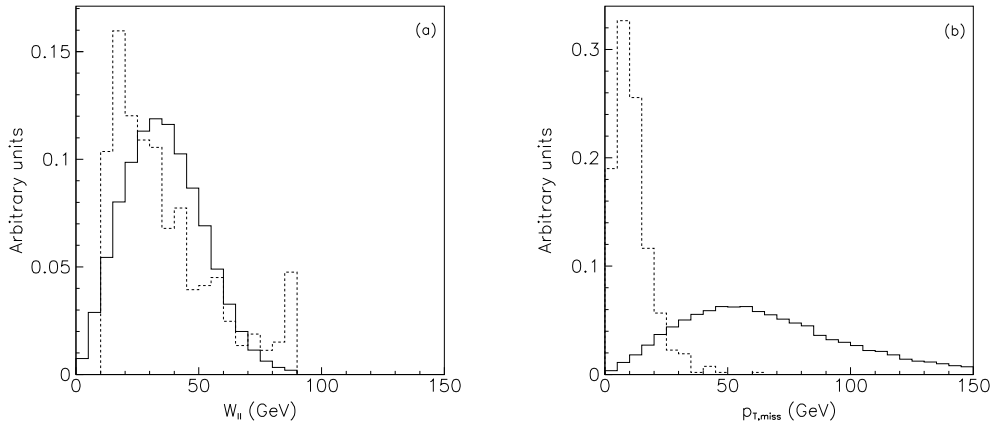

Figure 6.8: (a) Di-lepton invariant mass and (b) missing transverse momentum for signal (with $m_H = 160$ GeV, solid) and $Z/\gamma^* \to ee/\mu\mu$ background (dashed). Histograms normalised to 1.

$Z \to ee/\mu\mu$ events is observed, since the majority of these events have already been rejected by the cut of $W_{ll} < 90$ GeV applied during the Lepton Angular cuts. An additional cut requiring $W_{ll} < 85$ GeV will eliminate the rest of the background events with W_{ll} around the Z mass with a negligible effect on the signal. The majority of the W_{ll} distribution for the Z/γ^* background, though, takes lower values consistent with being from $\gamma^* \to ee/\mu\mu$ events. However, the signal has a very similar distribution and there is no opportunity for further background reduction.

Secondly, since there are no neutrinos involved in the final state for the Z/γ^* process a smaller amount of missing transverse momentum is expected compared to the signal process, which has two neutrinos in the final state. The p_T^{miss} distributions for the signal and Z/γ^* background are shown in Fig. 6.8b. The tendency for much lower missing transverse momentum in Z/γ^* events is clearly illustrated, therefore applying a cut on the minimum p_T^{miss} should eliminate a large proportion of this background whilst leaving the signal largely untouched. The *$ee/\mu\mu$ cuts* are therefore defined as

$$W_{ll} \leq 85 \text{ GeV} \;\; ; \;\; p_T^{miss} \geq 25 \text{ GeV} . \tag{6.8}$$

The application of the $ee/\mu\mu$ cuts to signal and background processes is shown in

the sixth line of Table 6.8. Whilst the signal rate has been reduced by only $\approx 10\%$ the rate for the Z/γ^* background is drastically cut so that it is considerably less than that for the $e\mu$ background; the signal to background ratio is now $\approx 2.1/1$ for $m_H = 160$ GeV. Finally the lepton identification efficiency of 0.9 per lepton is applied to signal and backgrounds, shown in the last line of Table 6.8.

6.2.3 Results for the $ee/\mu\mu$ channel

The acceptance cuts outlined above are applied to signal events for Higgs boson masses in the range $m_H = 120 - 200$ GeV and all background processes. The signal and background rates and signal to background ratios after all cuts are shown in Table 6.9. Comparing with the results for the $e\mu$ channel shown in Table 6.7 the $ee/\mu\mu$ channel has an inferior signal to background ratio for all values of the Higgs boson mass, to be expected due to the additional background processes that have been considered. A signal to background ratio greater than 1/1 is still found for a mass range of $m_H = 150 - 190$ GeV, however.

The signal significance of the $ee/\mu\mu$ channel for integrated luminosities of 5, 10 and 30 fb^{-1} is shown as a function of Higgs boson mass in Fig. 6.9. With 5 fb^{-1} of data it is not possible to obtain a 5σ signal for any value of the Higgs boson mass, but with 10 fb^{-1} a 5σ discovery may be claimed for $m_H = 160 - 180$ GeV. After

m_H (GeV)	120	130	140	150	160	170	180	190	200
S (fb)	0.27	0.69	1.33	2.21	3.43	3.58	2.99	2.05	1.60
B (fb)	1.64	1.67	1.69	1.68	1.67	1.66	1.66	1.65	1.65
S/B	0.16	0.41	0.79	1.31	2.06	2.15	1.80	1.24	0.97

Table 6.9: Signal and background rates in fb and signal to background ratios after application of all cuts for the $ee/\mu\mu$ channel.

3 years of low luminosity running (30 fb^{-1}) the discovery range is $m_H = 140 - 200$ GeV. Compared to the $e\mu$ channel the discovery potential of the $ee/\mu\mu$ channel for a SM Higgs boson is less with the lower luminosities of 5 and 10 fb^{-1} , but with 30 fb^{-1} of data it is still possible to claim a 5σ discovery for $m_H = 140 - 200$ GeV, albeit with a lower signal significance. Therefore the $ee/\mu\mu$ channel does provide additional discovery potential for an intermediate mass Higgs boson even with the extra background processes considered.

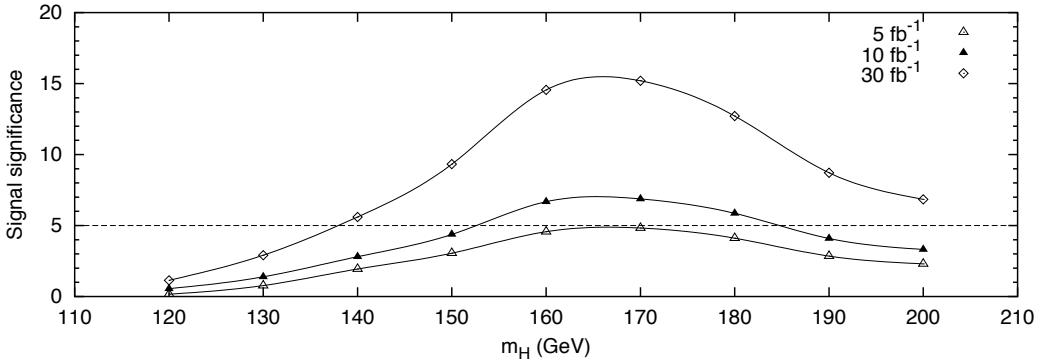

Figure 6.9: Signal significance as a function of Higgs mass for $ee/\mu\mu$ channel with integrated luminosities of 5, 10 and 30 fb^{-1}.

6.3 Combined $e\mu$ and $ee/\mu\mu$ channels

To maximise the discovery potential for an intermediate mass Higgs boson produced via weak boson fusion the results from $H \to WW^{(*)} \to e^{\pm}\mu^{\mp}p_T^{miss}$ and $H \to WW^{(*)} \to (e^+e^-/\mu^+\mu^-)p_T^{miss}$ channels described in Sections 6.1 and 6.2 should be combined. In this section the combined $e\mu$ and $ee/\mu\mu$ results will be presented, the effect of systematic uncertainties on signal and background rates discussed and the results compared with those found for other Higgs boson discovery channels. Finally, a method for determining the Higgs boson mass using the transverse mass will be presented.

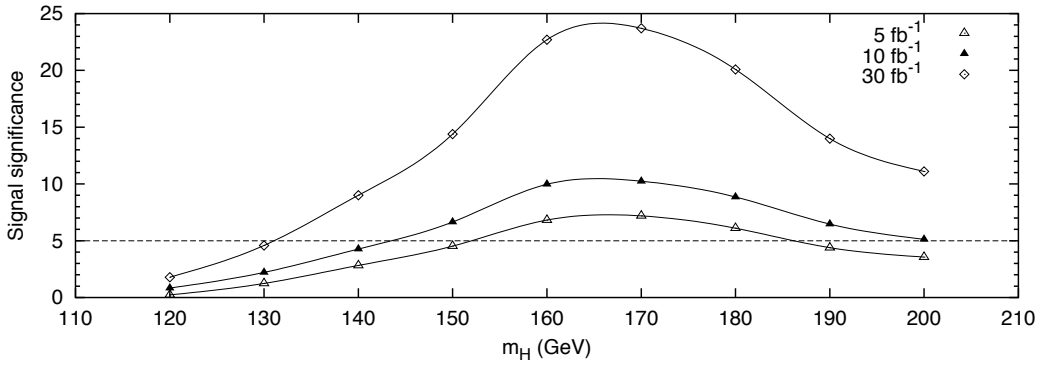

Figure 6.10: Signal significance as a function of Higgs boson mass for combined $e\mu$ and $ee/\mu\mu$ channels with integrated luminosities of 5, 10 and 30 fb^{-1}.

6.3.1 Combined results of $e\mu$ and $ee/\mu\mu$ channels

The combined signal significance of the $e\mu$ and $ee/\mu\mu$ channels σ_{tot} is calculated by adding the individual signal significances $\sigma_{e\mu}$ and $\sigma_{ee/\mu\mu}$ in quadrature,

$$\sigma_{tot} = \sqrt{\sigma_{e\mu}^2 + \sigma_{ee/\mu\mu}^2}\,. \tag{6.9}$$

The combined signal significance is shown as a function of Higgs boson mass for integrated luminosities of 5, 10 and 30 fb^{-1} in Fig. 6.10. With 5 fb^{-1} of data a 5σ signal can now be obtained for the mass range $m_H = 160-180$ GeV, an improvement over either the $e\mu$ or $ee/\mu\mu$ channels alone. With 10 fb^{-1} the discovery range has been increased to $m_H = 150 - 200$ GeV, but with 30 fb^{-1} there is no improvement over either channel alone in terms of discovery range, still $m_H = 140 - 200$ GeV, although the actual signal significance has been increased and is now well above the 5σ level for all of this mass range.

Therefore the combined WBF $H \to WW^{(*)} \to e^{\pm}\mu^{\mp}p_T^{miss}$ and $H \to WW^{(*)} \to (e^+e^-/\mu^+\mu^-)p_T^{miss}$ channels appear to provide excellent discovery potential for an intermediate mass Higgs boson with $m_H = 140 - 200$ GeV. However, the effect of systematic uncertainties on the expected signal and background rates have not yet been considered. These are especially important for the channels considered here

since the lack of a mass peak means that a signal can only be observed through an excess of events above the expected SM background.

6.3.2 Systematic uncertainties on signal and backgrounds

There are two ways in which systematic uncertainties can affect the discovery potential of the channels studied in Sections 6.1 and 6.2. Firstly systematic uncertainties may be defined on signal and backgrounds due to limited knowledge at present, which should be improved before data taking at ATLAS begins. Examples of this could include Monte Carlo predictions, which are undergoing continual improvement, and calibration of detector efficiencies for lepton identification and jet reconstruction, which will not be known definitively until construction of the detector is completed. Therefore the signal and background rates quoted here may be adjusted by the time that ATLAS running starts, and the effect of this on the signal significance can be addressed by considering worst case scenarios of a reduction in signal rate and an increase in background rate. Secondly, the observation of a signal in these channels relies purely upon an excess of events above the expected Standard Model background. Even after Monte Carlo modelling of the background and tuning to data some systematic uncertainty on the number of background events will remain. The effect of this is that an increased excess of signal events over the expected background is required to claim a discovery relative to the background being known exactly.

Potential sources of systematic uncertainties

All events used for the analyses of the $e\mu$ and $ee/\mu\mu$ channels presented in Sections 6.1 and 6.2 were generated with the internal processes of the PYTHIA Monte Carlo (apart from the EW backgrounds which will be mentioned later). It should be remembered that Monte Carlo event generators are only models and must be treated with an inherent degree of uncertainty. To provide an independent cross check on

the results obtained from events generated with PYTHIA signal and background events have also been generated with the HERWIG Monte Carlo, with ATLFAST again providing the detector model.

Considering the signal first, a comparison between identical analyses of PYTHIA and HERWIG generated events for the $e\mu$ channel (using the optimised cuts) is shown in Table 6.10. After all cuts have been applied the rates from the two different analyses agree to within $\approx 5\%$, with the rate from the HERWIG analysis being slightly higher for $m_H = 140$ and $m_H = 160$ GeV, but slightly lower for $m_H = 180$ GeV. However, different stages of the analysis affect the signal rate quite differently for the two event generators. For instance, the forward tagging cuts reject more events in the PYTHIA analysis for all values of m_H. The separation of tagging jets for both analyses is shown in Fig. 6.11a; the HERWIG generated signal events tend towards slightly larger tagging jet separations and the cut applied on minimum tagging jet separation therefore rejects fewer events with HERWIG. The central jet veto also rejects more events for the signal for PYTHIA generated events. However, the lepton angular cuts reject more events when HERWIG is used; the charged leptons in HERWIG generated signal events tend to have slightly wider separations than in PYTHIA generated signal events, illustrated in Fig. 6.11b for the azimuthal opening angle of the leptons.

	$m_H = 140$ GeV		$m_H = 160$ GeV		$m_H = 180$ GeV	
	Pythia	Herwig	Pythia	Herwig	Pythia	Herwig
Basic Acceptance	8.41	9.00	18.7	20.1	19.1	20.6
+ Forward Tagging	4.71	5.39	10.8	12.6	11.4	13.2
+ Central Jet Veto	4.39	5.31	10.1	12.4	10.6	12.9
+ Lepton Angular	1.77	1.98	4.25	4.56	3.84	3.88
+ Real τ rejection	1.64	1.71	4.04	4.12	3.61	3.49
+ Lepton ID efficiency	1.32	1.39	3.27	3.33	2.92	2.82

Table 6.10: Comparison between PYTHIA and HERWIG generated signal events. Rates are in fb.

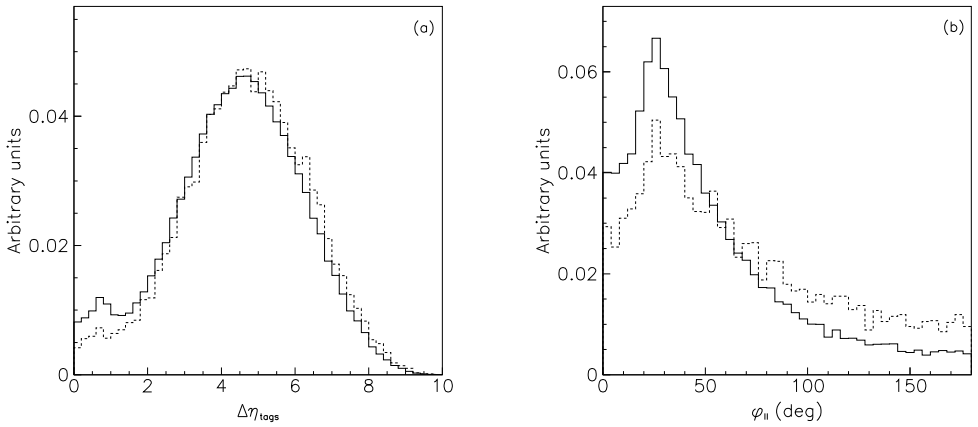

Figure 6.11: (a) Separation of tagging jets and (b) azimuthal opening angle of leptons for signal ($m_H = 160$ GeV) events generated with PYTHIA (solid line) and HERWIG (dashed line). Histograms normalised to 1.

For the background only $t\bar{t} + jets$ events have been generated with HERWIG, since this process accounts for the majority of the background for the $e\mu$ channel. A comparison of identical analyses performed on PYTHIA and HERWIG generated $t\bar{t} + jets$ events is shown in Table 6.11. After all cuts have been applied the rates for the two different analyses are almost identical. In common with the signal events, though, different stages of the analysis affect the $t\bar{t} + jets$ rate in different ways.

For the PYTHIA generated events the forward tagging cuts reject a greater proportion of events, a consequence of HERWIG generated events having a tendency

	Pythia	Herwig
Basic Acceptance	3740	3220
+ Forward Tagging	83.3	97.1
+ Central Jet Veto	41.2	38.2
+ Lepton Angular	1.00	1.02
+ Real τ rejection	0.92	0.90
+ Lepton ID efficiency	0.75	0.73

Table 6.11: Comparison between PYTHIA and HERWIG generated $t\bar{t} + jets$ background events. Rates are in fb.

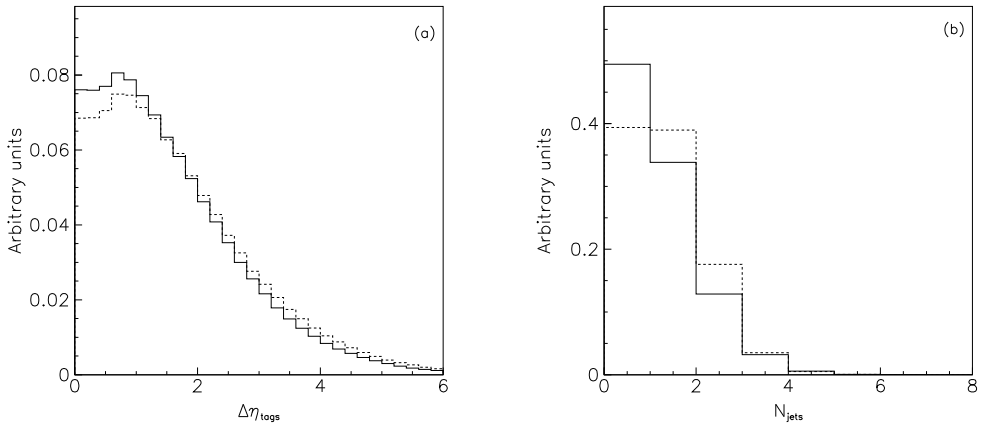

Figure 6.12: (a) Separation of tagging jets and (b) jet multiplicity in the veto region for $t\bar{t} + jets$ background events generated with PYTHIA (solid line) and HERWIG (dashed line). Histograms normalised to 1.

for slightly wider tagging jet separations (see Fig. 6.12a), whereas the central jet veto rejects more of the HERWIG generated events, due to a greater jet multiplicity in the veto region (see Fig. 6.12b). Therefore although some differences are seen between the PYTHIA and HERWIG analyses for both signal and $t\bar{t} + jets$ background events, the final rates predicted are in reasonable agreement and so a degree of confidence about these results may be taken.

Of the other background processes the two EW backgrounds could only be generated by interfacing the original matrix element code used in Ref. [18] to PYTHIA, which then added initial and final state radiation and hadronisation. These results should therefore be treated with some caution until an independent generation of the EW processes is available. For the total background rate of the $ee/\mu\mu$ channel the $Z/\gamma^* \rightarrow ee/\mu\mu$ process is very important. However, due to its large initial cross-section even with the 32 million generated events used here the statistics are very low after all cuts have been applied; the predicted rate for this process therefore carries some amount of uncertainty. Finally, the background processes that have not been considered, such as $b\bar{b}$ production, could also lead to an increased background rate.

Another potential source of systematic uncertainties on both the signal and background rates come from the proton structure functions. The CTEQ5L set of proton structure functions have been used for all event generation in this thesis. However, the initial cross-sections for both signal and background processes can vary by as much as 10% when different sets of structure functions are used, and this may consequently cause differences in the signal and background rates after all acceptance cuts have been applied.

As well as the uncertainties intrinsic to the Monte Carlo event generation detector effects should also be taken into account. For instance, in the analysis performed here a lepton identification efficiency of 0.9 per lepton has been applied to the signal and background rates after all cuts. This is only a nominal figure and the actual situation will almost certainly be more complicated with some degree of spatial variation due to the construction of the detector, and also different efficiencies for electrons and muons due to the different detector subsystems used. Another feature essential to this study is forward jet tagging. As was mentioned in Section 5.5.3 whilst comparisons of forward jet tagging efficiencies between the ATLFAST fast detector simulation and full detector simulation are favourable for $|\eta| < 4$, at larger pseudorapidities it was found that ATLFAST gave a higher efficiency. Whilst this should not affect the rates for the QCD backgrounds, where the jets are generally in the central regions of the detector, the signal and EW background processes have characteristic forward jets. An over-estimation of the jet-finding efficiency in this region by ATLFAST will imply that the signal rates given here may be slightly optimistic, although similarly the EW background rates would also be too large.

Signal significance for worst case scenario

In the event of the signal and background rates given here are in fact changed due to systematic uncertainties such as those mentioned above it is important that the potential effect on the signal significance is investigated. This is done by considering worst case scenarios where the calculated signal and background rates after all

cuts are decreased and increased respectively to take into account systematic uncertainties. Two different scenarios of nominal systematic uncertainties are applied; a moderate scenario of a 10% decrease in the signal rate and a 50% increase in the background rate, and a more severe scenario where a 20% decrease in the signal rate is accompanied by a 100% increase in the background rate.

Signal significances for the combined $e\mu$ and $ee/\mu\mu$ channels with no systematic uncertainties, the moderate scenario and the severe scenario are shown for integrated luminosities of 5, 10 and 30 fb^{-1} in Figs. 6.13a, 6.13b and 6.13c respectively. With an integrated luminosity of 5 fb^{-1} and no systematic uncertainties applied to the signal or background rates a 5σ signal can be obtained for $m_H = 160 - 180$ GeV. By imposing the moderate scenario of systematic uncertainties the Higgs boson mass range for which a 5σ signal can be observed is limited to $m_H = 160 - 170$ GeV, and with the severe scenario it is not possible to claim a 5σ discovery for any value of m_H. With 10 fb^{-1} of data the discovery range of $m_H = 150 - 200$ GeV without the application of any systematic uncertainties is reduced to $m_H = 150 - 190$ GeV with the moderate scenario and $m_H = 160 - 180$ GeV with the severe scenario. Finally, with 30 fb^{-1} of data the discovery range of $m_H = 140 - 200$ GeV with no systematic uncertainties is not changed by either the moderate scenario or severe scenarios, although the actual signal significance is considerably reduced.

Therefore whilst the Higgs mass range for which a 5σ discovery can be claimed is reduced considerably by a reduction in signal rate and increase in background rate at lower luminosities, with the full 30 fb^{-1} of data provided by 3 years of low luminosity running a 5σ signal can still be observed for $m_H = 140 - 200$ GeV even when a doubling of the background rate is considered. It may be concluded that the discovery potential of these channels for an intermediate mass Higgs boson is robust against changes in signal and background rate at the levels investigated here.

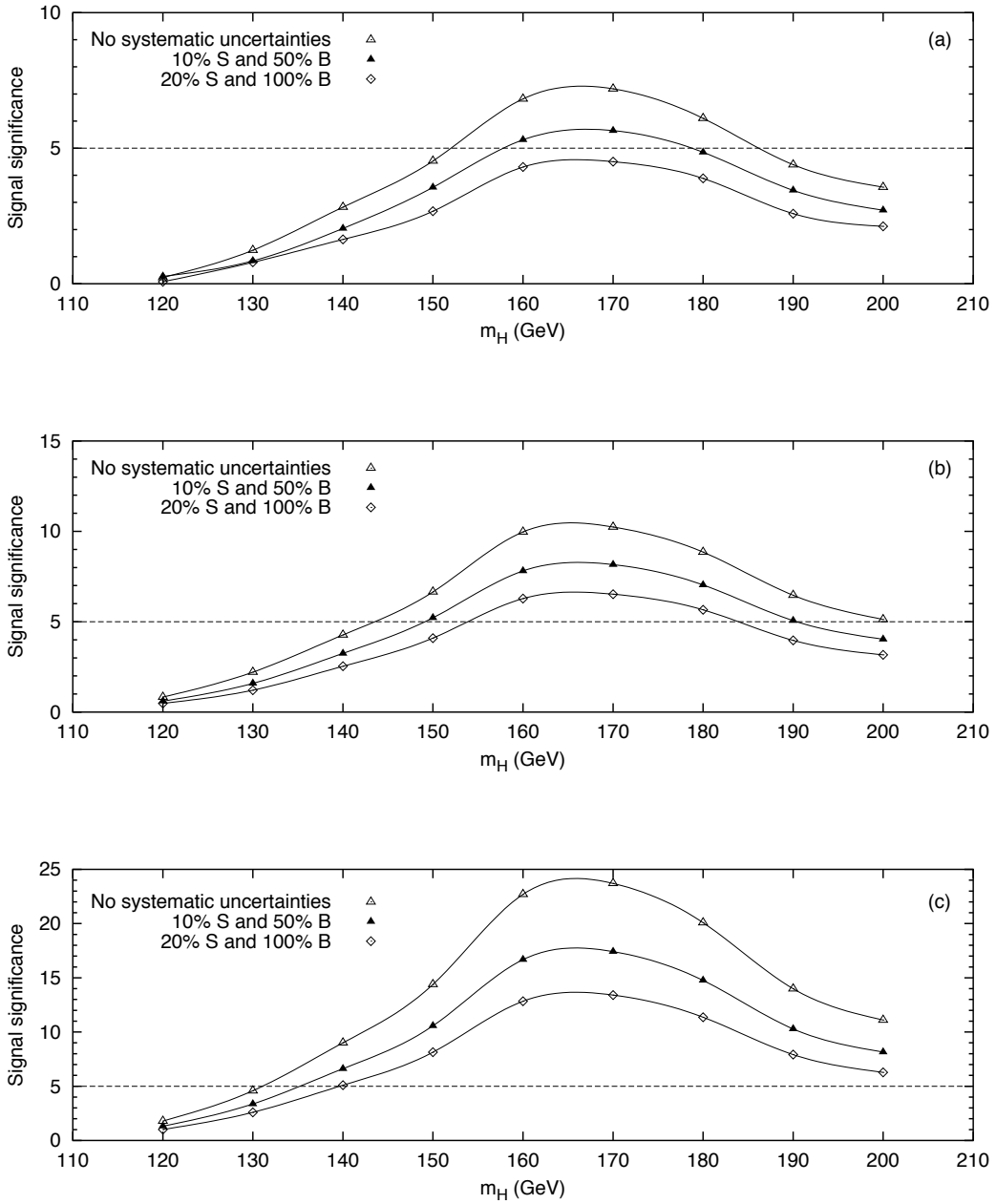

Figure 6.13: Signal significance for combined $e\mu$ and $ee/\mu\mu$ channels with systematic uncertainties on signal and background rates for integrated luminosities of (a) 5 fb^{-1}, (b) 10 fb^{-1} and (c) 30 fb^{-1}.

Systematic uncertainty on absolute background rate

As no mass peak can be reconstructed for either of the channels considered here due to the neutrinos in the final state a signal can only be observed as an excess of events above the expected Standard Model background. An excellent knowledge of the background is therefore required. Whilst it is expected that by tuning Monte Carlo simulation of the background to experimental data it will be possible to calculate the number of expected background events with a reasonable degree of accuracy some amount of systematic uncertainty on the absolute background rate will remain. This will affect the ability to claim a discovery, with a greater excess of events needing to be observed relative to a situation where the background is known exactly.

The presence of a systematic uncertainty on the background can be incorporated by smearing the distribution of the expected number of background effects due to statistical uncertainties with a distribution representing the systematic uncertainty. This can be done pragmatically by combining the standard deviation $\sqrt{B}$ of a Gaussian distribution of background events centred at B in quadrature with the systematic uncertainty ΔB on the number of background events to give a new effective background distribution with standard deviation $\sqrt{B}_{sys}$:

$$\sqrt{B}_{sys} = \sqrt{B + \Delta B^2}\,. \tag{6.10}$$

The signal significance is now quoted in terms of $S/\sqrt{B}_{sys}$. The effect on the signal significance for the combined $e\mu$ and $ee/\mu\mu$ channels of both a 5% and 10% systematic uncertainty on the absolute knowledge of the background rate is shown for an integrated luminosity of 30 fb^{-1} in Fig. 6.14. Due to the favourable signal to background ratio only a small decrease in signal significance is seen even with a 10% systematic uncertainty on the background, and the discovery range is not affected. The signal significance is still well above the 5σ level for the Higgs boson mass range $m_H = 140 - 200$ GeV.

Therefore whilst a more rigorous statistical treatment of a systematic uncertainty on the knowledge of the background rate will ultimately be needed it is not expected

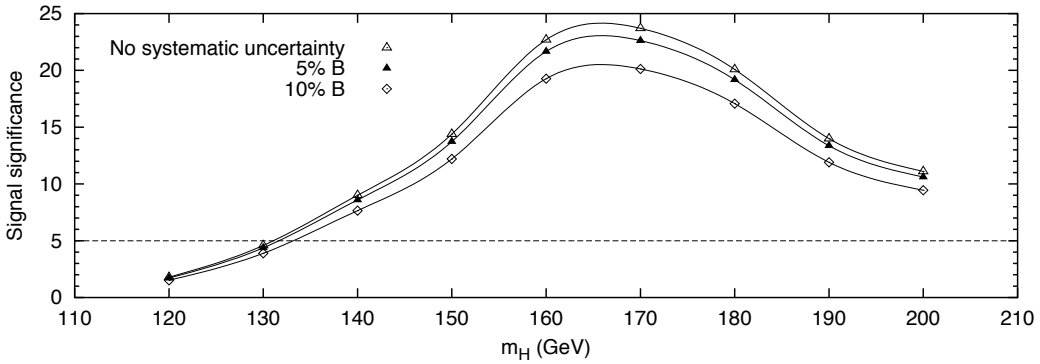

Figure 6.14: Signal significance for combined $e\mu$ and $ee/\mu\mu$ channels with a systematic uncertainty on the absolute knowledge of the background rate, for an integrated luminosity of 30 fb^{-1}.

that an uncertainty at the 10% level will adversely affect the discovery potential.

6.3.3 Comparison with other channels

Now that the signal and backgrounds for the WBF $H \to WW^{(*)} \to l^+l^-p_T^{miss}$ channel have been studied in some detail, as have the effect of systematic uncertainties, the results obtained can be compared against those for other channels investigated for the ATLAS experiment. In the intermediate mass region the two other important channels are direct (Higgs produced by gluon fusion) $H \to ZZ^{(*)} \to 4l$ [81] and direct $H \to WW^{(*)} \to l^+l^-p_T^{miss}$ [83]. The signal significances for these channels are shown as a function of Higgs mass in Fig. 6.15, accompanied by the results found here for WBF $H \to WW^{(*)} \to l^+l^-p_T^{miss}$. The significances for both the direct and WBF $H \to WW^{(*)} \to l^+l^-p_T^{miss}$ channels include a 5% systematic uncertainty on the absolute knowledge of the background rate.

The WBF $H \to WW^{(*)} \to l^+l^-p_T^{miss}$ channel gives the most favourable signal significance for the mass range $m_H = 160 - 180$ GeV by a considerable margin. This is the most important region to cover as $H \to ZZ^{(*)} \to 4l$ is suppressed. For lower and higher values of m_H the $H \to ZZ^{(*)} \to 4l$ channel has a larger signal

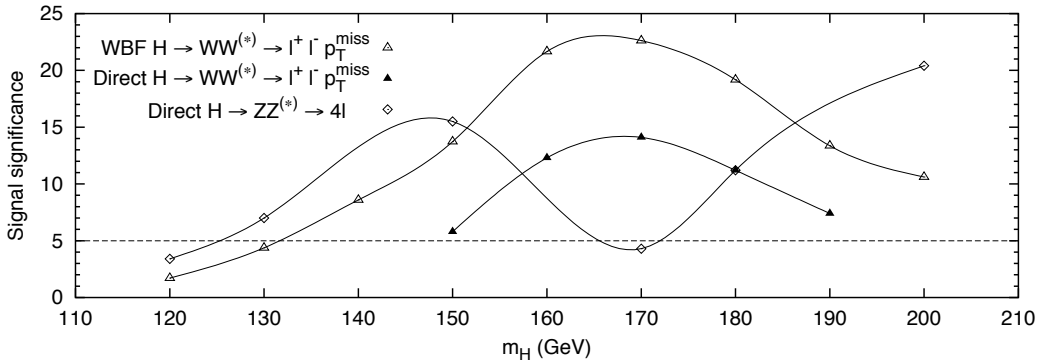

Figure 6.15: Signal significance with 30 fb^{-1} luminosity for WBF $H \to WW^{(*)} \to l^+l^-p_T^{miss}$, direct $H \to WW^{(*)} \to l^+l^-p_T^{miss}$ (from Ref. [83]) and direct $H \to ZZ^{(*)} \to 4l$ channels (from Ref. [81]).

significance, but the WBF $H \to WW^{(*)} \to l^+l^-p_T^{miss}$ channel will still be able to provide an independent confirmation of any discovery.

Another benefit of the WBF $H \to WW^{(*)} \to l^+l^-p_T^{miss}$ channel over its direct counterpart is that it appears to be less susceptible to systematic uncertainties due to its superior signal to background ratio. For the direct $H \to WW^{(*)} \to l^+l^-p_T^{miss}$ channel the signal to background ratio is less than 1/1, and increasing the systematic uncertainty on the background rate from 5 to 10% reduces the signal significance from 14.1 to 8.6 for $m_H = 170$ GeV. For WBF $H \to WW^{(*)} \to l^+l^-p_T^{miss}$ the effect is much smaller, with a decrease in signal significance from 22.6 to 20.1. It is also interesting to note that in the mass range $m_H = 160 - 180$ GeV where the $H \to ZZ^{(*)} \to 4l$ channel is suppressed a discovery can be made with the WBF $H \to WW^{(*)} \to l^+l^-p_T^{miss}$ channel with an integrated luminosity of only 5 fb^{-1}, equivalent to just 6 months of low luminosity running (see Fig. 6.10).

6.3.4 Determination of the Higgs boson mass

As previously mentioned, no mass peak can be reconstructed for the channels considered in this study due to the neutrinos in the final state. However information on

the Higgs boson mass can be extracted from the transverse mass. Assuming that the two charged leptons are emitted in the same direction, and in the opposite direction to the two neutrinos (see Section 5.4.1) then the transverse mass m_T is given by [83]

$$m_T = \sqrt{2p_T^{ll}p_T^{miss}\left(1 - \cos\Delta\phi\right)} \tag{6.11}$$

where p_T^{ll} is the transverse momentum of the charged lepton system, p_T^{miss} is the missing transverse momentum (equivalent to the neutrino system) and $\Delta\phi$ is the azimuthal opening angle between the charged lepton system and the missing transverse momentum.

The transverse mass distributions for the $e\mu$ signal with $m_H = 140$, 160 and 200 GeV are shown in Fig. 6.16. The hard upper edge of the distribution lies very close to the actual Higgs mass for both $m_H = 140$ and $m_H = 160$ GeV. The upper edge of the distribution is not so well defined for $m_H = 200$ GeV, since for higher values of m_H the assumption that the W's are produced at threshold in the rest frame of the Higgs boson starts to break down and the lepton and neutrino from each W decay are not necessarily produced back-to-back. The same distributions are shown added to the background in Fig. 6.17. Although the shape of the background distribution is quite similar to that of the signal the upper edges of the distributions can still just be seen. Even a crude subtraction of the background, for instance subtracting one event from each m_T bin (a rough average value for the background), should allow the Higgs boson mass to be determined to within $\approx 5 - 10$ GeV. However, it should be remembered that in reality it will obviously only be possible to have unit numbers of events in each m_T bin. Since the number of expected signal events is relatively small it would be expected that wider bins would be needed to eliminate statistical fluctuations, thereby reducing the accuracy with which the Higgs boson mass could be calculated from the transverse mass. Even if a signal for a SM Higgs boson is seen through an excess of events in the $H \to WW^{(*)} \to l^+l^-p_T^{miss}$ channel an accurate determination of its mass will probably have to be left to a channel where a mass peak can be reconstructed, for instance the $H \to ZZ^{(*)} \to 4l$ channel

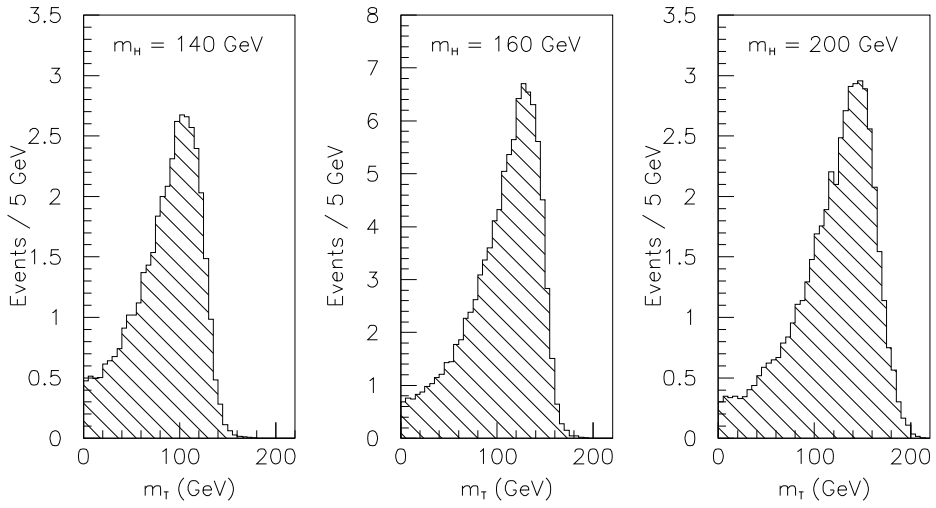

Figure 6.16: Transverse mass distribution of signal for $e\mu$ channel with $m_H = 140$, 160 and 200 GeV, shown as number of events per 5 GeV m_T bin for an integrated luminosity of 30 fb^{-1}.

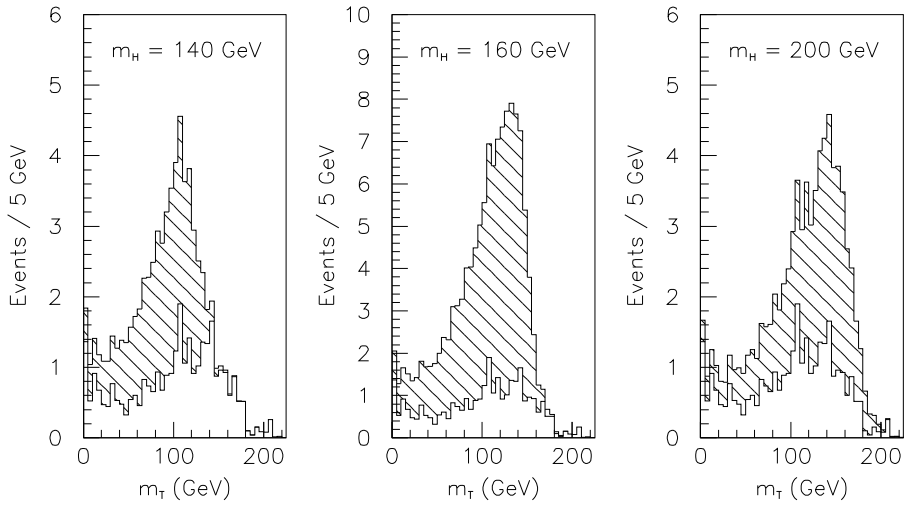

Figure 6.17: Transverse mass distribution of signal (hatched) added to background (plain) for $e\mu$ channel with $m_H = 140$, 160 and 200 GeV, shown as number of events per 5 GeV m_T bin for an integrated luminosity of 30 fb^{-1}.

for the intermediate mass region investigated here.

6.4 $H \to WW^{(*)} \to l^+l^-p_T^{miss}$ for a light Higgs boson

Given that the final LEP results appeared to be consistent with a Higgs boson of mass $m_H \approx 115$ GeV the search for a light Higgs at the LHC is very important. Whilst several channels have been investigated by the ATLAS Collaboration for observing a light Higgs boson, such as $H \to \gamma\gamma$ and $H \to b\bar{b}$ (see Section 5.3), the weak boson fusion $H \to WW^{(*)} \to l^+l^-p_T^{miss}$ channel has recently been investigated in the context of a light Higgs boson via a parton level study, and it was found that a 5σ signal could be isolated with an integrated luminosity of 35 fb^{-1} for $m_H = 115$ GeV [19].

In this section the acceptance cuts developed in Sections 6.1 and 6.2 for an intermediate mass Higgs boson are optimised specifically for the case of a light Higgs boson with $110 \leq m_H \leq 120$ GeV, and additional cuts investigated to maximise the signal significance.

6.4.1 Optimisation of acceptance cuts for a light Higgs boson

The first stage of the analysis is to perform an optimisation of the acceptance cuts specifically for a light Higgs boson. This is done in a similar manner as was described in Section 6.1.3, but for signal events with $m_H = 110$, 115 and 120 GeV. The optimum combination of acceptance cuts for a light Higgs boson is

$$\begin{aligned} \Delta\eta_{tags} \geq 3.7 \quad &; \quad W_{jj} \geq 600 \text{ GeV} \\ \phi_{ll} \leq 40^\circ \quad &; \quad \cos\theta_{ll} \geq -1.0 \\ \Delta R_{ll} \leq 1.0 \quad &; \quad W_{ll} \leq 60 \text{ GeV}\,. \end{aligned} \tag{6.12}$$

	signal	background					
		$t\bar{t}+jets$	$WW+jets$		$\tau\tau+jets$		Total
			EW	QCD	EW	QCD	
Basic Acceptance	0.843	3740	9.00	16.2	2.85	198	3970
+ Forward Tagging	0.433	77.5	4.62	1.44	0.935	11.9	96.4
+ Central Jet Veto	0.403	37.6	4.51	1.30	0.929	10.5	54.8
+ Lepton Angular	0.137	0.420	0.066	0.007	0.158	0.179	0.830
+ Real τ rejection	0.133	0.408	0.063	0.007	0.027	0.056	0.561
+ Light cuts	0.132	0.240	0.042	0.004	0.027	0.056	0.367
+ Lepton ID efficiency	0.107	0.194	0.034	0.003	0.022	0.045	0.298

Table 6.12: Signal (for $m_H = 115$ GeV) and background rates in fb for the $e\mu$ channel using cuts optimised for a light Higgs boson.

The cuts on ϕ_{ll} and ΔR_{ll} are both made much tighter to exploit the relatively small separation of the leptons; for lower values of m_H the assumption that the W bosons are produced at rest in the rest frame of the Higgs boson is increasingly valid. Conversely, the cut on $\cos\theta_{ll}$ is eliminated altogether. The cut on the di-lepton invariant mass is also tightened, to be expected for lower m_H since W_{ll} can be no greater than half the Higgs boson mass.

These cuts are applied to the signal and backgrounds for the $e\mu$ channel, and the results are shown in Table 6.12. Compared to the analysis for an intermediate mass Higgs boson shown in Table 6.6 the background rate after the Real τ rejection cuts have been applied is more than a factor of two smaller with the acceptance cuts optimised for a light Higgs boson. However, this is offset by a much smaller signal rate. The signal rate for a 115 GeV Higgs boson is a factor of 30 smaller after the Real τ rejection cuts than was found for a 160 GeV Higgs boson in Section 6.1.3. The signal to background ratio for a Higgs boson with $m_H = 115$ GeV is only $\approx 1/5$.

Therefore as it stands this channel does not look very promising for a light Higgs boson, and additional cuts are necessary to reduce the background further if it is to prove at all useful for the discovery of a light Higgs boson.

6.4.2 Additional acceptance cuts for a light Higgs boson

The first additional acceptance cut that can be considered for a light Higgs boson is on the transverse mass m_T. Fig. 6.17 shows that the m_T distribution for the background tends towards relatively high values, whereas the signal will have the transverse mass constrained to less than the Higgs boson mass. A cut on the maximum allowed transverse mass should reduce the background rate whilst having a negligible effect on the signal rate. Another cut exploiting the relative closeness of the charged leptons is also applied, on the separation of the leptons in pseudorapidity $\Delta\eta_{ll}$. The *Light cuts* are therefore defined as

$$M_T \geq 125 \text{ GeV} \;\; ; \;\; \Delta\eta_{ll} \geq 1.0\,. \tag{6.13}$$

The result of the application of these cuts is shown in the sixth line of Table 6.12. Whilst the signal rate is not significantly reduced the dominant background processes $t\bar{t} + jets$ and EW $WW + jets$ are both cut by a third or more; the signal to background ratio is now $\approx 1/3$. Finally the lepton ID efficiency of 0.9 per lepton is applied to all signal and background rates, shown in the final line of Table 6.12.

The expected number of signal and background events for both the $e\mu$ and $ee/\mu\mu$ channels are shown in Table 6.13 for an integrated luminosity of 30 fb^{-1}. The $ee/\mu\mu$ channel also includes the additional backgrounds used in Section 6.2 and the use of the $ee/\mu\mu$ cuts defined in Eqn. (6.8). For all values of m_H and for both channels the signal to background ratio is less than 1/1, and the expected number of signal events is small. The signal significances are also shown, calculated using Poisson statistics due to the relatively low number of events. The signal significances are very low; even with both channels combined for the most promising mass, $m_H = 120$ GeV the signal significance is only 1.9. Even increasing the luminosity to 100 fb^{-1} (and ignoring the additional problems associated with high luminosity running, for instance pile-up affecting the central jet veto) it is still not possible to obtain a 5σ signal for $m_H = 110 - 120$ GeV.

Therefore it may be concluded that the WBF $H \to WW^{(*)} \to l^+l^-p_T^{miss}$ channel does

not appear to be favourable for the discovery of a light Higgs boson with $m_H \approx 115$ GeV. This is primarily due to a very low signal rate even before acceptance cuts are applied; in this mass region the branching ratio for $H \to WW$ is less than 10%, whereas in the favourable intermediate mass region it is the dominant decay mode for a SM Higgs boson.

	$e\mu$ channel			$ee/\mu\mu$ channel		
m_H (GeV)	110	115	120	110	115	120
no. S events	1.68	3.22	5.77	1.77	3.41	6.50
no. B events	8.93	8.93	8.93	22.5	22.5	22.5
S/B	1/5.3	1/2.8	1/1.6	1/13	1/6.6	1/3.5
σ_{poiss}	0.24	0.87	1.47	0.27	0.47	1.25

Table 6.13: Number of signal and background events, signal to background ratio and signal significances calculated using Poisson statistics (σ_{poiss}) of $e\mu$ and $ee/\mu\mu$ channels for a light Higgs boson, with an integrated luminosity of 30 fb^{-1}.

6.5 Summary

The potential for the discovery of a light or intermediate mass Standard Model Higgs boson through production by weak boson fusion and subsequent decay via $H \to WW^{(*)} \to l^+l^- p_T^{miss}$ has been investigated with particle level analysis. First, the $H \to WW^{(*)} \to e^\pm\mu^\mp p_T^{miss}$ channel is studied. This was originally suggested in Ref. [18] where a parton level analysis found that a signal could be observed with an integrated luminosity of only 5 fb^{-1} for the intermediate mass range $m_H = 140-190$ GeV. Whilst the particle level study gives a slightly more pessimistic view, with a lower signal rate and higher background rate, after optimisation of the acceptance cuts and forward jet tagging methods discovery ranges at the 5σ level of $m_H = 160-170$ GeV with an integrated luminosity of 5 fb^{-1}, $m_H = 150-190$ GeV with 10 fb^{-1} and $m_H = 140-200$ GeV with 30 fb^{-1} of data are found.

The $H \to WW^{(*)} \to (e^+e^-/\mu^+\mu^+)p_T^{miss}$ channel is also investigated. Additional

backgrounds must be included for lepton pair-production processes which lead to a large increase in the total background rate when an identical analysis as for the $e\mu$ channel is used. The development of extra cuts taking advantage of, predominantly, the difference in the missing transverse momentum distributions between the signal and the $Z/\gamma^* \to ee/\mu\mu$ background enable the total background to be reduced to a level only slightly greater than for the $e\mu$ channel. The signal significance is below the 5σ level for an integrated luminosity of 5 fb^{-1}, but with 10 fb^{-1} of data the discovery range is $m_H = 160 - 180$ GeV and with 30 fb^{-1} of data is the same as for the $e\mu$ channel, $m_H = 140 - 200$ GeV, albeit at lower signal significance.

The results found for the individual $e\mu$ and $ee/\mu\mu$ channels are combined to give the overall discovery potential for the WBF $H \to WW^{(*)} \to l^+l^- p_T^{miss}$ channel. For both channels combined the discovery range for a SM Higgs boson is increased to $m_H = 160 - 180$ GeV with an integrated luminosity of 5 fb^{-1} and $m_H = 150 - 200$ GeV with 10 fb^{-1}. With 30 fb^{-1} of data the discovery range of both channels combined is not improved over either separately, but the significance is increased and is well above the 5σ level for the mass range $m_H = 140 - 200$ GeV. The effect of systematic uncertainties causing a decrease in the signal rate and an increase in the background rate are also investigated. Although the discovery potential at the lower luminosities of 5 and 10 fb^{-1} are restricted by this, with the full 30 fb^{-1} of data afforded by three years of low luminosity running even a 20% decrease in signal and 100% increase in background does not reduce the 5σ discovery range. The inclusion of a systematic uncertainty on the absolute knowledge of the background rate also does not appear to adversely affect the discovery potential. The methods presented here are therefore concluded to be reasonably robust against systematic uncertainties.

The results obtained for the WBF $H \to WW^{(*)} \to l^+l^- p_T^{miss}$ channel are compared against previously proposed methods for the discovery of an intermediate mass SM Higgs boson, namely the direct-produced $H \to ZZ^{(*)} \to 4l$ and $H \to WW^{(*)} \to l^+l^- p_T^{miss}$ channels. For the Higgs boson mass range $m_H = 160{-}180$ GeV the channel

studied here is found to be the most promising, and even though for a lighter or heavier Higgs the $H \to ZZ^{(*)} \to 4l$ channel gives a larger signal significance WBF $H \to WW^{(*)} \to l^+l^-p_T^{miss}$ will be able to provide independent confirmation of any discovery. The ability to extract information on the Higgs boson mass for the WBF $H \to WW^{(*)} \to l^+l^-p_T^{miss}$ channel using the transverse mass is also studied. Whilst the transverse mass distributions do give an indication of m_H it is expected that an accurate determination will have to be left to a channel where a mass peak can be reconstructed, for instance $H \to ZZ^{(*)} \to 4l$.

Finally, the WBF $H \to WW^{(*)} \to l^+l^-p_T^{miss}$ channel is investigated in the context of a search for a light Higgs boson with mass $m_H \approx 115$ GeV. Even with the development of additional acceptance cuts only very low signal significances are found, predominantly due to a low signal rate before the application of cuts. No discovery potential for $m_H = 110 - 120$ GeV with this channel is found.

Chapter 7

Conclusions

The Large Hadron Collider at CERN is currently under construction and when completed will provide new capabilities for particle physics. At the energies that it will be able to provide it is almost certain that new physics will emerge to improve our current understanding of the elementary particles. To be able to make these discoveries it is essential that the detectors at the LHC are able to work effectively, both initially and after being subject to several years in a radiation environment harsher than found in any previous experiment. In this thesis elements of both detector performance and searches for new physics have been presented for the ATLAS experiment, and the important findings will be summarised below. In addition, areas where future work could prove fruitful will be highlighted.

The irradiation of silicon microstrip detectors for the ATLAS SCT at a dedicated proton irradiation facility has allowed the effect of radiation damage to be studied through measurements of their leakage currents performed during irradiation. Throughout irradiation the detectors are held under bias and cooled to the expected operating temperature of the SCT. A model of leakage current evolution with proton fluence is developed from parameterisations of bulk radiation damage effects on both leakage current and the effective doping concentration. Two regions are predicted. At low fluences a linear increase in current with fluence is expected;

analysis of measured leakage currents showed a small systematic shift from this, but no phenomenon could be conclusively identified to explain the observed behaviour. At high fluences an increase in leakage current proportional to the square root of the fluence is expected; no systematic deviation from this behaviour is observed. The radiation damage parameters α, the current-related damage constant, and β, the rate of acceptor creation, are calculated from leakage currents measured during irradiation at temperatures of -8 to -10°C and found to be

$$\begin{aligned} \alpha(20°\mathrm{C}) &= (4.84 \pm 0.13) \times 10^{-17}\ \mathrm{A\,cm^{-1}} \\ \beta &= 0.0630 \pm 0.0018\ \mathrm{cm^{-1}} \end{aligned}$$

in good agreement with those previously published for proton irradiation. The evolution of bulk detector characteristics both during proton irradiation and for a scenario representing operation in the ATLAS detector are modelled. The observed change in leakage currents during proton irradiation is well represented by the model, and the changes in leakage current and full depletion voltage predicted for operation at ATLAS are in agreement with previous experimental studies. However, significant increases in full depletion voltage during operational periods of the LHC are predicted, due to the creation of unstable acceptors that subsequently anneal away completely during maintenance periods. Even taking this into account, though, the detectors are still predicted to remain within safe operational parameters for the whole lifetime of the ATLAS experiment.

Therefore whilst the techniques developed here for studying the radiation damage of ATLAS detectors have enabled important parameters to be calculated it should be remembered that some discrepancies were seen in the low-fluence behaviour that would warrant further study. Two possibilities remain to explain the observations, leakage current annealing and surface damage effects. The former could be investigated with a dedicated experiment for low temperature, short time-scale annealing in a controlled environment. The latter could be investigated by comparing the behaviour during irradiation of simple diodes, where the lack of a significant area of silicon-oxide interface implies that surface effects should be negligible, with that for

segmented microstrip detectors. Measurements of this kind would help to confirm the findings of this thesis.

One of the most important areas of particle physics that will be investigated at ATLAS is the origin of electroweak symmetry breaking. In the Standard Model one Higgs boson is predicted; theoretical constraints limit its mass to less than 1 TeV, and experimental searches at LEP have ruled out $m_H < 114.1$ GeV. The whole of this mass range can be covered at the LHC, but the light and intermediate mass region of $m_H = 115 - 200$ GeV is favoured by precision fits to electroweak data. A Higgs boson produced by weak boson fusion then decaying via $H \rightarrow WW^{(*)} \rightarrow l^+l^-p_T^{miss}$ gives a distinctive signature due to the two forward tagging jets from the scattered quarks, and has been investigated as a possible discovery channel for an intermediate mass Higgs. Acceptance cuts allow the signal to be isolated from the main Standard Model backgrounds with a signal to background ratio greater than one for the majority of the intermediate mass range. It has been found that a 5σ discovery can be made for the mass range $m_H = 160 - 180$ GeV with just 5 fb^{-1} of data, extended to $m_H = 150 - 200$ GeV with 10 fb^{-1} and $m_H = 140 - 200$ GeV with with 30 fb^{-1}. This complements the $H \rightarrow ZZ^{(*)} \rightarrow 4l$ channel, which is suppressed in the region $m_H = 160 - 180$ GeV. Furthermore, the WBF $H \rightarrow WW^{(*)} \rightarrow l^+l^-p_T^{miss}$ channel is found to be robust against systematic uncertainties, either as a decrease in signal rate and increase in background rate or an uncertainty on the absolute knowledge of the background rate. However, determination of the Higgs boson mass is limited to information that can be derived from the transverse mass and the use of this channel for the discovery of a light Higgs boson with $m_H \approx 115$ GeV does not appear to be possible.

Overall the WBF $H \rightarrow WW \rightarrow l^+l^-p_T^{miss}$ channel appears to be very promising for the discovery of an intermediate mass Higgs boson at ATLAS within a relatively short time-scale. Several features remain, though, that should be studied in more detail. Firstly this channel relies upon the ability to tag jets effectively in the far forward regions of the detector. It is not certain whether the ATLFAST fast detector

model used here treats jet finding efficiencies correctly in this region, which could imply that the signal rates quoted here are slightly optimistic. A full investigation of forward jet tagging is therefore of great importance, and is currently under way in the context of searches for Higgs production via weak boson fusion. Secondly, given that the channel studied here looks likely to be the first to provide a discovery for an intermediate mass Higgs boson it is important that the ability to determine the Higgs boson mass from the transverse mass be investigated in greater depth than was performed here.

With the construction of both the Large Hadron Collider and the ATLAS experiment now in progress and the first data expected to be taken by the middle of this decade the future for particle physics is very exciting. With the discovery of new phenomena almost certain, whether it be the Standard Model Higgs boson considered here or one of its alternatives, we can look forward to an increased knowledge of the microscopic world around us.

Bibliography

[1] D. Perkins, Introduction to high energy physics, Addison-Wesley, 1987.

[2] F. Halzen, A. Martin, Quarks and leptons: an introductory course in modern particle physics, Wiley, 1984.

[3] W. Rolnick, The fundamental particles and their interactions, Addison-Wesley, 1994.

[4] D. Groom, et al., Review of particle physics, The European Physical Journal C15 (2000) 1.

[5] The LEP working group for Higgs boson searches, Search for the Standard Model Higgs boson at LEP, hep-ex/0107029 (2001).

[6] The Large Hadron Collider; Conceptual Design, CERN/AC/95-05(LHC) (1995).

[7] ATLAS Collaboration, Technical Proposal for a general purpose pp experiment at the Large Hadron Collider at CERN, CERN/LHCC/94-43 (1994).

[8] CMS Collaboration, CMS, the Compact Muon Solenoid: technical proposal, CERN/LHCC/94-38 (1994).

[9] LHCb Collaboration, LHCb Technical Proposal. A Large Hadron Collider beauty experiment for precision measurements of CP violation and rare decays, CERN/LHCC/98-4 (1998).

[10] ALICE Collaboration, ALICE - Technical proposal for A Large Ion Collider Experiment at the CERN LHC, CERN/LHCC/95-71 (1995).

[11] ATLAS Collaboration, ATLAS Inner Detector Technical Design Report, Volume 1, CERN/LHCC/97-16 (1997).

[12] ATLAS Collaboration, ATLAS Inner Detector Technical Design Report, Volume 2, CERN/LHCC/97-17 (1997).

[13] ATLAS Collaboration, Calorimeter Performance Technical Design Report, CERN/LHCC/96-40 (1996).

[14] ATLAS Collaboration, Liquid Argon Calorimeter Technical Design Report, CERN/LHCC/96-41 (1996).

[15] ATLAS Collaboration, Tile Calorimeter Technical Design Report, CERN/LHCC/96-42 (1996).

[16] ATLAS Collaboration, Muon Spectrometer Technical Design Report, CERN/LHCC/97-22 (1997).

[17] ATLAS Collaboration, ATLAS detector and physics performance technical design report Volume I, CERN/LHCC/99-14 (1999).

[18] D. Rainwater, D. Zeppenfeld, Observing $H \to W^+W^- \to e^\pm\mu^\mp \not{p}_T$ in weak boson fusion with dual forward jet tagging at the CERN LHC, Phys. Rev. D57 (1999) 111.

[19] N. Kauer, et al., $H \to WW$ as the discovery mode for a light Higgs boson, Phys. Lett. B503 (1-2) (2001) 113–120.

[20] S. Sze, Physics of semiconductor devices, John Wiley and Sons, 1981.

[21] A. Bar-Lev, Semiconductors and electronic devices, Prentice-Hall International, 1984.

[22] F. Sauli (Ed.), Instrumentation in high energy physics, World Scientific, 1992, Ch. 1.

[23] W. Leo, Techniques for nuclear and particle physics experiments, Springer-Verlag, 1994.

[24] A. Vasilescu, G. Lindström, Displacement damage in silicon, on-line compilation: http://sesam.desy.de/~gunnar/si-dfuncs.html.

[25] H.-J. Ziock, et al., Temperature dependence of the radiation induced change of depletion voltage in silicon PIN detectors, Nucl. Instr. and Meth. A342 (1994) 96–104.

[26] M. Moll, Radiation damage in silicon particle detectors - microscopic defects and macroscopic properties, Ph.D. thesis, University of Hamburg (1999).

[27] G. Lindström, et al., Radiation hardness of silicon detectors - a challenge from hign energy physics., Nucl. Instr. and Meth. A426 (1999) 1.

[28] A. Chilingarov, et al., Radiation studies and operational projections for silicon in the ATLAS inner detector, Nucl. Instr. and Meth. A360 (1995) 432–437.

[29] R. Wunstorf, Radiation hardness of silicon detectors: current status, IEEE Trans. Nucl. Sci. 44 (3) (1997) 806–814.

[30] G. Lindström, et al., Radiation damage effects in silicon detectors, DESY Report 90-109 (1990).

[31] S. J. Bates, The effects of proton and neutron irradiations on silicon detectors for the LHC, Ph.D. thesis, Darwin College (1993).

[32] R. Wunstorf, et al., Damage-induced surface effects in silicon detectors, Nucl. Instr. and Meth. A377 (1996) 290–297.

[33] Y. Unno, ATLAS silicon microstrip semiconductor tracker (SCT), Nucl. Instr. and Meth. A453 (2000) 109–120.

[34] I. Dawson, C. Buttar, The radiation environment in the ATLAS inner detector, Nucl. Instr. and Meth. A453 (2000) 461–467.

[35] F. Bopp, et al., New parton structure functions and minijets in the 2-component dual parton model, Phys. Rev. D49 (1994) 3236.

[36] P. Aurenche, Multiparticle production in a 2-component dual parton model, Phys. Rev. D45 (1992) 92.

[37] A. Fassò, A. Ferrari, J. Ranft, P. Sala, FLUKA: present status and future developments, in: A. Menzione, A. Scribano (Eds.), Proc IV Int. Conf on Calorimetry in High Energy Physics, La Biodola, 1993, p. 493.

[38] I. Dawson, Private communication.

[39] M. Glaser, et al., New irradiation zones at the CERN-PS, Nucl. Instr. and Meth. A426 (1999) 72–77.

[40] G. Lindström, et al., Radiation hard silicon detectors - developments by the RD48 (ROSE) collaboration, Nucl. Instr. and Meth. A466 (2001) 308–326.

[41] K. Bernier, et al., Calibration of secondary emission monitors of absolute proton beam intensity in the CERN SPS north area, CERN 97-07 (1997).

[42] Thermo Haake, Thermo Haake HQ, Dieselstr. 4, Karlsruhe, BW 76227, Germany.

[43] Pickering Interfaces Ltd., Stephenson Road, Clacton-On-Sea, Essex, CO15 4NL, UK.

[44] Keithley Instruments Ltd., Unit 2 Commerce Park, Brunel Road, Theale, Reading, Berkshire, RG7 4AB, UK.

[45] CAEN S.p.A, Via Vetraia, 11, 55049-Viareggio (LU), Italy.

[46] National Instruments Corporation (UK) Ltd., 21 Kingfisher Court, Hambridge Road, Newbury, Berkshire, RG14 5SJ, UK.

[47] G. Casse, et al., Introduction of high oxygen concentrations into silicon wafers by high-temperature diffusion, Nucl. Instr. and Meth. A438 (1999) 429–432.

[48] S. Albergo, et al., Comparitive study of $\langle 111 \rangle$ and $\langle 100 \rangle$ crystals and capacitance measurements on Si strip detectors in CMS, Il Nuovo Cimento 112A (11) (1999) 1261–1269.

[49] G. Casse, et al., Comparison between ATLAS forward microstrip detectors made on 6" $\langle 100 \rangle$ and 4" $\langle 111 \rangle$ crystal orientation silicon wafers, Il Nuovo Cimento 112A (11) (1999) 1253–1259.

[50] T. Akimoto, et al., Characteristics of irradiated silicon microstrip detectors with $\langle 100 \rangle$ and $\langle 111 \rangle$ substrates, Nucl. Instr. and Meth. A466 (2001) 354–358.

[51] F. Lemeilleur, et al., Study of characteristics of silicon detectors irradiated with 24 GeV protons between -20°C and +20°C, Nucl. Instr. and Meth. A360 (1995) 438–444.

[52] A. Sullivan, An approximate relation for the prediction of dose rate from radioactivity induced in high energy particle accelerators, Health Physics 23 (1972) 253–255.

[53] I. Dawson, Private communication.

[54] C. Gössling, et al., Influence of surface damage on highly segmented silicon detectors, Il Nuovo Cimento 112A (11) (1999) 1369–1376.

[55] D. Menichelli, et al., Modelling of observed double-junction effect, Nucl. Instr. and Meth. A426 (1999) 135–139.

[56] G. Casse, et al., Study of evolution of active volume in irradiated silicon detectors, Nucl. Instr. and Meth. A426 (1999) 140–146.

[57] C. Leroy, et al., Study of charge transport in non-irradiated and irradiated silicon detectors, Nucl. Instr. and Meth. A426 (1999) 99–108.

[58] E. Borchi, et al., A two-level model for heavily irradiated silicon detectors, Nucl. Instr. and Meth. A425 (1999) 343–346.

[59] G. Casse, Private communication.

[60] M. Moll, E. Fretwurst, G. Lindström, Leakage current of hadron irradiated silicon detectors - material dependence, Nucl. Instr. and Meth. A426 (1999) 87.

[61] S. Bates, et al., Proton irradiations of silicon detectors with different resistivities, IEEE Trans. Nucl. Sci. 43 (3) (1995) 1002–1008.

[62] T. Kondo, Yearly operation profile of the ATLAS SCT detectors, ATLAS Internal Note INDET-NO-203 (1998).

[63] A. Ruzin, Recent results from the RD-48 (ROSE) Collaboration, Nucl. Instr. and Meth. A447 (2000) 116–125.

[64] D. Morgan, P. Riedler, et al., Annealing study of ATLAS prototype silicon microstip detectors, ATLAS internal note INDET-NO-199 (1998).

[65] L. Andricek, et al., Radiation hard strip detectors for large-scale silicon trackers, Nucl. Instr. and Meth. A436 (1999) 262–271.

[66] L. Andricek, et al., Evaluation of strip detectors on oxygenated silicon for the ATLAS SCT forward region, ATLAS internal note ATL-INDET-2001-003 (2001).

[67] H. Becker, et al., A proposal for improving the thermal design of the ATLAS SCT end-caps, ATLAS internal note ATL-INDET-2000-019 (2000).

[68] P. Higgs, Broken symmetries, massless particles and gauge fields, Phys. Lett. 12 (1964) 132.

[69] P. Higgs, Spontaneous symmetry breakdown without massless bosons, Phys. Rev. 145 (1964) 1156.

[70] S. Glashow, Partial symmetries of weak interactions, Nuc. Phys. 22 (1961) 579.

[71] S. Weinberg, A model of leptons, Phys. Rev. Lett. 19 (1967) 1264.

[72] B. Lee, et al., Weak interactions at very high energies: the role of the Higgs boson mass, Phys. Rev. D16 (1977) 1519.

[73] G. Altarelli, G. Isidori, Lower limit on the Higgs mass in the Standard Model: an update, Phys. Lett. B337 (1994) 141.

[74] T. Hambye, K. Riesselmann, Matching conditions and Higgs boson mass upper bounds reexamined, Phys. Rev. D55 (1997) 7255.

[75] E. Tournefier, Electroweak results from LEP and SLC and tests of the Standard Model, hep-ex/0105091 (2001).

[76] A. Djouadi, J. Kalinowski, M. Spira, HDECAY: a program for Higgs boson decays in the Standard Model and its supersymmetric extension, hep-ph/9704448 (1997).

[77] R. Barate, et al., Observation of an excess in the search for the Standard Model Higgs boson at ALEPH, Phys. Lett. B495 (1-2) (2000) 1–17.

[78] F. Abe, et al., Search for Higgs bosons produced in association with a vector boson in $p\overline{p}$ collisions at $\sqrt{s} = 1.8$ TeV, Phys. Rev. Lett. 81 (26) (1998) 5748–5753.

[79] M. Roco, Higgs searches at the Tevatron: Run 1 results and Run 2 prospects, FERMILAB-Conf-00/203-E (2001).

[80] M. Carena, J. Conway, H. Haber, J. Hobbs, Report of the Tevatron Higgs Working Group, hep-ph/0010338 (2000).

[81] ATLAS Collaboration, ATLAS detector and physics performance technical design report Volume II, CERN/LHCC/99-15 (1999).

[82] T. Sjöstrand, PYTHIA 5.7 and JETSET 7.4, Computer Physics Commun. (82) (1994) 74.

[83] K. Jakobs, T. Trefzger, SM Higgs searches for $H \to WW^{(*)}l^+\nu\, l^-\nu$ with a mass between 150-190 GeV at LHC, ATLAS internal note ATL-PHYS-2000-015 (2000).

[84] V. Cavasinni, D. Costanzo, Search for $WH \to WWW \to l^{\pm}\nu\, l^{\pm}\nu$ jet-jet, using like-sign leptons, ATLAS Internal note ATL-PHYS-2000-013 (2000).

[85] D. Rainwater, D. Zeppenfeld, K. Hagiwara, Searching for $H \to \tau\tau$ in weak boson fusion at the CERN LHC, Phys. Rev. D59 (1) (1998) 4037.

[86] T. Plehn, D. Rainwater, D. Zeppenfeld, A method for identifying $H \to \tau\tau \to e^{\pm}\mu^{\mp} \not{p}_T$ at the CERN LHC, Phys. Rev. D61 (9) (2000) 3005.

[87] D. Rainwater, Intermediate mass Higgs searches in weak boson fusion, Ph.D. thesis, University of Wisconsin - Madison (1999).

[88] D. Zeppenfeld, Collider physics, hep-ph/9902307 (1999).

[89] V. Barger, et al., Strong W^+W^- scattering signals at pp supercolliders, Phys. Rev. D42 (1990) 3052–3077.

[90] M. Dittmar, H. Dreiner, How to find a Higgs boson with a mass between 155 and 180 GeV at the CERN LHC, Phys. Rev. D55 (1) (1997) 167–172.

[91] M. Dittmar, H. Dreiner, $h^0 \to W^+W^- \to l^+l'^-\nu_l\, \bar{\nu}_{l'}$ as the dominant SM Higgs search mode at the LHC for $M_{h^0} = 155 - 180$ GeV, hep-ph/9703401 (1997).

[92] G. Marchesani, et al., HERWIG a Monte Carlo event generator for simulating Hadron Emission Reactions With Interfering Gluons, Computer Phys. Commun. 67 (1992) 465.

[93] G. Corcella, et al., HERWIG 6: an event generator for Hadron Emission Reactions With Interfering Gluons (including supersymmetric processes), hep-ph/0011363 (2000).

[94] E. Richter-Was, D. Froidevaux, L. Poggioli, ATLFAST 2.0 a fast simulation package for ATLAS, ATLAS Internal note ATL-PHYS-98-131 (1998).

[95] H. Lai, et al., Global QCD analysis of parton structure of the nucleon: CTEQ5 parton distributions, Eur. Phys. J. C12 (2000) 375–392.

[96] Parton level code provided by D. Zeppenfeld. Interface written by R.Mazini.

[97] D. Cavalli, et al., Search for $A/H \to \tau\tau$ decays, ATLAS Internal Note PHYS-NO-051 (1994).